

**CHARACTERISATION OF
STEADY-STATE AND TIME-
VARYING STRUCTURE-BORNE
SOUND SOURCES USING A
RECEPTION PLATE TO PREDICT
IN SITU SOUND PRESSURE LEVELS**

Thesis submitted in accordance with the requirements of the
University of Liverpool for the degree of Doctor of Philosophy

by

Steffi Reinhold

Acoustics Research Unit
School of Architecture
University of Liverpool

August 2021

Abstract

This thesis examines the accuracy in characterising structure-borne sound sources using a heavyweight reception plate at low-frequencies. Statistical Energy Analysis (SEA) is then used to predict maximum Fast time-weighted levels, L_{Fmax} , from time-varying sources such as building machinery in heavyweight buildings.

An experimentally validated Finite Element Method (FEM) model of a heavyweight reception plate was used to assess the power input from steady-state structure-borne sound sources. Numerical and experimental investigations of the spatial variation in velocities of a single-contact source showed that the highest velocities occurred at plate corners/edges; hence, determining the reception plate power by only sampling in the central plate zone led to an underestimation of up to 9 dB below 100 Hz. Sampling approaches were developed to avoid this problem and to reduce the measurement positions by combining the plate velocities at corners/edges and the central zone using an empirical weighting and an area weighting. Area weighting led to <2 dB errors in the reception plate power between 20 Hz to 2 kHz for single-contact sources. FEM was used to determine the power input from multiple-contact sources representing mechanical domestic appliances such as white goods with zero- and random-phase forces between the four contacts and different source orientations on the reception plate. FEM investigations were able to avoid the issue in real measurements where information of the phase relationship between source contacts are rarely known. A bias error could be avoided by excluding all positions underneath the machine along with the reverberation distance from the contacts.

For the prediction of time-varying structure-borne sound power excitation with SEA at the design stage, it was proposed to use an empirical correction to convert short equivalent continuous levels, L_{eq} , into L_{Fmax} levels. A reception plate was used to quantify the maximum time-varying power input, $\max\{L_{eq,125ms}\}$, to allow prediction of L_{Fmax} with SEA using an empirical correction in heavyweight buildings. Predictions of L_{Fmax} were validated against experiments in a room below a concrete floor for direct sound transmission. Comparison between predicted and measured L_{Fmax} in one-third octave bands gave results within ± 3 dB. To simplify this approach, a single-number empirical correction was assessed that could be used in SEA-based models. In addition, it was shown that L_{AFmax} can be estimated from predicted L_{Fmax} values in one-third octave bands to within 0.4 to 2.5 dB. A case study using a real time-varying source on a reception plate was used to reproduce the empirical correction from ramped noise signals, for which the comparison gave similar results.

*“There are two things that are necessary to our work:
Tireless perseverance and the willingness to throw away something
that you put a lot of time and effort into.”*

*“Zwei Dinge sind zu unserer Arbeit nötig:
Unermüdliche Ausdauer und die Bereitschaft, etwas, in das man viel
Zeit und Arbeit gesteckt hat, wieder wegzuwerfen.“*

Albert Einstein

Acknowledgment

The extremely long processing time resulted from the breadth of the topic as well as the problem of duality as a part-time student outside the company and as a contract worker. That the research, despite some doubts, was nevertheless completed in this form, I would like to thank all the remarkable people who helped me, were driving me forward, gave me the courage and incredible patience.

I wish to express my sincere appreciation to my primary supervisor Prof Carl Hopkins, secondary supervisor Prof Barry Gibbs and the soul of the laboratory Dr Gary Seiffert for their guidance, encouragement and constant help.

Most of all, I would like to express my sincere gratitude to Prof Carl Hopkins, who had to endure a lot but never lost faith in me and always tried to get me back to the ground. Carl needed to have the most patience for me and accompanied me as well as possible through my ups and downs. Our discussions, which did not always end with the same opinion, nevertheless guided me through my research in an indescribable good way. I would also like to highlight my sincere appreciation for his time during my numerous stays in Liverpool, which enabled me to be part of the other extreme of very intensive support so that during this time, all other ARU members had to compromise on this matter. That is why my sincerest and deepest thanks go to Carl for his incredible patience, excellent supervision, understanding of my problems and more.

I would particularly like to thank Prof Barry Gibbs for the technical discussions and his very wise advice to "making everything as simple as possible", which, if not always, had a more positive effect on me to finish this thesis. Further, I would like to express my sincere thanks to Barry for his great support in providing literature. The meals that Barry invited me during my time in Liverpool are also unforgettable. They were very entertaining, enjoyable and pleasant.

Special thanks to Dr Gary Seiffert for his encouraging manner that made a lot of things appear easier with funny anecdotes and the necessary help with setting up and performing measurements. To this day, I don't know how Gary did it, but Gary was always there and had always an open ear to my acoustic problems or my issues outside of them.

I gratefully acknowledge my thesis committee, Dr Laurent Galbrun and Dr Pyoung Jik Lee, for their insightful comments and valuable suggestions for this thesis.

Last but not least, I would like to thank Prof Berndt Zeitler for his support and the associated additional time made available to prepare this thesis.

Thank you!

Table of contents

Table of contents	ix
List of tables.....	xv
List of figures	xix
List of abbreviations	xxxiii
List of symbols	xxxv
1 Introduction	1
1.1 Background	1
1.2 Literature review	8
1.2.1 Review of structure-borne sound sources characterisation for building equipment	8
1.2.1.1 General development.....	8
1.2.1.2 Development of the reception plate method.....	10
1.2.1.3 Measurement uncertainty with the reception plate method.....	12
1.2.1.4 Analytical and numerical modelling of the reception plate	17
1.2.1.5 Assessment of the time-varying structure-borne sound power on the reception plate.....	19

Table of contents

1.2.2	Review of prediction models to determine sound pressure levels in buildings	20
1.2.2.1	Steady-state sources	20
1.2.2.2	Time-varying sources.....	22
1.3	Statement of the problem	23
1.4	Objectives.....	26
1.5	Layout of the thesis	27
2	Theory and prediction models	31
2.1	Introduction.....	31
2.2	Bending wave theory and prediction modelling for structure-borne sound characterisation.....	32
2.2.1	Thin plate theory	32
2.2.2	Modal response	35
2.2.3	Diffuse field response	37
2.2.4	Damping.....	38
2.2.5	Mobility.....	40
2.3	Finite Element Method (FEM).....	43
2.3.1	Governing equations for dynamic analysis using FEM	44
2.3.1.1	Eigenvalue analysis.....	46
2.3.1.2	Frequency response analysis.....	48
2.3.2	FEM modelling procedure	49
2.3.2.1	Shell elements	52
2.3.2.2	Damping.....	54
2.3.2.3	Boundary conditions	58
2.3.2.4	Loads	58
2.3.2.5	Mesh.....	59
2.3.2.6	Analysis types	60
2.3.3	FEM data processing for harmonic structural response calculation	62
2.4	Statistical Energy Analysis (SEA).....	63
2.4.1	Power balance equations of direct sound transmission (two-subsystem) SEA	65
2.4.1.1	Modal parameters.....	67
2.4.1.2	Loss factors	67
2.4.1.3	Radiation efficiency	69

2.4.1.4	Energy	71
2.4.1.5	Power input	72
2.4.2	Proposal for the prediction of L_{Fmax} from time-varying sources using SEA based on short L_{eq}	72
2.5	Structure-borne sound power characterisation	75
2.5.1	Direct injection for single- and multiple-contact sources.....	75
2.5.2	Reception plate power	76
2.5.2.1	Theory	76
2.5.2.2	Characteristic reception plate power and installed power for real walls and floors.....	77
2.5.2.3	Potential issues with low-frequency characterisation.....	78
2.6	Summary	81
3	Test constructions and experimental work	83
3.1	Introduction	83
3.2	Test facilities	83
3.2.1	Reception plate test rig	84
3.2.2	Laboratory with suppressed flanking transmission	85
3.3	Measurement of sound, vibration and force.....	86
3.3.1	Measurement system and software.....	87
3.3.2	Excitation and response techniques.....	87
3.3.2.1	Impact hammer.....	87
3.3.2.2	Shaker.....	88
3.3.2.3	Accelerometer	90
3.3.2.4	Microphone	90
3.3.3	Experimental Modal Analysis (EMA).....	91
3.3.3.1	Test method for EMA	91
3.3.3.2	Modal parameter identification	93
3.3.4	Driving-point mobility.....	96
3.3.5	Radiation efficiency.....	99
3.3.6	Spatial variation in plate velocity	101
3.3.7	Time-varying excitation for L_{eq} and L_{Fmax} measurements.....	104
3.3.7.1	Time-varying signals.....	104
3.3.7.2	Analysis of time-varying signals using multi-buffer measurements	106
3.4	Material parameters of the reception plate	121

Table of contents

3.4.1	Concrete plate.....	122
3.4.1.1	Young's modulus	122
3.4.1.2	Damping.....	123
3.4.2	Viscoelastic material	125
3.4.2.1	Dynamic stiffness.....	125
3.4.2.2	Damping.....	128
3.5	Summary	129
4	Reception plate: Experimental validation of FEM models	131
4.1	Introduction.....	131
4.2	FEM modelling	132
4.3	Verification of the FEM code and calculation	136
4.4	Validation of the FEM model with experiments.....	139
4.4.1	Eigenfrequencies and corresponding mode shapes.....	139
4.4.2	Damping	148
4.4.2.1	FEM model of the reception plate.....	148
4.4.2.2	Loss factors from FEM and measurements.....	150
4.4.3	Mobility	157
4.5	Spatial variations in plate velocity under harmonic forced response..	158
4.6	Investigation into the role of rigid body modes	164
4.7	Summary	172
5	Reception plate: Assessment of sampling strategies	175
5.1	Introduction.....	175
5.2	Sampling strategies to estimate the reception plate power	176
5.2.1	Empirical weighting as an individual approach	176
5.2.2	Area weighting as a general approach	178
5.3	Validation of sampling strategies.....	180
5.3.1	Excitation positions from single- and multiple-contact sources in FEM and measurements	180
5.3.2	Single-contact sources assessed by FEM and measurements .	183
5.3.3	Multiple-contact sources assessed by FEM	193
5.4	Discussion	201
5.5	Summary	201

6 Empirical relationships between L_{Fmax} and short L_{eq} for time-varying signals	205
6.1 Introduction	205
6.2 Diffuse field assumption for test constructions	206
6.3 Empirical correction from short L_{eq} to L_{Fmax}	207
6.3.1 Specific empirical correction for known time-varying signals	207
6.3.2 Single-number empirical correction	221
6.4 Summary	222
7 Prediction of L_{Fmax} from time-varying structure-borne sound sources in heavyweight buildings	225
7.1 Introduction	225
7.2 Experimental validation of L_{Fmax} prediction using empirical corrections	226
7.2.1 Specific empirical correction	227
7.2.1.1 Prediction of $L_{v,Fmax}$ on the separating floor	229
7.2.1.2 Prediction of $L_{p,Fmax}$ in the receiving room	231
7.2.2 Single-number empirical correction	233
7.3 Consideration of L_{AFmax} from frequency-dependent L_{Fmax} in the field situation	234
7.3.1 Specific empirical correction	236
7.3.2 Single-number empirical correction	237
7.4 Summary	239
8 Case study: Toilet flush	241
8.1 Introduction	241
8.2 Source description	242
8.2.1 Sanitary installation system	242
8.2.2 Operating mode of a time-varying toilet flush cycle	244
8.3 Experiments on the reception plate test rig	247
8.3.1 Processing of short L_{eq} and L_{Fmax}	248
8.3.2 Empirical correction from short L_{eq} to L_{Fmax}	258
8.3.3 Comparison with time-varying signals of ramped noise	260

Table of contents

8.3.3.1	Specific empirical correction	260
8.3.3.2	Single-number empirical correction.....	264
8.4	Discussion	268
8.5	Summary	268
9	Conclusions	271
9.1	Introduction.....	271
9.2	Structure-borne sound power characterisation using a reception plate.....	272
9.3	Prediction of L_{Fmax} from time-varying signals using SEA.....	274
9.4	Suggestions for future work.....	276
9.4.1	Structure-borne sound power characterisation using a reception plate	277
9.4.2	Prediction of L_{Fmax} from time-varying signals using SEA	278
	References.....	279
	Appendices.....	293

List of tables

Table 4-1.	Reception plate using partial coverage with viscoelastic material: Verification of FEM eigenfrequencies for the whole body mode through comparison with the analytical value.	138
Table 4-2.	Reception plate using partial coverage with viscoelastic material: Eigenfrequencies from EMA and FEM for a reception plate with idealised free boundaries and from EMA and FEM for the reception plate of the experimental set-up using partial coverage with viscoelastic material.	141
Table 4-3.	Reception plate using partial coverage with viscoelastic material: Standing wave pattern from EMA and FEM models for a reception plate with idealised free boundaries and the reception plate of the experimental set-up using partial coverage with viscoelastic material.	143
Table 4-4.	Reception plate using partial coverage with viscoelastic material: Comparison of MAC values from EMA (complex-to-real or complex modes) and FEM eigenfunctions using a reception plate with idealised free boundaries (real modes) and the reception plate of the experimental set-up using partial coverage with viscoelastic material (real and complex modes).....	147
Table 4-5.	Reception plate using partial coverage with viscoelastic material: Standard deviation, s , determined of measured and predicted (FEM) velocity levels in one-third octave bands over the plate surface from single-contact sources at excitation positions 1S and 5S.	163
Table 6-1.	Wav files of 125 ms ramp duration with ramp levels of 10/20/30/40 dB: The specific empirical correction,	

List of tables

	$L_{Fmax} - \max\{L_{eq,125ms}\}$, with regard to minimum (MIN), maximum (MAX) and average (AVG) levels.	216
Table 6-2.	Wav files of 500 ms ramp duration with ramp levels of 10/20/30/40 dB: The specific empirical correction, $L_{Fmax} - \max\{L_{eq,125ms}\}$, with regard to minimum (MIN), maximum (MAX) and average (AVG) levels.	217
Table 6-3.	Wav files of 1 s ramp duration with ramp levels of 10/20/30/40 dB: The specific empirical correction, $L_{Fmax} - \max\{L_{eq,125ms}\}$, with regard to minimum (MIN), maximum (MAX) and average (AVG) levels.	218
Table 6-4.	Wav file of 2 s ramp duration with ramp levels of 10/20/30/40 dB: The specific empirical correction, $L_{Fmax} - \max\{L_{eq,125ms}\}$, with regard to minimum (MIN), maximum (MAX) and average (AVG) levels.	219
Table 6-5.	Wav files of 5 s ramp duration with ramp levels of 10/20/30/40 dB: The specific empirical correction, $L_{Fmax} - \max\{L_{eq,125ms}\}$, with regard to minimum (MIN), maximum (MAX) and average (AVG) levels.	220
Table 7-1.	Wav files of 125 ms, 500 ms, 1 s, 2 s and 5 s ramp durations with ramp levels of 10/20/30/40 dB: Difference between the predicted and measured A-weighted sound pressure levels, L_{AFmax} , when using the specific empirical correction.....	237
Table 7-2.	Wav files of 125 ms, 500 ms, 1 s, 2 s and 5 s ramp durations with ramp levels of 10/20/30/40 dB: Difference between the predicted and measured A-weighted sound pressure levels, L_{AFmax} , when using the single-number empirical correction.....	239
Table 8-1.	Case study of a toilet flush: Information on the peak of ramp A with regard to ramp durations and ramp levels for two toilet flush cycles.	251
Table 8-2.	Case study of a toilet flush: The specific empirical correction, $L_{Fmax} - \max\{L_{eq,125ms}\}$, with regard to minimum (MIN), maximum (MAX) and average (AVG) levels using the peak in ramp A of the filtered toilet flush signal for ‘toilet flush 1’ and ‘toilet flush 2’ from Table 8-1 measured on the horizontal and vertical reception plate.....	259
Table 8-3.	Case study of a toilet flush: Comparison of the specific empirical correction, $L_{Fmax} - \max\{L_{eq,125ms}\}$, using the empirical weighted velocity levels for ‘toilet flush 1’ and ‘toilet flush 2’ from Table 8-1 measured on the horizontal	

and vertical reception plate as well as empirical weighted velocity levels for ramped noise signals measured on the horizontal reception plate from (a) the 500 ms ramp with ramp levels of 10/20/30 dB and (b) the 1 s ramp with ramp levels of 10/20/30 dB.....264

List of figures

Figure 1-1.	General schematic representation of the sound transmission between rooms through the power injection of mechanical domestic appliances under operating conditions.	2
Figure 1-2.	Schematic representation of airborne sound for a noise system adapted from [22].	4
Figure 1-3.	Schematic representation of structure-borne sound for a noise system adapted from [22].	4
Figure 1-4.	Structure-borne sound power input from different machinery under steady-state operating conditions into the low-mobility reception plate measured according to [36, 37].	6
Figure 1-5.	Schematic representation of the surface area projection from a piece of machinery onto a plate-like structure.	7
Figure 2-1.	Driving-point mobility and schematic circuit representation for a mass-spring-dashpot system adapted from [71].	42
Figure 2-2.	FEM modelling flow chart: Processing phases and sources of errors.	50
Figure 2-3.	Typical hysteresis loops of energy dissipated per cycle with regard to the force-displacement relationship [96]: (a) non-linear damping (e.g. solid material under high stress) and (b) linear damping (e.g. solid material under low stress and viscoelastic material).	55
Figure 2-4.	Example of a linear sine sweep function with normalised uniform amplitude over the time for a frequency range from 1 Hz to 2.5 kHz.	59
Figure 2-5.	Power flow of multi-modal contributions of all individual mode pairs between two coupled subsystems.	64

List of figures

Figure 2-6.	Schematic representation of a two-subsystem SEA model for a coupled plate-room system with all occurring power flows.	65
Figure 2-7.	Average time between two successive reflections from boundaries on different finite plate and room boundaries.	74
Figure 2-8.	Schematic representation of a SEA based isolated reception plate model with the occurring power flow.	77
Figure 2-9.	Schematic representation of rigid body modes for (a) whole body (or bouncing) mode with translational motion in the z -axis, (b) rocking mode with rotational motion about the x -axis and (c) rocking mode with rotational motion about the y -axis.	79
Figure 3-1.	Schematic representation of the horizontal concrete reception plate.	84
Figure 3-2.	Schematic representation of the floor test facility representing a building-like situation in heavyweight buildings.	86
Figure 3-3.	Electrodynamic inertial shaker operating under white noise input: Force spectrum as a function of frequency (upper graph) and the difference between upper and lower frequency (lower graph). The red dashed lines indicate the three ranges, which have (1) the suspension resonance, (2) approximately constant acceleration at the exciter table and (3) the moving element resonance.	89
Figure 3-4.	EMA measurement set-up using the 21×29 grid for the roving hammer test with positioned accelerometers (left) and an illustrative impact hit on a corner grid point close to an accelerometer (right).	92
Figure 3-5.	Measurement set-up for driving-point mobility (arrows on accelerometers indicate the axis of maximum sensitivity).	97
Figure 3-6.	Reception plate: Effect of impact hammer with rubber, plastic and steel tips for (a) force impulse, (b) force autospectra, (c) velocity autospectra close to the driving point and (d) coherence between force and velocity signals.	98
Figure 3-7.	Measurement of driving-point mobility using impact hammer with rubber, plastic and steel tips indicating the crossover frequency at 400 Hz for (a) the reception plate and (b) the floor in the building-like situation.	99
Figure 3-8.	Measurement set-up for the spatial variation in plate velocity (left) and the direct injected power (right).	101

- Figure 3-9. Effects of rectangular and Hanning windows using (a) spectral characteristics in the time domain, (b) spectral characteristics in the frequency domain, (c) weighted 10 Hz sinusoid in the time domain, (d and e) corrected and not corrected resulting spikes of 10 Hz sinusoid respectively in the frequency domain..... 103
- Figure 3-10. Example of time-varying signals formed from white noise with ramp durations of 125 ms, 500 ms, 1 s, 2 s and 5 s and an increasing and decreasing ramp level of 20 dB. 105
- Figure 3-11. Multi-buffer measurements for velocity levels measured on the reception plate using (a) $L_{F,125ms}$ levels starting from a time of 0 s up to 12 s with maximum hold, (b) $L_{eq,125ms}$ levels starting from a time of 0 s up to 12 s with maximum hold and (c) the difference between $\max\{L_{eq,125ms}\}$ at the time where $L_{Fmax} = \max\{L_{F,125ms}\}$ (blue line) and $\max\{L_{eq,125ms}\}$ at the time that velocity levels no longer increase (red line). The time-varying signal has a 5 s ramp and a 20 dB ramp level..... 110
- Figure 3-12. Time-varying signal with a ramp duration of 5 s and a ramp level of 40 dB processed with the MATLAB SLM in the time domain: (a) input signal, (b) input signal filtered in TOBs and (c) input signal filtered in TOBs and weighted by the Fast time-weighting constant running from the start of the signal to the current time, t 112
- Figure 3-13. Comparison of the time at which L_{Fmax} occurs with the MATLAB SLM and PULSE using (a) a 500 ms ramp with a 40 dB ramp level and (b) a 5 s ramp with a 40 dB ramp level..... 116
- Figure 3-14. Comparison of L_{Fmax} levels from the MATLAB SLM, $\max\{L_{F,125ms}\}$ and L_{Fmax} levels from PULSE (upper graph) and the difference between $\max\{L_{F,125ms}\}$ levels from PULSE and L_{Fmax} levels from the MATLAB SLM and PULSE (lower graph) using (a) a 500 ms ramp with a 40 dB ramp level and (b) a 5 s ramp with a 40 dB ramp level. 117
- Figure 3-15. Comparison of the time at which $\max\{L_{eq,125ms}\}$ occurs with the MATLAB SLM and PULSE using (a) a 500 ms ramp with a 40 dB ramp level and (b) a 5 s ramp with a 40 dB ramp level..... 118
- Figure 3-16. Comparison of $\max\{L_{eq,125ms}\}$ levels from the MATLAB SLM and PULSE (upper graph) and the difference between

List of figures

	$\max\{L_{eq,125ms}\}$ levels from PULSE and the MATLAB SLM (lower graph) using (a) a 500 ms ramp and 40 dB ramp level and (b) a 5 s ramp and 40 dB ramp level.....	119
Figure 3-17.	PULSE measurements stored as consecutive 125 ms time slices in multi-buffers for pressure levels measured in the field situation using $\max\{L_{AF,125ms}\}$ levels for (a) a 500 ms ramp with a 40 dB ramp level and (b) a 5 s ramp with a 40 dB ramp level.	121
Figure 3-18.	Measurement set-up for the quasi-longitudinal phase velocity of the horizontal reception plate (arrow on accelerometers indicate the axis of maximum sensitivity).....	123
Figure 3-19.	Measurement set-up for the dynamic stiffness of the viscoelastic material.	126
Figure 3-20.	Driving-point mobility of an SDOF system using a concrete cube and viscoelastic material at resonance to quantify the dynamic stiffness from experiments.....	128
Figure 4-1.	FEM models of a reception plate (a) with free boundaries and using (b) partial coverage with viscoelastic material and (c) full coverage with viscoelastic material.	135
Figure 4-2.	Verification of FEM using the driving-point mobility of a lumped mass-spring-dashpot system compared to analytical results and supplemented by experimental results. Measured data is from the dynamic stiffness measurement for the viscoelastic material (taken from Figure 3-20).....	137
Figure 4-3.	Reception plate using partial coverage with viscoelastic material: Comparison of eigenfrequencies from EMA and FEM for a reception plate with idealised free boundaries and from EMA and FEM for the reception plate of the experimental set-up using partial coverage with viscoelastic material.	140
Figure 4-4.	Reception plate using partial coverage with viscoelastic material: Mode count in one-third octave bands from EMA and FEM eigenfrequencies.	142
Figure 4-5.	Reception plate using partial coverage with viscoelastic material: Comparison of EMA (complex-to-real or complex modes) and FEM eigenfunctions using MAC for (a) a reception plate with idealised free boundaries (real modes), (b) the reception plate of the experimental set-up using partial coverage with viscoelastic material (real modes) and (c) the	

	reception plate of the experimental set-up using partial coverage with viscoelastic material (complex modes).	146
Figure 4-6.	Effects of damping analysed by FEM using an isolated reception plate with structural damping and equivalent viscous damping with regard to partial and full coverage with viscoelastic material.	150
Figure 4-7.	Reception plate using partial coverage with viscoelastic material: Comparison of loss factors determined from measurements using driving-point mobility (Y_{dp}), EMA (ζ) and structural reverberation time (T_s) and the FEM model using driving-point mobility (Y_{dp}).	153
Figure 4-8.	Reception plate using partial and full coverage with viscoelastic material: Comparison of loss factors determined from FEM models using driving-point mobility (Y_{dp}).	154
Figure 4-9.	Modal overlap factor from measurements using combined driving-point mobility (Y_{dp}), EMA (ζ) and structural reverberation time (T_s) and FEM models using driving-point mobility (Y_{dp}). NB The modal overlap factor of the reception plate for the experimental set-up from measurements and FEM is assessed with the interpolation lines in the indicated frequency range from Figure 4-7.	155
Figure 4-10.	Reception plate using partial coverage with viscoelastic material: Reverberation distance determined from measurements using driving-point mobility (Y_{dp}), EMA (ζ) and structural reverberation time (T_s) and the FEM model using driving-point mobility (Y_{dp}).	156
Figure 4-11.	Reception plate using partial coverage with viscoelastic material: Driving-point mobility at excitation positions 1Y and 2Y. The green coloured area represents the partial coverage with viscoelastic material underneath the plate edges.	157
Figure 4-12.	Reception plate using partial coverage with viscoelastic material: Comparison of the driving-point mobility from measurements and the FEM model at excitation positions (a) 1Y and (b) 2Y.	158
Figure 4-13.	Reception plate using partial coverage with viscoelastic material: Single-contact sources at excitation positions 1S and 5S. NB The green coloured area represents the partial	

List of figures

	coverage with viscoelastic material underneath the plate edges.	160
Figure 4-14.	Reception plate using partial coverage with viscoelastic material: Contour plots of measured and predicted (FEM) velocity levels in one-third octave bands over the plate surface from a single-contact source at excitation position 1S. NB Velocity levels are normalised to the highest level on each individual contour plot.	161
Figure 4-15.	Reception plate using partial coverage with viscoelastic material: Contour plots of measured and predicted (FEM) velocity levels in one-third octave bands over the plate surface from a single-contact source at excitation position 5S. NB Velocity levels are normalised to the highest level on each individual contour plot.	162
Figure 4-16.	Reception plate using partial coverage with viscoelastic material: Comparison of the direct injected power and the reception plate power for (a-c) rigid body modes and (d-f) bending modes. The grey shaded area identifies the damping control region. The difference refers to the injected power minus the reception plate power with horizontal lines indicating ± 1 dB.	166
Figure 4-17.	Reception plate using partial coverage with viscoelastic material: Nyquist plots from the driving-point mobility of two-pole filters using single mass-spring-dashpot systems during force excitation for (a-c) rigid body modes and (d-l) bending modes.	168
Figure 4-18.	Reception plate using partial coverage with viscoelastic material: (Upper graph) Comparison of the direct injected power and the reception plate power using single mass-spring-dashpot systems of 3 rigid body modes and 27 bending modes for narrowband and TOBs. (Lower graph) Difference between direct injected power and the reception plate power in TOBs.	171
Figure 4-19.	Reception plate using partial coverage with viscoelastic material: Comparison of 'ideal' and '6th order Butterworth' filters using the direct injected power of 30 modes (3 rigid body modes and 27 bending modes from Figure 4-18).	172
Figure 5-1.	Reception plate using partial coverage with viscoelastic material (green): Schematic representation of the four corners (red) and the central zone area (blue) on the reception plate using the empirical weighting approach for velocity samples.	177

Figure 5-2. Reception plate using partial coverage with viscoelastic material: Specified weighting factor using the empirical weighting approach for velocity samples.178

Figure 5-3. Reception plate using partial coverage with viscoelastic material (green): Schematic representation of areas for corners (red), edge strips (orange) and the central zone (blue) using the area weighting approach for velocity samples.179

Figure 5-4. Reception plate using partial coverage with viscoelastic material excited by (a) single-contact sources at positions 1S, 2S, 3S, 4S and 5S, (b) multiple-contact sources that are aligned parallel to the plate edges at positions 1MP, 2MP, 3MP and 4MP and (c) multiple-contact sources that are aligned at an angle to the plate edges at positions 1MA, 2MA, 3MA and 4MA. NB The green coloured area represents the partial coverage with viscoelastic material underneath the plate edges.....182

Figure 5-5. Reception plate using partial coverage with viscoelastic material: Difference between the direct injected power and the reception plate power with plate velocities using (a) average of all nodes from FEM predictions of a single-contact source for excitation positions 1S, 2S, 3S, 4S and 5S and (b) average of all grid points from measurements of a single-contact source for excitation positions 1S and 5S.....185

Figure 5-6. Reception plate using partial coverage with viscoelastic material: Difference between the direct injected power and the reception plate power with plate velocities using (a) average of nodes in the central zone (≥ 0.5 m away from boundaries) from FEM predictions of a single-contact source for excitation positions 1S, 2S, 3S, 4S and 5S and (b) average of grid points in the central zone (≥ 0.5 m away from boundaries) from measurements of a single-contact source for excitation positions 1S and 5S.186

Figure 5-7. Reception plate using partial coverage with viscoelastic material: Difference between the direct injected power and the reception plate power with plate velocities using (a) average of the four corner nodes from FEM predictions of a single-contact source for excitation positions 1S, 2S, 3S, 4S and 5S and (b) average of grid points of the four corners from measurements of a single-contact source for excitation positions 1S and 5S.....187

Figure 5-8. Reception plate using partial coverage with viscoelastic material: Difference between the direct injected power and

	the reception plate power with plate velocities calculated using empirical weighted average from (a) FEM predictions of a single-contact source for excitation positions 1S, 2S, 3S, 4S and 5S and (b) measurements of a single-contact source for excitation positions 1S and 5S. NB The 95% confidence intervals are shown from 10 different random sets of plate velocity positions that satisfy the area weighting requirements.	188
Figure 5-9.	Reception plate using partial coverage with viscoelastic material: Difference between the direct injected power and the reception plate power with plate velocities calculated using area-weighted average from (a) FEM predictions of a single-contact source for excitation positions 1S, 2S, 3S, 4S and 5S and (b) measurements of a single-contact source for excitation positions 1S and 5S. NB The 95% confidence intervals are shown from 10 different random sets of plate velocity positions that satisfy the area weighting requirements.	190
Figure 5-10.	Reception plate designs that differ from the reception plate using partial coverage with viscoelastic material: FEM predictions of a single-contact source for excitation positions 1S, 2S, 3S, 4S and 5S – Difference between the direct injected power and the reception plate power using plate velocities calculated from area-weighted average in terms of (a) a reception plate with free boundaries and (b) a reception plate using full coverage with viscoelastic material. NB The 95% confidence intervals are shown from 10 different random sets of plate velocity positions that satisfy the area weighting requirements.	192
Figure 5-11.	Reception plate using partial coverage with viscoelastic material: FEM predictions of a multiple-contact source having four contacts (i.e. white goods) and sides aligned parallel to the plate edges with zero-phase difference between the forces for excitation positions 1MP, 2MP, 3MP and 4MP using (a) the difference between the direct injected power and the reception plate power with averaged plate velocities from all nodes and (b) contour plots of velocity levels over the plate surface at 500 Hz with markers indicating the excitation positions.	194
Figure 5-12.	Reception plate using partial coverage with viscoelastic material: FEM predictions of a multiple-contact source having four contacts (i.e. white goods) and sides aligned parallel to the plate edges with zero-phase difference	

- between the forces for excitation positions 1MP, 2MP, 3MP and 4MP using (a) the difference between the direct injected power and the reception plate power with averaged velocities by excluding all nodes underneath the machine and up to 0.1 m away from the four contacts (indicated by white area) and (b) contour plots of velocity levels over the plate surface at 500 Hz with markers indicating the excitation positions. 195
- Figure 5-13. Reception plate using partial coverage with viscoelastic material: FEM predictions of a multiple-contact source having four contacts (i.e. white goods) and sides aligned at an angle to the plate edges with zero-phase difference between the forces for excitation positions 1MP, 2MP, 3MP and 4MP using the difference between the direct injected power and the reception plate power with averaged velocities (a) from all nodes and (b) by excluding all nodes underneath the machine and up to 0.1 m away from the four contacts. 197
- Figure 5-14. Reception plate using partial coverage with viscoelastic material: FEM predictions of a multiple-contact source having four contacts (i.e. white goods) and sides aligned parallel to the plate edges with random-phase difference between the forces for excitation positions 1MP, 2MP, 3MP and 4MP using the difference between the direct injected power and the reception plate power with averaged velocities (a) from all nodes and (b) by excluding all nodes underneath the machine and up to 0.1 m away from the four contacts. 198
- Figure 5-15. Reception plate using partial coverage with viscoelastic material: FEM predictions of a multiple-contact source having four contacts (i.e. white goods) – Difference between the direct injected power and the reception plate power calculated using the area-weighted velocity level by excluding all positions underneath the machine and up to 0.1 m away from each contact for (a) zero-phase forces with sides aligned parallel to the plate edges, (b) zero-phase forces with sides aligned to an angle to the plate edges and (c) random-phase forces with sides aligned parallel to the plate edges. NB The 95% confidence intervals are shown from 10 different random sets of plate velocity positions that satisfy the area weighting requirements..... 200
- Figure 6-1. Wav file of 20 s white noise: $L_{Fmax} - \max\{L_{eq,125ms}\}$ using the signal played directly into the measurement system..... 208
- Figure 6-2. Wav files of 125 ms ramp duration with ramp levels of 10/20/30/40 dB: The specific empirical correction,

	$L_{Fmax} - \max\{L_{eq,125ms}\}$, is shown for (a) the signal directly played into the measurement system, (b) the vibration field of the signal played into the shaker on the reception plate, (c) the vibration field of the signal played into the shaker on the concrete floor in the building-like situation and (d) the sound field in the receiving room from the signal played into the shaker on the concrete floor in the building-like situation.	211
Figure 6-3.	Wav files of 500 ms ramp duration with ramp levels of 10/20/30/40 dB: The specific empirical correction, $L_{Fmax} - \max\{L_{eq,125ms}\}$, is shown for (a) the signal directly played into the measurement system, (b) the vibration field of the signal played into the shaker on the reception plate, (c) the vibration field of the signal played into the shaker on the concrete floor in the building-like situation and (d) the sound field in the receiving room from the signal played into the shaker on the concrete floor in the building-like situation.	212
Figure 6-4.	Wav files of 1 s ramp duration with ramp levels of 10/20/30/40 dB: The specific empirical correction, $L_{Fmax} - \max\{L_{eq,125ms}\}$, is shown for (a) the signal directly played into the measurement system, (b) the vibration field of the signal played into the shaker on the reception plate, (c) the vibration field of the signal played into the shaker on the concrete floor in the building-like situation and (d) the sound field in the receiving room from the signal played into the shaker on the concrete floor in the building-like situation.	213
Figure 6-5.	Wav files of 2 s ramp duration with ramp levels of 10/20/30/40 dB: The specific empirical correction, $L_{Fmax} - \max\{L_{eq,125ms}\}$, is shown for (a) the signal directly played into the measurement system, (b) the vibration field of the signal played into the shaker on the reception plate, (c) the vibration field of the signal played into the shaker on the concrete floor in the building-like situation and (d) the sound field in the receiving room from the signal played into the shaker on the concrete floor in the building-like situation.	214
Figure 6-6.	Wav files of 5 s ramp duration with ramp levels of 10/20/30/40 dB: The specific empirical correction, $L_{Fmax} - \max\{L_{eq,125ms}\}$, is shown for (a) the signal directly	

played into the measurement system, (b) the vibration field of the signal played into the shaker on the reception plate, (c) the vibration field of the signal played into the shaker on the concrete floor in the building-like situation and (d) the sound field in the receiving room from the signal played into the shaker on the concrete floor in the building-like situation.....215

Figure 7-1. Experiments to determine the input data for the two-subsystem SEA model of a coupled room-plate system for (a) the installed vibrational input power of the ramped noise signals injected by a shaker for examples of 125 ms, 500 ms, 1 s, 2 s and 5 s ramps with a ramp level of 20 dB, (b) the radiation efficiency, (c) the loss factors of the plate and the room and (d) the coupling loss factors from the plate to the room (and vice versa).....228

Figure 7-2. Wav files of 125 ms, 500 ms, 1 s, 2 s and 5 s ramp durations with ramp levels of 10/20/30/40 dB: The specific empirical correction of velocity levels in terms of predicted $L_{v,Fmax}$ minus measured $L_{v,Fmax}$ for (a) 125 ms ramp, (b) 500 ms ramp, (c) 1 s ramp, (d) 2 s ramp and (e) 5 s ramp.....230

Figure 7-3. Wav files of 125 ms, 500 ms, 1 s, 2 s and 5 s ramp durations with ramp levels of 10/20/30/40 dB: The specific empirical correction of sound pressure levels in terms of predicted $L_{p,Fmax}$ minus measured $L_{p,Fmax}$ for (a) 125 ms ramp, (b) 500 ms ramp, (c) 1 s ramp, (d) 2 s ramp and (e) 5 s ramp.232

Figure 7-4. Wav files of 125 ms, 500 ms, 1 s, 2 s and 5 s ramp durations with ramp levels of 10/20/30/40 dB: The single-number empirical correction of predicted and measured sound pressure levels in terms of predicted $L_{p,Fmax}$ minus measured $L_{p,Fmax}$ 234

Figure 7-5. Wav files of 125 ms, 500 ms, 1 s, 2 s and 5 s ramp durations with ramp levels of 10/20/30/40 dB: Comparison of L_{AFmax} and $\max\{L_{AF,125ms}\}$ levels in terms of measured $L_{AF,125ms}$ and $L_{F,125ms}$ 235

Figure 7-6. Wav files of 125 ms, 500 ms, 1 s, 2 s and 5 s ramp durations with ramp levels of 10/20/30/40 dB: Comparison of the specific empirical correction using predicted and measured A-weighted sound pressure levels, L_{AFmax} 237

List of figures

Figure 7-7. Wav files of 125 ms, 500 ms, 1 s, 2 s and 5 s ramp durations with ramp levels of 10/20/30/40 dB: Comparison of the single-number empirical correction using predicted and measured A-weighted sound pressure levels, L_{AFmax} 238

Figure 8-1. Case study of a toilet flush: (a) measurement set-up for the pre-wall installation system (Geberit GIS) with sanitary equipment, (b) the toilet, (c) the load-bearing frame including the installations of the cistern and the fresh- and wastewater pipes and (d) cork layered brackets which fix the frame to the reception plate test rig [37]. This sanitary installation system is installed without the installation shaft for the fresh- and wastewater supply..... 243

Figure 8-2. Case study of a toilet flush. Time-varying velocity levels in terms of $L_{F,125ms}$ in the free run during a flush cycle: (a) the summed velocity levels in one-third octave bands over time are shown from multi-buffer measurements on (b) the horizontal reception plate and (c) the vertical reception plate. 246

Figure 8-3. Case study of a toilet flush: Definition of ramps A, B and C from the flushing process for (a) the summed velocity levels from all the filters over time and multi-buffer measurements from (b) to (g) in order to obtain their ramp levels over time using the single frequency band at which the highest ramp durations occur. 247

Figure 8-4. Case study of a toilet flush: Repeatability using L_{Fmax} of ramp A determined from six toilet flush cycles on (a) the horizontal reception plate and (b) the vertical reception plate. 250

Figure 8-5. Case study of a toilet flush: Multi-buffer measurements for velocity levels in terms of $L_{F,125ms}$ starting from a time of 0 s up to 7 s with maximum hold measured on (a) the horizontal reception plate and (b) the vertical reception plate. The time-varying operating cycle is based on the example ‘toilet flush 1’ in Table 8-1..... 254

Figure 8-6. Case study of a toilet flush: Multi-buffer measurements for velocity levels in terms of $L_{F,125ms}$ starting from a time of 0 s up to 7 s with a free run measured on (a) the horizontal reception plate and (b) the vertical reception plate. The time-varying operating cycle is based on the example ‘toilet flush 1’ in Table 8-1. 255

Figure 8-7. Case study of a toilet flush: Multi-buffer measurements for velocity levels in terms of $L_{eq,125ms}$ starting from a time of 0 s up to 7 s with maximum hold measured on (a) the horizontal reception plate and (b) the vertical reception plate. The time-varying operating cycle is based on the example ‘toilet flush 1’ in Table 8-1.256

Figure 8-8. Case study of a toilet flush: Difference between $L_{F,125ms}$ in the free run and L_{Fmax} and difference between $\max\{L_{F,125ms}\}$ and L_{Fmax} when measured on (a) the horizontal reception plate and (b) the vertical reception plate. The time-varying operating cycle is based on the example ‘toilet flush 1’ in Table 8-1.257

Figure 8-9. Case study of a toilet flush: The specific empirical correction, $L_{Fmax} - \max\{L_{eq,125ms}\}$, using the peak in ramp A of the filtered toilet flush signal for (a) ‘toilet flush 1’ and (b) ‘toilet flush 2’ from Table 8-1 measured on the horizontal and vertical reception plate.259

Figure 8-10. Case study of a toilet flush: Comparison of the specific empirical correction, $L_{Fmax} - \max\{L_{eq,125ms}\}$, using the empirical weighted velocity levels for ‘toilet flush 1’ from Table 8-1 measured on the horizontal and vertical reception plate as well as the empirical weighted and area-weighted velocity levels for ramped noise signals measured on the horizontal reception plate from (a) the 500 ms ramp with ramp levels of 10/20/30 dB and (b) the 1 s ramp with ramp levels of 10/20/30 dB.262

Figure 8-11. Case study of a toilet flush: Comparison of the specific empirical correction, $L_{Fmax} - \max\{L_{eq,125ms}\}$, using the empirical weighted velocity levels for ‘toilet flush 2’ from Table 8-1 measured on the horizontal and vertical reception plate as well as the empirical weighted and area-weighted velocity levels for ramped noise signals measured on the horizontal reception plate from (a) the 500 ms ramp with ramp levels of 10/20/30 dB and (b) the 1 s ramp with ramp levels of 10/20/30 dB.263

Figure 8-12. Case study of a toilet flush: $L_{Fmax} - \max\{L_{eq,125ms}\} - 6$ dB using the empirical weighted velocity levels for ‘toilet flush 1’ from Table 8-1 measured on the horizontal and vertical reception plate as well as the empirical weighted and area-weighted velocity levels for ramped noise signals measured

List of figures

on the horizontal reception plate from (a) the 500 ms ramp with ramp levels of 10/20/30 dB and (b) the 1 s ramp with ramp levels of 10/20/30 dB.266

Figure 8-13. Case study of a toilet flush: $L_{Fmax} - \max\{L_{eq,125ms}\} - 6$ dB using the empirical weighted velocity levels for ‘toilet flush 2’ from Table 8-1 measured on the horizontal and vertical reception plate as well as the empirical weighted and area-weighted velocity levels for ramped noise signals measured on the horizontal reception plate from (a) the 500 ms ramp with ramp levels of 10/20/30 dB and (b) the 1 s ramp with ramp levels of 10/20/30 dB.267

List of abbreviations

AC	Alternating Current
ACC	Accelerometer
AVG	Average
B&K	Brüel & Kjær
CEN	European Committee for Standardization
CHP	Combined Heat and Power
CMIF	Complex Mode Indicator Function
CPB	Constant Percentage Bandwidth (1/n-octave analysis)
CST	Constant Strain Triangle
DASHPOT1	Ground-to-node dashpot element acting in a fixed direction
DASHPOT2	Node-to-node dashpot element acting in a fixed direction
DKT	Discrete Kirchhoff Triangle
DOF	Degree of Freedom
EMA	Experimental Modal Analysis
EN	European Standards
ESEA	Experimental Statistical Energy Analysis
FBC	Free Boundary Conditions
FEM	Finite Element Method
FFT	Fast Fourier Transform
FRF	Frequency Response Function
GIS	Geberit Installation System
IEC	International Electrotechnical Commission
IEPE	Integrated Electronics Piezo Electric
ISO	International Organization for Standardization

List of abbreviations

JIS	Japanese Industrial Standards
MAC	Modal Assurance Criterion
MAX	Maximum
MDOF	Multiple Degree of Freedom
MIN	Minimum
MLS	Maximum Length Sequence
MVHR	Mechanical Ventilation with Heat Recovery
NFD	Natural Frequency Deviation
ÖNORM	Austrian Standards International
PCVM	Partial Coverage with Viscoelastic Material
PDE	Partial Differential Equation
PE	Polyethylene
PE-X	Cross-linked Polyethylene
PSD	Power Spectral Density
RFP	Rational Fraction Polynomial
RMS	Root-Mean-Square
SC	Sub-Committee
SDOF	Single Degree of Freedom
SEA	Statistical Energy Analysis
SIA	Swiss Society of Engineers and Architects
SLM	Sound Level Meter
SPRING1	Ground-to-node spring element acting in a fixed direction
SPRING2	Node-to-node spring element acting in a fixed direction
STRI3	Three-node triangular facet thin shell element
TC	Technical Committee
TEDS	Transducer Electronic Data Sheet
TOB	Third Octave Band
TS	Technical Specification
TSEA	Transient Statistical Energy Analysis
VDI	Association of German Engineers
WG	Working Group
2D	Two-Dimensional
3D	Three-Dimensional

List of symbols

a	Acceleration (m/s^2), piston radius (m)
c_0	Phase velocity of sound in air (m/s)
c_B	Bending phase velocity (m/s)
c_{eq}	Equivalent viscous damping coefficient (Ns/m)
c_g	Group velocity (m/s)
$c_{g(B)}$	Group velocity for bending waves (m/s)
c_L	Quasi-longitudinal phase velocity (m/s)
d	Distance (m)
d_{mfp}	Mean free path (m)
e_{max}	Largest dimension of an element (m)
f	Frequency (Hz)
f_0	Resonance frequency/eigenfrequency (Hz)
$f_{B,\text{thin}}$	Thin plate limit for bending waves (Hz)
f_c	Centre frequency (Hz), critical frequency (Hz)
f_l and f_u	Lower and upper band-edge frequency limit (Hz)
f_{max}	Maximum frequency (Hz)
h	Thickness (m)
i	Imaginary unit, $\sqrt{-1}$
k	Spring stiffness (N/m), acoustic wavenumber (radians/m)
k_B	Bending wavenumber (radians/m)
m	Mass (kg)

List of symbols

n	Total number of samples, mode number
$n(f)$	Modal density (modes per Hz)
p	Sound pressure (Pa), modal pole (radians/s)
q	Generalised displacement (m)
q_0	Maximum generalised displacement at resonance (m)
\dot{q}	Generalised velocity (m/s)
\ddot{q}	Generalised acceleration (m/s ²)
r_{rd}	Reverberation distance (m)
s	Structural damping, standard deviation
s'	Dynamic stiffness per unit area (N/m ³)
t	Time (s)
t_{mfp}	Time for waves to travel the mean free path (s)
v	Velocity (m/s)
v_{rms}	Root-mean-square velocity
w	Displacement (m)
x, y, z	Cartesian/global/local coordinates (m)
A	Absorption area (m ²), residue (m/(Ns))
A_T	Total absorption area (m ²)
B	Bandwidth (Hz)
B_p	Bending stiffness per unit width of a plate (Nm)
B_p^*	Complex bending stiffness per unit width of a plate (Nm)
C	Damping (Ns/m)
D	Constitutive matrix (Nm)
E	Young's modulus (N/m ²), Energy (J)
E^*	Complex modulus of elasticity (N/m ²)
E'	Storage modulus (N/m ²)
E''	Loss modulus (N/m ²)
F	Force (N)
F_d	Damping force (N)
F_{rms}	Root-mean-square force (N)
G	Shear modulus (N/m ²)
G^*	Complex shear modulus (N/m ²)

G'	Storage shear modulus (N/m ²)
G''	Loss shear modulus (N/m ²)
H	Frequency response function (m/Ns ²)
I	Identity matrix, $\begin{bmatrix} 1 & & \\ & \ddots & \\ & & 1 \end{bmatrix}$
I_p	Moment of inertia of the cross-sectional area (m ⁴)
K	Stiffness (N/m)
K^*	Complex stiffness (N/m)
K'	Real part of stiffness (N/m)
K''	Imaginary part of stiffness (N/m)
L	Coupling length between connected plates (m)
L_{AFmax}	A-weighted maximum Fast time-weighted sound level (dB)
L_{eq}	Equivalent continuous sound level (dB)
$L_{eq,125ms}$	Short (125 ms) equivalent continuous sound level (dB), also used as $\max\{L_{eq,125ms}\}$: maximum short (125 ms) equivalent continuous sound level (dB)
L_{Fmax}	Maximum Fast time-weighted sound level (dB)
L_p	Sound pressure level (dB)
L_T	Total length of all room edges (m)
L_v	Velocity level (dB)
$L_{v,AW}$	Area-weighted velocity level
$L_{v,EW}$	Empirical weighted velocity level
L_x, L_y, L_z	x -, y - and z -dimensions (m)
L_r	Time-weighted level (dB)
M	Mass/inertia (kg), moment per unit width (N), modal overlap factor
N	Mode count in a frequency band, interpolation function, frequency lines, total number of degrees of freedom, samples, etc.
N_{tot}	Total number of nodes for the entire reception plate
N_v	Number of nodes for the viscoelastic material
Q	Product of the complex force and velocity (W)
R	Damping constant (Ns/m)
S	Surface area (m ²)
S_C	Area of the corners (m ²)
S_{CZ}	Area of the central zone (m ²)

List of symbols

S_{ES}	Area of the edge strips (m ²)
S_{LP}	Area of the load plate (m ²)
S_T	Area of all room surfaces (m ²)
S_{tot}	Area for the entire reception plate (m ²)
S_V	Area for the viscoelastic material (m ²)
T	Reverberation time (s), integration time (s)
T_s	Structural reverberation time (s)
U	Perimeter (m)
U_0	Maximum elastic stored energy (J)
V	Volume (m ³)
W	Power (W)
W_{char}	Characteristic power (W)
W_d	Dissipated energy (J)
W_{ij}	Transmitted power from subsystem i to subsystem j (W)
W_{in}	Power input (W)
W_{inj}	Injected power (W)
W_{inst}	Installed power (W)
W_{rad}	Radiated power (W)
W_{rec}	Reception plate power (W)
X	Empirical weighting factor (-)
Y	Mobility (m/Ns)
Y_{dp}	Driving-point mobility (m/(Ns))
$Y_{dp,\infty}$	Driving-point mobility of a thin infinite plate (m/(Ns))
Y_R	Receiver mobility (m/(Ns))
Y_S	Source mobility (m/(Ns))
γ	Shear strain, structural damping factor
δ	Logarithmic decrement
ε	Strain
ε_0	Maximum strain at resonance
ζ	Damping ratio
η	Loss factor
η_{coup}	Coupling loss factor

η_{ii}	Internal loss factor of subsystem i
η_{ij}	Coupling loss factor from subsystem i to subsystem j
η_{int}	Internal loss factor
η_{rad}	Radiation loss factor
η_{tot}	Total loss factor
λ	Eigenvalue ($1/s^2$), eigenvalue with the unit of mobility (m/Ns), wavelength (m)
λ_B	Bending wavelength (m)
ν	Poisson's ratio (-)
π	Ludolph's number, 3.14159...
ρ	Density (kg/m^3)
ρ_0	Density of air (kg/m^3)
ρ_s	Mass per unit area (kg/m^2)
σ	Stress (N/m^2), radiation efficiency, damping decay constant (radians/s)
τ	Transmission coefficient, exponential time constant (s)
φ	Phase angle (rad)
$\tan \varphi$	Loss tangent
ϕ	Characteristic beam function, normalised eigenvector of a mode shape
χ	Viscous damping parameter
ψ	Eigenvector of a mode shape, frequency-dependent amplitude vector
ω	Angular frequency, $\omega = 2\pi f$ (radians/s)
ω_0	Angular resonance frequency/eigenfrequency (radians/s)
Γ	Boundary subjected to the element surface
Δf	Frequency bandwidth (Hz), frequency resolution (Hz)
$\Delta f_{3\text{dB}}$	3 dB bandwidth or half-power bandwidth (Hz)
Δt	Velocity-time propagation difference (s)
Λ	Spectral/eigenvalue matrix ($1/s^2$)
Λ^*	Complex eigenvalue ($1/s^2$)
Φ	Mass-normalised modal matrix
Ψ	Real-valued normal mode matrix, force vector (N)

List of symbols

Ψ^*	Complex eigenvector
Ω	Angular eigenfrequency (Hz), spatial element domain
∂	Partial derivative
∇	Spatial differential operator
∇^2	Laplace operator, $\nabla^2 = \frac{\partial^2}{\partial x^2} + \frac{\partial^2}{\partial y^2}$
∇^4	Biharmonic operator, $(\nabla^2)^2 = \left(\frac{\partial^2}{\partial x^2} + \frac{\partial^2}{\partial y^2} \right)^2 = \frac{\partial^4}{\partial x^4} + \frac{2\partial^4}{\partial x^2\partial y^2} + \frac{\partial^4}{\partial y^4}$
\cup	Assemblage operator
∞	Infinity
$\text{diag}(\)$	Diagonal matrix
$\lg()$	Logarithm base 10
$\Im\{ \}$	Imaginary part
$\Re\{ \}$	Real part
$\angle\{ \}$	Phase angle
$[\]$	Matrix
$\{ \}$	Vector
$ $	Magnitude
$\langle \rangle$	Mean value
$\langle \rangle_f$	Frequency average
$\langle \rangle_{f,s}$	Frequency and spatial average
$\langle \rangle_{t,s}$	Temporal and spatial average
X^H	Complex conjugate transpose (Hermitian transpose) of variable X
X^T	Transpose of variable X
\underline{X}	Complex value of variable X
X^*	Complex conjugate of variable X
\hat{X}	Peak/amplitude value of variable X

1 Introduction

1.1 Background

Europeans spend the vast majority of their time (up to 90%) indoors [1, 2]. In addition to the thermal, visual and air quality of a building environment, the indoor acoustic quality also has an impact on comfort, health and working performance [3, 4]. In dwellings, studies from the United Kingdom and Sweden have shown that audible noise sources such as domestic appliances can be perceived by the occupants due to poor sound insulation even if the standard requirements on airborne and impact sound insulation are met [5, 6, 7].

A specific noise issue in residential buildings is due to disturbing noise from domestic appliances such as washing machines, tumble dryers, dishwashers, boilers, pumps, combined heat and power units (CHPs), sanitary installations and other mechanical building machinery. This type of installation can cause structure-borne and airborne sound in the building. In the past few decades, these building installations and machinery in residential buildings have increased significantly due to the automation processes, the implementation of machine learning using smart building management technology as well as the high technical standards for mechanical devices to improve comfort, efficiency, sustainability and safety. These are used to save time and reduce costs. This contrasts with the need for privacy, protection and comfort in residential

buildings. For this purpose, the standard ISO/TS 19488 [8] defines the quantification of sound classes in dwellings in terms of different levels of acoustic comfort for the airborne and impact sound insulation, noise from service equipment, etc.

Estimating the sound transmission using prediction models is needed at the design stage of buildings to avoid or reduce the noise from mechanical service equipment or automated building machinery. In recent years, Statistical Energy Analysis (SEA) and simplified SEA-based models (EN 12354 series [9, 10, 11]) have been established to provide a framework that is ideally suited for predicting direct and flanking sound transmission for airborne and impact sources when the source operates under steady-state conditions. Figure 1-1 shows a general procedure to sound transmission caused by a source in operation that injects airborne/liquid-borne/structure-borne sound into a wall and/or a floor in the source room, travels throughout the building structure and finally radiates into the receiving room.

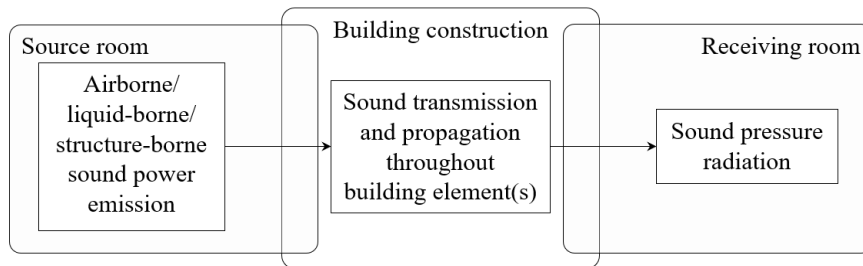


Figure 1-1. General schematic representation of the sound transmission between rooms through the power injection of mechanical domestic appliances under operating conditions.

For radiated sound levels into the receiving room, it is important to emphasise that some European regulations on installation noise such as ÖNORM B 8115-2 [12] in Austria, SIA 181 [13] in Switzerland and VDI 4100 [14] in Germany refer to an A-weighted maximum Fast time-weighted sound pressure level, L_{AFmax} . The prediction of impact sound insulation due to transient excitation in terms of maximum Fast time-weighted sound pressure levels, L_{Fmax} , using

Transient SEA (TSEA) has been already successfully investigated for short transients from dropped objects, e.g. from a rubber ball with only a short structural contact time of ≈ 20 ms [15, 16]. This requires measurements of the blocked force to assess the transient excitation. At present, this approach has been validated for heavy impacts from the ISO rubber ball and bang machine on heavyweight floors with and without floating floors [17, 18]. The construction industry, engineers and consultancies often prefer simplified prediction models such as the EN 12354 standard series [9, 10, 11], and TSEA calculations would be considered too complex to include in these standards. For this reason, there is a need for alternative and simplified procedures that could be used to estimate L_{Fmax} and L_{AFmax} .

For the majority of building machinery, the structure-borne sound power injected into the structure is the dominant contribution to the sound pressure level in the receiving rooms nearby, whereas the airborne component is sometimes negligible. The liquid-borne sound of domestic appliances (gases and/or fluids) mainly leads to structure-borne sound through vibrating ducts, pipes, hoses, hydraulic motors, central heating systems, valves, etc. when they are in direct contact with a building component [19].

Airborne sound power is characterised in a reverberation room [20] or anechoic (or semi-anechoic) chamber [21] using standard laboratory measurement methods to obtain the input data for predictions of sound transmission in buildings. For engineering estimates of the radiated sound pressure level in other rooms, it is not always necessary to know the position of an airborne sound source or the room dimensions. Therefore, the power input data from airborne sound sources can be relatively straightforward to include in SEA models using a source-path-receiver model (Figure 1-2) [19, 22].

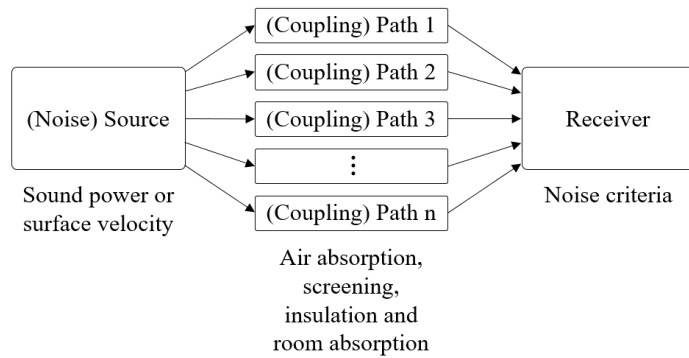


Figure 1-2. Schematic representation of airborne sound for a noise system adapted from [22].

In contrast, the structure-borne sound power injected by vibrating machinery into a receiving structure through their connection points is a more complex physical process due to the interaction between the source and receiver. This requires source characterisation as a function of its activity (e.g. free velocity or blocked force) which is independent of the passive dynamic properties of the receiver structure as a function of mobility. By combining the source activity and the passive properties of the receiver, it is possible to calculate the power injected into the structure, which allows predictions with regard to a vibro-acoustic source-transmission-path-receiver model (Figure 1-3) in buildings [19, 22, 23].

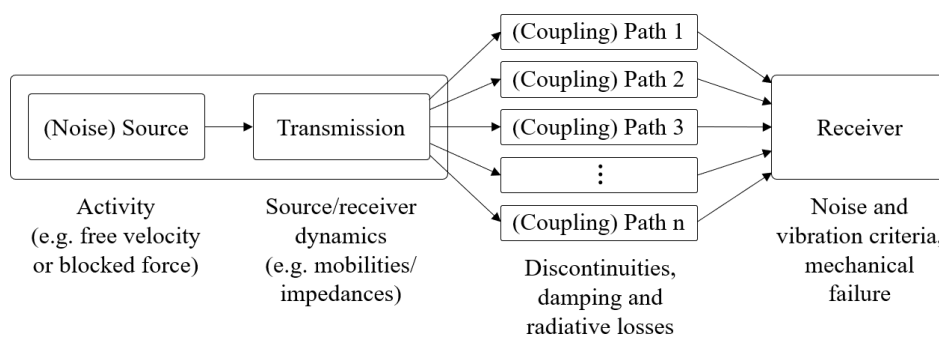


Figure 1-3. Schematic representation of structure-borne sound for a noise system adapted from [22].

Different approaches are available to quantify the injected power of a structure-borne sound source which can be considered as either direct or indirect methods. With direct methods, the main purpose is to collect large data sets on vibration sources at the contact points. The concept of structure-borne sound characterisation can be incorporated in prediction models. However, direct methods sometimes have rotational moment mobility and translational force measurement errors [24] since the installation in practice can be different at the contacts. Errors in moment measurements occur due to the currently available sensor technique, which does not easily allow direct measurement of torques at the source contacts [25, 26, 27]. Typically, this is still solved by alternative procedures of indirect measurement using the substitution method. In addition, for the measurement of direct load force data, an appropriate implementation without altering installation conditions as a coupling function of the transverse source-receiver interaction is difficult or not feasible.

Indirect methods circumvent these issues by measuring the response velocity of the receiving structure instead of the response force at the machinery contacts [28]. For building machinery, there is evidence that the injected power by torque excitation in a passive receiver structure at the interface is generally negligible for mobilities of a low-mobility reception plate and/or plate-like construction elements in heavyweight buildings [29, 30, 31]. For heavyweight structures, it is generally accepted that the force-injected component of power is more important than the moment component [19, 29, 32]. Another argument in favour of indirect measurements is that in engineering practice, and in particular with manufacturers, reliable and reduced data sets for laboratory characterisation methods concerning vibrational source power must be provided, which can be easily measured and transferred to different building constructions. The reception plate method as a simplified indirect measurement technique is commonly used to quantify the structure-borne sound power of machinery in heavyweight buildings. For this purpose, the vibration-induced power of a

source with any number of contact points and geometry on an isolated plate [33, 34] is obtained as described in EN 15657 [35].

Figure 1-4 shows examples of building machinery with multiple-contact points/lines having surface area projections (see Figure 1-5) onto the reception plate from 0.3 to 0.5 m² that are tested according to the earlier version of EN 15657 [35] (referred to as EN 15657-1 [36]) to determine their structure-borne sound power input. It can be seen that the mechanical installations assessed on the reception plate typically possess tonal characteristics when running under steady-state operating conditions. In the low-frequency range, these structure-borne sound sources with components of tonal characteristics tend to significantly inject power into a wall and/or floor that varies from approximately 20 to 250 Hz depending on the type of machinery.

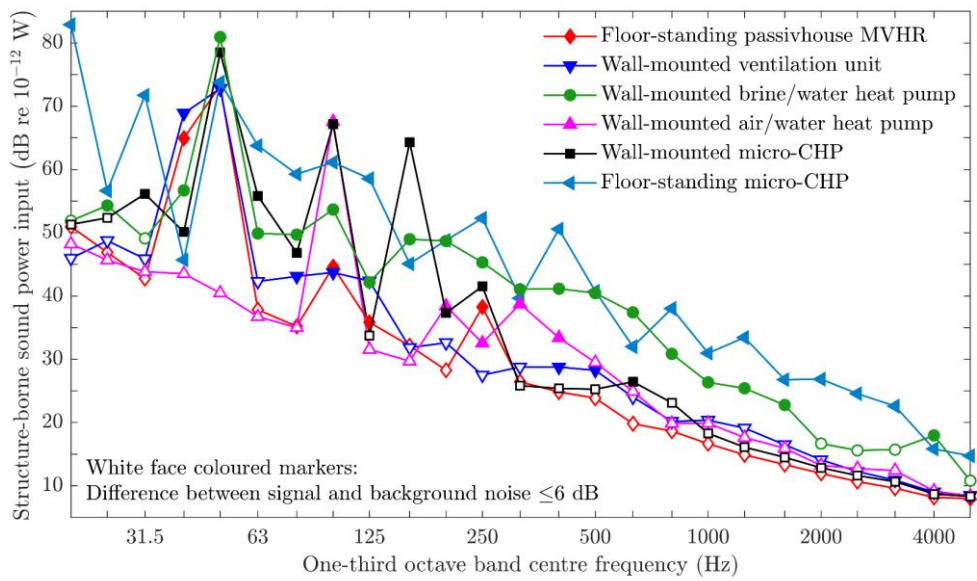


Figure 1-4. Structure-borne sound power input from different machinery under steady-state operating conditions into the low-mobility reception plate measured according to [36, 37].

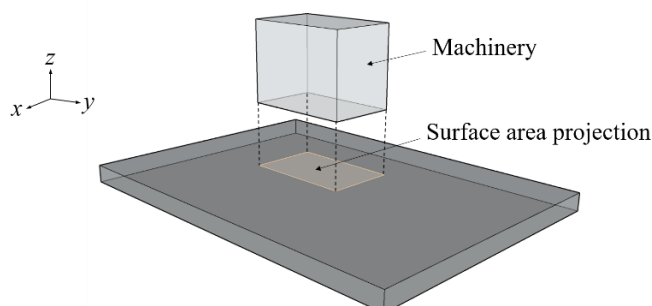


Figure 1-5. Schematic representation of the surface area projection from a piece of machinery onto a plate-like structure.

The simplified indirect measurement method using a multimodal, highly damped reception plate has inherent uncertainties [19, 38, 39, 40, 41], particularly when the reception plate power is estimated from the plate surface velocity using only a few measurement positions and the loss factor determined from the reverberation method. Due to the low modal density of thick, stiff reception plates, errors caused by inappropriate sampling strategies are mainly apparent at low frequencies [33, 42]. In the low-frequency range, errors also occur with loss factors from coupled reception plates caused by the energy that returns from other connected structural elements [43, 44, 45], and isolated reception plates provoked flat amplitude-frequency response from the highly damped supports [46]. To avoid measurement uncertainties, the power substitution method can be used, but this is potentially time-consuming when a source has many point-, line- or plane-contacts. A European round-robin test with five participating laboratories on the reception plate method showed that the standard deviation of (a) the loss factor was 3 dB at low frequencies and decreased to 1 dB at higher frequencies and (b) the plate velocity was within ≈ 4 dB for the characterisation of a three-contact source in the mid- and high-frequency range, but there were larger standard deviations up to ≈ 6 dB at low frequencies [47]. Thus, the challenge remains to increase the accuracy of the reception plate method in the low-frequency range.

1.2 Literature review

There is a large amount of literature on machinery noise and vibration as well as the prediction of sound transmission in buildings. This section reviews the literature with a focus on the characterisation of the structure-borne sound power input from building machinery and the estimation of L_{Fmax} levels using reception plates and SEA predictions in heavyweight buildings.

1.2.1 Review of structure-borne sound sources characterisation for building equipment

The review of the structure-borne sound characterisation is divided into five sections. The general development of structure-borne sound characterisation is briefly discussed in Section 1.2.1.1, followed by the approach relating to reception plates in Section 1.2.1.2. Section 1.2.1.3 introduces the uncertainty analysis that arises for measurements when the measurement methodology is based on simplifications. Analytical and numerical models for the reception plate are reviewed in Section 1.2.1.4. Section 1.2.1.5 reviews approaches to assess time-varying structure-borne sound sources.

1.2.1.1 General development

Up to the late 1970s, the advancement of the vibrational source characterisation slowed after the comprehensive work on physical fundamentals and applications of the structure-borne sound subject by Cremer and Heckl (1967, German version and 1973, English version) [48, 49] – see also Ungar (1980) [50].

In 1978, Kihlman [51] addressed the pressing need for structure-borne sound source data and pointed out that new measurement methods needed to be established to deal with this issue. The measurement methods available at this time for the characterisation of structure-borne sound sources generally led to insufficient prediction data that did not contribute to the structure-borne sound

reduction from machinery, e.g. due to insufficient machine isolation or local and structural resonance conditions of bearings. Kihlman's paper underlines the importance of this topic in a discussion about the idea of direct and indirect measurement procedures as well as the demand for developing standards for more feasible and more suitable measurement methods to precisely acquire data from structure-borne sound sources through practical research.

Ungar (1980) [50] emphasised Kihlman's statement and noted that structure-borne sound tends to be the dominant component, particularly below 100 Hz. His report also highlighted the relevant parameters needed for the prediction of the vibrational machine activity and the passive parameters needed for the machine foundation.

Based on this discussion, an international working group, the ISO/TC 43/SC 1/WG 22, was founded in 1980 to develop standardised procedures for the characterisation of structure-borne sound sources according to the paper by ten Wolde and Gedefelt (1987) [24]. In their paper, various methods based on vibration source solutions were presented which relate to the ability to deliver power and the need for the characterisation of machinery using (a) the comparison of the injected power from machines of similar types and dimensions, (b) the assessment of compliance with the injected power specification for an upper limit, (c) the generation of power input data for predictions and (d) the design of low-noise building machinery.

In the last three decades, intensive research has been carried out to develop different structure-borne characterisation methods, such as the effective mobility method [52], the interface mobility method [53], the mobility-based power mode method [54, 55], the multipole expansion method [56], the source descriptor and the coupling function [57, 58, 59], the pseudo and equivalent forces [60], the terminal power method [61] and the reception plate method [22, 33, 62, 63]. A more detailed review of the various characterisation methods of structure-borne sound sources is undertaken in papers, e.g. by Petersson and Gibbs (2000) [23] as well as Bonhoff and Petersson (2010) [64, 65].

Of particular interest in this thesis is the reception plate method in the subject of structure-borne sound characterisation, and the reasons for this are discussed in more detail in the following sections.

1.2.1.2 Development of the reception plate method

The first measurement method of a reception plate can be attributed back to Cremer and Heckl (1967, 1973) [48, 49] and was developed for point excitation based on the relationship between the vibration power input (potential energy density) and the radiation velocity (kinetic energy density) in the reverberant field of the plate. This procedure is equivalent to the acoustic power and absorption in a reverberation chamber (free field method) [20].

However, an infinite plate as a simplified solution for structure-borne sound source characterisation was assumed to have the characteristics of a diffuse or random vibration field for which the response of an isolated finite plate can approximate in practice with increasing frequency. In the paper by ten Wolde and Gadefelt (1987) [24], an isolated plate was described with viscoelastic supports with (a) sufficiently high modal density for bending waves, (b) light damping and (c) plate mobility corresponding to real receiving structures.

Heckl (1988) [62] described a practical structure-borne sound characterisation procedure for single-contact sources attached to a structure as the reverberation method for which only bending vibrations were considered when estimating the plate-source power. In contrast to the airborne sound power, it was pointed out that this method does not constitute the pure structure-borne sound power of the source activity because this quantity still depends on the mobility of the structural system. Another point raised in this paper concerned the strength of multiple-contact sources, the structure-borne sound power of which may be defective assessed when treated as single-contact sources. Suggestions such as using the reciprocity principle and structural mobility (or impedance) methods were addressed to avoid this issue. Wittstock et al. (2011) [47] or Höller and Gibbs (2018) [42] later showed for the low-mobility reception plate that the

installed power can be successfully estimated for high-mobility sources with any number of contacts and geometries. In the situation that the force strength from multiple-contact sources is known, the injected power into the reception plate is estimated from the multiple contact variables at the drive point from the source contact interface. The simplest solution is to arithmetically average the individual variable types obtained from the drive point on the plate. Su et al. (1995) [54] provided a solution in this framework in which the power flow between several perpendicular forces via single point contacts for linear systems were considered using a real-valued mobility matrix with upper and lower bounds. Ji et al. (2003) [55] extended this principle to a mobility-based power flow mode method for an array of point forces attached to a receiver.

In addition to Heckl's highlighted work (1988) [62], this type of practical structure-borne sound source characterisation using a reception plate became the focus of numerous other studies that were carried out in the 1990s to 2020s. From these studies, concepts for the reception plates were specified in terms of the high-mobility plate for velocity sources with low mobility, $|Y_S| \ll |Y_R|$, and the low-mobility plate for force sources with high mobility, $|Y_S| \gg |Y_R|$, or a combination of these, called a two-stage reception plate method [66].

Currently, the simplified concept of the reception plate method can be seen as the most practical and reliable characterisation approach of steady-state vibro-acoustic sources, which provides suitable reduced input data for the prediction in buildings using SEA or simplified SEA-based models. Of particular interest are, for instance, the various studies by Gibbs and co-workers (1994, 1995, 2007, 2008, 2009) [22, 33, 66, 67, 68, 69] who have contributed significantly to the general principles of the characterisation of structure-borne sound sources using reception plates for predictions in lightweight or heavyweight buildings.

Späh's doctoral thesis (2006) [30] converted the low-mobility reception plate fundamentals from a thin or thick metal plate to a thick concrete plate to enable structure-borne sound source characterisation for heavyweight buildings. In the

first publication of EN 12354-5 [11] dealing with building machinery and sanitary installations, Späh's development of the reception plate on a power basis provided the necessary link to meet the input data requirements in heavyweight buildings. For this purpose, the concrete reception plate was strongly damped using viscoelastic supports (assumed to have a spring resonance frequency below 20 Hz) around the edges to reduce low-frequency wave reflections and reproduce an equivalent to the edge losses of building structures. Indeed, Späh was aware that the low-mobility concrete plate could be in contradiction with the required reverberant field conditions due to the low modal overlap and the low mode counts at low frequencies. This work showed that this type of reception plate had an approximation to a diffuse bending wave field in the mid- and high-frequency range but not at low frequencies. Späh and Gibbs set the number of detected modes that should be present in each frequency band to five to meet the assumptions for the diffuse vibration field [30, 33]. Finally, the results indicated that a reverberant field occurs at and above 800 Hz when using the modal density as an indicator [30].

Concerning the diffuse field, there are analogies to the sound field in room acoustics where Schröder (1954) [70] defined a crossover frequency which indicates the threshold of a room between the low-frequency range dominated by the resonance behaviour and the high-frequency range dominated by the statistic reverberation behaviour. Schröder's cut-off frequency is based on a modal overlap factor of three [71]. Regarding the design of a low-mobility plate, Davis (2006) [72] also suggested the target of the modal overlap factor to be three. However, based on Späh's and Gibbs work [30, 33], the isolated heavyweight reception plate was included in the standard EN 15657 [35] (referred to as EN 15657-1 [36]).

1.2.1.3 Measurement uncertainty with the reception plate method

Due to the relative simplicity of the reception plate method, work by Gibbs et al. (2009, 2013, 2015, 2016) [19, 38, 39, 40, 41] has considered the measurement

uncertainties. Potential uncertainties of the structure-borne sound characterisation have been identified with the data reduction to determine single equivalent values in terms of spatial averages and magnitudes of the source strength and receiver mobility in one-third octave bands. Round-robin test results (2016) [40] investigated the inherent measurement uncertainties in the spatial average velocity and the total loss factor.

Spatial average velocity

The uncertainty of the spatial average velocity samples over the surface of an isolated concrete reception plate was considered in Späh's work (2006) [30]. It was observed that the highest velocity levels of the vibration field were at plate edges and corners rather than in the central zone. To avoid uncertainties when sampling the vibration field over the plate surface to determine the reception plate power, it was recommended to use a minimum of twelve randomly distributed positions placing ten in the central zone and two near to edges. This can be assumed to be specific to the reception plate that was used and does not take account of high velocities in the corners. In addition, it was stated that the response positions should be considered with a distance between each response position of at least 350 mm, and the response positions should be located at least 1000 mm away from the source excitation position. As a result, the velocity sampling led to higher uncertainty above 100 Hz than below 100 Hz [30, 33]. This contrasts with the low modal density of a reception plate, where the vibration response is dominated by well-separated bending modes. Because it was pointed out that there was a sufficient modal density with at least five modes in each band for the reception plate given at and above the 800 Hz band. However, the velocity sampling resulted in an estimate of the reception plate power that was within ± 2 dB of the exact value for a single-contact source [30, 33].

Schevenels (2011) [73] experimentally investigated the influence of the direct field and the edge effect for the location of response positions using an ISO

tapping machine on top of a small concrete plate with four feet that rested on the isolated concrete reception plate. (NB: The edge effect of a free vibrating plate referred to stored bending wave energy at edges and corners being large compared to the central zone.) It was concluded that the direct field affected the frequency bands below 100 Hz, but it was negligible at higher frequencies. In contrast, the edge effect for response positions was classified as disadvantageous above 200 Hz due to resulting constant larger velocity levels of ≈ 5 dB at the plate edges. But these response positions led to similar velocity levels compared to the other velocity levels at low frequencies. It has been suggested that uncertainties in velocity measurements on the reception plate were reduced when the positions at a distance of 100 mm from the plate edges were excluded. In addition, it was stated that the positions should be placed at least 200 mm away from each other [74]. This may be problematic because the influence of the direct field and the edge effect was not systematically investigated with regard to the spatial variation of the velocity over the plate surface; moreover, these effects were not considered in the context of a sampling strategy for velocity levels. Hence, this thesis investigates both the spatial variation of velocity levels over the plate surface and an appropriate sampling strategy for velocity because both direct field and edge effects occur for isolated plates with freely vibrating boundaries.

In connection with sampling strategies, a previous version of EN 15657 (2017) [35] (referred to as EN 15657-1 (2009) [36]) required at least six response positions over the plate surface. In this edition of the standard, it was recommended to measure the vibration field at positions that were only in the central zone of the plate, while positions near the source contacts and the plate corners/edges were excluded. In the current edition of the standard, EN 15657 (2017) [35], it is still suggested to use at least six positions of velocity measurements. In this standard, the measurement positions at edges or corners are not taken into account, but the distance between the measurement positions and the source contacts is specified with a minimum distance of 100 mm as a

result of the work carried out for this thesis that was presented at conferences [75, 76] and in a CEN/TC 126/WG 7 meeting at Paris on 27/09/2016.

Loss factor

Various research has been carried out to obtain the loss factor from coupled reception plates and isolated reception plates.

In Späh's work (2006) [30], the loss factor of the isolated horizontal concrete reception plate was changed using viscoelastic material so that it was similar to the loss factor of walls and floors in a heavyweight building. The loss factor was determined from structural reverberation time measurements using a Maximum Length Sequence (MLS) with the reversed filter technique [77] carried out according to EN ISO 10848-1 [78] to give T_{20} (evaluation range of the reverberation time is 20 dB). Below 100 Hz, the uncertainty in the loss factor was significantly higher than above 100 Hz. The reception plate power was found to be within ± 2.0 dB of the exact value for a single-contact source [33].

Scheck (2011) [31] derived a loss factor for the same reception plate from a structural reverberation time of T_{20} with MLS analysis using the conventional procedure [78] between 200 Hz and 5 kHz and the reversed filter technique [77] below 200 Hz that was approximately the same order of magnitude as Späh's estimate of the loss factor.

Hopkins and Robinson (2013, 2014) [44, 45] used TSEA and SEA to quantify the errors that can occur if the evaluation range for the structural reverberation time is too long. For a completely isolated reception plate, there should be no energy returning to the plate from other parts of the structure due to its 'isolation'; hence, the decay curve should be relatively straight that would allow use of evaluation ranges up to 30 dB. However, for a coupled reception plate (i.e. a plate rigidly connected to other walls or floors), it was shown that a very short evaluation range of 5 dB to give T_5 was necessary to avoid significant errors.

Padois et al. (2019) [46] investigated the influence of various structural reverberation time descriptors on an isolated steel reception plate. For

assessment of the loss factor, they applied structural reverberation times of T_3 , T_6 , T_{10} , T_{20} and T_{30} determined from the impulse response decay method. Below 100 Hz, this led to the shortest decay rates (highest loss factors). Only low frequencies below 100 Hz were compared against modal damping using the half-power bandwidth method, which were closest to T_3 , T_6 and T_{10} .

Errors in the estimate of the structure-borne sound power

Späh (2006) [30], and Späh and Gibbs (2009) [33] used a single-contact source represented by a broadband noise powered shaker for measurements based on their developed sampling strategy (see previous subsection ‘*Spatial average velocity*’ in this section) on an isolated horizontal concrete reception plate to determine the reception plate power which was validated with the direct injected power. Experiments on this specified sampling approach showed an underestimation of the reception plate power in one-third octave bands with an error up to 5 dB below 100 Hz, and between 125 Hz and 1.25 kHz, the reception plate power was typically obtained with an error of ≤ 1 dB.

Scheck (2011) [31] used an isolated vertical concrete reception plate and a broadband noise excitation derived by a shaker with one contact point to compare the reception plate power from fifteen velocity positions (presumably based on the recommendations of references [30, 33]) and the direct injected power. Overall, the reception plate power gave errors within ± 2 dB from 63 Hz to 1.25 kHz, only at 50 Hz, there appeared an exception with an error increasing up to 3 dB. For a coupled horizontal concrete reception plate, the reception plate power was determined with an error of up to 4 dB below 100 Hz, and between 125 Hz and 1.25 kHz [31], the errors in the reception plate power were similar to references [30, 33].

Höller and Gibbs (2018) [42] observed the same trend when experiments were taken for a customised multiple-contact source with four contact points using force transducers with an electrodynamic shaker arranged perpendicular to the plate and mounted on the top on a thick isolated metal plate. The plate mobility

was an order of magnitude smaller than the source mobility, the shaker was driven by pink noise, and the reception plate power was obtained from nine randomly distributed positions in plate velocity in the central zone and one near an edge. An error of up to 8 dB below 100 Hz was observed, which decreased above 100 Hz to an error that was similar to that found in Späh's work [30, 33].

To assess the repeatability and uncertainty with a reception plate for structure-borne sound characterisation, a round-robin test using a low-mobility plate was carried out in five European laboratories in association with CEN/TC 126/WG 7. For the round-robin test, the reception plate power was converted into the characteristic power, which is independent of the coupled receiver properties, using mobility methods [54, 79, 80]. However, Wittstock et al. (2011) [47] presented the results from this round-robin test which achieved reasonably good agreement of ± 4 dB for the independent source power known as characteristic reception plate power in terms of the standard deviation of reproducibility.

As an alternative measurement method, the power substitution method can be used to determine the reception plate power for isolated or coupled plates. This avoids some of the uncertainties with the velocity and loss factor measurements as shown for a single-contact source by Scheck (2011) [31] and a source with four contacts by Höller and Gibbs (2018) [42]. However, the substitution technique can be time-consuming if a source with known structure-borne sound power has to be mounted at the positions of the source contact points of a multiple-contact source with unknown structure-borne sound power on the reception plate.

1.2.1.4 Analytical and numerical modelling of the reception plate

The reception plate has been computationally modelled in various studies [27, 30, 32, 73, 81] using both the semi-analytical approach based on the modal summation of beam functions with regard to the mobility method (e.g. refer to Leissa (1969) [82] and Gardonio and Brennan (2005) [80]) and FEM as computational technique (e.g. Zienkiewicz et al. (2005) [83] and Bathe (2014)

[84]) to carry out numerical experiments. FEM was developed by Hrennikoff (1941) [85], Courant (1943) [86], and Prager and Synge (1947) [87], who introduced the discretisation concept of a continuous domain into a set of discrete sub-domains or elements. The name “*Finite Element Method*” or “*FEM*” for short was firstly coined by Clough (1960) [88], and the first FEM textbook on the basics of structural and continuum mechanics was attributed to Zienkiewicz (1967) [89]. There are many textbooks and papers on the use of FEM with plate/shell elements for bending analysis (e.g. [90, 91, 92]) and the relationship between wavelength and element size (e.g. [49, 93, 94, 95]). In this thesis, a FEM model of the reception plate is experimentally validated against measurements so that it can be used for numerical simulations to assess sampling procedures for the plate velocity.

Späh (2006) [30] created a reception plate model with free boundaries using a semi-analytical approach. Due to the lack of viscoelastic material, the results showed that the simulated driving-point mobility led to a frequency shift with differences of resonances and anti-resonances below 100 Hz using the experimentally determined driving-point mobility as a benchmark for validation.

Höller (2013) [27] also used the semi-analytical approach to model the reception plate with free boundaries but additionally simulated the same freely vibrating reception plate in FEM. Both simulations of the reception plate were compared with measurements using the driving-point mobility, for which the FEM results showed better agreement in resonances and anti-resonances above 100 Hz than the results from the semi-analytical approach. Below 100 Hz, these models of a reception plate with free boundary conditions gave larger differences compared to measurements since the viscoelastic supports on which the plate rests were not taken into account.

Schevenels (2011) [73] created a FEM model of a concrete reception plate with viscoelastic supports using the material properties of the density, Young's modulus and Poisson's ratio from the manufacturer's technical datasheet. According to his comparison of the driving-point mobility from FEM and

measurements, the FEM results showed sharper resonance peaks with frequency shifts in resonances and anti-resonances similar to those from Späh's and Höller's studies [27, 30]. This indicates that the viscoelastic material may have been insufficiently incorporated into the FEM model.

Since previous work on analytical and numerical models did not or insufficiently consider the damping effects of the highly damped reception plate, it is necessary to acquire knowledge of the damping theory in FEM in order to be able to model the dynamic behaviour correctly. For the damping theory, Lazan (1968) [96] provided a comprehensive fundamental textbook that conveys an in-depth knowledge and understanding of various damping mechanisms that affect the dynamic behaviour of viscoelastic material and other materials.

1.2.1.5 Assessment of the time-varying structure-borne sound power on the reception plate

At present, there is very little published research on the characterisation of structure-borne sound sources under time-varying operating conditions on the reception plate; hence, this is the main aspect of the investigation in this thesis.

Wittstock and Bietz (2009) [97] predicted an impulse signal induced by a shaker (sampled from a hammer with a plastic tip giving an impulse length of 1 ms and integration time of 512 ms obtained on a steel plate) on low- and high-mobility reception plates. The time-integrated transient signal was normalised to the time-averaged steady-state signal, which was fed to a frequency-dependent correction with differences of up to 20 dB. The results indicated that when comparing the experimentally obtained free velocity and blocked force with a validated lumped parameter model of the shaker and reception plate, the lumped parameter model was underestimated up to 10 dB at low frequencies and overestimated by up to 11 dB at high frequencies.

1.2.2 Review of prediction models to determine sound pressure levels in buildings

The review with regard to prediction models for assessing sound pressure levels in buildings consists of two separate sections that highlight the basic developments for steady-state excitation from sources in Section 1.2.2.1 and time-varying excitation from sources in Section 1.2.2.2.

1.2.2.1 Steady-state sources

Building acoustics, along with ships, automobile and aerospace vehicles, has a long history of using SEA to predict sound and vibration transmission. The building industry was one of the earliest and most active industry to develop this steady-state based prediction technique. A summation of the early developments of the approximately eight-year SEA history (1962 to 1970) was given by Lyon (1970) in his publication “*What good is statistical energy analysis*” [98] – including a short and concise description of the SEA expression. SEA is based on the fundamental law of coupling power proportionality or power balance between the subsystems for which the power flow from high modal energy to low modal energy occurs [99, 100]. A comprehensive and constructive description of the SEA theory has been the subject in textbooks, e.g. by Lyon and DeJong (1995) [101] and Craik (1996) [102].

From a building acoustics point of view, SEA is used to investigate the sound transmission of complex structures, particularly in terms of the sound radiation into adjacent rooms caused by an injected steady-state power into building structures. Hodges and Woodhouse (1986) [103], and Lyon and DeJong (1995) [101] defined several basic assumptions that are required to meet sufficiently accurate results with SEA and are valid in building acoustics.

Crocker and Price (1969) [104] showed the prediction of airborne sound into rooms on either side of an aluminium plate due to mechanical excitation of the

plate. The three-subsystem model achieved reasonably good agreement between theoretical and experimental results.

Gibbs (1974) [105] predicted the sound pressure energy within a room considering direct and indirect transmission that was caused by a random plate or wall vibration. The SEA parameters such as modal density, coupled loss factor, total loss factor and radiation resistance were obtained from theory as well as experiments taking into account the bending wave, the longitudinal wave and the transverse wave at corners, X- and T-junctions for the transmission coefficients to estimate the modal energy of a vibrating concrete plate. The results indicated that the plate vibration predominantly transmitted bending waves into the connected plates, while the longitudinal and transverse waves were negligibly small in the context of sound transmission (see also Gibbs and Gilford (1976) [106]).

Craik (1982) [107] used SEA to predict direct and flanking sound transmission for bending waves in built-up structures and radiated sound pressure levels in the diffuse sound field in multiple dwellings. For excitation, he employed a sound source and a vibrational source. In his SEA study, the coupling loss factors were determined by predictions and experimental work using a simplified ESEA method in which the latter only considered the energy levels of two subsystems. However, the comparison of the SEA and measurement energy levels showed good agreement for both types of sources at the mid and high frequencies, while larger errors from the vibrational source occurred at low frequencies due to the uncertainties in the predicted coupling loss factors. Craik and co-workers (1991) [108] then investigated these uncertainty problems in SEA predictions at low frequencies and came to the conclusion that this is caused by the low number of resonance modes within a frequency band which restrict the modal energy exchange between the subsystems (refer also to Hopkins (2000, 2002, 2007) [71, 109, 110]).

The simplified SEA models that form the European standard series EN 12354 [9, 10, 11] are mainly based upon the contributions of Gerretsen (1979, 1986,

1993) [111, 112, 113]. To predict the sound transmission throughout partitions, separating floors and flanking structures in dwellings, Gerretsen (1979, 1986) [111, 112] developed a simplified SEA-based calculation model excited by a diffuse sound field or impact force in the source room to estimate the sound reduction index in the receiving room; this work has been incorporated in EN 12354-1 [9] and EN 12354-2 [10]. The simplified SEA-based prediction model was further progressed by Gerretsen (1993) [113] describing the principles of machinery noise in terms of source strength as airborne and impact sound transmission through a building and taking into account the reciprocal relationship between these two mixed transmission types. Using these basics for the prediction of service equipment in heavyweight buildings, CEN/TC 126/WG 2 published the first draft of the simplified SEA-based prediction model in EN 12354-5 (2009) [11] (refer to prEN 12354-5 (2004) [114] for propagation models for airborne sound according to EN 12354-1 [9] and structure-borne sound according to EN 12354-2 [10]).

1.2.2.2 Time-varying sources

Most research studies on time-varying predictions have been carried out for mechanical excitation by a heavy impulse force (e.g. rubber ball, bang machine) with an impact time of ≈ 20 ms that mainly excites the floor in the low-frequency range. In this context, Kimura and Inoue (1989) [115] used the impedance method to estimate the difference between the maximum peak and energy integral levels resulting in differences from 5 to 10 dB. They indicated that the difference decreased with increasing frequency. Consequently, it was proposed to take into account an empirical correction term when predicting L_{Fpeak} from measured L_{Fmax} .

Schönwald et al. (2010) [116, 117] indicated that L_{Fmax} is influenced by room volume and absorption although this is not considered for heavy impact measurements in the Japanese standard JIS A 1418-2 [118]. They proposed a correction for an impulse response (e.g. rubber ball) as a function of the

reverberation time determined from the relationship between $L_{F_{\text{peak}}}$ and $L_{F_{\text{max}}}$ to adjust $L_{F_{\text{max}}}$ to the receiving room conditions.

Hopkins and co-workers (2014, 2015, 2018) [15, 16, 17, 18] used TSEA to determine the Fast time-weighted sound and vibration levels, $L_{p,F_{\text{max}}}$ and $L_{v,F_{\text{max}}}$, in heavyweight buildings using the measured force time-history of a rubber ball source and human footsteps. For this, a normalised transient power input was corrected to account for that the normalised transient power over the time duration of the transient force. The results showed close agreement between measured and predicted values for heavy impact sources such as the rubber ball and footsteps.

1.3 Statement of the problem

The sound and vibration from building machinery or other service equipment can be a nuisance for occupants of heavyweight buildings and have an adverse effect on their living comfort, health and working performance. The resulting sound pressure levels from these sources are primarily transmitted by the structure-borne sound component rather than their airborne sound [19]. Hence, there is a necessity to provide reliable solutions to quantify the structure-borne sound power that can be used in prediction models. For this purpose, industry and engineers are looking for simplified methods to predict and assess noise transmission in buildings at the design stage.

Direct and indirect measurement methods are available for the characterisation of structure-borne sound sources, as indicated in Sections 1.1 and 1.2.1.1. Indirect methods are suited to building acoustics due to their simplified data acquisition. The reception plate method is an indirect method specified in EN 15657 [35]. It is a practical engineering solution that allows determining strictly reduced, reliable and robust data in one-third octave bands from steady-state vibrating sources with point, line or surface connections to the

receiver interface. It is often used to obtain the power input from structure-borne sound sources with a steady-state operating cycle for SEA or simplified SEA-based prediction models (e.g. EN 12354-5 [11] for the calculation of sound pressure levels due to service equipment) in heavyweight buildings.

The structure-borne sound power measurement results shown in Figure 1-4 (Section 1.1) demonstrate the importance of minimising measurement uncertainties at low frequencies. Large measurement uncertainties with the reception plate method [19, 38, 39, 40, 41] occur at low frequencies in the spatial average velocity and loss factor. For uncertainties that occur with loss factor measurements on coupled and isolated reception plates, a suitable approach has been provided from the studies by Robinson and Hopkins [44, 45] and these can be mitigated. However, the large variation in the vibration field over the plate surface remains a cause of high measurement uncertainty at low frequencies [27, 30, 33, 42]. This is mainly due to a low modal density since the response of the vibration field is dominated by well-separated bending modes [30]. Beyond that, no consideration of rigid body modes of the reception plate has been made in previous studies [27, 30, 33, 42]. Consequently, there is little or no knowledge of the combination of rigid body modes and low-frequency bending modes on the validity of reception plate measurements at low frequencies. In addition, there is no validated numerical model (e.g. FEM) of a heavyweight reception plate with viscoelastic supports that can be used to predict and assess uncertainties in sampling strategies for plate vibration at low frequencies.

At present, the structure-borne sound power characterisation using the reception plate method according to EN 15657 [35] is restricted to steady-state excitation from vibrating sources to quantify the equivalent continuous level, L_{eq} . But most building machinery has time-varying operating conditions, e.g. starting of a pump or gas engine, a washing machine on spin or drainage, a toilet flush, etc. In most cases, this means that the automated or mechanically based machine has time-varying cycles where the injected structure-borne power can

rapidly increase and/or decrease over very short time periods. For this reason, some European building regulations (e.g. ÖNORM B 8115-2 [12] in Austria, SIA 181 [13] in Switzerland and VDI 4100 [14] in Germany) on installation noise require measurements in terms of L_{Fmax} instead of L_{eq} .

In heavyweight buildings, the assessment of the impact sound insulation from transient excitations with a short impact contact time in terms of L_{Fmax} can be predicted using TSEA. For impact sound insulation of heavyweight floors (with or without floating floors), TSEA requires measurements of the blocked force for which the approach has been successfully validated from a heavy impact by the rubber ball, bang machine and human footsteps [17, 18]. However, a full TSEA model is more complex than the simplified SEA-based model preferred by industry in the European standard EN 12354 [9, 10, 11]; hence, it is not feasible to incorporate it into this standard. Currently, there is no validated approach that would allow SEA or simplified SEA-based models to predict L_{Fmax} levels in heavyweight buildings due to time-varying power input from building machinery or building equipment that has been measured on the reception plate. This is addressed in this thesis in order to develop a practical and simplified engineering procedure for the prediction of sound levels from time-varying building machinery. The aim is to estimate L_{Fmax} from SEA or simplified SEA-based models using an empirical correction that has been determined in this thesis.

Hence, the two main problems, where a challenge remains, are (1) a reliable characterisation of power input on the reception plate at low frequencies and (2) the ability to predict L_{Fmax} from SEA or SEA-based prediction models.

1.4 Objectives

The two main objectives of this thesis relate to improving and extending the application of the reception plate method; these are (1) the characterisation of structure-borne sound sources under steady-state conditions using a heavyweight reception plate at low frequencies and (2) the prediction of sound levels due to structure-borne sound excitation from sources under time-varying conditions in heavyweight buildings for which the power input data are determined on a heavyweight reception plate. Both parts aim to provide physical reliable data for the structure-borne sound characterisation and prediction based on simplifying the measurement and prediction while maintaining suitable accuracy.

The contributions to the characterisation of structure-borne sound sources under steady-state conditions using a heavyweight reception plate aim at the following:

- To develop and validate a FEM model of a heavyweight reception plate which incorporates the viscoelastic supports around the edges. This would allow prediction of the total loss factor of the reception plate at the design stage to assess how much viscoelastic material is needed.
- To use the validated FEM model of a heavyweight reception plate to develop a sampling strategy for vibration measurements that will allow lower uncertainty and more accurate spatial velocity levels to determine the reception plate power from single- and multiple-contact sources. This will take into account positions with lower vibration levels in the central zone as well as higher vibration levels near corners and/or edges without requiring time-consuming measurements in a fine regular grid over the entire plate surface.
- To investigate the accuracy of the reception plate power below the first bending mode in order to assess whether the frequency range with rigid body modes can be used to give valid low-frequency power estimates.

The prediction of sound pressure levels due to structure-borne sound excitation from sources under time-varying conditions in heavyweight buildings focuses on:

- Assessing the potential for a simplified empirical correction to estimate L_{Fmax} levels from short L_{eq} levels using time-varying signals with different measurement situations.
- Identifying whether the reception plate could be used to capture the structure-borne sound power from time-varying sources using short L_{eq} data. This could then be used as power input data for the SEA prediction in conjunction with an empirical correction to convert the sound pressure levels from short L_{eq} to L_{Fmax} .
- Validating the empirical correction using a case study on the heavyweight reception plate to confirm whether it is feasible to predict L_{Fmax} levels from short L_{eq} levels.

1.5 Layout of the thesis

The layout of the chapters is as follows:

1. A review of the underlying theory and applied experimental methods (Chapter 2 and Chapter 3).
2. The development and experimental validation of FEM models of the reception plate (Chapter 4).
3. New sampling strategies to determine the steady-state structure-borne sound power on the reception plate and validation with *in situ* measurements (Chapter 5).

4. A new approach using an empirical correction to predict $L_{F_{\max}}$ and $L_{AF_{\max}}$ from time-varying vibration excitations with SEA and validation with *in situ* measurements (Chapter 6 and Chapter 7).
5. A case study on a real time-varying source on a reception plate (Chapter 8).
6. A summary of the conclusions (Chapter 9).

Chapter 2 describes the underlying theory of bending waves and prediction models for sound and vibration using FEM in terms of structure-borne sound characterisation and SEA. The basic concepts related to relevant equations and parameters are explained to understand and solve the prediction methods and their applications to bending mode theory and frequency analysis. Two challenges are highlighted for the two main investigated objectives: potential issues with the low-frequency characterisation of steady-state structure-borne sound power and the prediction of $L_{F_{\max}}$ from short (125 ms) L_{eq} at maximum, $\max\{L_{\text{eq},125\text{ms}}\}$, for covering the time-varying structure-borne sound power.

Chapter 3 contains the details on the test constructions in terms of the reception plate for structure-borne sound characterisation and *in situ* measurements for sound and vibration to determine $L_{F_{\max}}$ and short (125 ms) L_{eq} for direct transmission in a building-like situation as well as the experimental procedures. It describes measurement procedures including Experimental Modal Analysis (EMA), mobility and damping to validate the FEM models of a reception plate. The experimental investigations of ramped noise signals with their signal processing in relation to $L_{F_{\max}}$ and $\max\{L_{\text{eq},125\text{ms}}\}$ are discussed to provide a basis for SEA predictions.

Chapter 4 introduces the FEM modelling procedure, verifies the numerical incorporated spring-dashpot elements with an analytical approach of a single mass-spring-damper system and validates the FEM models using experimental

data from EMA, damping and mobility. Two single-contact source positions on the FEM model and experimental set-up of the reception plate are used to investigate numerically and experimentally the spatial variation in plate velocities. An analytical approach of single mass-spring-damper systems and a multi-modal system is used to discuss the role of rigid body modes below bending modes at low frequencies.

Chapter 5 covers the development of vibration sampling strategies on the reception plate for structure-borne sound characterisation. Single-contact source excitations are used to initially validate the new sampling approaches to an empirical weighted and area-weighted velocity approach from FEM and measurements, which is extended in FEM to multiple-contact sources representing typically white goods with zero- and random-phase forces between the contacts.

Chapter 6 looks at empirical strategies for correcting the offset between L_{Fmax} and $\max\{L_{eq,125ms}\}$ used for time-varying signals. The determined empirical corrections are discussed on the base of ramped noise signals that are played directly into a measurement system and into a shaker on a reception plate and a floor in a building-like situation. For the latter *in situ* measurement situation, also the radiated sound into the receiving room is recorded. The empirical corrections assessed from measurements are highlighted as a ramp- and level-dependent (specific) and a single-number approach for time-varying signals.

Chapter 7 deals with the SEA prediction of time-varying structure-borne sound sources with regard to velocity and sound pressure levels in terms of L_{Fmax} with a structure-borne sound power input that corresponds to the maximum power input over a short time period, $\max\{L_{eq,125ms}\}$, by making use of the empirical corrections in Chapter 6. It then assesses whether the prediction of L_{AFmax} from predicted L_{Fmax} levels is feasible. The estimated results from SEA predictions are discussed in comparison with measurements.

Chapter 1

Chapter 8 has a case study to experimental validate a time-varying structure-borne sound source. A sanitary installation system is chosen because the toilet flush provides an example of a time-varying operation cycle with more than one contact point. The reception plate test rig is used to assess the relationship between $\max\{L_{\text{eq},125\text{ms}}\}$ and L_{Fmax} levels. The determined empirical correction from the toilet flush is discussed to check whether the empirical correction from a real time-varying source can reproduce the empirical correction obtained from ramped noise signals in Chapter 6.

Chapter 9 summarises the findings and rounds off with possible future work.

2 Theory and prediction models

2.1 Introduction

Bending wave motion is used to characterise the structure-borne sound power on the reception plate and is responsible for sound radiation from walls and floors. This chapter describes the theory for bending waves on plates in Section 2.2 in terms of thin plate theory along with modal characteristics, damping, mobility and radiation efficiency.

The two prediction models used in the thesis are FEM, which is described in Section 2.3, and SEA in Section 2.4. The theory and fundamental equations for FEM, which is used to model the reception plate, and SEA, which considers a coupled plate-cavity subsystem to model a floor radiating into a room, are introduced. As SEA predicts steady-state response, a proposal is made on how SEA could be used to predict L_{Fmax} from short L_{eq} for this thesis.

The theory for the characterisation of structure-borne sound power is described in Section 2.5. For the characterisation of the structure-borne sound power input into plate-like structures, consideration is given to issues relating to rigid body modes and spatial variation of the vibrational response.

2.2 Bending wave theory and prediction modelling for structure-borne sound characterisation

In the building acoustics frequency range (50 Hz to 5 kHz), most solid wall or floor structures can be modelled using thin plate bending theory where the plate thickness is much smaller than the wavelength. Bending waves are of particular interest because they are directly excited by most types of machinery that apply forces perpendicular to the plate surface (and also by sound waves in air). Bending wave theory based on the classical two-dimensional (2D) thin plate theory from Kirchhoff and Love [119, 120] is introduced. The plate's modal response approach, diffuse field assumption and damping effects with regard to bending waves are summarised. Since damping has a significant influence on the vibrational response, mechanical mobility is emphasised as a form of bending wave excitation.

As well as the out-of-plane response from bending waves, there are in-plane waves. When bending waves impinge on connections between plate structures, this can lead to the generation of longitudinal and transverse shear waves that often contribute to structure-borne sound transmission in the mid- and high-frequency range.

2.2.1 Thin plate theory

For thin plates, Kirchhoff-Love plate theory [119, 120] is commonly applied to solve dynamic and propagation problems based on pure bending deformation in the linear domain. The middle surface is used to reduce the three-dimensional (3D) space to a 2D space.

For wave propagation problems, it is common to identify thin plates by referring the plate thickness, h , to the bending wavelength, λ_B , such that $h \leq \lambda_B/6$ [49]. Thin plate theory can be used if the following further basic assumptions are met [121, 122]:

1. The plate material is homogeneous, isotropic and elastic, which allows that Hooke's law based on the constitutive relation between strain and stress, $\sigma = B_p \varepsilon$, holds.
2. The deflections are fully described by the transverse displacements of the normal to the vertical dimensions using $w(x, y, z) = w(x, y)$.
3. The initially flat mid-surface of the plate is a neutral axis, which remains straight and unstretched during bending, and the normal perpendicular to the mid-surface remains perpendicular during deformation.
4. The deflections are a fraction of the plate thickness, $w/h \leq 1/5$, so that the transverse shear strains are considered negligible, $\gamma_{xz} = \gamma_{yz} = 0$, and the normal strain of the mid-surface may be assumed to be zero, $\varepsilon_z = 0$.
5. The stress normal to the mid-surface vanishes throughout the thickness, $\sigma_z = 0$, compared to the other variations of stress components.

Free out-of-plane (bending) vibrations of a homogeneous, isotropic and elastic thin rectangular plate with constant thickness can be summarised on the formulation of small transverse deflections and stresses that are described by the angular torsional displacements, resultant in-plane forces, bending and twisting moments according to the Kirchhoff assumptions. Thus finally leads to the governing harmonic equation of motion for bending waves (homogeneous Partial Differential Equation (PDE) of fourth-order) on a thin homogeneous, isotropic and elastic thin plate in free vibration that is given by

$$\left(B_p \nabla^4 + \rho_s \frac{\partial^2}{\partial t^2} \right) w(x, y, t) = F_z(x, y) \quad (2.1)$$

with

$$B_p = \frac{EI_p}{(1-\nu^2)} \quad (2.2)$$

and

$$\nabla^4 = (\nabla^2)^2 = \left(\frac{\partial^2}{\partial x^2} + \frac{\partial^2}{\partial y^2} \right)^2 = \frac{\partial^4}{\partial x^4} + \frac{2\partial^4}{\partial x^2 \partial y^2} + \frac{\partial^4}{\partial y^4} \quad (2.3)$$

where B_p is the bending stiffness, $I_p = h^3/12$ is the moment of inertia of the cross-sectional area, E and ν are Young's modulus and Poisson's ratio respectively, ρ_s is the mass per unit area, F_z is an applied external force (e.g. point load) and ∇^4 is the biharmonic differential operator equivalent to the squared Laplacian differential operator, ∇^2 .

To obtain the response of propagation of out-of-plane waves, Eq. (2.1) is solved in the absence of external forces by assuming a harmonic displacement excitation, $w(x, t) = \hat{w}e^{i(\omega t - k_x x)}$, applied in the x -direction which results in the bending wavenumber of the plate, $k_B = k_x$, by [71]

$$k_B = \sqrt[4]{\frac{\omega^2 \rho_s}{B_p}} = \frac{2\pi}{\lambda_B} \quad (2.4)$$

and the bending phase velocity of the plate, $c_{B,p}$, as

$$c_{B,p} = \frac{\omega}{k_B} = \sqrt[4]{\frac{\omega^2 B_p}{\rho_s}} = \lambda_B f \quad (2.5)$$

where \hat{w} is an arbitrary constant, λ_B is the bending wavelength, ω is the angular frequency and f is the angular frequency cycle per second. The group velocity, $c_{g(B),p}$, describes the velocity of energy propagation and is twice the phase velocity (Eq. (2.5)) and is calculated using

$$c_{g(B),p} = \frac{\partial \omega}{\partial k_B} = c_{B,p} + \frac{\partial c_{B,p}}{k_B} k_B = 2c_{B,p} \quad (2.6)$$

2.2.2 Modal response

For the free, time-dependent harmonic motion of a rectangular plate as a 2D extension of the beam, the local out-of-plane mode shapes of thin rectangular plates, $\psi_{pq}(x, y)$, may be determined from the product of characteristic beam functions, $\phi_p(x)$ and $\phi_q(y)$, as [80, 82]

$$\psi_{pq}(x, y) = \phi_p(x)\phi_q(y) \quad (2.7)$$

where p and q are the number of nodal lines in x - and y -directions respectively. This is a superposition of the response of one beam aligned in the x -direction and another beam in the y -direction assuming no coupling between the separate beam motions. In references [80, 82], various boundary conditions with the associated zeros of the gamma functions for characteristic beam functions are given, which have to satisfy $x=0$ and $x=L_x$ or $y=0$ and $y=L_y$ along the edges.

For vibration problems, the beam function approach is appropriate when plates have simply-supported or clamped boundaries. However, in the context of an isolated reception plate where the plate edges are similar to free boundaries, calculations with beam functions can cause errors [27]. The semi-analytical approach assumes that the plate deflection is a superposition without any cross-coupling of the beam functions in x - and y -directions. This approach does not take into account the elastic deformation of the material by contraction (and expansion) arising from the Poisson's ratio effect. This becomes important for plates with free boundaries according to reference [27].

The corresponding out-of-plane mode eigenfrequencies of thin rectangular plates with dimensions of L_x and L_y for various types of boundary conditions can be approximated by [80, 82]

$$f_{pq} = \frac{\pi}{2} \sqrt{\frac{B_p}{\rho_s}} \frac{\xi_{pq}}{L_x} \quad (2.8)$$

with ξ_{pq} as a dummy variable for

$$\xi_{pq}^2 = G_x^4(p) + G_y^4(q) \left(\frac{L_x}{L_y} \right)^4 + 2 \left(\frac{L_x}{L_y} \right)^2 \left[\nu H_x(p) H_y(q) + (1-\nu) J_x(p) J_y(q) \right] \quad (2.9)$$

where f_{pq} is the eigenfrequency in the group of the order p and q of corresponding bending modes, G , H and J are the frequency coefficients of the related boundary conditions along plate edges that are valid for $x=0$ and $x=L_x$ or $y=0$ and $y=L_y$. The frequency coefficients for a plate with various boundary conditions along the edges can be found in the literature (e.g. [80, 82]).

For an isolated reception plate that is supported on resilient material [30, 33], the boundaries can be considered to be free or relatively unconstrained. In contrast, the boundary conditions for structural plate-like elements in buildings are seldom known exactly. Therefore, when the modal density, $n(f)$, is required, statistical descriptors are commonly used as an alternative and simplified approach. For high frequencies, the asymptotic modal density of a plate with any boundary conditions can be estimated by [102]

$$n(f) = \frac{S}{2} \sqrt{\frac{\rho_s}{B_p}} \quad (2.10)$$

where S is the surface area of the plate. At low frequencies, the boundary conditions become more important and a correction can be used to estimate the modal density for free boundaries using [72]

$$n_{\text{FFFF}}(f) = \frac{S}{2} \sqrt{\frac{\rho_s}{B_p}} + \frac{1}{2} \sqrt{\frac{2\pi}{f}} \left(\frac{L_x + L_y}{\pi} \right) \sqrt{\frac{\rho_s}{B_p}} \quad (2.11)$$

where the subscript FFFF denotes the four free edges of the plate.

2.2.3 Diffuse field response

Idealised vibration fields can be used to simplify prediction models. One such idealisation is the diffuse field. A diffuse field can be described by bending waves with uniform energy intensity and random phase arriving with equal probability from any angle.

For a finite plate, the diffusivity of a vibration field is equivalent to the equipartition of energy amongst resonant modes [123] so that the average energy is nearly the same for all modes with an uncorrelated response amplitude. This assumes a sufficiently high number of modes and a large modal overlap factor per frequency band [101]. For the number of modes of a thin plate, the mode count, N , as a statistical quantity is introduced and can be calculated by

$$N = n(f) \Delta f = n(f) B \quad (2.12)$$

where Δf is the interval of a given frequency band with a bandwidth B . Diffuse bending field conditions on a plate can be expected when $N \gg 1$ and the plate is asymmetric.

With regard to bending waves of thin plates, the modal overlap factor, M , describes the average number of modal resonances that fall within the half-power modal bandwidth, $\Delta f_{3\text{dB}}$, and is obtained from [101, 102]

$$M = \frac{\Delta f_{3\text{dB}}}{\Delta f} = f \eta n(f) \quad (2.13)$$

where Δf is the average modal spacing between adjacent mode frequencies and η is the loss factor. A modal overlap factor larger than unity, $M \gg 1$, can be associated with high modal density and/or high damping causing broader

resonance amplitudes that yield to an increasingly uniform resonant response. In contrast, the modal overlap is mostly much less than unity, $M \ll 1$, due to low density and/or low damping at low frequencies, which results in well-separated resonances that dominate the resonant response.

The reverberation distance, r_{rd} , is commonly used to partition the response into a diffuse field and a direct field. For a finite plate, the reverberation distance is derived by [101]

$$r_{rd} = \frac{\omega \eta S}{4\pi c_{B,p}} \quad (2.14)$$

which is frequency-dependent due to dispersive bending waves [71]. Beyond the reverberation distance, the response is primarily determined by the diffuse field.

2.2.4 Damping

From bending waves, damping occurs by internal losses from the conversion into heat due to dissipated energy, coupling losses due to energy transmission to other connected plate-like elements at boundaries and coupling losses due to radiation or dissipation into a fluid.

The dependence of the total loss factor, η_{tot} , is composed of the sum of the internal loss factor, η_{int} , and both coupling loss factors, η_{coup} and η_{rad} , from boundaries and radiation respectively. Hence, the total loss factor is taken the form

$$\eta_{tot} = \eta_{int} + \eta_{coup} + \eta_{rad} \quad (2.15)$$

Further discussion based on the coupling and total loss factors which are used for SEA predictions can be found in Section 2.4.1.2.

The internal loss factor of the plate material results from the phase difference between stress and strain and is equivalent to the complex modulus using [96]

$$\eta_{\text{int}} = \frac{E''}{E'} \quad (2.16)$$

where E' and E'' are the real and imaginary parts of the complex modulus of elasticity respectively. Hence, material damping can be incorporated into the analytical approach of a thin rectangular plate (refer back to Eq. (2.1)) where bending stiffness as a function of elastic modulus becomes complex (refer back to Eq. (2.2)). The damping can then be considered by making bending stiffness complex, $B_p^* = B_p(1 + i\eta)$ [49]. More information on material damping, which is often referred to as the structural (or hysteretic) damping mechanism used in FEM approximations in the frequency domain, is introduced in more detail in Section 2.3.2.2.

However, the coupling loss factor with reference to boundaries or transmission between two plates based on energy incident upon edges can be calculated with knowledge of the group velocity, c_g , and the transmission coefficient, τ , using [107]

$$\eta_{\text{coup}} = \frac{c_g L \tau}{\pi S \omega} \quad (2.17)$$

where L is the coupling length of the plate to other connected plates. Thus, this loss factor due to coupling between plates can be directly related to the transmission coefficient. Whereas the coupling loss factor for radiation from a plate into a fluid is defined by [49]

$$\eta_{\text{rad}} = \frac{\rho_0 c_0 \sigma}{\pi \rho_s \omega} \quad (2.18)$$

where ρ_0 and c_0 are the density and the phase velocity of the surrounding fluid respectively and σ is the radiation efficiency. Thus, the loss factor due to radiation from the plate is proportional to the radiation efficiency.

2.2.5 Mobility

The concept of mechanical mobility as a function of frequency, $Y(\omega)$, is a representation of a complex Frequency Response Function (FRF) consisting of amplitude and phase that reflects the modal dynamic property of a structure. At the resonance frequencies, the peaks in the amplitude of the mechanical mobility occur due to the eigenfrequencies that are under damping control. The mechanical mobility is a measure of the ratio of the force, $F(\omega)$, acting at a point by mechanical impulse or harmonic excitation and velocity, $v(\omega)$. Both the driving-point mobility and transfer mobility are used in the experimental work in this thesis.

The complex driving-point mobility, Y_{dp} , is defined by the ratio of the transverse velocity response, v , to the force, F , at the same point on the plate and is given by

$$Y_{dp} = \frac{v}{F} \quad (2.19)$$

Using the subscript i for the same excitation and response location on the plate, the driving-point mobility, $Y_{dp} = Y_{ii}$, can be reformulated to

$$Y_{ii} = \frac{v_i}{F_i} \quad (2.20)$$

The complex transfer mobility, Y_{ij} , describes the ratio between the velocity and force applied in the same transverse direction where the excitation and response location on the plate are different. This gives the following equation

$$Y_{ij} = \frac{v_j}{F_i} \quad (2.21)$$

where the subscripts i and j denote the excitation and response positions respectively. In experimental work with EMA (Section 3.3.3), the transfer

inertance, H_{ij} , is measured instead of the transfer mobility by replacing the velocity in the numerator with acceleration, a_j .

A Single Degree of Freedom (SDOF) lumped mass-spring-dashpot system as shown in Figure 2-1 can be used to represent a single mode of vibration and to assess the driving-point mobility. This gives the driving-point mobility for an SDOF system as [49]

$$Y_{dp} = \frac{1}{\eta\omega_0 m + i\left(\omega m + \frac{k}{\omega}\right)} \quad (2.22)$$

where $i = \sqrt{-1}$ is the imaginary part denotation, ω_0 is the undamped angular frequency of oscillation, m is the mass and k is the spring stiffness. Note that the mobility amplitude, which includes alternating peaks (or crests) and troughs, decreases with increasing damping. From the real part of the mobility peak value at the undamped resonance frequency of Eq. (2.22), the initial 3 dB down point defines the damping control region by the half-power bandwidth, Δf_{3dB} , (see Figure 2-1). At frequencies below the half-power bandwidth, the left-side region towards lower frequencies is controlled by the stiffness, $f < (f_0 - \Delta f_{3dB}/2)$, and the right-side region towards higher frequencies is controlled by the mass, $f > (f_0 + \Delta f_{3dB}/2)$ [71]. Approximations for these regions can be written as follows

$$\begin{aligned} Y_{dp} &\approx \frac{i\omega}{k} && \text{for } f < (f_0 - \Delta f_{3dB}/2) \\ Y_{dp} &\approx \frac{1}{i\omega m} && \text{for } f > (f_0 + \Delta f_{3dB}/2) \end{aligned} \quad (2.23)$$

where f_0 is the undamped resonance frequency.

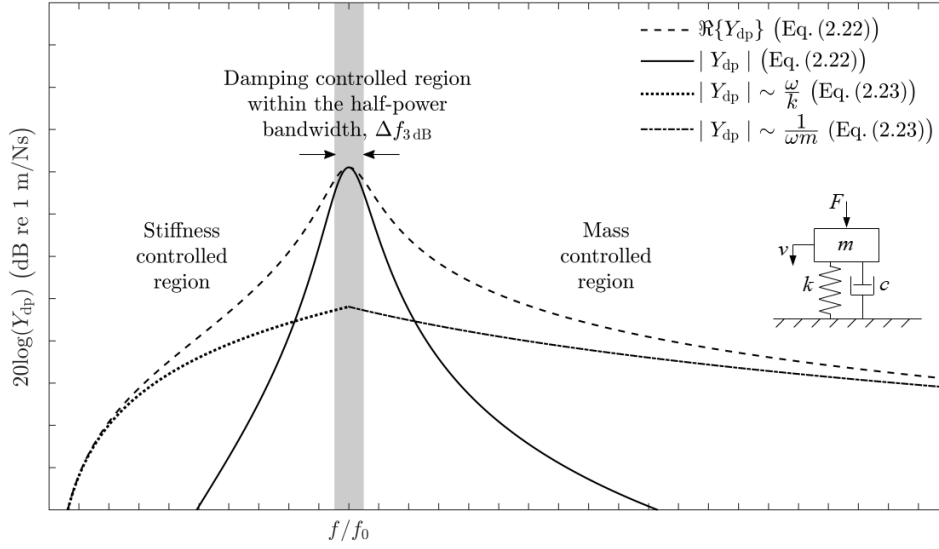


Figure 2-1. Driving-point mobility and schematic circuit representation for a mass-spring-dashpot system adapted from [71].

For a finite plate with arbitrary boundary conditions and an infinite number of local out-of-plane modes, Eq. (2.22) can be used to assess the overall response to the local modes by modal summation of the response from all SDOF mass-spring-dashpot systems [71] or using the analytical expression of the modal expansion at the driving point [49, 71]

$$Y_{dp,pq} = \frac{i4\pi}{\rho_s S} \sum_{p=1}^{\infty} \sum_{q=1}^{\infty} \frac{\psi_{pq}^2(x,y)}{[\omega_{pq}^2(1+i\eta) - \omega^2]} \quad (2.24)$$

where ω_{pq} is the angular eigenfrequency and $\psi_{pq}(x,y)$ is the corresponding mode shape at the location in terms of the force excitation and the velocity response on the receiver structure. Thus, Eq. (2.24) uses beam functions, $\phi_p(x)$ and $\phi_q(y)$, for the modal drive and response functions as indicated in Section 2.2.2.

Although finite plates are considered in practice, the concept of an infinite plate is a useful approximation for damped multi-modal systems when frequency-average mobilities are taken into account. Note that an infinite plate

can be considered as a finite plate with perfectly absorbing boundaries. The driving-point mobility of an infinite thin plate, $Y_{dp,\infty}$, is real and frequency-independent that can be written with reference to the plate's central zone as [49]

$$Y_{dp,\infty} = \frac{1}{8\sqrt{B_p\rho h}} \quad (2.25)$$

and at a plate edge as

$$Y_{dp,\infty} = \frac{1}{3.5\sqrt{B_p\rho h}} \quad (2.26)$$

where ρ is the density. The infinite plate mobility is often used to scale finite plate mobilities due to changes in material or thickness and to assess mobility measurements to see if the infinite plate mobility is a reasonable approximation.

2.3 Finite Element Method (FEM)

FEM has become an increasingly popular, versatile and powerful numerical tool in science and engineering design/analysis in order to understand and predict the dynamic and vibration behaviour of structures. Originally, FEM as a deterministic method was intended as a tool for dynamic analysis with long wavelengths, which led to computational inefficiency and longer computational time costs at high frequencies with decreasing wavelengths.

Continuous progress in computer technology has also spurred developments in FEM, which enables a solution to be studied in a broader frequency range depending on the complexity and accuracy requirements desired in the FEM model. This thesis deals with the vibration response of rectangular heavyweight plates, which are performed with the FEM simulation software package Abaqus/CAE 6.14-2 (called Abaqus for short) from Dassault Systèmes SIMULIA.

2.3.1 Governing equations for dynamic analysis using FEM

FEM is a numerical approximation method of PDEs to solve a physical phenomenon of a finite number of DOFs compared to the continuum theory that appears with an infinite number of DOFs. This numerical approximation technique uses the geometry of a physical system in which the computation domain to be analysed is divided into numerous small sub-domains (the process of so-called mesh generation). The subdomains are referred to as finite elements or patches that are reconnected at nodes located on the element boundaries. The unknown field variables within a discrete domain are approximated by interpolation (or shape) functions and the corresponding known coefficients of the nodal DOF [83, 84]. For each element, the local set of PDEs, along with its imposed constraints, is converted into a local set of simultaneous algebraic equations to describe the element characteristics [83].

Dynamic analysis is used to approximate the response within an element at its nodal DOFs using the principle of virtual work, which finally leads to the global response over all elements. The individual elements of the dynamic system are assumed to take into account the inertia, damping and stiffness effects. Hence, after the assembling of the individual algebraic element equations with regard to the consolidated element characteristics, the resulting global equilibrium equation of motion (homogeneous PDE of second-order) is finally derived by [83, 84]

$$[M]\{\ddot{q}\} + [C]\{\dot{q}\} + [K]\{q\} = \{F\} \quad (2.27)$$

with the following assignments of the global assembled FEM domain

$$\begin{aligned}
[M] &= \bigcup_{e=1}^{N_{el}} \int_{\Omega^{(e)}} \rho [N]^{(e),T} [N]^{(e)} d\Omega^{(e)} \\
[C] &= \bigcup_{e=1}^{N_{el}} \int_{\Omega^{(e)}} \chi [N]^{(e),T} [N]^{(e)} d\Omega^{(e)} \\
[K] &= \bigcup_{e=1}^{N_{el}} \int_{\Omega^{(e)}} [B]^{(e),T} [D]^{(e)} [B]^{(e)} d\Omega^{(e)} \\
\{F\} &= \bigcup_{e=1}^{N_{el}} \int_{\Omega^{(e)}} [N]^{(e),T} \{F_b\}^{(e)} d\Omega^{(e)} + \bigcup_{e=1}^{N_{el}} \int_{\Gamma^{(e)}} [N]^{(e),T} \{F_t\}^{(e)} d\Gamma^{(e)} + \sum \{F_p\}
\end{aligned} \tag{2.28}$$

where $[M]$, $[C]$ and $[K]$ are the inertia, damping and stiffness matrices, $\{q\}$, $\{\dot{q}\}$ and $\{\ddot{q}\}$ are the generalised displacement, velocity and acceleration vectors, $\{F\}$ is the generalised force vector, $\{F_b\}$ and $\{F_t\}$ are external distributed forces in terms of body loads and surface tractions, $\{F_p\}$ includes all applied concentrated forces (e.g. point loads), ρ is the mass density of the material, χ is the viscous damping parameter, $[B]$ is the strain-displacement matrix combining the differential operator $[\nabla]$ and the interpolation function matrix $[N]$, $[D]$ is the constitutive matrix, Ω is the spatial element domain, Γ is the boundary subjected to the element surface, \bigcup is the operator of the assemblage process over N_{el} -th elements, the superscripts (e) and T denote the elements within a discrete domain and transpose value.

However, damping effects stem from the energy dissipation mechanism in real physical systems, which can be described by frequency-independent structural (or constant hysteretic) damping in the frequency domain. For this reason, the concept of complex stiffness, $[K^*]$, is introduced by

$$[K^*] = [K'] + i[K''] = (1 + i\eta)[K] \tag{2.29}$$

where $[K']$ and $[K'']$ are the matrices of the real and imaginary part of the stiffness respectively and η is the loss factor (which is also referred to as the

structural damping factor, γ). Using only this concept of the complex stiffness from Eq. (2.29) in Eq. (2.27) to account for the internal damping effects associated with the dissipated energy converted into heat, the equation of motion takes the form as follows

$$[M]\{\ddot{q}\} + (1 + i\eta)[K]\{q\} = \{F\} \quad (2.30)$$

In Section 2.3.2.2, the structural (or hysteretic) damping is introduced in more detail.

2.3.1.1 Eigenvalue analysis

Eigenvalue extraction analysis is used to identify the basic dynamic characteristics of a linear and time-invariant structural system with regard to eigenfrequencies and corresponding mode shapes. For a free structural damped N -DOF system with no external loading, the eigenvalue problem can be written in terms of the harmonic response, $\{q\} = \{\psi\} e^{i\omega t}$ and $e^{i\omega t} \neq 0$, as

$$(-\lambda[M] + (1 - i\eta)[K])\{\psi\} = 0 \quad (2.31)$$

where $\{\psi\}$ is the frequency-dependent amplitude vector in the change of the generalised displacement field $\{q\}$ and $\lambda = \omega^2$ is the eigenvalue of the system. The non-trivial eigenvalue problem solution of Eq. (2.31) may lead to complex eigenvalues, $[\Lambda^*] = \pm(1 + i\eta)[\Omega_n^2]$, and complex eigenvectors, $[\Psi^*]$.

Note that for an unconstrained or a ‘nearly unconstrained’ system with low damping, the modal stiffness matrix vanishes for rigid body modes [124] resulting in three translational and three rotational rigid body modes at or close zero frequency. For a relatively unconstrained system due to strongly damped supports, it can be assumed that some of the six rigid body modes are non-zero in the low-frequency suspension. Rigid body modes are modes that translate or rotate without flexible deformation. This influence is most important as it can be

expected for a modelled isolated reception plate supported on resilient material [30, 33] (viscoelastic material).

However, an important property of eigenvalue extraction or modal analysis is that each particular eigenvector coincides with particular eigenvalues where the matrices $[M]$ and $[K]$ are symmetrical. For proportional damping, the mass and complex stiffness matrices can be assumed to become symmetric-diagonal with real-valued normal modes, which occurs when the loss factor is associated with a global presence; hence, each element possesses the same loss factor (e.g. due to lightly constant damping like structural damping with evenly over all elements distributed internal loss factor of a single material). Proportional damping satisfies the orthonormal mode conditions and with reference to the generalised mass normalisation, the orthogonality criteria are given by

$$[\Phi]^T [M] [\Phi] = [I] \quad [\Phi]^T (1 + i\eta) [K] [\Phi] = \text{diag}([\Lambda]) \quad (2.32)$$

where $[\Phi] = [\Psi][m_i^{-1/2}]$ is the mass-normalised modal matrix [125], $[\Lambda]$ is the diagonal spectral matrix, $[\Psi]$ is the corresponding real-valued normal mode matrix and $[I] = [\dots 1 \dots]$ is the identity matrix.

In contrast, non-proportional damping leads to a complex stiffness matrix that does not become diagonal, and the normal modes are complex-valued for any DOF amplitude that includes both magnitude and phase angle. For structural damping, this can be assumed if the FEM model consists of different materials (e.g. due to substructures or spring-dashpot systems that are highly damped and/or not evenly distributed over the elements). Then the FEM model possesses locally aligned damping. It may be possible that the orthogonality criteria can also be fulfilled for the complex eigenvectors by generalising them with respect to the phase angle, which is allocated to 0 or 180 degrees to obtain real-valued eigenvectors [125] (see Section 3.3.3.2).

2.3.1.2 Frequency response analysis

Frequency response analysis is used to study steady-state excitation of linear dynamic problems in terms of the perturbation approach in the frequency domain. This analysis type is a computationally expensive method to identify the intrinsic system characteristics due to the state of displacements, strains and stresses under harmonic motion. The harmonic excitation is generally applied as a concentrated force load in the form of a sine/cosine with a constant amplitude and frequency or a frequency sweep with constant amplitude.

For a linear structural damped system subjected to a defined harmonic load that produces a harmonic response, the approach for the force and displacement vectors can be written as [126]

$$\begin{aligned}\{q\} &= \{\hat{q}\} e^{i\omega t} = (\Re\{\hat{q}\} + i\Im\{\hat{q}\}) e^{i\omega t} \\ \{F\} &= \{\hat{F}\} e^{i\omega t} = (\Re\{\hat{F}\} + i\Im\{\hat{F}\}) e^{i\omega t}\end{aligned}\quad (2.33)$$

where $\Re\{ \}$ and $\Im\{ \}$ are the real and imaginary parts with regard to the amplitude of displacement, $\{\hat{q}\}$, and force, $\{\hat{F}\}$, vectors. Differentiating and substituting Eq. (2.33) into the dynamic equilibrium equation (Eq. (2.30)) results in the frequency response equation by

$$[-\omega^2 [M] + (1 + i\eta)[K]](\Re\{\hat{q}\} + i\Im\{\hat{q}\}) = (\Re\{\hat{F}\} + i\Im\{\hat{F}\}) \quad (2.34)$$

or in matrix notation

$$\begin{bmatrix} [K] - \omega^2 [M] & i\eta [K] \\ -i\eta [K] & -([K] - \omega^2 [M]) \end{bmatrix} \begin{Bmatrix} \Re\{\hat{q}\} \\ i\Im\{\hat{q}\} \end{Bmatrix} = \begin{Bmatrix} \Re\{\hat{F}\} \\ i\Im\{\hat{F}\} \end{Bmatrix} \quad (2.35)$$

Hence, both Eq. (2.34) and Eq. (2.35) allow determining the unknown complex FRFs of the nodal displacements concerning the amplitudes and phase angle shifts at a given frequency. The direct steady-state dynamic analysis (Section 2.3.2.6) applied in this thesis uses this frequency response algorithm.

2.3.2 FEM modelling procedure

FEM comprises three design process stages, namely the pre-processing phase, processing phase and post-processing phase, as indicated in Figure 2-2.

The pre-processing phase is divided into three models of conception, mathematics and discretisation. In the conceptual model, the physical system is modelled under idealised or simplified assumptions by omitting superfluous details. The mathematical model involves the formulation of equilibrium algorithms using PDEs that contains the input data for the physical system from the conceptual model. The discretised model is generated by meshing the system geometry in combination with the definition of the solution algorithm from the mathematical model [127].

The processing phase is carried out by the computational analysis of the FEM program composing the sets of governing matrix equations from the pre-processed input data [128]. Thus, the nodal field quantities of interest (e.g. displacements, frequencies and harmonic responses) for the post-processing phase are analysed.

The post-processing phase includes the graphical display and the generation of output/report files. The solver log file should always be checked for possible errors and/or warnings if the numerical analysis was not already been aborted by the FEM program during the solution phase.

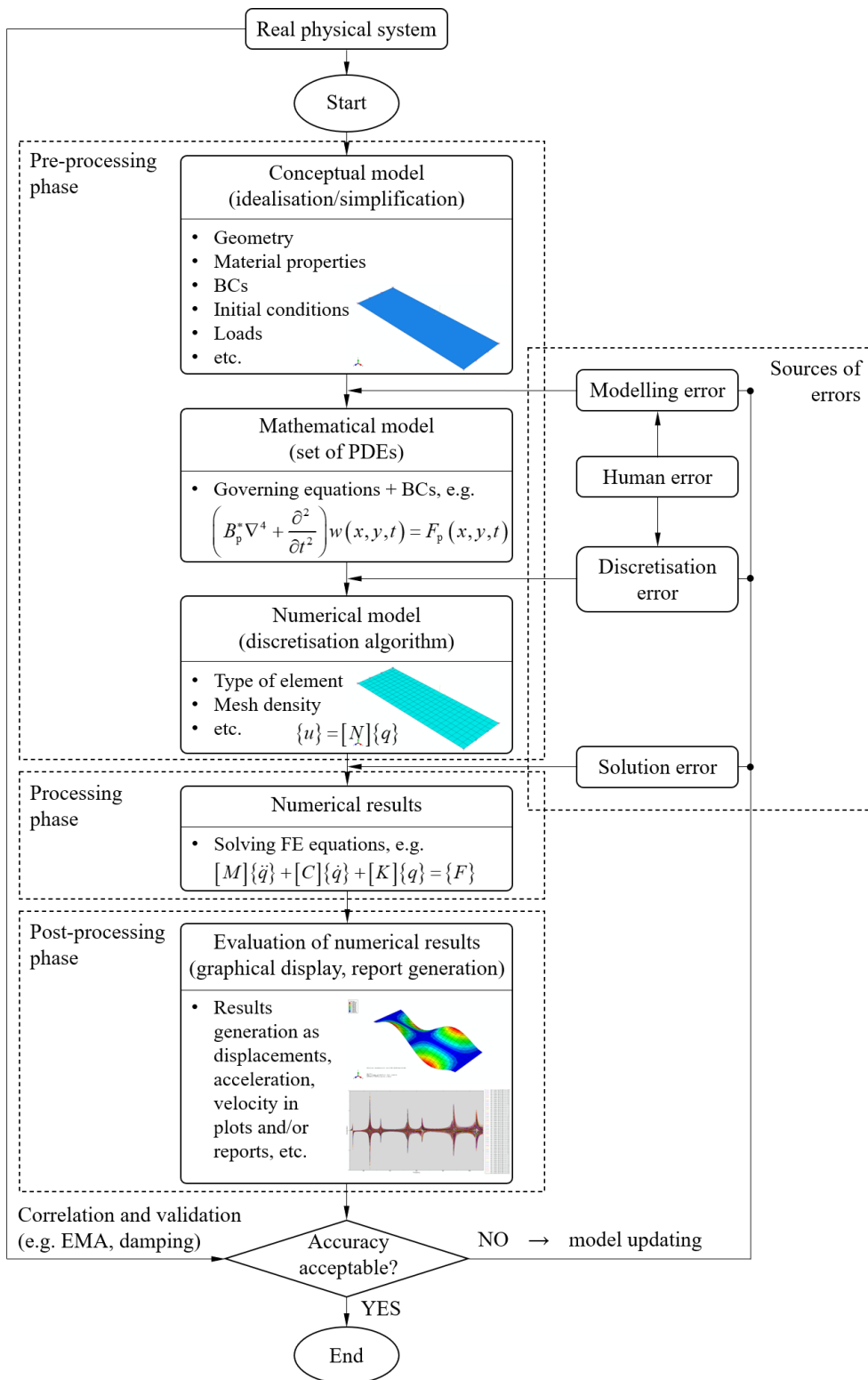


Figure 2-2. FEM modelling flow chart: Processing phases and sources of errors.

FEM models should always be verified, correlated and validated in order to assess the calculation accuracy and control the below-named sources of errors. Verification is the process that proofs an accurate implementation of the FEM code with analytical solutions (Section 4.3). Correlation and validation are the processes in which the numerical results are compared with corresponding experimental data of the physical system (Section 4.4).

The main sources of errors in FEM (see Figure 2-2) are described below [129]:

- Human error caused by the user misuse of the FEM software due to lack of experience in selecting incorrect input data and incorrect modelling of the physical system (e.g. creating a poorly constrained FEM model).
- Modelling errors caused by idealisation or simplification of the physical system due to an incorrect setting of the system geometry with regard to the selection of an unsuitable element type or an incorrect assumption of boundary conditions which can lead to an incorrect dynamic system characteristic. Incorrect choices of material parameters, loads, etc. are regarded as further sources of errors in this context.
- Discretisation errors caused by converting the real physical system into a numerical system through the choice of a coarse piecewise subdivision (adequacy of mesh density).
- Solution errors caused by numerical integration methods and binary floating-point numbers, which limits the calculation accuracy of computers and leads to truncation and round-off errors.

The following sections contain relevant information on the choice made for the FEM simulation with Abaqus in the pre-processing phase.

2.3.2.1 Shell elements

Abaqus distinguishes between three main element groups as 1D (line), 2D (membrane/shell) and 3D (solid/volume) elements [126] with linear and quadratic basis functions (linear represents corner nodes and quadratic represents corner nodes with additional surface-to-surface nodes) which contain a multitude of elements with different properties and behaviours. However, FEM supports two plate theories that are suitable for solving vibration problems. These are called Kirchhoff-Love thin plate theory [119, 120] and Reissner-Mindlin thick plate theory [130, 131]. The thin plate theory elements can be found in the 2D and 3D main element groups. It should be noted that the difference between the two plate theories is that Reissner-Mindlin thick plate theory is an extension of Kirchhoff-Love thin plate theory by taking into account the transverse shear caused by the plate thickness.

This thesis uses Kirchhoff-Love thin plate theory [119, 120] (refer back to Section 2.2.1) because the studied concrete plate with a thickness of 100 mm and dimensions of 2.8 m \times 2 m satisfies the assumption that requires the thickness related to the wavelength with $\lambda_b/6 \geq 0.1$ at 2 kHz. This can be transferred to the shell element formulation so that for an isotropic material such as concrete, the ratio of the thickness to the smallest length is less than 1/15 [126]. The concrete material also fulfils the demands on homogenous, isotropic and elastic properties so that Hooke's law holds. It can also be expected that a concrete plate undergoes only small-strain deformation due to the high material strength and stiffness in which it can be assumed that $w/h \leq 1/5$ is satisfied. Hence, the upper-frequency limit is attained at 2 kHz to apply thin plate theory with regard to the shortest feasible covered wavelength according to Kirchhoff and Love [119, 120]. To further support this, the first thickness-shear vibration over the surface at 17.6 kHz is calculated from the frequency limit for pure bending waves, $f_{B,thin}$, using [49]

$$f_{B,\text{thin}} = \frac{2\pi}{6^2\sqrt{12}} \frac{c_{L,p}}{h} \approx \frac{c_{L,p}}{2h} \quad (2.36)$$

with

$$c_{L,p} = \sqrt{\frac{E}{\rho(1-\nu^2)}} \quad (2.37)$$

where $c_{L,p}$ is the quasi-longitudinal phase velocity. Thus, the thickness-shear vibration of the modelled FEM plate does not affect the frequency range that is considered up to 2 kHz. The latter statement explicitly underlines again that the consideration of Reissner-Mindlin thick plate theory [130, 131] for the selection of suitable elements can be excluded. Hence, shell elements can be used to model this thin concrete plate.

From the above-mentioned 2D and 3D groups, shell elements can be further divided into conventional and continuum shell elements. Conventional shell elements include displacement and rotational DOFs, while continuum shell elements only consist of displacement DOFs. Even if the latter ones have kinematic and constitutive behaviour similar to that of the conventional shell elements [126], but they may not correctly capture plate bending problems. Hence, it may be referred to as the choice of 3D conventional shell elements that are commonly used for building components such as walls and floors. In Abaqus, these types of elements include shell elements that can change their behaviour from thin to thick plate theory with increasing thickness (i.e. S3, S3R, S3RS, S4, S4R, S4RS, S4RSW). But they also contain shell elements that are only limited to thin plate theory (i.e. STRI3, STRI65, S4R5, S8R5, S9R5) [126].

For the thin plate modelled in this thesis, a 3D conventional shell element [126] was therefore selected using the so-called STRI3 stress/displacement element, which neglects the transverse-shear deformation effects over the entire thickness. The STRI3 element is a three-node triangular facet thin-shell element. It is based on a combination of a Discrete Kirchhoff Triangle (DKT) element

according to the analytical approach provided by Batoz [90] on linear plate bending interpolation functions and a Constant Strain Triangle (CST) membrane element using an approximation of infinitesimal strain deformations. This combination of DKT and CST membrane elements leads to six active DOFs per node [126] (three displacement and three rotational DOFs). The sixth DOF is a rotation DOF along the z -direction, often referred to as the drilling DOF. This results in an improvement of the element behaviour with regard to proper rotation constraints and allows a reasonable connection to other elements with six DOFs [91]. In addition, the plate bending solutions can be expected sufficiently accurate due to linear curvature variation when an appropriate mesh is used [126].

2.3.2.2 Damping

In FEM, various modelling options are available to define damping mechanisms. The application of damping with regard to the data input location strongly depends on the analysis method for the respective selected damping mechanism in Abaqus. This thesis uses linear material damping in the form of linear structural (and element) damping for the reception plate, which rests on a resilient interlayer made from viscoelastic material. Note that the structural damping may lead to a physical non-causal behaviour in the time domain and should primarily only be considered in the frequency domain [132]. In the FEM models, structural damping can be applied with frequency domain, direct steady-state dynamic analysis (see Section 2.3.2.6).

Damping in any structure set into vibration has dissipating effects due to the conversion of mechanical energy into irreversible thermal energy. Note that most solid materials differ from a perfect elastic behaviour under stress exposure, so it is referred to as rather exhibiting an anelastic behaviour even under low stress [96]. Hence, the dissipating damping mechanism can be represented by a cyclic stress-strain or force-displacement curve that forms a hysteresis loop – see Figure 2-3. In the frequency domain, the direct energy dissipation based on the

loss factor, η , equivalent to the structural damping factor, γ , (Abaqus uses the denotation s), is given in the form [96]

$$\eta = \frac{W_d}{2\pi U_0} \quad (2.38)$$

where W_d is the total energy dissipated described by the enclosed area of a hysteresis loop and U_0 is the elastic stored energy at a maximum obtained from a triangle area in the force-displacement curve (see Figure 2-3a and b).

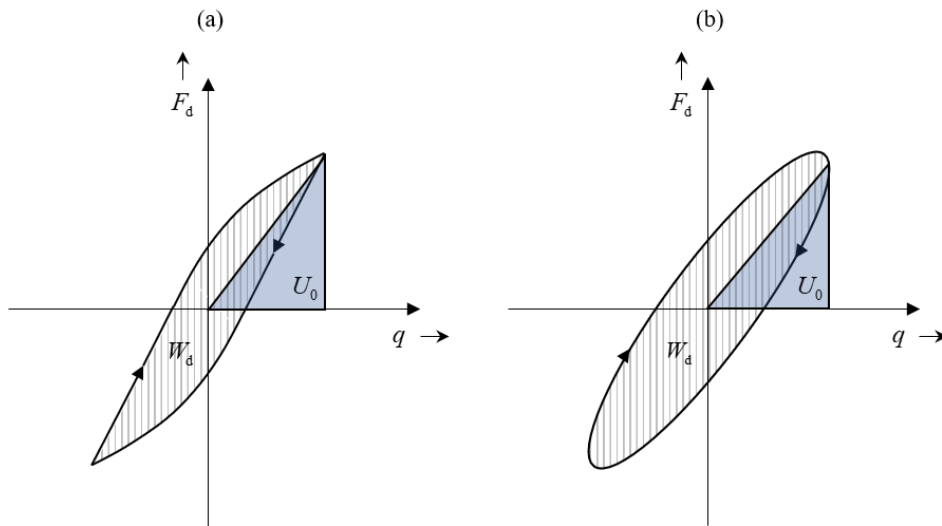


Figure 2-3. Typical hysteresis loops of energy dissipated per cycle with regard to the force-displacement relationship [96]: (a) non-linear damping (e.g. solid material under high stress) and (b) linear damping (e.g. solid material under low stress and viscoelastic material).

For an anelastic material with regard to internal friction, the solution of Eq. (2.38) is obtained using the energy dissipated and maximum potential energy based on the relation between integrated stresses and strains, which results in a loss factor given by

$$\eta = \frac{1}{2\pi} \frac{\pi E'' \varepsilon_0^2}{E' \varepsilon_0^2 / 2} = \frac{E''}{E'} = \tan \varphi \quad (2.39)$$

where ε_0 is the maximum strain at resonance, E' and E'' are the storage and loss modulus as parts of the complex (or dynamic) modulus of elasticity and

$\tan \varphi$ is the loss tangent which expresses the 90° phase shift between stress and strain at which strain lags stress. For viscoelastic material, the parts of the complex modulus of elasticity, E' and E'' , can be exactly replaced by the parts of the complex shear modulus, G' and G'' . Hence, this implies that the structural damping is based upon the concept of the complex modulus of elasticity, $E^* = E' + iE'' = (1 + i\eta)E$, and complex shear modulus for viscoelastic materials, $G^* = G' + iG'' = (1 + i\eta)G$. (NB Anelasticity of solid materials can be assumed to be linear when the stress amplitude is sufficiently small and less than fatigue. In this situation, the hysteresis loop takes the form of an ellipse – see Figure 2-3b.)

The spring dashpot system is based on the Kelvin-Voigt model (Hooke's elastic spring and Newtonian damper connected in parallel) to describe the simultaneous anelastic and dissipative material mechanism as a replacement to the structural or equivalent viscous material damping. Hence, according to Eq. (2.38), the loss factor of the entire system with regard to the energy dissipated and its potential energy using the integrated damping force and generalized displacement can be written as

$$\eta = \frac{1}{2\pi} \frac{\pi c_{eq} \omega q_0^2}{k q_0^2 / 2} = \frac{c_{eq} \omega}{k} \quad (2.40)$$

where q_0 is the maximum generalised displacement at resonance and c_{eq} is the equivalent viscous damping coefficient. However, the complex modulus of elasticity, complex shear modulus and equivalent viscous damping are proportional to the complex stiffness (or the so-called compression modulus), $K^* = K' + iK'' = (1 + i\eta)K$ as has already been introduced in Eq. (2.29) from Section 2.3.1.

Due to the lagging phase shift, the loss factor described in Eq. (2.39) and Eq. (2.40) can be brought into a relationship with linear experimental resonant methods in which the damping measure quantities can be derived by

$$\eta = \frac{\Delta f_{3dB}}{f_0} = 2\zeta = \frac{\delta}{2} \quad (2.41)$$

where $\Delta f_{3dB}/f_0$ represents the half-power bandwidth method, ζ is the damping ratio from FRF data at resonance, while δ is the logarithmic decrement assessed from amplitude decay rates, e.g. by structural reverberation time data. In this thesis, the half-power bandwidth method was used to determine the loss factor from the calculated driving-point mobility.

In Abaqus, it is possible to model the structural damping directly with `*DAMPING, STRUCTURAL` (input file usage) [126] in order to capture the actual linear anelastic behaviour of most elastic solid materials [96] that are exposed to a small harmonic load. This type of damping leads to a complex stiffness matrix when energy dissipating effects of a material due to internal friction are implemented in FEM. The direct use of structural damping in the material section was based on the internal loss factor, η_{int} , which corresponds to twice the damping ratio, ζ , (Eq. (2.41)).

To model the highly damped viscoelastic material in the form of a linear system according to the Kelvin-Voigt model (see Eq. (2.40)), connected in parallel spring-dashpot elements can be used as a special case of structural damping in Abaqus to represent the complex stiffness matrix (see Eq. (2.29)). These elements operate in a fixed direction which must be aligned to the global or local coordinate system by node-to-ground (input file usage: `*SPRING1` and `*DASHPOT1`) or node-to-node (input file usage: `*SPRING2` and `*DASHPOT2`) connectivity with regard to the specification of up to six DOFs [126]. The modelled grounded spring-dashpot elements were assigned with two DOFs in global coordinates due to the behaviour acting in a fixed direction. The spring-dashpot elements having two DOFs allow for transverse action in global coordinates, which are comparable to spring-dashpot elements having one DOF assigned in local coordinates and acting in the same direction. This means that the action of the grounded spring-dashpot systems was oriented perpendicular to

the plate's mid-surface in order to take into account the viscoelastic damping for the translational displacement. As an alternative, the local spring- and dashpot-like axial connectors can be incorporated into the FEM model.

2.3.2.3 Boundary conditions

Boundary conditions are classified into two categories: (a) essential or geometrical boundary conditions and (b) natural boundary conditions. When using essential boundary conditions, kinematic constraints are assigned by a primary variable in the form of DOF-restrictions like displacements and translations, which are satisfied in an exact sense and imposed explicitly in the space domain. Natural boundary conditions are static constraints based on a secondary variable like forces and tractions that will be automatically satisfied in the variational formulation [133].

The boundary condition modelling in this thesis relates to free boundary conditions, which belong to the natural boundary conditions since they have no kinematic restrictions and therefore are automatically solved by the applied variational weak formulation. However, partial restricted boundary conditions do not offer a completely free vibrating structure and can be assigned to essential boundary conditions if grounded spring-dashpot elements are used for the viscoelastic material. Those spring-dashpot elements impose vibratory partial restraints on the structure along the direction of translational displacement or deformation due to the lock in the associated DOFs involved.

2.3.2.4 Loads

External acting forces are typically applied as loads in FEM. In Abaqus, various mechanical loads are available, such as concentrated force, moment, pressure, shell edge load, line load, etc.

In general, forces are defined by concentrated loads when using dynamic analysis. The force can be applied to any nodal or a set of nodal DOFs specified in direction for magnitude and phase to capture the vibrational response of a structure. The direct steady-state dynamic analysis (see Section 2.2.5) employed

in this present research work enables the application of a harmonic excitation where a concentrated force load is driven by a uniform sweep at a given series of successive frequencies [126] as indicated in Figure 2-4.

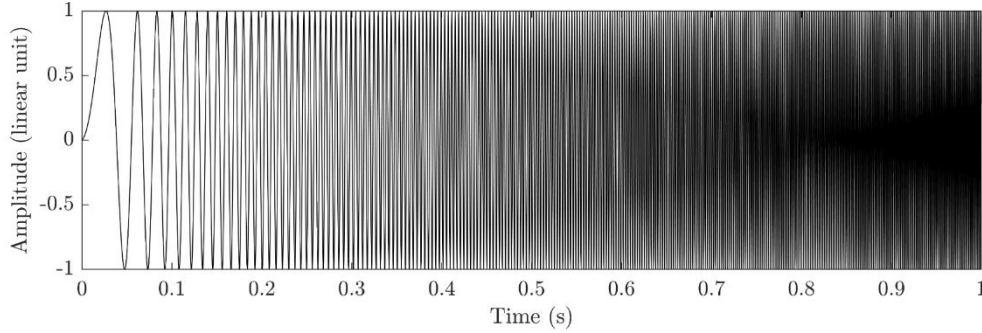


Figure 2-4. Example of a linear sine sweep function with normalised uniform amplitude over the time for a frequency range from 1 Hz to 2.5 kHz.

2.3.2.5 Mesh

The subdivision of the geometry domain into numerous small simple elements like triangles or quadrilaterals, which finally gives the discretised domain, can be seen as an important key to obtain reliable and reasonable results of a physical problem in FEM. The discretisation process of linear structural-acoustic vibration problems is related to the frequency-dependent variation of the element size per wavelength. Besides the choice of the element type, the mesh density significantly influences the accuracy of analysis results, which leads to a decrease in computation efficiency with increasing frequency.

As a rule of thumb of a vibro-acoustic analysis, at least six elements per wavelength are required for the highest simulation frequency because this corresponds to the smallest wavelength of interest. In the present thesis, the focus is set on bending vibrations of a thin homogeneous isotropic plate so that the following equation for the above common rule of thumb with regard to a sufficient mesh assignment with a reliable accuracy applies [49, 93]

$$e_{\max} \leq \frac{\lambda_B}{6} \quad \text{or} \quad k_B e_{\max} \leq 1 \quad (2.42)$$

where e_{\max} is the largest dimension of the element. Some authors [94, 95] also suggest the use of a smaller element dimension that would increase the element number per wavelength to at least ten in order to reduce the error of accuracy. Mesh refinement considerably increases the computational cost and storage. With at least six elements per wavelength, the relationship between the upper-frequency limit and bending wavelength is given by

$$f_{\max} \leq \frac{c_{B,p}}{6e_{\max}} \quad (2.43)$$

where f_{\max} is the maximum frequency selected in FEM analysis.

In the present FEM model, the frequency sweep wave was defined from the loading conditions for a frequency range from 1 Hz to 2.5 kHz in order to ensure that a frequency range from 20 Hz to 2 kHz can be covered for the numerical investigations. For the upper band edge frequency considered at 2 kHz, the shortest bending wavelength corresponds to $\lambda_b = 0.565$ m, which leads to less than eight elements per wavelength and a STRI3 element dimension of 50 mm \times 50 mm \times 70 mm. Thus, a finer mesh was assigned than the rule of thumb of at least six elements per wavelength.

2.3.2.6 Analysis types

This thesis focuses on linear dynamic analysis for free and forced vibrations, which is a subsection of stress-strain analysis. The advantage of stress-strain analysis is that it can be performed experimentally, which enables the opportunity to correlate and validate the simulation with a real physical structure. Linear dynamic analysis can be conducted by a linear perturbation procedure using direct, modal-based or subspace-based steady-state dynamic analyses [126].

The use of frequency analysis is intended for the solution of the dynamic behaviour of a structure with regard to its eigenfrequencies and mode shapes under free and damped vibrations. The governing equations that arise from a

linear eigenvalue problem in terms of non-zero damping are given in Section 2.3.1.1. An eigenvalue extraction analysis and/or a complex eigenvalue extraction analysis solves the eigenfrequencies and mode shapes of a structural system. Based on proportional damping conditions where the mass or complex stiffness matrices can be diagonalized for structural damping, it is sufficient to apply an eigenvalue extraction analysis in order to obtain only real-valued eigenfrequencies and eigenvectors of the mode shapes. But if the structural damping incorporated into the simulation tends to be non-proportional (non-evenly damping distribution), and therefore the mass or stiffness matrices can be expected to be non-diagonal where the normal modes are complex-valued. In this case, a complex eigenvalue extraction analysis can be used. Note that the performance of a complex eigenvalue extraction analysis requires a prior eigenvalue extraction analysis in Abaqus [126].

To solve forced vibrations, the direct scheme of dynamic analysis under steady-state excitation (linear perturbation analysis) is the most accurate but also the most computationally expensive algorithm. This results from the fact that the harmonic response in terms of the physical DOFs of the FEM model is directly calculated using the system properties such as mass, damping and stiffness [126] in the frequency domain (see Section 2.3.1.2). The load condition is subjected to an externally applied frequency sweep (see Section 2.3.2.4), and the results such as the complex velocities, accelerations or reaction forces can be adapted to suit the frequency range according to the investigation requirements. Direct steady-state dynamic analysis is used in this research because it takes into account the viscoelastic properties [126] and provides the most accurate solution to a linear structural dynamic problem.

2.3.3 FEM data processing for harmonic structural response calculation

For direct steady-state dynamic analysis, the frequency range from 1 Hz to 2.5 kHz is linearly partitioned into 2500 data points which correspond to a frequency resolution of 1 Hz to assess the structure-borne sound power with regard to the force and velocity. The uniform applied force was used as the scalar product for power calculations. In contrast, the generated magnitudes of velocity as a function of linear frequency data points were converted into n -th spatial average Root-Mean-Square (RMS) velocities, $\langle v_{\text{rms}}^2 \rangle$, depending on the sampling strategy of power calculations using

$$\langle v_{\text{rms}}^2 \rangle(f) = \frac{1}{n} \sum_{i=1}^n \left(\frac{v_i(f)}{\sqrt{2}} \right)^2 \quad (2.44)$$

For one-third octave bands defined according to IEC 61260-1 [134], these absolute velocity values were further averaged over N linear narrowband frequency lines into the associated one-third octave band using the following equation

$$\langle v_{\text{rms}}^2 \rangle(f_c) = \sum_{f=f_1}^{f_u} \frac{\langle v_{\text{rms}}^2 \rangle(f)}{N} \quad (2.45)$$

where f_c is the centre frequency, f_1 is the lower band-edge frequency limit and f_u is the upper band-edge frequency limit.

Comparison of fractional octave band data is more useful than narrow bands because FEM data depend on the simplification of the actual structural system in terms of geometry, boundary conditions and damping, which can lead to shifts in the eigenfrequencies.

2.4 Statistical Energy Analysis (SEA)

SEA is a prediction method that is widely applied in branches of engineering like building acoustics, ship, automobile and aerospace vehicles [101]. From a building acoustical point of view, SEA is used to predict the sound transmission related to the sound radiation from walls and floors into rooms due to mechanical devices. A simplified SEA-based model is defined in the standard series of EN 12354 [9, 10, 11] for use by industry.

Figure 2-5 shows the basic SEA concept, which can be related to two linear homogeneous and coupled oscillators that have coupling power proportionality between the subsystems where the averaged power flow is from subsystems with high modal energy to those with low modal energy [100]. This procedure can be described through the direction of energy exchange during processes in nature and technology known from thermodynamics as entropy. As shown in Figure 2-5, these two oscillators can be extended to two multi-modal subsystems with the assumption that the total net power flow, W_{ij} , between two coupled subsystems i and j from N modes in a specified frequency band can be expressed by [101]

$$W_{ij} \equiv \omega \eta_{ij} \left(E_i - \frac{N_i}{N_j} E_j \right) \quad (2.46)$$

where η_{ij} is the coupling loss factor from subsystem i to subsystem j , and E_i and E_j are the stored energy in subsystems i and j respectively. The coupling power proportionality is valid for multi-modal coupled subsystems when the consistency relation is given by [101, 102]

$$\eta_{ij} N_i = \eta_{ji} N_j \quad (2.47)$$

and the following assumptions are satisfied [101, 103]:

- Weak or light coupling between subsystems where the energy flow is only dependent on the local properties of the subsystem.
- Equipartition of modal energy, which means that all modes of a subsystem have the same energy content and their modal response functions are incoherent.
- Energetic equivalence of eigenmodes in a subsystem shows a uniform distribution of eigenfrequencies in the considered frequency band for which the diffuse field assumptions are achieved.
- The damping of modes of a subsystem is approximately the same and not too high.
- Statistically independent excitation on the subsystems due to uncorrelated external forces so that the energies can be summed linearly.

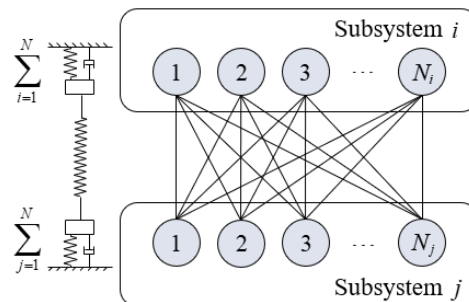


Figure 2-5. Power flow of multi-modal contributions of all individual mode pairs between two coupled subsystems.

SEA enables the study of the interactions of complex structures or fluid systems excited by the random power input (usually white noise) and describes the energy exchange between two or more subsystems as a function of mode groups within a given frequency band, typically one-third octave bands. Subsystems may consist of a coupled space and structure, coupled structures or any combination. For a complete characterisation of the SEA model, it is necessary to know the statistical description of multi-modal structural parameters with regard to the damping (internal and coupling loss factors) and

the modal density. The results of the statistical consideration are that SEA gives spatial average energies of the response.

With increasing frequency, the number of participating subsystems modes in the frequency bands increases and subsystems are referred to as being ‘multi-modal’. The statistical approach provides closer estimates of the mean response since the average response of an ensemble of many similar systems is used for the prediction of transmitted energy between subsystems. At low frequencies, the spacing between the participating modes can be relatively wide, and SEA predictions may be less accurate when compared with a single system with specific geometry.

2.4.1 Power balance equations of direct sound transmission (two-subsystem) SEA

In this thesis, a simple SEA model of two conservatively coupled subsystems is used as depicted in Figure 2-6. The two coupled subsystem model represents a plate with the subsystem i and a room with the subsystem j . The structure-borne sound power input is injected to subsystem i as $W_{in,i}$ with power transfer between the two subsystems i and j due to the coupling as W_{ij} and W_{ji} and dissipated power that depends on the subsystem damping as $W_{d,i}$ and $W_{d,j}$.

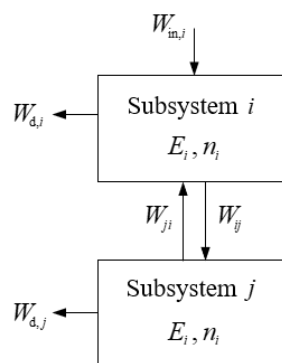


Figure 2-6. Schematic representation of a two-subsystem SEA model for a coupled plate-room system with all occurring power flows.

The fundamental equation of SEA is built upon the law of energy conservation, which states that the energy input into a subsystem must correspond to the averaged energy that leaves this subsystem by internal damping and mechanical coupling to other subsystems. Therefore, the power balance equation for the subsystem i in steady-state conditions [101] is given by

$$W_{\text{in},i} = W_{\text{d},i} + \sum_{i \neq j} W_{ij} \quad (2.48)$$

The dissipated power relates to the stored energy, E_i , within the subsystem i by the internal loss factor, η_{ii} , using

$$W_{\text{d},i} = \omega \eta_{ii} E_i \quad (2.49)$$

where ω is the centre frequency of the band. From Eq. (2.46), the net power flow between the subsystem i and j with the use of consistency relation (Eq. (2.47)) can be calculated by

$$W_{ij} = \omega (\eta_{ij} E_i + \eta_{ji} E_j) \quad (2.50)$$

where η_{ij} is the coupling loss factor from subsystem i to subsystem j (and vice versa for η_{ji}). Replacing Eq. (2.49) and Eq. (2.50) into Eq. (2.48), the power balance equation can be reformulated to

$$\begin{aligned} W_{ij} &= \omega (\eta_{ii} E_i + \eta_{ij} E_i - \eta_{ji} E_j) \\ 0 &= \omega (\eta_{jj} E_j + \eta_{ji} E_j - \eta_{ij} E_i) \end{aligned} \quad (2.51)$$

or in matrix notation

$$\begin{bmatrix} W_{\text{in},i} \\ 0 \end{bmatrix} = \omega \begin{bmatrix} \eta_{ii} + \eta_{ij} & -\eta_{ji} \\ -\eta_{ij} & \eta_{jj} + \eta_{ji} \end{bmatrix} \begin{bmatrix} E_i \\ E_j \end{bmatrix} \quad (2.52)$$

2.4.1.1 Modal parameters

The modal density can be expressed by

$$n(f) = \frac{N}{\Delta f} = \frac{N}{B} \quad (2.53)$$

where the bandwidth, B , is typically a one-third octave band for which

$$B = 0.23 f_c \quad (2.54)$$

A more detailed description of the uncorrelated wavefield with regard to the diffuse field conditions has already been derived in Section 2.2.3. The eigenvalues and modal density of rectangular plates as a 2D structural system have been introduced in Eq. (2.8) and Eq. (2.10) respectively from Section 2.2.2.

For a 3D cavity representing a box-shaped room, the eigenfrequencies, f_{pqr} , can be calculated by [135]

$$f_{pqr} = \frac{c_0}{2} \sqrt{\left(\frac{p}{L_x}\right)^2 + \left(\frac{q}{L_y}\right)^2 + \left(\frac{r}{L_z}\right)^2} \quad (2.55)$$

and the modal density, $n_{3D}(f)$, can be determined from [135]

$$n_{3D}(f) = \frac{4\pi f^2 V}{c_0^3} + \frac{\pi f S_T}{2c_0^2} + \frac{L_T}{8c_0} \quad (2.56)$$

where L_x , L_y and L_z are the room dimensions, S_T is the total area of the room surfaces and L_T is the total length of all room edges.

2.4.1.2 Loss factors

The internal loss factor of homogeneous isotropic structures is described by the conversion of energy into heat. Typically, this type of loss factor of structural subsystems is taken from textbooks or measured from the energy dissipation when decoupled from all other structural subsystems. The internal loss factor of structures was introduced in Sections 2.2.4 and 2.3.2.2.

For a room, the internal loss factor can be defined by the total absorption area, which reduces the energy by conversion into heat and can therefore no longer be reflected by the surrounding room boundaries. In the above described SEA model (refer back to Section 2.4.1), the room is considered as the subsystem j ; hence, the internal loss factor of the room is used with the notation, η_{jj} , which can be determined by [102]

$$\eta_{jj} = \frac{c_0 A_{T,j}}{8\pi f V_j} \quad (2.57)$$

where $A_{T,j}$ is the total absorption area and V_j is the volume of the room.

The SEA model in this thesis only considers the direct transmission without any flanking paths so that the coupling losses due to radiation have only to be assessed for the prediction of the uncorrelated energy on the plate and in the room. The plate-to-room coupling loss factor per radiation cycle can be described as a fraction of energy losses that are transmitted from subsystem i to subsystem j , which is given by [49]

$$\eta_{ij} = \frac{\rho_0 c_0 \sigma_i}{\omega \rho_{s,j}} \quad (2.58)$$

The calculation of the room-to-plate coupling loss factor, η_{ji} , from subsystem j to subsystem i can be estimated using the consistency relationship according to Eq. (2.47).

The total loss factor, $\eta_{\text{tot},i} = \eta_i$, of the subsystem i is determined by the sum of the overall damping mechanism in terms of the internal loss factor and coupling loss factor using

$$\eta_{\text{tot},i} = \eta_i = \eta_{ii} + \sum_{\substack{j=1 \\ j \neq i}}^n \eta_{ij} \quad (2.59)$$

which corresponds to the total loss factor that can be calculated from the reverberation time using [71]

$$\eta_{\text{tot}} = \frac{6 \ln 10}{\omega T} = \frac{2.2}{fT} \quad (2.60)$$

where T is the reverberation time from either rooms or structures. For structures, the notation T_s is typically used instead of T . For rooms, a decay over 15 dB or 20 dB is often measured and extrapolated to a decay rate of 60 dB. However, the structural reverberation time with a decay range of 20 dB leads to an error when the energy returns from coupled plate-like structures such as walls or floors in buildings; hence, it is often necessary to use a shorter evaluation range such as 5 dB [44, 45]. Note that this was taken into account for structural reverberation time measurements when the total loss factor was assessed for real physical plate-like structures.

For masonry walls and concrete floors, an empirical approximation of the total loss factor is given by [136]

$$\eta_{\text{tot}} = \eta_{\text{int}} + \frac{1}{\sqrt{f}} \quad (2.61)$$

where the first term denotes the internal losses of the material and the second term is an estimate of structural coupling losses for heavyweight walls and floors that are connected to other walls and floors on all sides (in this estimate, radiation losses can be considered negligible).

2.4.1.3 Radiation efficiency

Sound radiation from bending waves on a structure into the adjacent acoustic fluid is commonly described in terms of radiation efficiency, σ , which is proportional to the radiation loss factor from Eq. (2.18). The radiation efficiency is characterised by the relationship of the equivalent radiated sound power and the uniform radiated power by a baffled circular piston at frequencies for which

the piston radius, a , greatly exceeds the acoustic wavenumber, k , with $ka \gg 1$ [49, 71]; hence, the radiation efficiency may be written as

$$\sigma = \frac{W_{\text{rad}}}{S\rho_0c_0 \langle v^2 \rangle_{t,s}} \quad (2.62)$$

where W_{rad} is the radiated sound power and $\langle v^2 \rangle_{t,s}$ is the temporal and spatial average mean-square velocity. Equation (2.62) is only relevant for vibrating structures that have a radiation efficiency close to unity when the radiated power of an element and the power of the baffled piston with the same area and spatial average mean-squared velocity is in the same order of magnitude [71].

Bending waves have dispersive behaviour [71], so the phase velocity depends on frequency; hence, a plate has a single frequency, f_c , the so-called critical frequency, where the structure has the strongest radiation when the bending and sound phase velocity match (i.e. $c_{\text{B,p}} = c_0$). The critical frequency is given by

$$f_c = \frac{c_0^2}{2\pi} \sqrt{\frac{\rho_s}{B_p}} = \frac{c_0^2 \sqrt{3}}{\pi h c_{\text{L,p}}} \quad (2.63)$$

For lightly damped homogeneous plates (which tends to apply in heavyweight buildings), the approach provided by Leppington [137, 138, 139] is commonly used for one-third octave bands. In the bands below the critical frequency, the radiation efficiency is given by

$$\sigma = \frac{U}{\pi\mu k S \sqrt{\mu^2 - 1}} \left[\ln\left(\frac{\mu+1}{\mu-1}\right) + \frac{2\mu}{\mu^2 - 1} \right] \left[C_{\text{BC}} C_{\text{BO}} - \mu^{-8} (C_{\text{BC}} C_{\text{BO}} - 1) \right] \quad (2.64)$$

for $f < f_c, \mu > 1$

where U is the perimeter of the plate, C_{BC} is the boundary condition constant ($C_{\text{BC}} = 1$ for simply-supported boundaries and $C_{\text{BC}} = 2$ for clamped boundaries) and C_{BO} is the plate boundary orientation constant for the baffle surrounding the plate edges ($C_{\text{BO}} = 1$ for the infinite rigid baffle lying within the plate plane and $C_{\text{BO}} = 2$ for the infinite rigid baffle along the perimeter that is perpendicular to

the plate surface) and $\mu = \sqrt{f_c/f}$. In the given frequency bands above the critical frequency, the radiation efficiency is given by

$$\sigma = \frac{1}{\sqrt{1-\mu^2}} \quad \text{for } f > f_c, \mu < 1 \quad (2.65)$$

At the critical frequency, the radiation efficiency is given by

$$\sigma = \sqrt{kL_1} \left(0.5 - 0.15 \frac{L_1}{L_2} \right) \quad \text{for } f = f_c, \mu \approx 1 \quad (2.66)$$

where L_1 is the smaller and L_2 is the larger side-length of the plate in x - y dimensions respectively. In the case of heavyweight buildings constructed by masonry and concrete plates, a semi-empirical adjustment is used to account for the vanishing peak contribution of the radiation efficiency at the critical frequency. Below the critical frequency, the radiation efficiency is set to $\sigma = 1$ when $\sigma > 1$ for all lower frequency bands. At and above the critical frequency, the radiation efficiency can be set to $\sigma = 1$ [71].

2.4.1.4 Energy

The modal energy response of the two subsystems can be calculated by solving power balance Eq. (2.50) or Eq. (2.51). It is assumed that the losses by damping and coupling are known. Hence, the vibrational energy stored in the plate, E_i , of the subsystem i can be written as

$$E_i = m \langle v^2 \rangle_{t,s} \quad (2.67)$$

and the equivalent acoustic energy, E_j , stored in the room of the subsystem j is given by

$$E_j = \frac{V \langle p^2 \rangle_{t,s}}{\rho_0 c_0} \quad (2.68)$$

where $\langle p^2 \rangle_{t,s}$ is the temporal and spatial average mean-square sound pressure.

2.4.1.5 Power input

The SEA matrix requires knowledge of the steady-state power input, for which this thesis is concerned with the structure-borne sound power input. The power input into a heavyweight wall or floor can be estimated using a reception plate for which the characterisation of structure-borne sound sources with regard to the direct injected power and the reception plate power using an isolated reception plate (that links to basic SEA theory) is discussed in Section 2.5.

2.4.2 Proposal for the prediction of L_{Fmax} from time-varying sources using SEA based on short L_{eq}

In this thesis, there is a need to predict maximum Fast time-weighted levels, L_{Fmax} , for which the proposal is to use SEA based upon short equivalent continuous levels, L_{eq} , and then derive an empirical correction factor to determine L_{Fmax} levels from short L_{eq} levels.

SEA essentially considers steady-state signals where vibration or sound pressure can be detected by linear integration with reference to RMS amplitudes over a specific time. This leads to equivalent continuous levels having the same energy as a fluctuating signal for the same stated time interval, which can be written in the following form

$$L_{eq} = 20 \lg \left(\frac{1}{T} \int_0^T \frac{X(t)}{X_0} dt \right) \quad (2.69)$$

where T is the integration time, X is an instantaneous variable with regard to the velocity or sound pressure and X_0 is the corresponding reference quantity. With the aid of waterfall diagrams from multi-buffer measurements that display the amplitude, frequency and time axes (or automated peak detectors), the maximum L_{eq} values can be determined experimentally or using time signals with a step-by-step conversion in the MATLAB software as introduced and discussed with the focus on the treatment of measurements in Section 3.3.7.2.

For time-weighted levels, L_τ , the RMS detector uses an exponential integration over differing time intervals within a measurement period. Hence, the time-weighted level is determined using

$$L_\tau(t) = 20 \lg \left(\frac{1}{\tau} \int_{-\infty}^t \frac{X(\xi)}{X_0} \exp\left(-\frac{t-\xi}{\tau}\right) d\xi \right) \quad (2.70)$$

where ξ is a dummy variable of time integration and τ is the exponential time constant for Fast (F) and Slow (S) time-weighting as specified in IEC 61672-1 [140]. The Fast time-weighting has a time constant of 125 ms and is commonly used in building acoustics to assess the response to a transient or time-varying source. The maximum level is detected by a maximum hold function within a specified period of time.

SEA was formulated on the basis that it would be suited to structures and spaces with high modal densities such that it would be reasonable to assume diffuse fields. For a diffuse field, the average time taken for a wave to travel the mean free path, t_{mfp} , i.e. between two successive diffuse reflections from boundaries, is given by [15, 141]

$$t_{\text{mfp}} = \frac{d_{\text{mfp}}}{c_g} \quad (2.71)$$

where c_g indicates the group velocity with reference to $c_{g(B)}$ for a 2D subsystem and c_0 for a 3D cavity subsystem and d_{mfp} is the mean free path. For a finite plate, the mean free path is the average distance that a wave travels between two successive reflections from the plate boundaries using [49, 142]

$$d_{\text{mfp}} = \frac{\pi S}{U} \quad (2.72)$$

For a cavity or space, the mean free path is defined as the average distance that a wave travels between two successive reflections from the room boundaries using [49]

$$d_{\text{mfp}} = \frac{4V}{S_T} \quad (2.73)$$

Figure 2-7 shows the average time taken for waves to travel the mean free path for different areas and volumes.

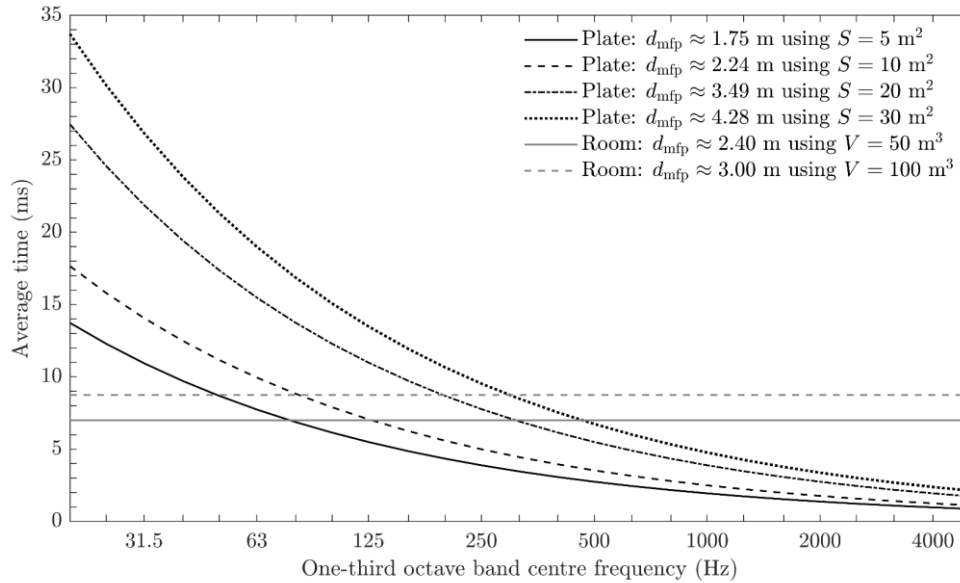


Figure 2-7. Average time between two successive reflections from boundaries on different finite plate and room boundaries.

However, the time-to-mean free path should be treated as a lower bound and has therefore to be sufficiently smaller than the time-weighting function used in the RMS detector in order to guarantee accurate results.

This thesis assesses whether it is possible to derive an empirical correction factor that can be used to predict L_{Fmax} from short L_{eq} levels for the structure-borne sound transmission and radiation into nearby rooms in heavyweight buildings. The Fast time-weighting used for L_{Fmax} corresponds to a time constant of 125 ms; hence, this thesis intends to use a short L_{eq} with a minimum time period of 125 ms.

2.5 Structure-borne sound power characterisation

The structure-borne sound power is required as input data in SEA models in order to be able to predict machinery noise at the design stage over the frequency range of interest, especially at low frequencies. The underlying theory for structure-borne sound source characterisation with regard to the direct injected power with single- and multiple-contact sources is given in Section 2.5.1 and with the reception plate power described in Section 2.5.2.

2.5.1 Direct injection for single- and multiple-contact sources

For single-contact sources with only perpendicular vibration forces, the injected power, W_{inj} , is straightforwardly determined from the real part of the complex power, $\Re\{Q\}$, as the product of the complex force, \underline{F} , and complex velocity, \underline{v} , at the coupling interface of the source and receiver using

$$W_{inj} = \frac{1}{2} \Re\{\underline{F}^* \underline{v}\} \quad (2.74)$$

where the superscript * indicates the complex conjugate. The real part of the injected power indicates the structure-borne noise contribution of the source actuator that is transmitted into the receiver structure.

For sources connected at multiple-contact points to a receiver structure that is only driven by perpendicular vibration forces, the injected structure-borne sound power becomes [55]

$$W_{inj} = \frac{1}{2} \Re\{\underline{F}^* \underline{v}\} = \frac{1}{2} \Re[\underline{F}^H Y \underline{F}] = \frac{1}{2} \Re[\underline{\Psi}^H \Lambda \underline{\Psi}] = \frac{1}{2} \sum_{n=1}^N |\underline{\Psi}_n|^2 \lambda_n \quad (2.75)$$

where Y is the real, symmetric and non-negative mobility matrix of the receiving structure and the superscript H denotes the complex conjugate transpose (Hermitian transpose) value. The term $\underline{F}^H Y \underline{F}$ can be re-expressed as $\underline{\Psi}^H \Lambda \underline{\Psi}$ using an orthogonal transformation where Λ is the diagonal matrix of

the real eigenvalues λ_n of Y with units of mobility and $\underline{\Psi}$ is the corresponding complex force vector [54, 55].

2.5.2 Reception plate power

This section on reception plate power is divided into three parts which deal with the general theory of the reception plate method in Section 2.5.2.1, the characterisation of the structure-borne sound power and its conversion into an installed structure-borne sound power for building components in Section 2.5.2.2. Section 2.5.2.3 of this reception plate power section discusses potential issues with low-frequency characterisation.

2.5.2.1 Theory

The reception plate method provides an indirect estimate of the structure-borne sound power injected by a high-mobility source in the installed operating conditions on an isolated low-mobility plate. Hence, this method is only valid for force sources with a mobility that is considerably larger than the mobility of the receiver ($|Y_S| \gg |Y_R|$) [30, 33].

In the application of SEA, the power input from a structure-borne sound source, W_{in} , into an isolated plate is equal to the power dissipated, W_d , which is generated as the plate bending wave response that follows the law of energy conversion in the diffuse field. Note that the structure-borne sound power into a plate with free boundaries will be referred to from now on as reception plate power, $W_{in} = W_{rec}$. Figure 2-8 depicts such an isolated plate model based on an energetic method without any coupling; hence, only one subsystem is considered.

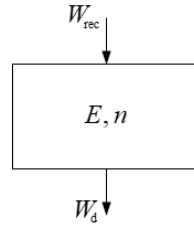


Figure 2-8. Schematic representation of a SEA based isolated reception plate model with the occurring power flow.

According to Eq. (2.49), the reception plate power under steady-state operation conditions of single- or multiple-contact sources can be determined from the energy and the total loss factor using [49]

$$W_{\text{rec}} = \omega \eta E = \omega \eta m \langle v^2 \rangle_{t,s} \quad (2.76)$$

For the reception plate as a single subsystem SEA approach, the total loss factor consists only of the energy losses due to inherent material dissipation. The energy losses from radiation are negligible, and there are no significant energy losses by coupling to other structures because the plate rests on viscoelastic supports.

The reception plate method is the preferred laboratory approach for measuring the source activity performance of domestic equipment or machinery with any number of contact points and geometry. This is due to the simplicity, practical and robust nature of this method of structure-borne sound source characterisation to gather the input data for the prediction of sound transmission into nearby rooms in heavyweight buildings. This method has been issued as a laboratory measurement standard in EN 15657 [35].

2.5.2.2 Characteristic reception plate power and installed power for real walls and floors

In order to obtain an independent source characterisation, the reception plate power is normalised by the ratio of the infinite plate mobility for a plate with the same material and thickness, $Y_{\text{dp},\infty,\text{rec}}$, (see Eq. (2.25) and Eq. (2.26)) over the real part of the spatial averaged plate mobility for perpendicular forces at the drive

point of the source-plate interface contacts, $\Re\{Y_{dp,rec}\}$, (see Eq. (2.19)). In particular, this correction compensates the reception plate power for its modal behaviour, which results in the characteristic power, W_{char} , given by

$$W_{char} = W_{rec} \frac{Y_{dp,\infty,rec}}{\Re\{Y_{dp,rec}\}} \quad (2.77)$$

The characteristic power can then be converted to the installed power, W_{inst} , for real floors and walls by determining the spatial average point mobilities of the building element over the contact points, $\Re\{Y_{dp,inst}\}$, and infinite mobility of the reception plate using

$$W_{inst} = W_{char} \frac{\Re\{Y_{dp,inst}\}}{Y_{dp,\infty,rec}} \quad (2.78)$$

If the measured driving-point mobility is not available, the infinite plate mobility of the building element, $Y_{dp,\infty,inst}$, can be used to estimate the installed power in the mid- and high-frequency range [34]; hence, Eq. (2.78) can be reformulated to

$$W_{inst} = W_{char} \frac{Y_{dp,\infty,inst}}{Y_{dp,\infty,rec}} \quad (2.79)$$

However, both Eq. (2.78) and Eq. (2.79) provide the structure-borne sound power input data for the prediction with regard to SEA (refer back to Section 2.4) or simplified SEA-based models according to EN 12354-5 [11].

2.5.2.3 Potential issues with low-frequency characterisation

As noted in Section 2.5.2.1, the reception plate method based on a modal SEA approach is used to quantify the energy stored in bending modes that has been injected by a steady-state structure-borne sound source into an isolated reception plate. For an isolated reception plate that is supported by resilient material, there will also be rigid body motion at low frequencies as indicated in Section 2.3.1.1.

This leads to the question, does the existence of rigid body modes cause any problem or error in characterising the structure-borne sound sources on a reception plate below the first bending mode? This could be important because the characterisation of structure-borne sound sources on a highly damped reception plate could extend the currently used lower limit of 50 Hz to the frequency of the first rigid body mode. Recall that a free plate has six DOFs which results in six rigid body modes without bending deformations that are at or near 0 Hz (refer back to Section 2.3.1.1). Due to the highly damped viscoelastic layer that supports an isolated reception plate, three of these rigid body modes will occur at frequencies at or near the higher bouncing mode (see Figure 2-9). Those three rigid body modes are expected to be whole body (or bouncing) and rocking modes. The effect of rigid body modes on structure-borne sound power characterisation with isolated reception plates has not been addressed in previous studies [27, 30]. This was partly because it was assumed that rigid body motions at the suspension would occur below 20 Hz [30, 33]. SEA is based on groups of oscillators, and rigid body modes can be considered as oscillators. While the SEA equations apply to any system with a modal response, the accuracy of the reception plate undergoing rigid body motion has not been assessed. Therefore, this thesis has investigated the accuracy of the reception plate equation when rigid body modes and bending modes are present.

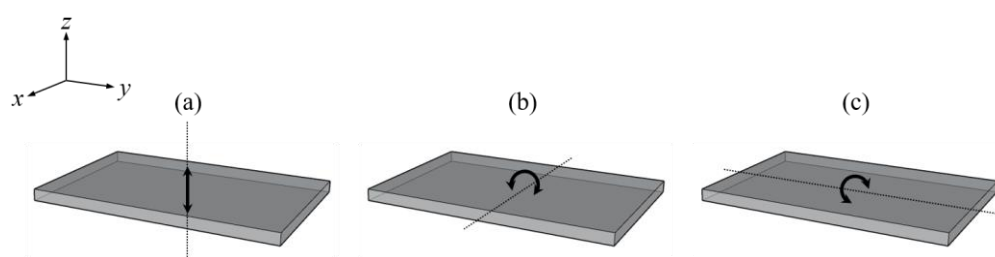


Figure 2-9. Schematic representation of rigid body modes for (a) whole body (or bouncing) mode with translational motion in the z -axis, (b) rocking mode with rotational motion about the x -axis and (c) rocking mode with rotational motion about the y -axis.

Another important low-frequency issue occurs with widely spaced bending modes in the low-frequency bands, which can cause significant spatial variation

in the bending vibration field. When the reception plate rests on viscoelastic material to increase the damping and avoid pronounced resonances, this leads to a related question for a laboratory setting up a reception plate. Is it possible to predict the loss factor for a reception plate rested on resilient supports at the design stage in order to obtain the amount of resilient material that is needed? This question is addressed in Section 4.4.2 through the development of validated FEM models for an isolated reception plate.

Since a limited number of measurement positions on the plate surface are used to measure the average velocity response, the uncertainty can be expected to be greater at low frequencies. By accounting for higher vibration levels near corners and edges, it should be feasible to develop and validate a sampling procedure to avoid bias errors and increased uncertainty in the low-frequency range for the spatial vibration levels.

As the reception plate rests on viscoelastic material (to increase the damping), this leads to a large spatial variation in velocity levels (bending wave motion) at corners and edges where motion is only partly constrained by the viscoelastic material. Therefore, the reception plate behaves similarly to a plate with free boundary conditions or an isolated plate [30, 33]. As mentioned before (Section 2.2.3), at low frequencies, an increase in damping is beneficial as it results in a higher modal overlap between the individual modes having a larger width of modal resonances and a smoother response. The so-called partial constraint layer damping effect at corners and edges vanishes to higher frequencies when the velocity in the diffuse field becomes uniform. Hence, at low frequencies where the bending wavelengths are large, this requires careful sampling of velocity levels if only a few measurement positions are used to avoid potential bias.

In designing an isolated reception plate, the location of the excitation force also needs to be taken into account at low frequencies where the nodal and anti-nodal lines can be widely separated, and the response can be influenced by the source being located on nodal or anti-nodal lines. As most machinery has a

rectangular or square array of fixing points that are aligned along straight lines, it is potentially useful with a rectangular reception plate to angle the machine (machine not parallel to plate boundaries) or to have access to an experimentally validated FEM model to predict nodal lines before it is built.

2.6 Summary

This chapter introduced the underlying theory needed for later chapters to characterise the power input on an isolated reception plate that is then required to predict the structure-borne sound source transmission from a source exciting a heavyweight wall/floor that radiates into an adjacent room.

Bending wave theory and modelling of structure-borne sound characterisation were discussed in detail in relation to the objectives of this research study. In this context, the theoretical considerations on the assumptions on thin plate theory and various parameters based on the dynamic plate response were defined to support the underlying theory for FEM and SEA. These also provided the relevant theory for the experimental procedures for Chapter 3.

FEM is used to model the isolated reception plate in Chapters 4 and 5; hence, the underlying theory was introduced for the modelling procedure with the shell element STRI3, structural damping, boundary conditions, loads and mesh generation.

SEA was introduced as a model to predict sound transmission for steady-state signals along with a proposal to use this approach to predict L_{Fmax} from short L_{eq} for time-varying structure-borne sound sources such as building machinery. This proposal is assessed in Chapters 6 and 7.

The characterisation of structure-borne sound sources on a reception plate was described for two measurement methods, the direct injected power and the reception plate power, because it is relevant for data analysis of FEM predictions and measurements in Chapters 4 and 5. In addition, the theory on the installed

Chapter 2

power of real walls and floors obtained from the gathered power input on the reception plate and needed as input data for the SEA predictions in Chapters 6 and 7 were given. Furthermore, the potential issues of the structure-borne sound characterisation on the reception plate were defined for rigid body motions, spatial variation of the bending wavefield and source positions. Besides the measurement and SEA prediction of time-varying structure borne sound sources, this is another motivation for this research study.

3 Test constructions and experimental work

3.1 Introduction

This chapter gives an overview of the test constructions as well as experimental procedures and equipment. For this purpose, the laboratory facilities are described in Section 3.2 with sound, vibration and force measurements in Section 3.3. The experimental methods used to determine the material properties of the reception plate are included in Section 3.4.

3.2 Test facilities

The main facilities for the experimental work were the reception plate and a flanking laboratory. A heavyweight reception plate test rig (Section 3.2.1) was used for the characterisation of structure-borne-sound power of sources to validate a FEM reception plate model. A flanking laboratory with a separating floor (Section 3.2.2) was used to determine sound transmission in a building-like situation.

3.2.1 Reception plate test rig

The heavyweight reception plate test rig at the University of Applied Sciences Stuttgart consists of three structurally isolated, mutually perpendicular concrete plates (one horizontal plate and two vertical plates with areas that range from 5.34 m² to 6.85 m²) which form a corner of a room as described in EN 15657 [35]. For the laboratory experiments, only the 100 mm thick horizontal reception plate with an area of 5.60 m² (2.0 m × 2.8 m corresponding to a length to width ratio of 1:1.4) was used.

A schematic representation of this reception plate is shown in Figure 3-1. Around the four edges, the reception plate was supported using viscoelastic material Sylodamp HD 30 [143] that had a high internal loss factor to increase the overall damping of the plate. The viscoelastic supports are 100 mm thick (four layers of 25 mm) and have a total area of 2.73 m² (49% coverage). Low-density, low-stiffness mineral wool was filled within the cavity between the ground floor and resting reception plate on the resilient supports around the plate boundaries that were originally considered to reduce possible resonances in the sound field [33].

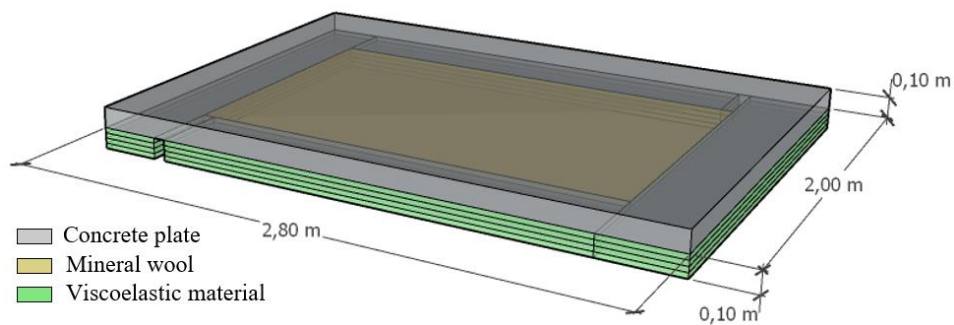


Figure 3-1. Schematic representation of the horizontal concrete reception plate.

Material properties of the concrete that formed the reception plate were assumed to be 0.005 for the internal loss factor and 0.3 for Poisson's ratio [71]. The density of 2300 kg/m³ was determined from the ratio of the weighted mass per unit volume, which was performed in a previous research study [30, 33]. The

Young's modulus of 25.9×10^9 N/m² was obtained from measurements of the quasi-longitudinal wave phase velocity as described in Section 3.4.1.1. The material properties of the viscoelastic material with a spring stiffness of 271003 N/m and damping constant of 497 Ns/m were determined using dynamic stiffness measurements as described in Section 3.4.2.

Note that the case study in Chapter 8 used both the horizontal and vertical reception plates. The vertical reception plate had a thickness of 100 mm and an area of 6.85 m² (2.2 m × 3.1 m corresponding to the same length to width ratio as the horizontal reception plate).

3.2.2 Laboratory with suppressed flanking transmission

Field measurements were carried out on a concrete separating floor located in a test facility for impact sound measurements (according to EN ISO 10140-5 [144]) at the University of Applied Sciences Stuttgart which resembles a building-like situation. The facility comprises two reverberation rooms, namely the top and the ground floor, where the latter is the receiving room that is used for sound pressure measurements in this thesis. The facility is decoupled from the laboratory's ground by resilient material to avoid structure-borne noise from the surrounding area.

A schematic representation of the floor test facility used for *in situ* measurements is shown in Figure 3-2. The reinforced concrete floor had a thickness of 140 mm and an area of 19.4 m² (4.22 m × 4.60 m corresponding to a length to width ratio of 1:1.1). Three supporting walls are made from 240 mm and one supporting wall is built from 175 mm heavyweight calcium silicate and provide suppressed flanking sound transmission through the addition of independent plasterboard linings. The independent linings on the 240 mm supporting walls have a 120 mm depth of cavity filled with mineral wool followed by a 50 mm steel frame with a 12.5 mm thick layer of plasterboard. The independent lining in front of the 175 mm supporting wall consists of a 75 mm depth of mineral wool filled cavity followed by a 50 mm steel frame and

a 25 mm double layered plasterboard. The receiving room has dimensions of 4.22 m × 4.60 m × 2.63 m that give a volume of 51.1 m³.

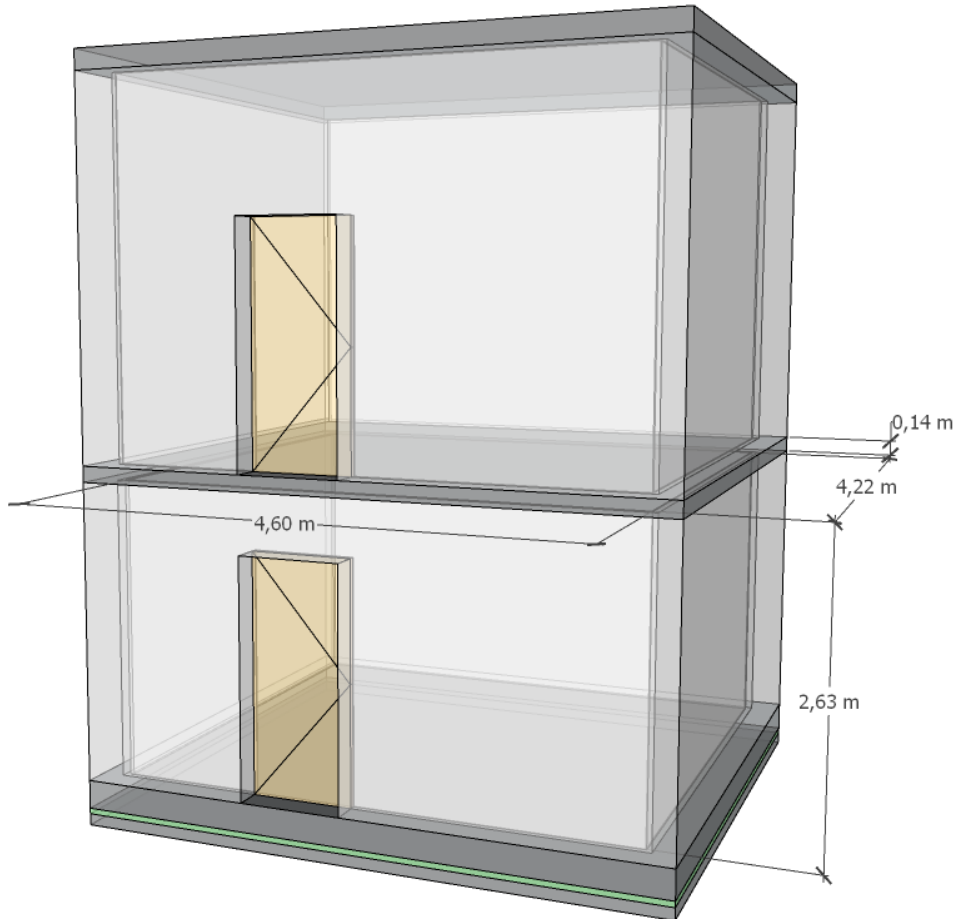


Figure 3-2. Schematic representation of the floor test facility representing a building-like situation in heavyweight buildings.

3.3 Measurement of sound, vibration and force

This section briefly introduces the data acquisition systems used with the measurement software in Section 3.3.1 and the excitation and response sensors in terms of impact hammers, shaker, accelerometers and microphones in Section 3.3.2. The measurement procedures for sound, vibration and force are discussed in Sections 3.3.3 to 3.3.7.

3.3.1 Measurement system and software

The main data acquisition system was from Brüel & Kjær (B&K) consisting of a combination of one 4/2-channel input/output LAN-XI module Type 3160-A-042 and two 6-channel input LAN-XI modules Type 3160-A-0460 in a wireless LAN-XI frontend frame Type 3660-C-100. This measurement system was controlled by the analysis software package B&K PULSE LabShop. In addition, a Norsonic dual-channel real-time analyser Type Nor840 was used for structural reverberation times using a Maximum Length Sequence (MLS) signal.

3.3.2 Excitation and response techniques

This section describes excitation using an impact hammer and electrodynamic inertial shaker along with the accelerometers and microphones used for the vibration and sound measurements.

3.3.2.1 Impact hammer

For mechanical point excitation, three different instrumented impact hammers were used from B&K, an Integrated Electronics Piezo Electric (IEPE) impact hammer Type 8206-003 with built-in Transducer Electronic Data Sheet (TEDS), a heavy-duty IEPE impact hammer Type 8207 with built-in TEDS and an impact hammer Type 8202. The impact hammer Type 8202 was connected to a B&K NEXUS conditioning amplifier Type 2693-A.

Impact hammers incorporate a force transducer in the hammer head with a hammer tip mounted on the top. The hammer tips are typically available as rubber, plastic and metal tips. When the hammer tip is relatively soft, a flat force spectrum only occurs in the low-frequency range before rolling off; hence, with increasing stiffness of the hammer tip material, the frequency range with a flat force spectrum becomes wider. Section 3.3.4 shows the input force-frequency range of these three hammer tips when the driving-point mobility is measured.

3.3.2.2 Shaker

A DataPhysics electrodynamic inertial shaker Type IV40 was used to inject steady-state and time-varying white noise signals for forced single point excitations of vibration measurements perpendicular to the surface. The shaker was controlled by a DataPhysics power amplifier Type GW-PA30E or an Acoustical Mfg Co Ltd. power amplifier Type QUAD 50E. These amplifiers convert the low-power input signal from the PC soundcard into an efficient high-power output signal to the shaker.

To measure the force applied by the shaker, an in-line force transducer (Kistler Type 9311B) was mounted under tension between two M6 (6 mm nominal diameter) metric internal thread steel nuts on both sides and was fastened between the steel bolts with M6 metric external threads of the shaker and stinger. The stinger was bonded to the structure by 2C-modified epoxy resin using DELO-DUOPOX 01 rapid. Note that the stinger has high stiffness in the axial direction but low bending and shear stiffness in the lateral direction.

The shaker can affect the applied force spectrum. For a white noise signal sent to the Type IV40 shaker, the force spectrum is shown in Figure 3-3. This can be described in terms of three frequency ranges between 20 Hz and 5 kHz. The first range, 20 to 50 Hz, contains the suspension resonance of the mass-spring system of the armature mass and its suspension system. The upper graph in Figure 3-3 indicates that the suspension resonance occurs at ≈ 34 Hz. Above the suspension resonance, the second range predominantly represents the white noise input signal with constant acceleration between 50 Hz and 2.5 kHz. In this range, the mass of the moving element dominates the motion of the exciter table [145]. At high frequencies (≥ 2.5 kHz), the third range contains the moving element (or axial) resonance caused by the coil that moves out-of-phase with the exciter table as the elastic armature structure is deformed [145, 146]. This moving element resonance was evident at ≈ 4 kHz. The difference between the upper and lower frequency of the provided characteristic uniform force level by the shaker is

depicted in the lower graph of Figure 3-3; a range of approximately ± 3 dB has been defined as representing the range unaffected by the shaker resonances.

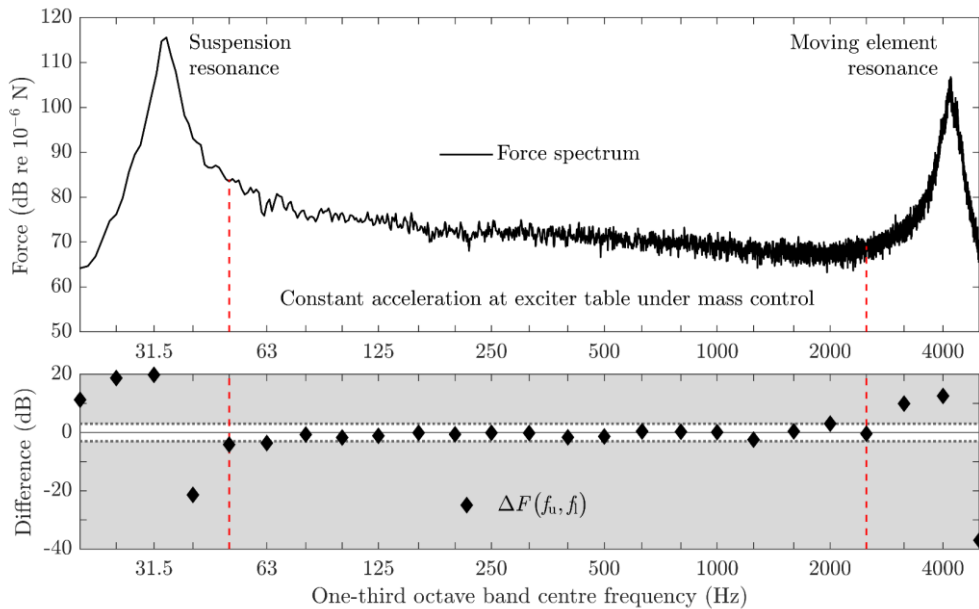


Figure 3-3. Electrodynamic inertial shaker operating under white noise input: Force spectrum as a function of frequency (upper graph) and the difference between upper and lower frequency (lower graph). The red dashed lines indicate the three ranges, which have (1) the suspension resonance, (2) approximately constant acceleration at the exciter table and (3) the moving element resonance.

Since tonal components often occur with structure-borne sound sources (refer back to Figure 1-4), the dynamic characteristic of the shaker gives the opportunity to assess white noise combined with a tonal component at low frequencies. In contrast, the high moving element resonance frequency is not typical behaviour for structure-borne sound injected by building machinery and is not considered (see also Figure 1-4). Hence, for the characterisation and prediction of a purely idealised structure-borne sound source with a single contact drive point, the electrodynamic inertial shaker enables assessment of a low-frequency tonal component and uniform excitation in the range from 20 Hz to 2 kHz.

3.3.2.3 Accelerometer

Vibration was measured using B&K IEPE accelerometers Type 4533-B-001 with a low-noise preamplifier and built-in TEDS (sensitivity of 1 mV/ms^{-2} , weight of 8.6 g) and accelerometers Type 4383-V (sensitivity of 3.16 pC/ms^{-2} , weight of 17 g) controlled by a NEXUS conditioning amplifier Type 2693-A and a charge conditioning amplifier Type 2635 respectively. With respect to the measurement response direction, both types of accelerometers characterise structural vibrations along a single axis of sensitivity. The signal measured on the heavyweight plate is unaffected by the low accelerometer mass relative to the plate mass. Moreover, these accelerometers have sufficiently high sensitivity to be suitable for low-frequency measurements.

Beeswax was used to attach accelerometers to the structure. This accelerometer mounting technique can lead to errors at high frequencies if beeswax is not carefully employed using a thin layer between the sensor and structure. This can lead to a mass-spring resonance caused by the beeswax. However, in this thesis, the measurements are below 4 kHz and are unaffected by this effect [147].

3.3.2.4 Microphone

Field measurements used G.R.A.S. microphones Type 40HL (sensitivity of 850 mV/Pa , polarisation voltage of 200 V), which comprise a $\frac{1}{2}$ " special high-sensitive free-field microphone with an integrated low noise preamplifier and built-in TEDS. This microphone allows measurements of sound levels close to the threshold of human hearing. In addition, $\frac{1}{2}$ " microphones from Norsonic were employed, which consisted of a combination of free-field microphone Type Nor1220 (sensitivity of 50 mV/Pa , polarisation voltage of 200 V) and preamplifier Type Nor1201.

3.3.3 Experimental Modal Analysis (EMA)

EMA is used to characterise the dynamic properties of a linear and time-invariant structure in the frequency domain where the mode vibration data as eigenvalues, eigenvectors and damping through a modal test procedure are obtained. The modal test procedure has two analysis steps, the measurement of FRFs introduced in Section 3.3.3.1 and the modal parameter extraction in a post-processing procedure described in Section 3.3.3.2. Note that the basic theory for a freely vibrating damped system was described in Section 2.3.1.1.

3.3.3.1 Test method for EMA

EMA was carried out on the reception plate using modal testing software (B&K PULSE LabShop MTC Type 7753) in conjunction with the data acquisition system (B&K LAN-XI frontend frame Type 3660-C-100 with modules Type 3160-A-042 and Type 3160-A-0460). The mobility technique was carried out by measuring inertance (acceleration over force) to determine the FRF matrix in the form of $[H_{ij}(\omega)] = \{a_j(\omega)\} / \{F_i(\omega)\}$ (refer back to Eq. (2.21)) with a 1 Hz frequency resolution.

FRFs were measured with roving impulsive excitation at each grid point using an impact hammer (B&K Type 8206-003 with aluminium tip) and twelve stationary accelerometer positions (B&K Type 4533-B-001). The use of multiple response reference points ensures detection of closely coupled modes, repeated roots or local modes of a structure [148]. For EMA, the plate was divided into a measurement grid of 21×29 lines resulting in a total of 609 grid points that corresponds to a 100 mm spacing between the multiple excitation points comprising six DOFs for a plate with free boundaries. Note that because of the large number of grid points and the frequency range from 20 Hz to 2 kHz, only the aluminium hammer tip was used. Figure 3-4 shows the EMA measurement set-up in terms of the grid for the roving hammer test with the placed

accelerometers and an illustrative impact hit on a corner grid point near an accelerometer to gauge the velocity response from the induced force.



Figure 3-4. EMA measurement set-up using the 21×29 grid for the roving hammer test with positioned accelerometers (left) and an illustrative impact hit on a corner grid point close to an accelerometer (right).

The setting of the hammer trigger was activated by a sufficiently high force to capture the force signal over the entire frequency range from 7 Hz to 2.5 kHz. For the Fast Fourier Transform (FFT) settings, the hammer weighting was applied with a transient window that contained the entire signal since the forced transient hammer hit had an excitation duration shorter than the record length. A rectangular window was used because there was no signal clipping and leakage as the signal response dropped near to zero or below the analyser noise floor faster than the analyser's time record for the length of signal coverage. The window time shift delay was set to 100 ms so that the hammer and accelerometer signals began recording the measurement at the same time. In the modal analysis software, the measured FRFs contained both the amplitude and phase, where each FRF data set consisted of an average of four hits for the individual grid points. The force and acceleration time history, cross power spectra and coherence functions were logged to monitor the quality of the measured data.

3.3.3.2 Modal parameter identification

From the multi-reference impact test described above, the FRF data sets were post-processed using modal analysis software (Vibrant Technology MEscopeVES V6.0) in the frequency domain to extract the modal parameter sets with the spatial domain algorithm Complex Mode Indicator Function (CMIF) using the Rational Fraction Polynomial (RFP) curve fitting method. The concept of CMIF is based on a singular value decomposition of the FRF matrix at each spectral line which can be expressed by [149]

$$[H(i\omega)] = [U(i\omega)][\Sigma(i\omega)][V(i\omega)]^H \quad (3.1)$$

where $[U(i\omega)]$ is the left singular matrix representing the approximated unscaled mode shapes, $[V(i\omega)]$ is the right singular matrix representing the approximated modal participation factors, both consisting of orthonormal unit length vectors, $[\Sigma(i\omega)]$ is the singular value matrix in descending order and $i\omega$ denotes the approximated complex damped frequency vector in the Laplace domain.

CMIF was used to identify the eigenvalues from the normal matrix at each spectral line by pre-multiplying the FRF matrix by its Hermitian matrix, $[H(i\omega)]^H [H(i\omega)]$. By this definition, the CMIF is a plot of log magnitude scale of frequency-dependent singular values of the FRFs that estimates the damped eigenfrequencies from the detected eigenvalues (roots) within the accuracy of frequency resolution and corresponding unscaled modes by [149]

$$CMIF_k(i\omega) = \lambda_k(i\omega) = \sigma_k^2(i\omega) \quad k = 1, 2, \dots, N_r \quad (3.2)$$

where $CMIF_k(i\omega)$ is the k -th CMIF, $\lambda_k(i\omega)$ is the k -th eigenvalue of the FRF matrix, $\sigma_k(i\omega)$ is the k -th singular value of the FRF matrix and N_r is the number of dominant modes that contribute to the final response. The FRF matrix was measured using acceleration and force; hence, the imaginary part was used

to solve Eq. (3.2). (NB The resonance peaks in the imaginary part of FRFs typically provide the narrowest peaks, which are well above the noise floor and allow easy identification of modes [150].)

Once the CMIF is resolved, the unscaled mode shapes, $\{u(i\omega_n)\}_k$, from the k -th detected root can be computed as [151]

$$\{u(i\omega_n)\}_k = [H(i\omega_n)] \{v(i\omega_n)\}_k \lambda(i\omega_n)_k \quad k = 1, 2, \dots, N_k \quad (3.3)$$

where $\{v(i\omega_n)\}_k$ is the equivalent mode participation factor and N_k is the number of detected repeated roots. Thereafter Eq. (3.3), the scaled mode shapes can be solved using the enhanced FRF matrix, $[\tilde{H}_n(i\omega)]$, from the FRF matrix, which is given by [151]

$$[\tilde{H}_n(i\omega)] = \{u(i\omega_n)\}^H [H(i\omega_n)] \{v(i\omega_n)\} \quad (3.4)$$

Applying the partial fraction expansion using the summation within any considered eigenfrequencies of several SDOF systems, the FRF matrix $[H(i\omega)]$, for a symmetrical MDOF system can be reformulated as follows [151]

$$[H(i\omega)] = \sum_{i=1}^{2N} \frac{[A_i]}{(i\omega_i - p_i)} = \sum_{i=1}^{2N} \frac{Q_i \{\phi_i\} \{\Upsilon_i\}^H}{(i\omega_i - p_i)} \quad (3.5)$$

with

$$p_i = -\sigma_i + i\omega_i = -\frac{\omega_i \zeta_i}{\sqrt{1 - \zeta_i^2}} + i\omega_i \quad (3.6)$$

where N is the number of modes, $[A_i]$ is the residue matrix, Q_i is the scaling constant, $\{\phi_i\}$ is the normalised mode shape vector, $\{\Upsilon_i\}$ is the modal participation factor matrix, p_i is the system pole, σ_i is the damping decay constant (or half-power bandwidth), ζ_i is the damping ratio and ω_i is the eigenfrequency. The fraction of critical damping can be written as

$$\zeta_i = \frac{\sigma_i}{\sqrt{\omega_i^2 + \sigma_i^2}} \quad (3.7)$$

where $\sqrt{\omega_i^2 + \sigma_i^2} = f_i$ indicates the undamped eigenfrequency. Equation (3.7) was multiplied by two according to Eq. (2.41) to give the loss factor. The EMA loss factors that lie within one-third octave bands were arithmetically averaged.

EMA typically leads to a complex modal matrix for any linear damped system. These complex test data were used to validate a FEM model which provides real-valued modes. Dependent on the type of damping applied in the FEM model, the FEM software package Abaqus allows the extraction of both real- and complex-valued modal parameters (refer back to Section 2.3.2.6). However, if the numerical data sets are real and the measured data sets are complex, it is necessary to convert the measured complex-valued modes into real-valued modes. A widely used approach is the simple method [125] of the complex-to-real conversion to adjust the phase angle, $\angle\{\phi_i\}$, between 0° and 180° that was carried out using following steps with (a) if $0^\circ \leq \angle\{\phi_i\} \leq 90^\circ$ then $\angle\{\phi_i\} = 0^\circ$, (b) if $270^\circ \leq \angle\{\phi_i\} \leq 360^\circ$ then $\angle\{\phi_i\} = 0^\circ$ and (c) if $90^\circ \leq \angle\{\phi_i\} \leq 270^\circ$ then $\angle\{\phi_i\} = 180^\circ$. From this, the complex normal mode shapes can be recalculated by the modified phase angle using

$$\begin{aligned} \Re\{\phi_i\} &= |\{\phi_i\}| \cos(\angle\{\phi_i\}) \\ \Im\{\phi_i\} &= |\{\phi_i\}| \sin(\angle\{\phi_i\}) = 0 \end{aligned} \quad (3.8)$$

which gives the real-valued normal mode shapes [125].

For a comparison of the errors in terms of eigenfrequencies and mode shape pairs from EMA and FEM, the Natural Frequency Deviation (NFD) and the Modal Assurance Criterion (MAC) respectively are carried out. The Natural Frequency Deviation (NFD) is given by

$$NFD(A, X) = \frac{|f_X - f_A|}{f_X} = \left| 1 - \frac{f_A}{f_X} \right| \quad (3.9)$$

The Modal Assurance Criterion (MAC) is assessed for correlating each single mode shape using [125]

$$MAC(A, X) = \frac{|\{\phi_X\}^T \{\phi_A\}|^2}{(\{\phi_X\}^T \{\phi_X\})(\{\phi_A\}^T \{\phi_A\})} \quad (3.10)$$

where the subscripts X and A indicate the experimental and numerical eigenfrequencies or mode shapes from EMA and FEM respectively. This results in a normalised real-valued scalar product quantity bounded between zero (uncorrelated mode pairs) and one (perfectly correlated mode pairs). Note that MAC can be used for both real and complex mode shape column vectors.

3.3.4 Driving-point mobility

For measurements of the driving-point mobility (previously defined in Section 2.2.5), an impact hammer (B&K Type 8202) and two stationary accelerometers (B&K Type 4383-V) with a conditioning amplifier (B&K NEXUS Type 2693-A) were used with the data acquisition system (B&K LAN-XI frontend frame Type 3660-C-100 with modules Type 3160-A-042 and Type 3160-A-0460) and analysis software (B&K PULSE LabShop). The FFT analysis was based on 6400 frequency lines and a frequency span of 6.4 kHz (resulting in a frequency resolution of 1 Hz) and a rectangular window that was suited to transient hammer hits with an excitation duration shorter than the record length. For measurements, the accelerometers were placed at a certain distance where the hammer hit was carried out in the centre along an imaginary line between the two pairs of accelerometers as indicated in Figure 3-5. Each measured driving-point mobility consisted of four averages. As the driving-point mobility is dependent on the wavelength, the accuracy of the frequency range

can be related to $k_B d \ll 1$ or $1/\lambda_B \leq 1/10$ [71], which requires the smallest possible distance between the accelerometer and excitation point.

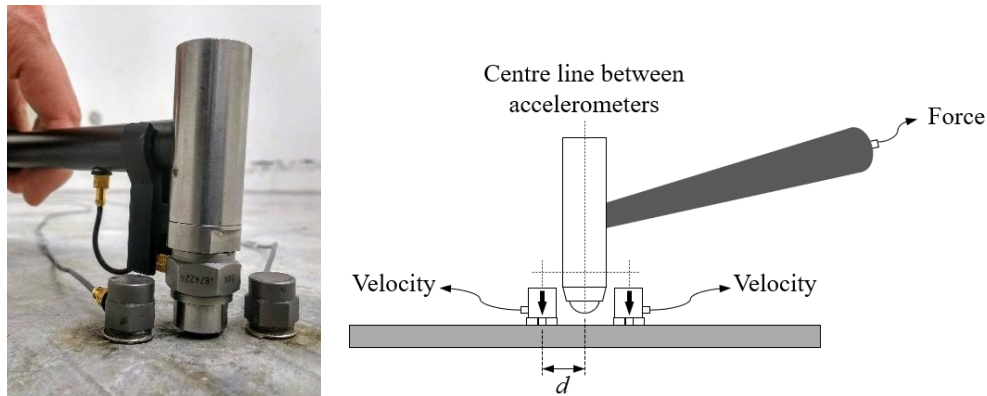


Figure 3-5. Measurement set-up for driving-point mobility (arrows on accelerometers indicate the axis of maximum sensitivity).

Due to the stiffness or resistance to deformation of the structure to be tested, the primary response bandwidth of a short-injected force impulse over time by the impact hammer can be controlled with varying stiffness of hammer tips. For the 100 mm concrete reception plate, the forces applied from the average of four hammer hits with the rubber, plastic and steel hammer tips are shown in Figure 3-6. Figure 3-6a shows that the measured structural excitation response for the three hammer tips leads to three different impulse shapes in the time domain. Figure 3-6b shows the force spectra with vertical limit lines where the maximum force level has dropped by 3 dB, which is 228 Hz for rubber, 853 Hz for plastic and 1.736 kHz for steel tips. Figure 3-6c shows the measured velocity autospectra. In Figure 3-6d, the coherence as the degree of linearity between the force and velocity signals is displayed. Figure 3-6c and Figure 3-6d also show the 3 dB vertical drop off-limit lines to indicate where the input force spectrum of the hammer with individual tips is assumed to be relatively uniform. The useful frequency range is sometimes defined up to the frequency at which it is 10 to 20 dB below the uniform level at low frequencies [152]. In addition, the coherence should be approximately unity to ensure that the driving-point mobility measurement is not affected by unwanted noise in the velocity signal.

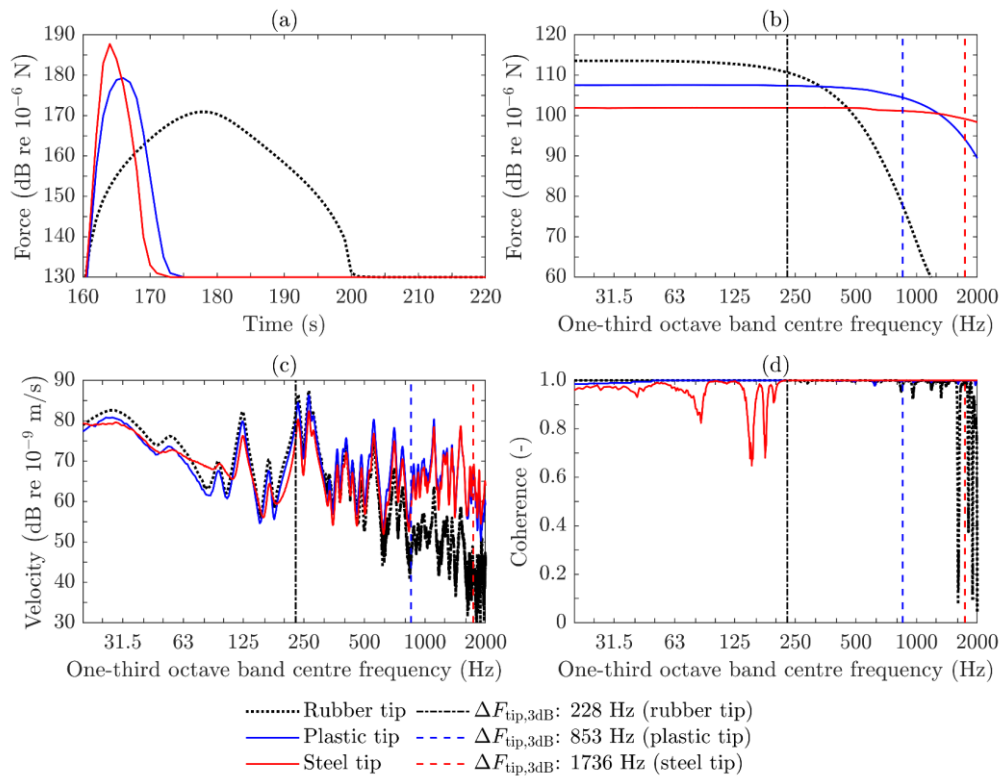


Figure 3-6. Reception plate: Effect of impact hammer with rubber, plastic and steel tips for (a) force impulse, (b) force autospectra, (c) velocity autospectra close to the driving point and (d) coherence between force and velocity signals.

To cover a frequency range up to 2 kHz, it is possible to combine the results from measurements using two different tips. Since the plastic tip has high coherence (>0.95) below 250 Hz, the rubber tip is not needed for measurements of the driving-point mobility at low frequencies, and therefore it is possible to combine only the plastic and steel tip results. The crossover frequency between the plastic and steel tips was set at 400 Hz with the maximum level of the plastic tip still being flat within ± 1 dB. The resulting combined driving-point mobility on the reception plate and the concrete floor in the building-like situation is shown in Figure 3-7, where there is seen to be close agreement between the driving-point mobilities for the plastic and rubber tip measurements.

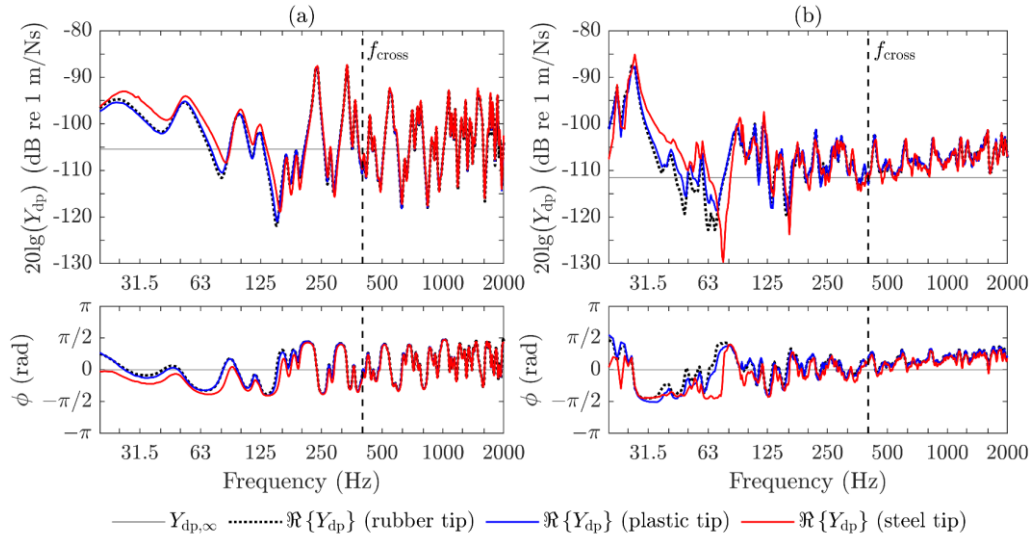


Figure 3-7. Measurement of driving-point mobility using impact hammer with rubber, plastic and steel tips indicating the crossover frequency at 400 Hz for (a) the reception plate and (b) the floor in the building-like situation.

The following equation is used to convert the narrowband driving-point mobility data into one-third octave bands [71]

$$\langle \Re \{ Y_{dp} \} \rangle_f = \frac{1}{f_u - f_l} \int_{f_l}^{f_u} \Re \{ Y_{dp} \} df \quad (3.11)$$

where $\langle \rangle_f$ is the frequency average value. Note that the real part of the measured driving-point mobility can also be used to estimate the modal density for a homogeneous structure using [49]

$$n(f) = 4m \langle \Re \{ Y_{dp} \} \rangle_{f,s} \quad (3.12)$$

where $\langle \rangle_{f,s}$ is the frequency and spatial average value.

3.3.5 Radiation efficiency

The radiation efficiency of the concrete separating floor required measurement of sound pressure in the receiving room and plate velocity. This was measured using the data acquisition system (B&K LAN-XI frontend frame Type 3660-C-100 with modules Type 3160-A-042 and Type 3160-A-0460) with

connected accelerometers (B&K Type 4533-B-001), microphones (G.R.A.S. Type 40HL) and electrodynamic inertial shaker (DataPhysics Type IV40) controlled by a power amplifier (Acoustical Mfg Co Ltd QUAD 50E) for signal conditioning in conjunction with the analysis software (B&K PULSE LabShop). The steady-state signal was assigned from the playback toolbox in the Adobe Audition software into the shaker via a USB audio adapter external soundcard (StarTech ICUSBAUDIO7D). For the experiments, four microphone positions were randomly distributed in the receiving room with seven accelerometer positions on the separating concrete floor respectively. This number was used to give sufficiently standard deviations whilst avoiding correlated positions. The electrodynamic inertial shaker was installed at three different excitation positions on the separating concrete floor and was driven by white noise created as wav file in MATLAB. Constant Percentage Bandwidth (CPB) analysis is used to record velocity from the floor vibration and sound pressure in the receiving room in a frequency range from 50 Hz to 3.15 kHz. From the measured mean-square pressure and velocity, the radiation efficiency can be calculated from

$$\sigma = \frac{A \langle p^2 \rangle_{t,s}}{4S \rho_0^2 c_0^2 \langle v^2 \rangle_{t,s}} \quad (3.13)$$

where A is the absorption area of the room obtained from reverberation time measurements according to EN ISO 3382 [153, 154] that is calculated using

$$A = \frac{0.161V}{T} \quad (3.14)$$

For the determination of the absorption area in the receiving room with Eq. (3.14), the reverberation time was measured using the dual-channel real-time analyser (Norsonic Type Nor840) with two connected free-field microphone (Norsonic Type Nor1220) and preamplifier (Norsonic Type Nor1201) systems.

3.3.6 Spatial variation in plate velocity

Experimental investigation into the spatial variation in reception plate velocity was carried out with the data acquisition system (B&K LAN-XI frontend frame Type 3660-C-100 with modules Type 3160-A-042 and Type 3160-A-0460) and analysis software (B&K PULSE LabShop). The plate was set into vibration using two different excitation positions of the electrodynamic inertial shaker (DataPhysics Type IV40 with power amplifier Type GW-PA30E) driven by white noise. For each shaker excitation position, the spatial plate velocity was determined from thirteen roving accelerometers (B&K Type 4533-B-001) over a total of 609 grid points that correspond to a grid of 100 mm \times 100 mm (same as used for EMA – see Section 3.3.3.1). On the left-side picture in Figure 3-8, the measurement set-up is displayed for the spatial velocity variation for one of the two shaker positions.

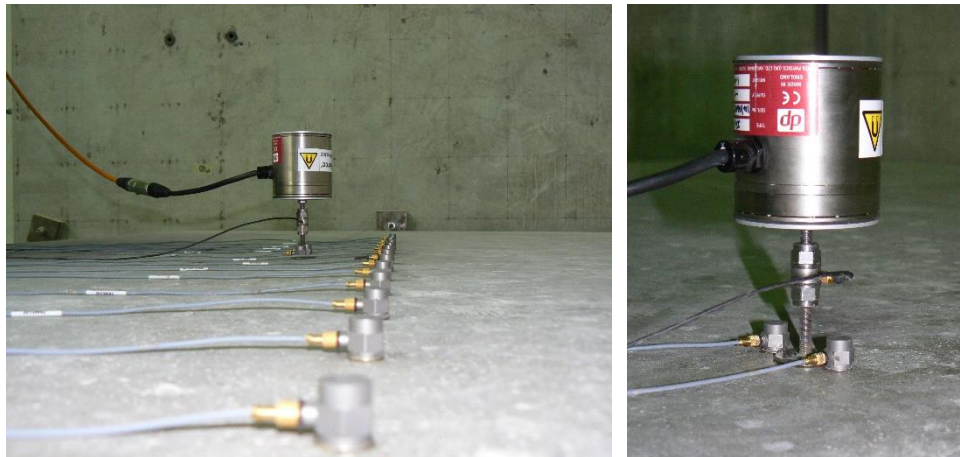


Figure 3-8. Measurement set-up for the spatial variation in plate velocity (left) and the direct injected power (right).

Since EN 15657 [35] does not specify filter or FFT analysis, the velocities were recorded in narrow bands using 6400 frequency lines (N) and 6.4 kHz frequency span (f_s), which gives a frequency resolution of 1 Hz ($\Delta f = f_s/N$). Further settings in the FFT analysis were made for a Hanning window with

66.79% overlap, linear averaging with 58 averages equivalent to a time of 20 s and a 7 Hz high-pass filter was used.

The Hanning window with overlap was utilised to reduce the spectral energy leakage of the FFT analysis of continuous signals due to removal of discontinuities at its boundaries that are associated with a rectangular window. This means that the Hanning window has the property of tapering a steady-state signal smoothly to zero at both edges, which at the same time also leads to a truncation of the continuous signal's overall amplitude; but this can be enhanced using the overlap at the start and end edges. A reduction in the leakage effect is associated with a widening of the main lobe and faster rolling-off side lobes due to more attenuation. Thus, the Hanning weighting results in an effective noise bandwidth that is 50% larger than the rectangular weighting, which corresponds to an effective noise bandwidth of 1.5 times Δf filter/line spacing that must be taken into account to compensate for the amplitude error [155, 156]. In contrast, the rectangular weighting has an effective noise bandwidth of Δf filter/line spacing that represents no weighting for the spectral amplitude. Hence, the measured narrowband velocities with regard to RMS amplitudes were combined to obtain one-third octave band values (refer back to Eq. (2.45)) by summing all narrowband energy between band edge frequencies and multiplying $1/\sqrt{1.5}$ for RMS units or subtracting $10\lg(1.5)$ for decibel units to account for the Hanning weighting [155, 156].

In Figure 3-9a and b, the comparison between the rectangular and Hanning window is shown with regard to the spectral characteristics in the time and frequency domain respectively. It can be seen that the main lobe width of the Hanning window of $f_0 = 4\Delta f$ is twice as wide as the main lobe width of the rectangular window, which is $f_0 = 2\Delta f$. Figure 3-9c, d and e display time and frequency domain examples of a windowed 10 Hz sinusoid with an RMS amplitude of one. (NB In Figure 3-9c, the dotted grey graph is the sinusoid

without window having a peak amplitude of ≈ 1.4 .) From this, the spectrum of a windowed sinusoid in the frequency domain gives an RMS amplitude of 1 at 10 Hz for the rectangular window – see Figure 3-9d and corrected RMS amplitudes of ≈ 0.82 at 10 Hz as well as ≈ 0.41 at 9 and 11 Hz for the Hanning window – see Figure 3-9e. For the Hanning window, Figure 3-9e also indicates the not corrected RMS amplitudes with values of ≈ 1 at 10 Hz as well as ≈ 0.5 at 9 and 11 Hz by the dotted orange spectral lines with white-faced markers.

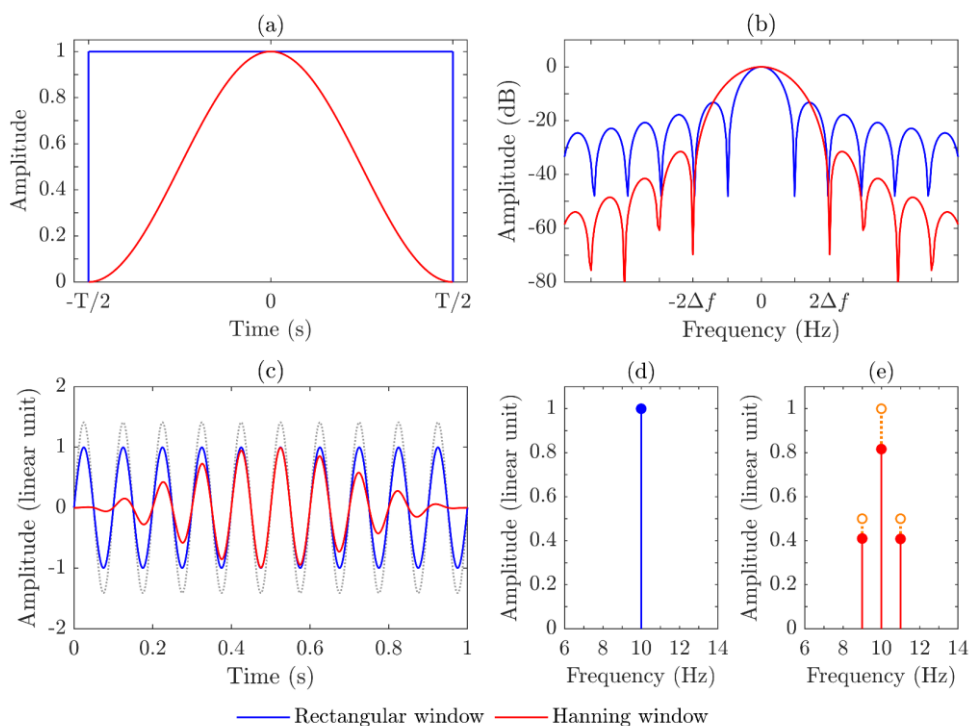


Figure 3-9. Effects of rectangular and Hanning windows using (a) spectral characteristics in the time domain, (b) spectral characteristics in the frequency domain, (c) weighted 10 Hz sinusoid in the time domain, (d and e) corrected and not corrected resulting spikes of 10 Hz sinusoid respectively in the frequency domain.

In addition, the measurements of the spatial average mean-square velocities are used to obtain the reception plate power since this thesis also compares the reception plate power against the direct injected power. Hence, the direct injected power by the shaker into the plate was simultaneously determined from a force transducer (Kistler Type 9311B) and two stationary accelerometers

(B&K Type 4533-B-001) that were each located on each side of excitation at the driving point. Measurement settings for narrowband powers in the FFT analysis were the same as the settings described for the spatial average mean-square velocities. However, instead of autospectra, the cross-spectra with the Power Spectral Density (PSD) unit between force and velocity was used to calculate the injected power according to Eq. (2.74) in narrow bands. The measurement set-up of the direct injected power is shown in Figure 3-8 (right side).

Since narrowband measurements are used for the reception plate power and the direct injected power, which are combined to form ‘ideal’ one-third octave bands, a fair comparison can be made between them. A comparison of filter and FFT analysis on the reception plate to determine one-third octave band values showed that they differed by only 0.1 dB on average with the largest difference in any band being 1.5 dB. Therefore, the findings in this thesis should apply to reception plate measurements using either filter or FFT analysis.

3.3.7 Time-varying excitation for L_{eq} and L_{Fmax} measurements

This section describes the signal processing used to determine velocity levels and sound pressure levels in terms of L_{Fmax} and short L_{eq} for the time-varying signals that were sent to the shaker (described in Section 3.3.7.1) and their analysis using multi-buffer processing (discussed in Section 3.3.7.2).

3.3.7.1 Time-varying signals

In this thesis, the aim is to establish an empirical relationship between short L_{eq} and L_{Fmax} for time-varying signals that increase and decrease over time to represent a piece of machinery that moves between different operating cycles. In MATLAB, twenty wav files of time-varying signals were generated using white noise that is ramped up and down in terms of amplitude.

When a signal is applied to each CPB filter, there is a time delay before the output amplitude is the same as the input amplitude. Therefore, each signal starts with a 1 s period of white noise to ensure that the CPB filters are activated. The

filter response time is approximately $Bt=1$ based on time-to-gradient/amplitude matching [157]. The lowest one-third octave band of interest is 50 Hz which corresponds to a response time of 0.09 s, and therefore a 1 s period is more than sufficient. After the 1 s of steady noise, there is a linear increase in amplitude (increasing ramp) followed by a linear decrease in amplitude (decreasing ramp) with ramp durations of 125 ms, 500 ms, 1 s, 2 s and 5 s. These ramps increase/decrease the level by 10, 20, 30 or 40 dB as indicated by the example shown in Figure 3-10.

The amplitude was normalised using peak normalisation to scale the wav file to the highest amplitude level, typically giving a target value of ± 1 , which represents 0 dBFS (decibels relative to full scale). This normalisation allows a fair comparison of the different ramped white noise signals [157] when determining L_{Fmax} and L_{eq} in any one-third octave frequency band as well as L_{AFmax} .

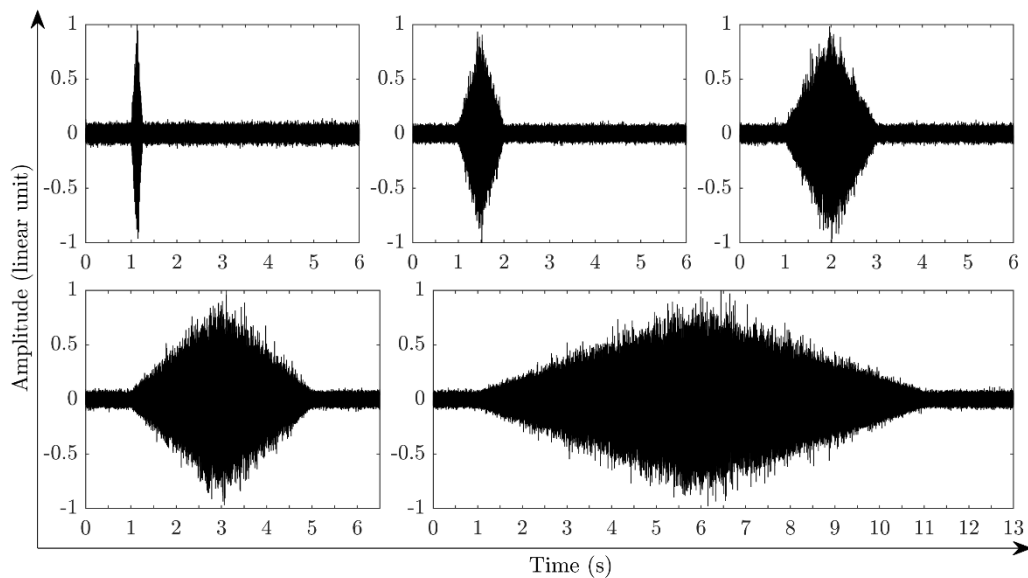


Figure 3-10. Example of time-varying signals formed from white noise with ramp durations of 125 ms, 500 ms, 1 s, 2 s and 5 s and an increasing and decreasing ramp level of 20 dB.

3.3.7.2 Analysis of time-varying signals using multi-buffer measurements

Measurements of time-varying signals were carried out using the data acquisition system (B&K LAN-XI frontend frame Type 3660-C-100 with modules Type 3160-A-042 and Type 3160-A-0460) and analysis software (B&K PULSE LabShop). The wav files were played directly into the measurement system (using the playback tool in Adobe Audition software) and routed to a USB audio adapter external soundcard (StarTech ICUSBAUDIO7D) leading to a power amplifier (Acoustical Mfg Co Ltd QUAD 50E) followed by an electrodynamic inertial shaker (DataPhysics Type IV40). This shaker was installed at three different positions to excite the concrete reception plate and the concrete floor in the building-like situation. The vibration on both the reception plate and the floor was measured using accelerometers (B&K Type 4533-B-001). In the building-like situation, the sound field in the receiving room was also measured using microphones (G.R.A.S. Type 40HL). The spatial average velocity was obtained in terms of $L_{eq,125ms}$, $L_{F,125ms}$ and L_{Fmax} using twenty combined accelerometer positions at the corners, edge strips and in the central zone (≥ 0.1 m away from plate boundaries) on the reception plate and seven randomly distributed accelerometer positions in the central zone (≥ 0.5 m away from plate boundaries) on the separating floor. The spatial average sound pressure level was also determined in terms of $L_{eq,125ms}$, $L_{F,125ms}$ and L_{Fmax} , as well as L_{AFmax} , using four randomly distributed microphone positions in the central volume of the room (≥ 0.7 m away from room surfaces).

A trigger was set on the analyser so that the measurement would begin at the onset of the time-varying signal from the wav file (i.e. with a trigger level sufficiently above the background noise). This used a 350 μ s negative delay. The analyser had a 7 Hz high-pass filter with CPB analysis carried out in one-third octave bands from 50 Hz to 3.15 kHz. In these CPB bands, L_{Fmax} was calculated using the exponential averaging mode with an exponential time constant (τ) of 125 ms that defines Fast time-weighting according to IEC 61672-1 [140]. CPB

analysis also used multi-buffers to determine $L_{\text{eq},125\text{ms}}$ and $L_{\text{F},125\text{ms}}$ in consecutive 125 ms time periods over the duration of the signal.

Recalling that the aim was to identify a relationship between $\max\{L_{\text{eq},125\text{ms}}\}$ and L_{Fmax} , it is reasonable to assume that both will occur in a 125 ms time slice near the top of the increasing ramp in the time-varying signal. There are three factors that could cause $\max\{L_{\text{eq},125\text{ms}}\}$ to occur in different 125 ms slices near the peak in the actual input signal.

The first factor is caused by the response time of CPB filters, which introduces a delay before the signal amplitude reaches the actual value. This delay varies with the filter centre frequency because it depends on the filter bandwidth [157]. For this reason, it is necessary to make sure that $L_{\text{eq},125\text{ms}}$ is identified separately for each CPB band. The second factor is the random fluctuations that occur in the ramped noise. Referring back to Figure 3-10, it can be seen that when the ramp time increases, the random fluctuations sometimes result in a high fluctuation just before or after the peak of the ramp. Because of these two factors, if the ‘maximum hold’ is enabled on the analyser to give $\max\{L_{\text{eq},125\text{ms}}\}$ from over the entire time period, the resulting value might not correspond to the portion of the signal that primarily determines L_{Fmax} . When a signal is played directly into the analyser, it is only these first two factors that apply. However, when the signal comes from a transducer such as an accelerometer on a plate or a microphone in a room then there is a third factor. This third factor depends on the propagation time of the direct signal from the source to the transducer position and the degree of reinforcement/cancellation between the direct and any reflected waves at the transducer position. A potential fourth factor could be caused by a delay in the triggering of the analyser, but because the 1 s steady noise at the beginning of each time-varying signal is well above background noise, this will often be negligible. Note that in the final application where a piece of machinery is exciting a reception plate, the intention is only that the

$\max\{L_{\text{eq},125\text{ms}}\}$ will be measured. Therefore, the issue of relating $\max\{L_{\text{eq},125\text{ms}}\}$ to the L_{Fmax} requires careful consideration if an empirical relationship is to be found between them.

Figure 3-11 is used to visualise the approach to analysis that was used with the multi-buffer measurements; this uses the time-varying input signal with a 5 s ramp and a 20 dB ramp level. In this example, the signal being processed was the resulting velocity that was measured on the reception plate.

A comparison was made of L_{Fmax} from PULSE with the maximum Fast time-weighted level from the 125 ms slice that uses exponential averaging, referred to as $L_{\text{F},125\text{ms}}$. Even though L_{Fmax} was calculated using a running exponential average, it was observed that $L_{\text{F},125\text{ms}}$ always had exactly the same value for all the time-varying signals. Figure 3-11a shows the velocity in terms of $\max\{L_{\text{F},125\text{ms}}\}$ values which are seen to slowly increase over the ramp period between 1 s and 6 s before reaching a maximum value and forming a plateau. The black line indicates the time (6 s) at which the peak in the ramp occurs in the input signal (i.e. for the unfiltered linear signal). The blue line indicates the time at which $\max\{L_{\text{F},125\text{ms}}\}$ occurs (i.e. the time at which the highest $L_{\text{F},125\text{ms}}$ value occurs in each one-third octave band since the start of the signal). Both the blue and black lines are independent of frequency, but the blue line occurs in a later time slice than the black line due to the combination of the three factors described above. The time difference between the blue and black lines differs depending on the time-varying signal. This time difference was equal to three 125 ms time slices for the 125 ms, 500 ms and 1 s ramp durations and six 125 ms time slices for the 2 s and 5 s ramp durations.

Having identified that $L_{F_{\max}}$ occurs an additional three to six 125 ms time slices after the peak in the unfiltered time-varying signal, it was necessary to find the time at which $\max\{L_{\text{eq},125\text{ms}}\}$ occurred. This is shown in Figure 3-11b where the velocity is plotted in terms of $\max\{L_{\text{eq},125\text{ms}}\}$. This identified the red line, which was the time after which $\max\{L_{\text{eq},125\text{ms}}\}$ no longer increased and was frequency-independent. It can be seen that $L_{\text{eq},125\text{ms}}$ continues to increase after the time at which $L_{F_{\max}}$ occurs (i.e. blue line). It is important to be aware of this issue because the aim is to relate $\max\{L_{\text{eq},125\text{ms}}\}$ to $L_{F_{\max}}$, and if the analyser was used to identify $\max\{L_{\text{eq},125\text{ms}}\}$ over the entire time period of the time-varying signal then $\max\{L_{\text{eq},125\text{ms}}\}$ would occur in a 125 ms time slice that did not relate to the resulting $L_{F_{\max}}$. Figure 3-11c shows the potential error that would occur if times up to the red line were used to determine $\max\{L_{\text{eq},125\text{ms}}\}$ rather than the blue line. This error is typically 0.3 to 1.3 dB. Therefore, to avoid this error the identification of $\max\{L_{\text{eq},125\text{ms}}\}$ was restricted to a time period beyond the actual peak in the time-varying signal that was an additional three 125 ms time slices for the 125 ms, 500 ms and 1 s ramp durations and an additional six 125 ms time slices for the 2 s and 5 s ramp durations. These delays for $L_{F_{\max}}$ and $\max\{L_{\text{eq},125\text{ms}}\}$ were checked against a Sound Level Meter (SLM) in MATLAB.

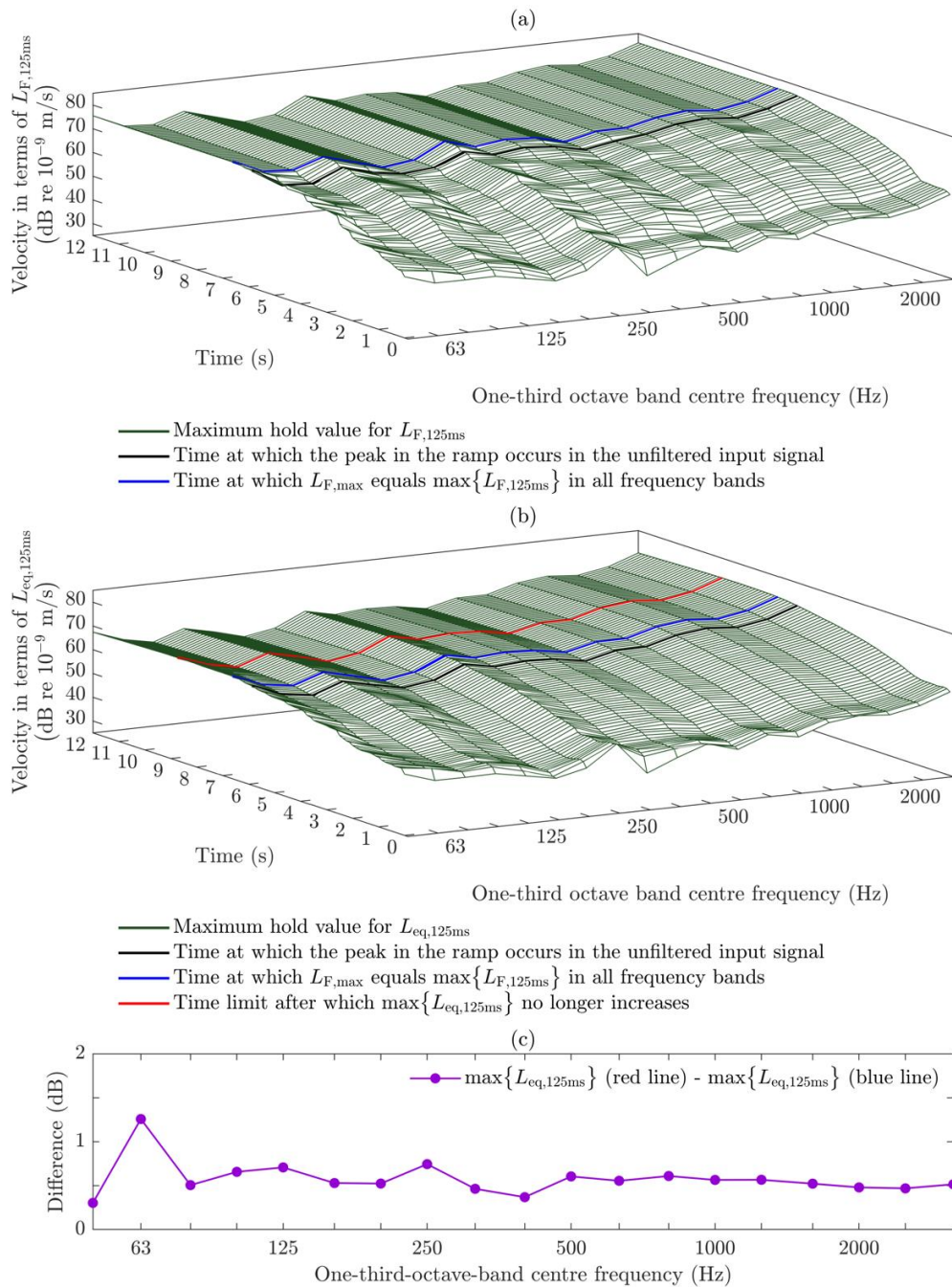


Figure 3-11. Multi-buffer measurements for velocity levels measured on the reception plate using (a) $L_{F,125ms}$ levels starting from a time of 0 s up to 12 s with maximum hold, (b) $L_{eq,125ms}$ levels starting from a time of 0 s up to 12 s with maximum hold and (c) the difference between $\max\{L_{eq,125ms}\}$ at the time where $L_{Fmax} = \max\{L_{F,125ms}\}$ (blue line) and $\max\{L_{eq,125ms}\}$ at the time that velocity levels no longer increase (red line). The time-varying signal has a 5 s ramp and a 20 dB ramp level.

The MATLAB SLM has low- and high-pass input filters, CPB filters and a time-varying detector. In the MATLAB SLM, the input signal passes through a 4th order Butterworth low-pass filter with a cutoff frequency of 20 kHz to avoid aliasing due to the Nyquist frequency of 22.3 kHz and a 6th order Butterworth high-pass filter with a cutoff frequency of 20 Hz. To obtain the frequency content of the signal, the pass filtered signal at the input is analysed with amplitude scaling in RMS values and a filter bank of one-third octave bands (6th order Butterworth – Class 1 filters). The one-third octave band filter design met the specifications from the standards IEC 61260-1 [134] and ANSI S1.11 [158], which only applies to centre frequencies greater than 20 Hz and less than 20 kHz. The range of valid centre frequencies depends on the rate of the specified sampling frequency [159]. With the specified sampling rate of 44.6 kHz, this corresponded to a one-third octave band range from 25 Hz to 16 kHz for these filters. The time-varying detector was equipped into the MATLAB SLM with an analogue filter in terms of a 1st order Butterworth low-pass filter, which is commonly used for digital filters, to feed the band filtered signal with the running RMS into an exponential weighting with a specified constant of 125 ms [160]. This detector design equals the requirements for the exponential time constant Fast according to IEC 61672-1 [140].

PULSE was used for signal processing, but in commercial equipment, the processes are not always fully described/known. Therefore, a comparison was made between PULSE and the MATLAB SLM because all aspects of the processing are defined for the latter. Note that the one-third octave band frequency range of interest is from 50 Hz to 3.15 kHz, and this range is discussed in this section. Calculations were carried out over the range from 25 Hz to 16 kHz, and comments are made in the text if there were any interesting features in these additional bands.

The time-varying signals as wav files were played directly into PULSE or the MATLAB SLM. Two examples are shown here for the time-varying signals using ramp durations of 500 ms and 5 s, both of which have an increase/decrease

ramp level of 40 dB. An example output from the MATLAB SLM is shown in Figure 3-12 for a 5 s ramp duration with a 40 dB ramp level. The unfiltered input signal shown in Figure 3-12a has a triangular-shaped ramp. After filtering, there is a ‘rounded peak’ in Figure 3-12b, which is due to the use of the decibel scale for the y-axis (examples of 50 Hz, 200 Hz and 1 kHz one-third octave band filters are shown). After Fast time-weighting, the time signal is as shown in Figure 3-12c. This shows that there are fluctuations in level near the ‘rounded peak’ (particularly evident at 50 Hz), and these are the reason why L_{Fmax} does not always occur exactly at the time of the peak in the ramped noise signal (this occurs at 6 s in Figure 3-12a).

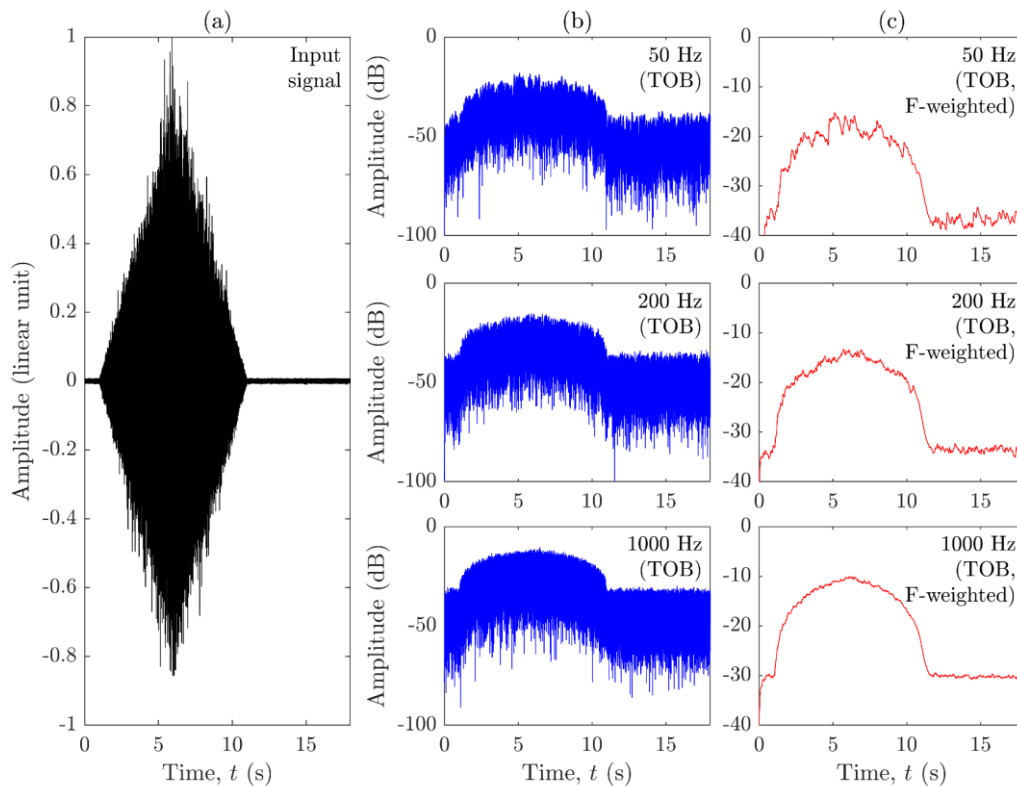


Figure 3-12. Time-varying signal with a ramp duration of 5 s and a ramp level of 40 dB processed with the MATLAB SLM in the time domain: (a) input signal, (b) input signal filtered in TOBs and (c) input signal filtered in TOBs and weighted by the Fast time-weighting constant running from the start of the signal to the current time, t .

Figure 3-13 allows a comparison of the time at which $L_{F_{\max}}$ and $\max\{L_{F,125\text{ms}}\}$ occur with the MATLAB SLM and PULSE respectively. From PULSE measurements, $\max\{L_{F,125\text{ms}}\}$ was determined from the start of the signal to the time at which the top of the ramp occurs in the input signal plus a fixed number of additional time slices. Three additional 125 ms time slices were used for the 500 ms ramp duration (i.e. an extra 375 ms) and six additional 125 ms time slices for the 5 s ramp duration (i.e. an extra 750 ms).

As a point of reference, Figure 3-13 shows the time at which the peak occurs in the ramp for the unfiltered signal is 1.5 s with the 500 ms ramp and 6 s with the 5 s ramp. For the 500 ms ramp, the times with the MATLAB SLM and PULSE are equal to or slightly higher than 1.5 s. For the 5 s ramp, the times with the MATLAB SLM and PULSE are equal to or slightly higher than 6 s in all one-third octave bands except 50, 63 and 200 Hz. In the 50 and 63 Hz one-third octave bands, the time is ≈ 5.3 s. The reason for a time that is < 6 s can be attributed to the random fluctuations with this slow ramp which cause large fluctuations near the peak (e.g. see Figure 3-12c). The value of ≈ 5.9 s at 200 Hz is likely to occur for the same reason, although the fluctuations are smaller (e.g. see also Figure 3-12c).

Between 50 Hz and 3.15 kHz, there is an approximately constant offset between the MATLAB SLM and PULSE for which the average time at which $L_{F_{\max}}$ occurs with the MATLAB SLM is 0.17 s for the 500 ms ramp and 0.12 s for the 5 s ramp before PULSE. In terms of absolute values, the maximum offset is 0.22 s at 50 Hz for the 500 ms ramp and 0.33 s at 80 Hz for the 5 s ramp, and the minimum offset is 0.07 s at 400 Hz for the 500 ms ramp and 0.04 s at 125 Hz for the 5 s ramp. The time offset in both ramp durations is similar. This is very unlikely to be caused by the trigger on PULSE as this was very sensitive with only a 350 μs negative delay. The fact that the minimum offset with PULSE is very small, but there is a large difference between minimum and maximum values, indicates a variable delay. Note that the MATLAB SLM uses time steps

of $\approx 23 \mu\text{s}$ (44.6 kHz sampling frequency) for the whole signal. PULSE outputs the start time for integer multiples of 125 ms, so it would be reasonable to expect that offsets of 125 ms could occur. It is assumed that this offset could be caused by the different filters used in the MATLAB SLM and PULSE. (NB There is no access to the Alternating Current (or short AC) filter signal output in commercial systems [157].)

Figure 3-14 shows the comparison of $L_{F_{\max}}$ from the MATLAB SLM and $\max\{L_{F,125\text{ms}}\}$ from PULSE. Between 50 Hz and 3.15 kHz, the average difference is 0.5 dB for the 500 ms ramp and 0.4 dB for the 5 s ramp with maximum and minimum differences of (a) 1.1 dB at 50 Hz and -0.1 dB at 200 Hz for the 500 ms ramp and (b) 1.1 dB at 50 Hz and -0.1 dB at 250 Hz for the 5 s ramp. PULSE gives identical $L_{F_{\max}}$ and $\max\{L_{F,125\text{ms}}\}$ levels (i.e. 0 dB difference in all frequency bands) when the $\max\{L_{F,125\text{ms}}\}$ levels correspond to the time at which the signal ramp peak occurs plus three additional 125 ms time slices for the 500 ms ramp and six additional 125 ms time slices for the 5 s ramp to the time are determined as indicated in Figure 3-11. However, the MATLAB SLM and PULSE are within ± 1 dB, and this provides evidence that the results in terms of $L_{F_{\max}}$ and $\max\{L_{F,125\text{ms}}\}$ from PULSE can be used with confidence.

The next step is to assess the time at which $\max\{L_{\text{eq},125\text{ms}}\}$ occurs, for which a comparison is made between $\max\{L_{\text{eq},125\text{ms}}\}$ from the MATLAB SLM and PULSE in Figure 3-15. Two values are shown for PULSE, one that is determined over the time period from the start of the signal to the time at which $L_{F_{\max}} = \max\{L_{F,125\text{ms}}\}$ and the other over the time period from the start of the signal to the time at which $\max\{L_{\text{eq},125\text{ms}}\}$ no longer increases. For both approaches, the time at which $\max\{L_{\text{eq},125\text{ms}}\}$ occurs in PULSE is higher than with the MATLAB SLM in all frequency bands between 50 Hz and 3.15 kHz. For the time period from the start of the signal to the time at which

$L_{F_{\max}} = \max \{L_{F,125\text{ms}}\}$, the average time difference is 0.32 s and 0.62 s for the 500 ms and 5 s ramps respectively. In contrast, for the time period from the start of the signal to the time at which $\max \{L_{\text{eq},125\text{ms}}\}$ no longer increases, the average time difference is 0.44 s and 1.74 s for the 500 ms and 5 s ramps respectively. This indicates that it is necessary to specify the time period to be considered when determining $\max \{L_{\text{eq},125\text{ms}}\}$ using an analyser such as PULSE.

The $\max \{L_{\text{eq},125\text{ms}}\}$ levels from the MATLAB SLM and PULSE are compared in Figure 3-16. In the frequency range from 50 Hz to 3.15 kHz, the results indicate that when using the time at which $L_{F_{\max}} = \max \{L_{F,125\text{ms}}\}$ occurs to obtain $\max \{L_{\text{eq},125\text{ms}}\}$ levels, the average difference is 0.3 dB and 0.5 dB for the 500 ms and 5 s ramps respectively. This is similar to the average difference between $L_{F_{\max}}$ from the MATLAB SLM and $\max \{L_{F,125\text{ms}}\}$ from PULSE (refer back to Figure 3-14). The maximum difference is 1.1 dB at 50 Hz for both ramps, and the minimum difference is -0.4 dB at 160 Hz for the 500 ms ramp and -0.6 dB at 315 Hz for the 5 s ramp. The average difference increases to 1.1 dB for the 500 ms ramp and 1.6 dB for the 5 s ramp when $\max \{L_{\text{eq},125\text{ms}}\}$ is determined to the time at which these levels no longer increase. Here, the maximum difference is 2.1 dB at 50 Hz for the 500 ms ramp and 2.3 dB at 2.5 kHz for the 5 s ramp, and the minimum difference is 0.1 dB at 160 Hz for the 500 ms ramp and 0.8 dB at 100 Hz for the 5 s ramp. When $\max \{L_{\text{eq},125\text{ms}}\}$ is determined from the MATLAB SLM and PULSE, there is reasonably close agreement when obtained from the time period up to which $L_{F_{\max}} = \max \{L_{F,125\text{ms}}\}$ compared to using the time at which $\max \{L_{\text{eq},125\text{ms}}\}$ no longer increases. In addition, the average offset for $\max \{L_{\text{eq},125\text{ms}}\}$ to the time at which $L_{F_{\max}} = \max \{L_{F,125\text{ms}}\}$ is similar to those average offsets between $L_{F_{\max}}$ from the MATLAB SLM and $\max \{L_{F,125\text{ms}}\}$ from PULSE.

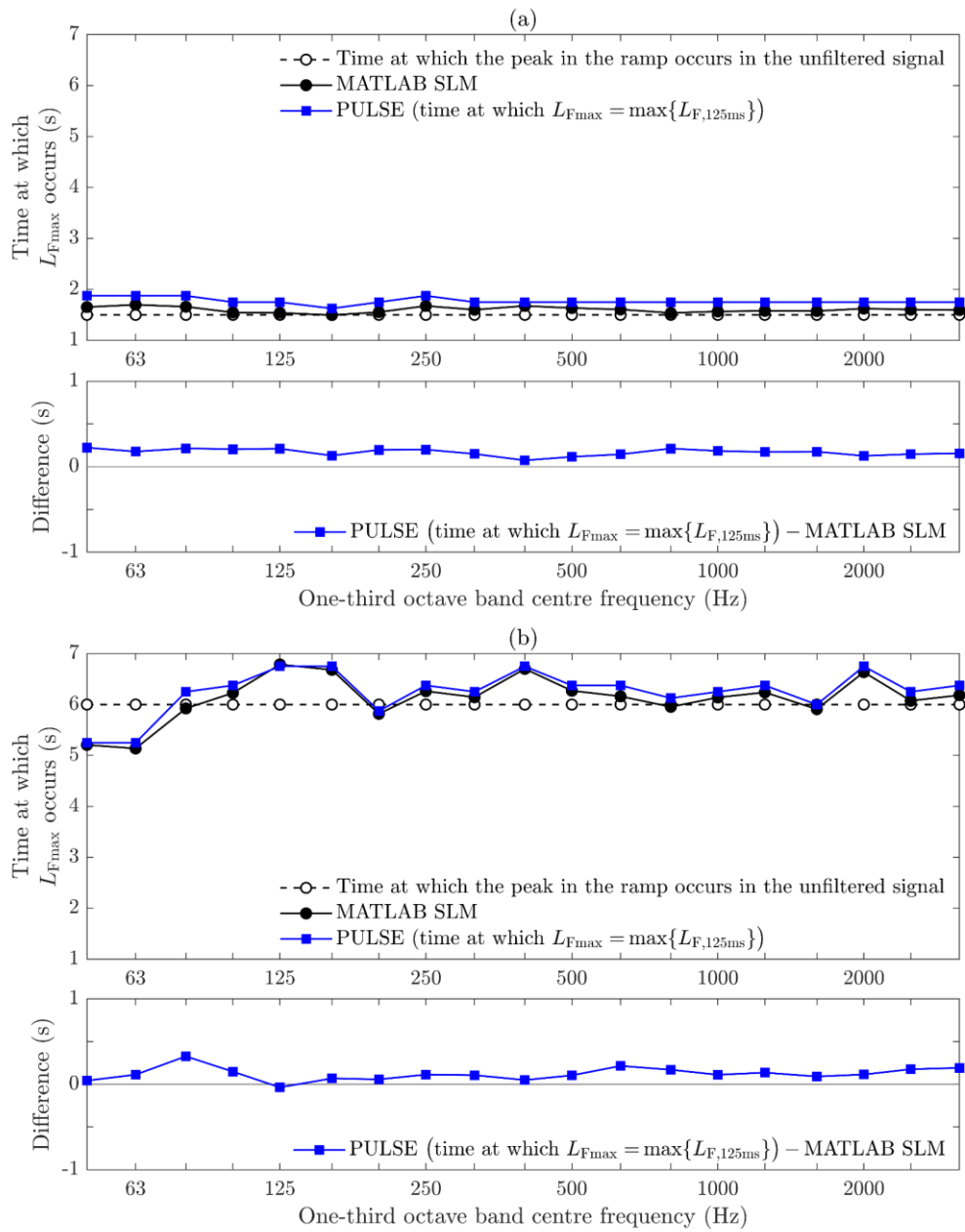


Figure 3-13. Comparison of the time at which $L_{F_{max}}$ occurs with the MATLAB SLM and PULSE using (a) a 500 ms ramp with a 40 dB ramp level and (b) a 5 s ramp with a 40 dB ramp level.

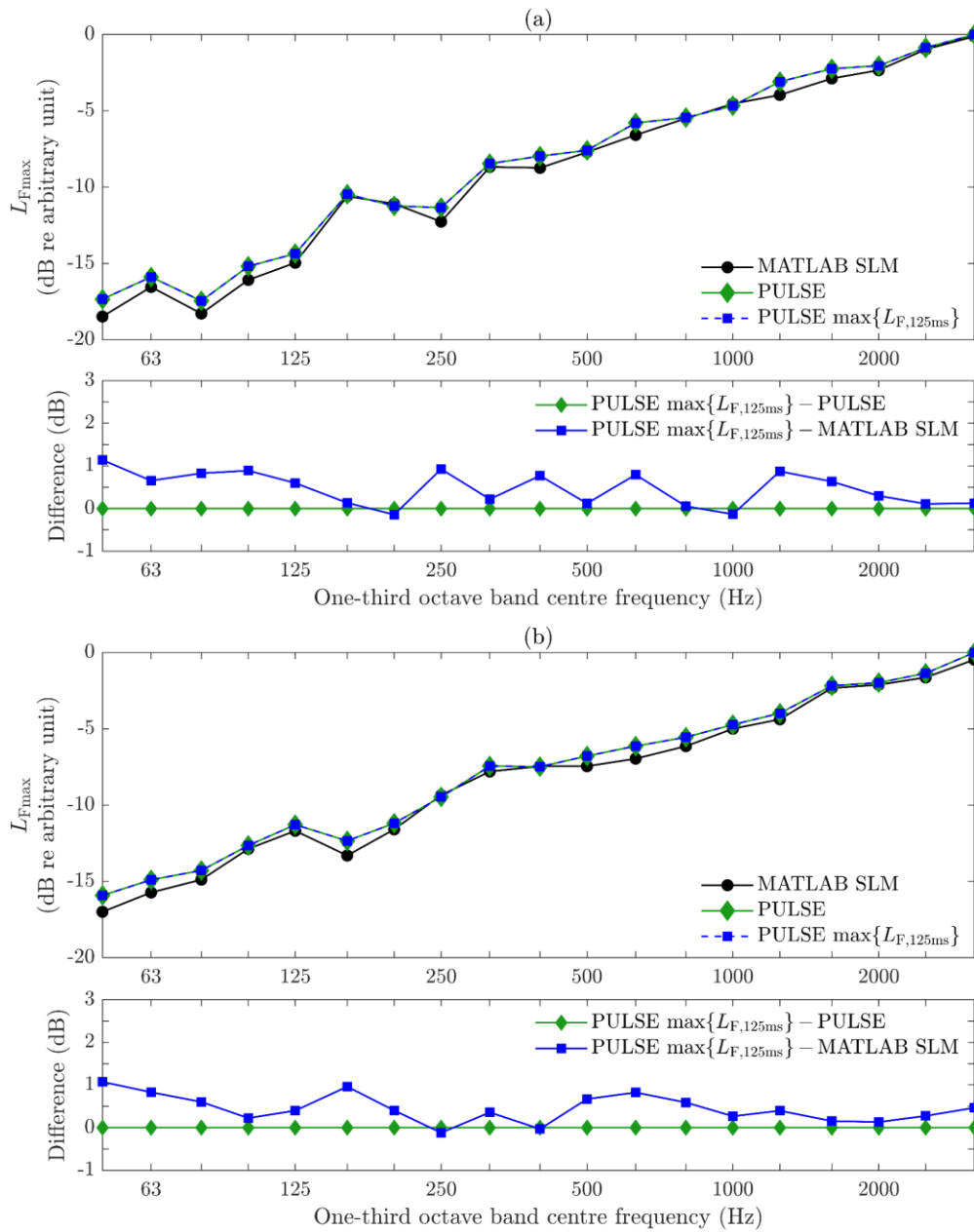


Figure 3-14. Comparison of L_{Fmax} levels from the MATLAB SLM, $\max\{L_{F,125ms}\}$ and L_{Fmax} levels from PULSE (upper graph) and the difference between $\max\{L_{F,125ms}\}$ levels from PULSE and L_{Fmax} levels from the MATLAB SLM and PULSE (lower graph) using (a) a 500 ms ramp with a 40 dB ramp level and (b) a 5 s ramp with a 40 dB ramp level.

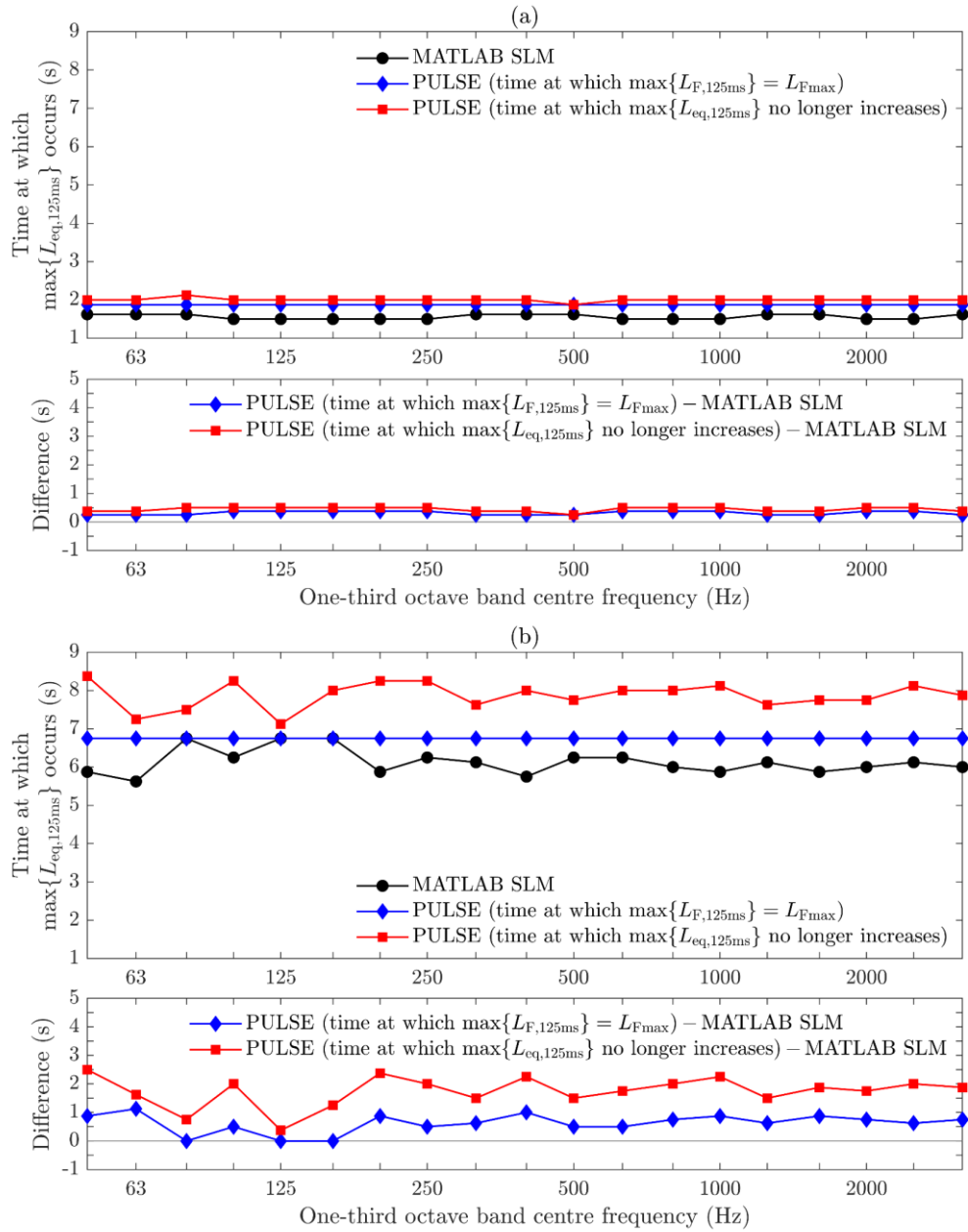


Figure 3-15. Comparison of the time at which $\max\{L_{eq,125ms}\}$ occurs with the MATLAB SLM and PULSE using (a) a 500 ms ramp with a 40 dB ramp level and (b) a 5 s ramp with a 40 dB ramp level.

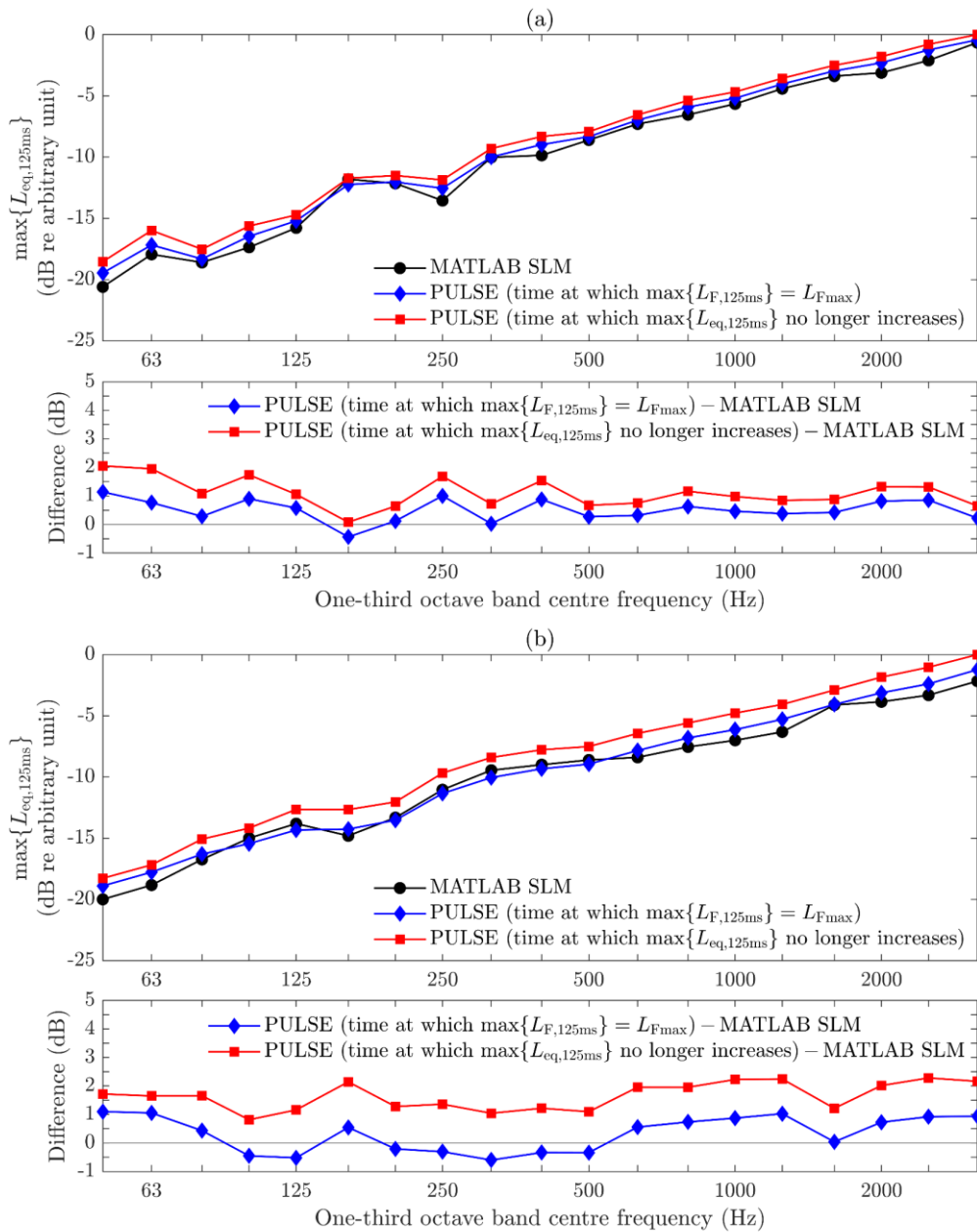


Figure 3-16. Comparison of $\max\{L_{eq,125ms}\}$ levels from the MATLAB SLM and PULSE (upper graph) and the difference between $\max\{L_{eq,125ms}\}$ levels from PULSE and the MATLAB SLM (lower graph) using (a) a 500 ms ramp and 40 dB ramp level and (b) a 5 s ramp and 40 dB ramp level.

In conclusion, determining $\max\{L_{F,125\text{ms}}\}$ and $\max\{L_{\text{eq},125\text{ms}}\}$ levels from PULSE in the time period up to the point at which $L_{F\text{max}} = \max\{L_{F,125\text{ms}}\}$ gives good agreement with $L_{F\text{max}}$ and $\max\{L_{\text{eq},125\text{ms}}\}$ levels obtained from the MATLAB SLM. From PULSE, the comparison of $L_{F\text{max}}$ and $\max\{L_{F,125\text{ms}}\}$ with a difference of 0 dB resulted in three additional 125 ms time slices for the 500 ms ramp and six additional 125 ms time slices for the 5 s ramp in the unfiltered input signal. In this situation, $L_{F\text{max}}$ and $\max\{L_{\text{eq},125\text{ms}}\}$ in one-third octave frequency bands from PULSE led to an absolute-valued offset ranging from 0.4 to 1.1 dB for the 500 ms ramp and 0.6 to 1.1 dB for the 5 s ramp compared to the MATLAB SLM between 50 dB and 3.15 kHz. In addition, the selection of $\max\{L_{\text{eq},125\text{ms}}\}$ to the time limit at which $\max\{L_{\text{eq},125\text{ms}}\}$ no longer increases is less suitable since the offset ascends to those from the MATLAB SLM. Note that when comparing the MATLAB SLM and PULSE, the 25 - 40 Hz and 4 - 16 kHz frequency bands gave results that were similar to the 50 Hz - 3.15 kHz frequency bands.

For the sound pressure signal in the field situation, $L_{AF\text{max}}$ was determined by the B&K PULSE analyser with exponential averaging using the time constant Fast (τ), a specified maximum hold time using the length of the wav files with five additional seconds for sufficient time stopping the measurement and A-weighting. The $L_{AF\text{max}}$ measurements were performed using a high-pass filter above 20 Hz and a low-pass filter below 6.4 kHz. The time-varying signal from the wav file was used as the trigger to onset the measurement analyser. Note that the data were saved as $L_{AF\text{max}}$ and simultaneously stored as consecutive 125 ms time slices to the multi-buffer; these are referred to as $L_{AF,125\text{ms}}$, for which the $\max\{L_{AF,125\text{ms}}\}$ estimate is carried out according to the description above for the identification of $\max\{L_{F,125\text{ms}}\}$ at the time at which $L_{F\text{max}} = \max\{L_{F,125\text{ms}}\}$.

Figure 3-17 shows $L_{AF,125ms}$ for the 500 ms and 5 s ramp durations with a 40 dB ramp level where the black vertical line indicates the time at which the peak in the ramp occurs, and the blue vertical line indicates the time at which $\max\{L_{AF,125ms}\} = L_{AFmax}$. Both $\max\{L_{AF,125ms}\}$ and $\max\{L_{F,125ms}\}$ reached a plateau in all one-third octave bands at the time at which the peak in the ramp occurs and three additional 125 ms time slices for the 500 ms ramp (Figure 3-17a) and six additional 125 ms time slices for the 5 s ramp (Figure 3-17b) in the unfiltered input signal. In the time between 0 and 1 s, it is possible to see the 1 s of steady noise, which reaches the plateau after a short delay of ≈ 0.5 s.

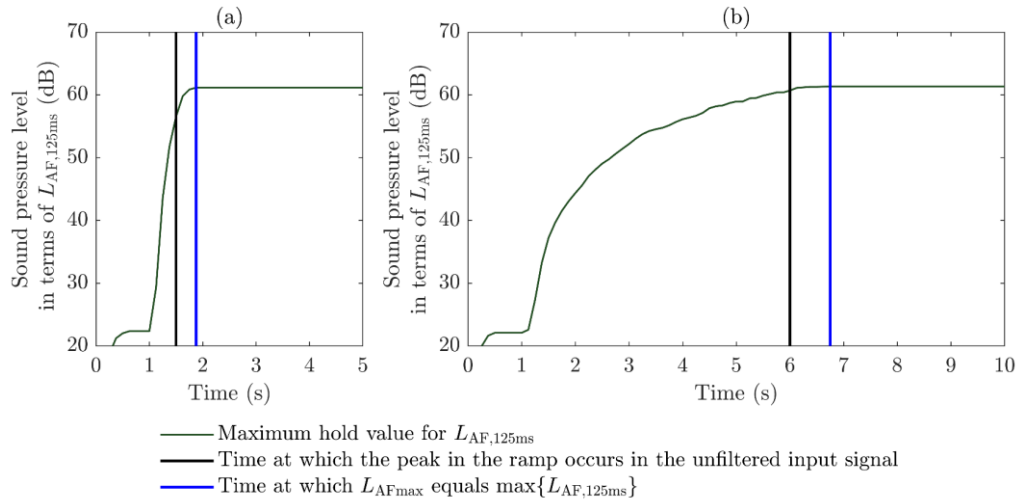


Figure 3-17. PULSE measurements stored as consecutive 125 ms time slices in multi-buffers for pressure levels measured in the field situation using $\max\{L_{AF,125ms}\}$ levels for (a) a 500 ms ramp with a 40 dB ramp level and (b) a 5 s ramp with a 40 dB ramp level.

3.4 Material parameters of the reception plate

FEM modelling of the reception plate required material properties to ensure the accuracy of the model. The measurement procedures for material parameters of the concrete reception plate are described in Section 3.4.1 and for the viscoelastic material Sylodamp HD 30 [143] in Section 3.4.2.

3.4.1 Concrete plate

The material properties of the concrete plate that were needed were the modulus of elasticity and the total loss factor. The measurements to determine these properties are described in Sections 3.4.1.1 and 3.4.1.2 respectively.

3.4.1.1 Young's modulus

As a measure of stiffness or resistance to elastic deformation, Young's modulus of the concrete reception plate was determined from quasi-longitudinal phase velocity measurements. Quasi-longitudinal waves were excited by an impact hammer (B&K Type 8207) with two accelerometers (B&K Type 4533-B-001) to record the velocity-time response using the data acquisition system (B&K LAN-XI frontend frame Type 3660-C-100 with modules Type 3160-A-042 and Type 3160-A-0460) and analysis software (B&K PULSE LabShop).

The two accelerometers were aligned on the plate surface with a separation distance of at least 1 m. Eight measurements were made with four across the length and four across the width of the plate. Figure 3-18 shows (a) a section of the measurement set-up and (b) an example of the measurement results. The quasi-longitudinal wave phase velocity was calculated using the ratio of the distance between the initial rising slope of the velocity-time from two simultaneously measured responses – this avoids errors due to reflections from the plate boundaries or other wave types [71, 161]. Hence, Young's modulus can be determined by

$$E = c_{L,p} \rho (1 - \nu^2) = \frac{d}{\Delta t} \rho (1 - \nu^2) \quad (3.15)$$

where d and Δt are the distance and the velocity-time propagation difference between both accelerometers respectively.

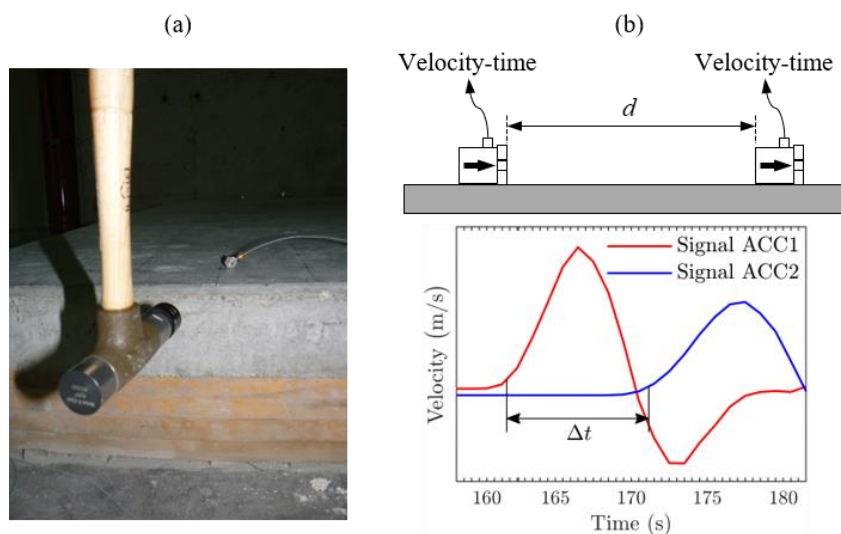


Figure 3-18. Measurement set-up for the quasi-longitudinal phase velocity of the horizontal reception plate (arrow on accelerometers indicate the axis of maximum sensitivity).

3.4.1.2 Damping

For measurements according to EN 15657 [35], the total loss factor of the reception plate is required to calculate the power input (see Eq. (2.76)). This is also required for the validation of the FEM model and numerical investigations in Chapters 4 and 5. The total loss factor of the reception plate as a measure of mechanical damping can be obtained from EMA, mobility and structural reverberation time measurements. These three different methods were experimentally investigated to assess the reception plate damping.

From the EMA data, the total loss factors of the reception plate were estimated using the fraction of critical damping ratio for each mode from the modal analysis (refer back to Section 3.3.3). Using Eq. (3.7), the loss factor was calculated as twice the damping ratio according to Eq. (2.41).

The total loss factor was also calculated from the modal peaks in the driving-point mobility measurements on the reception plate (refer back to Section 2.2.5) from the half-power bandwidth – see Eq. (2.41) in Section 2.3.2.2.

Structural reverberation time measurements according to EN ISO 10848-1 [78] are often used to determine the total loss factors in one-third octave bands,

which is based on a room acoustic measurement technique (EN ISO 3382 [153, 154]). This measurement method is also recommended in EN 15657 [35] as the preferred method to determine the loss factors of the reception plate. The measurements used two accelerometers (B&K Type 4383-V with charge amplifier B&K Type 2635). Point mechanical excitation was applied using an electrodynamic inertial shaker (DataPhysics Type IV40) connected to a power amplifier (DataPhysics Type GW-PA30E) in conjunction with the dual-channel real-time analysis system (Norsonic Type Nor840). The analyser used a Maximum Length Sequence (MLS) which generated a slowly built-up and rapidly decaying impulse response that is filtered in one-third octave bands and backward integrated using Schroeder's integration method [162]. MLS was necessary to enable signal processing that would allow accurate measurement of short reverberation times, particularly at low frequencies. To reduce the distortion error caused by bandpass filters in the decay curves to a minimum, reverse-filter (or time-reversed filter) analysis was used with the requirement that $BT > 4$. Backwards integration was employed with the impulse response sent backwards through the bandpass filters so that the distortion effect of the filter time delay on the acoustic decay curve was negligible [77]. However, the experiments used three different excitation positions, each with randomly distributed eight response positions, to ensure a reasonable arithmetic average for a representative loss factor estimate that is important for statistical relevance. (Note that EN ISO 10848-1 [78] requires at least three excitation positions and at least three response positions for structural reverberation time measurements.) The total loss factor was calculated according to Eq. (2.60) (see Section 2.4.1.2) using the structural reverberation time, $T_{s,X}$, with a decay rate of X dB. The choice of a decay rate of X dB is important to avoid estimation errors in structural reverberation times that can occur due to flat slope decays caused by highly damped structures and/or double slope decays caused by returning energy from coupled structures.

To determine the reverberant energy of the isolated reception plate to decay from the excited vibration level, this thesis uses structural reverberation times of T_5 below 100 Hz and T_{20} at and above 100 Hz. A structural reverberation time of T_5 was used at low frequencies because the reception plate exhibits highly damped resonance peaks that have amplitudes with flat increasing/decreasing slopes and therefore a short decay level. This led to the situation, a structural reverberation time decay level of T_{20} was not feasible, particularly at the resonance peaks amplitudes of rigid body modes. Note that shorter decay rates are also used for coupled reception plates, as the energy is turning back from connected structural components, which can occur from the low-frequency range to far into the mid-frequency range. This issue had to be considered for the concrete floor in the building-like situation where the estimation procedure of short structural reverberation times was applied that follows the approach described by Robinson and Hopkins [44, 45].

3.4.2 Viscoelastic material

The measurement methodology of the viscoelastic material properties with regard to the dynamic stiffness and from this calculated damping is presented in the following Sections 3.4.2.1 and 3.4.2.2 respectively.

3.4.2.1 Dynamic stiffness

The dynamic stiffness per unit area, s' , of the viscoelastic material as a component of the reception plate can be obtained from an experimental approach of the mass-spring resonance. According to EN 29052-1 [163], a cube with an edge length of 100 mm was placed on the top of the test specimen of the viscoelastic material Sylodamp HD 30 [143] for the static load having a mass of 2.45 kg to simulate a similar representative load of the reception plate. The viscoelastic material sample was also formed into a cube with a total height of 100 mm, which comprised a total of eight layers with a thickness of 12.5 mm

equivalent to the thickness of viscoelastic material around the reception plate boundaries (refer back to Section 3.2.1).

The static load (concrete cube) was excited with a broadband noise from an electrodynamic inertial shaker (DataPhysics Type IV40) controlled by a power amplifier (DataPhysics Type GW-PA30E) in conjunction with the data acquisition system (B&K LAN-XI frontend frame Type 3660-C-100 with a module Type 3160-A-042) and analysis software (B&K PULSE LabShop). The force injected by the shaker was recorded with a force transducer (Kistler Type 9311B) in the top centre of the concrete cube, where the resulting velocity response was measured with an accelerometer (B&K Type 4533-B-001) placed in the immediate vicinity of the drive point to obtain the driving-point mobility according to Eq. (2.19) in terms of the resonance frequency from the viscoelastic material. FFT analysis was carried out using 200 frequency lines, a frequency span of 200 Hz, a frequency resolution of 1 Hz, a Hanning window with 66.67% overlap, a linear averaging of 58 averages equivalent to a time of 20 s and a 7 Hz high-pass filter. Figure 3-19 shows the measurement with the load cube on top of the test specimen of the viscoelastic material that was placed on a concrete cube to determine the dynamic stiffness. Note that the cube test rig rests on springs and has a resonance frequency ≈ 3.3 Hz.

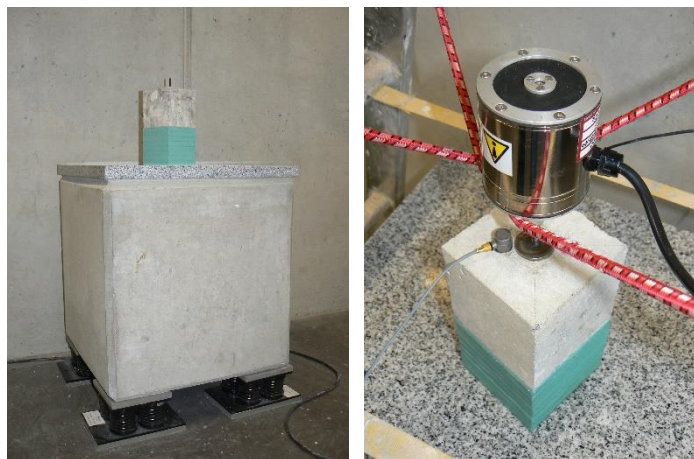


Figure 3-19. Measurement set-up for the dynamic stiffness of the viscoelastic material.

Since the measurement of the resonance frequency and thus the dynamic stiffness showed a dependence on the excitation force, three different excitation force strengths were used to extrapolate the resonance frequency to a force of 0 N by linear regression according to EN 29052-1 [163]. From the extrapolated resonance frequency in amplitude and phase from the driving-point mobility (see Figure 3-20), the apparent dynamic stiffness is derived from the maximum system response at the undamped resonance frequency, $f_0 \approx 53$ Hz, by

$$s' = 4\pi^2 \rho_s f_0^2 \quad (3.16)$$

Thus resulted in a value of $s' = 27.1$ MN/m³, which can be related to the spring stiffness using

$$k = 4\pi^2 m f_0^2 \quad (3.17)$$

with

$$f_0 = \frac{\omega_0}{2\pi} = \frac{1}{2\pi} \sqrt{\frac{k}{m}} \quad (3.18)$$

where m is the suspended mass of the static load applied (concrete cube). This then led to a value of $k = 271003$ N/m.

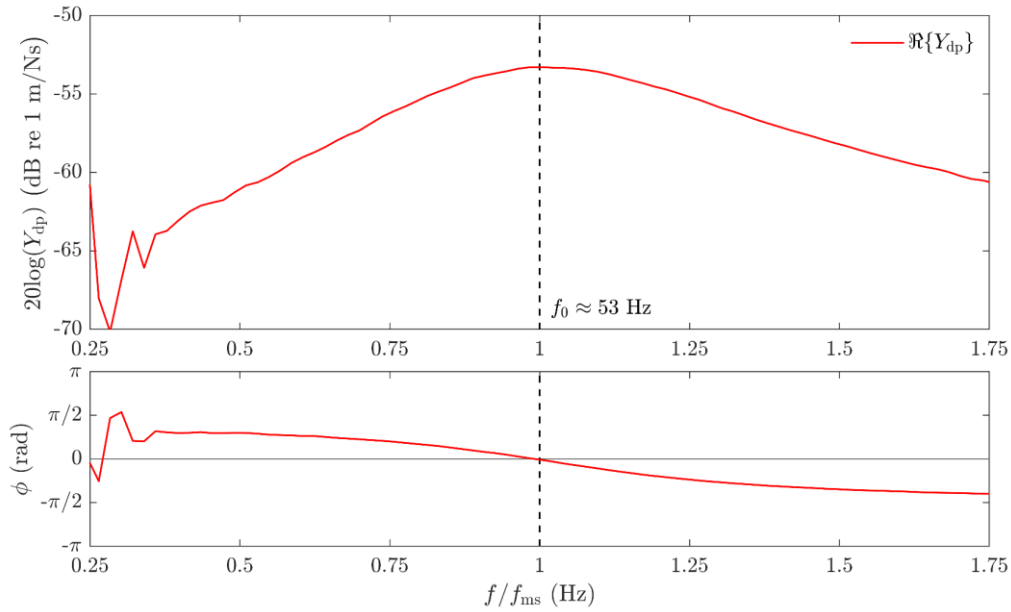


Figure 3-20. Driving-point mobility of an SDOF system using a concrete cube and viscoelastic material at resonance to quantify the dynamic stiffness from experiments.

3.4.2.2 Damping

Damping indicates that the stiffness and inertia forces become equal, which can be obtained from dynamic stiffness measurements at the peak value of the resonance frequency (refer back to Figure 3-20) using the half-power bandwidth method (see Eq. (2.41)). Thus, the internal loss factor of the viscoelastic material resulted in a value of $\eta_{\text{int}} = 0.61$. For the reason that the damping effects of the viscoelastic material were numerically modelled by spring-dashpot elements (refer back to Section 2.3.2.2), it is necessary to assess the damping constant, R . Recalling that the loss factor of the viscoelastic material is a measure of structural damping (see Section 2.3.2.2) and which can therefore be related to the damping constant as follows

$$R = \eta \omega_0 m = \eta \sqrt{km} \quad (3.19)$$

which was estimated with $R = 497$ Ns/m. Note that the damping constant can be replaced by the equivalent viscous damping coefficient, which is also a function of structural damping (see Eq. (2.40)) using

$$c_{\text{eq}} = \frac{\eta k}{\omega_0} = \eta \sqrt{km} \quad (3.20)$$

3.5 Summary

This chapter described the test facilities in relation to the reception plate test rig for structure-borne sound source characterisation and the floor test facility. It also described the measurement equipment with exciters/sensors and the experiments such as EMA, driving-point mobility, radiation efficiency, spatial variation in plate velocity and material properties in terms of dynamic stiffness and damping. In addition, signal processing was described and investigated for time-varying signals. These measurements provide a basis to validate the FEM reception plate model in Chapter 4 used for numerical experiments in Chapter 5 and to determine time-varying vibration and sound transmission using SEA predictions in the building-like situation for heavyweight buildings introduced in Chapters 6 and 7.

4 Reception plate: Experimental validation of FEM models

4.1 Introduction

This chapter describes the FEM modelling of the horizontal heavyweight reception plate when supported by highly damped viscoelastic material around the plate edges in Section 4.2. In Sections 4.3 and 4.4, the FEM reception plate model is subjected to verification and validation to ensure confidence in the numerical results respectively.

The validated FEM model of the reception plate is then used for numerical experiments with regard to the spatial variation in plate velocities discussed in Section 4.5. Since prediction models according to SEA or the SEA-based standard EN 15657 [35] for the reception plate method would typically be expected only to be useful (or valid) where there are bending modes, consideration is given to its use in the low-frequency range where there are only rigid body modes. For this reason, the role of rigid body modes is discussed in more detail in Section 4.6 to assess the characterisation capability of the reception plate at low frequencies.

4.2 FEM modelling

FEM modelling uses the Abaqus simulation software package to create the heavyweight reception plate with highly damped supports. A validated FEM model is required to carry out numerical experiments and predict the required field variables for the injected power and the reception plate power.

Figure 4-1 shows three different FEM models of isolated reception plates that are considered. The first FEM model with free boundaries represents an idealised simplification of the horizontal reception plate – see Figure 4-1a. The second FEM model with partially restricted boundaries corresponds to the experimental set-up of the horizontal reception plate, which rests on viscoelastic material at nodes along the plate edges and is referred to as partial coverage with viscoelastic material – see Figure 4-1b. The third FEM model is a reception plate that rests on the same area of viscoelastic material as the plate area; hence, it is referred to as full coverage with viscoelastic material – see Figure 4-1c. All models assume structural vibrations *in vacuo* (i.e. no sound radiation is considered in the model).

The numerical modelling of the concrete plate was carried out using the triangular thin-facet shell element STRI3, which follows Kirchhoff-Love thin plate theory [119, 120] (refer back to Section 2.3.2.1). The discretisation process resulted in a mesh size with an element side length of 50 mm × 50 mm × 70.7 mm, which corresponds to less than eight elements per wavelength and is compatible with an upper-frequency limit of 2 kHz (refer back to Section 2.3.2.5). The energy dissipated by the concrete was specified as linear structural damping with the direct data input entry using *DAMPING, STRUCTURAL with regard to the internal loss factor, $\eta_{\text{int}} = 2\zeta$, (refer back to Section 2.3.2.2). In addition, the material properties of the concrete plate were also considered with the density, ρ , Young's modulus, E , and Poisson's ratio, ν , as defined in Section 3.2.1.

The viscoelastic material was considered as an extension of linear structural damping and therefore implemented by spring-dashpot elements to a fictive ground plane using connected in parallel *SPRING1 and *DASHPOT1 with two DOFs that were allocated to global coordinates due to the fixed acting direction (refer back to Section 2.3.2.2). These spring-dashpot elements were modelled at the corresponding nodes of the STRI3 elements underneath the reception plate according to the experimental set-up (see Figure 4-1b for partial coverage and Figure 4-1c for full coverage). For the spring-dashpot systems connected to nodes underneath the plate in series, the experimentally determined spring stiffness, $k = 271003 \text{ N/m}$, and damping constant or equivalent viscous damping coefficient, $R = c_{\text{eq}} = 497 \text{ Ns/m}$, from Section 3.4.2 have to be altered depending on the coverage area with viscoelastic material and the resulting number of nodes; otherwise, the numerical reception plate would be severely overdamped.

An applicable correction factor was devised that multiplies the spring stiffness and the damping constant for the required combined coverage area and number of nodes. The correction factor comprises a first left-sided term for the full coverage area and belonging nodes and the multiplication of a second left-sided term that enhances the equation to the partial coverage area with associated node combination on the right-sided term. Thus, the equation is written as

$$\frac{S_{\text{tot}}}{S_{\text{LP}}N_{\text{tot}}} \cdot \frac{N_{\text{V}}S_{\text{V}}}{N_{\text{tot}}S_{\text{tot}}} = \frac{N_{\text{V}}S_{\text{V}}}{N_{\text{tot}}^2S_{\text{LP}}} \quad (4.1)$$

where N_{V} and N_{tot} are the number of nodes for the viscoelastic material and the entire reception plate respectively, S_{V} and S_{tot} are the areas for the viscoelastic material and the entire reception plate respectively and S_{LP} is the load plate area that was used as static plate load in form of a concrete cube with $S_{\text{LP}} = 0.01 \text{ m}^2$ from Section 3.4.2.1.

The FEM plate model with the partial coverage uses $N_v = 1264$ and $N_{tot} = 2337$, and the plate areas $S_v = 2.73 \text{ m}^2$ and $S_v = 5.6 \text{ m}^2$. Finally, the reassessment gave a spring stiffness of $k = 17123 \text{ N/m}$ and a damping constant of $R = 31.42 \text{ Ns/m}$. The modelling approach using Eq. (4.1) is validated in Appendix A.

FE-based modal analysis is obtained using real and complex eigenvalue analysis to predict real- and complex-valued modal parameters respectively (refer back to Sections 2.3.1.1 and 2.3.2.6). The real eigenvalue analysis is used for a reception plate with free boundaries and a reception plate of the experimental set-up using partial coverage with viscoelastic material. For the latter FEM model, the complex modes are also assessed because this plate incorporates the partially restrained boundaries due to the unevenly distributed spring-dashpot elements (refer back to Section 2.3.1.1). This aids comparison of the influence of proportional and non-proportional damping. If real eigenvalue analysis was carried out in FEM, then the complex-valued normal modes from EMA were converted into real-valued normal modes using the algorithm of complex-to-real conversion with the simple method [125] (refer back to Section 3.3.3.2). The damping of frequency modes is predicted with a resolution of 0.001 Hz using the half-power bandwidth method to ensure sufficient accuracy of the results, and the vibration levels across the plate surface are obtained with a resolution of 1 Hz.

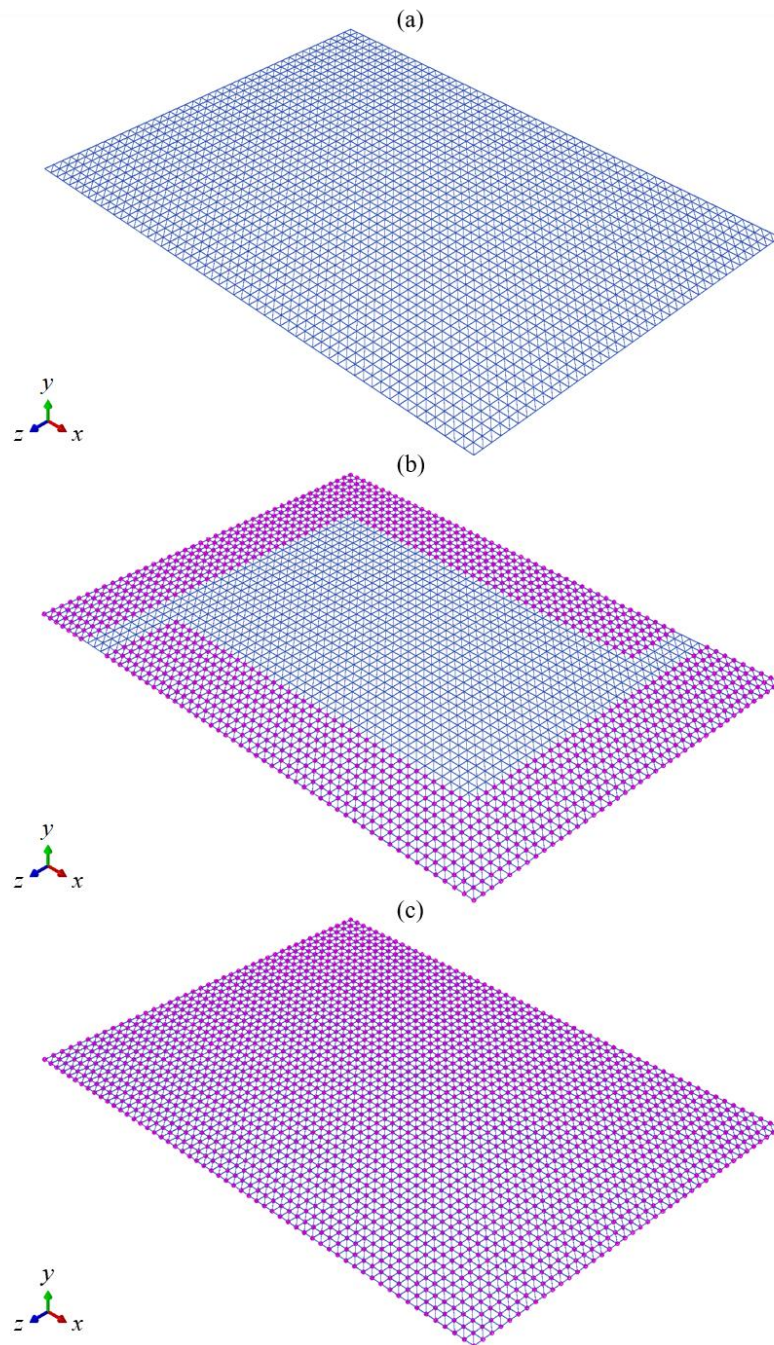


Figure 4-1. FEM models of a reception plate (a) with free boundaries and using (b) partial coverage with viscoelastic material and (c) full coverage with viscoelastic material.

4.3 Verification of the FEM code and calculation

To verify the FEM approach for the implementation of spring-dashpot elements, the driving-point mobility of a lumped mass-spring-dashpot system to evaluate the dynamic stiffness of the viscoelastic material (described in Section 3.4.2.1) was numerically determined for comparison with analytical calculations according to Eq. (2.22) from Section 2.2.5.

Figure 4-2 shows this FEM code verification of a lumped mass-spring-dashpot system concerning the analytical calculations and the numerical approximation of the driving-point mobility derived from the experimentally determined spring stiffness, $k = 271003 \text{ N/m}$, and damping constant, $R = 497 \text{ Ns/m}$, (or alternative the equivalent viscous damping coefficient, $c_{\text{eq}} = 497 \text{ Ns/m}$) at resonance. As supplementary information, the measured driving-point mobility is also included in Figure 4-2.

From Figure 4-2, the results generated by the numerical and analytical calculations of the driving-point mobility produces an identical order of magnitude. Thus, the required accuracy for this type of spring-dashpot element using *SPRING1 and *DASHPOT1 (refer back to Section 2.3.2.2) makes it reasonable to use this approach in order to incorporate the viscoelastic material into the FEM reception plate model. (NB In FEM, the viscoelastic material was also determined by the alternative of local spring- and dashpot-like axial connectors that gave the same result as the global spring-dashpot elements.) However, the obtained driving-point mobility from the dynamic stiffness measurements (see Section 3.4.2.1) also closely matches the FEM and analytical results with a difference of less than 1 dB at resonance.

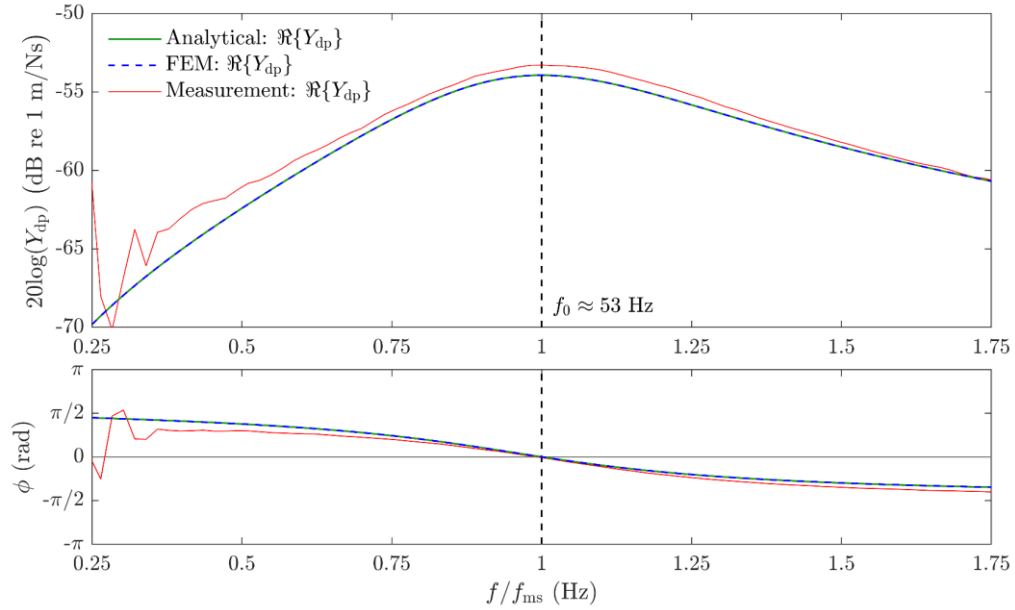


Figure 4-2. Verification of FEM using the driving-point mobility of a lumped mass-spring-dashpot system compared to analytical results and supplemented by experimental results. Measured data is from the dynamic stiffness measurement for the viscoelastic material (taken from Figure 3-20).

The next verification step was to consider the whole body mode frequency of the reception plate (partial coverage with viscoelastic material) and compare the eigenfrequency from FEM against the analytical calculation. With that step, the reliability of Eq. (4.1) is checked for the distribution of connected in parallel grounded spring-dashpot elements in series modelled underneath the plate nodes for a reception plate using partial coverage with viscoelastic material (see Figure 4-1b). Equation (3.18) is used for the analytical calculation to assess the eigenfrequency of the whole body mode in which the spring stiffness is additionally multiplied by the number of nodes where the viscoelastic material is applied. This results in the following modified equation of the resonance frequency, f_0 , using

$$f_0 = \frac{1}{2\pi} \sqrt{\frac{kN_v}{m}} \quad (4.2)$$

where m represents the mass of the reception plate and k is the corresponding spring stiffness in relation to the number of nodes for the viscoelastic material, N_v , as they are used according to Eq. (4.1).

The numerical calculations consider the two cases of proportional damping (real modes) and non-proportional damping (complex modes) – refer back to Section 2.3.1.1, recalling that the latter can occur by incorporating unevenly distributed spring-dashpot elements. As indicated in Table 4-1, the error between FEM and analytical calculations using $N_v = 1264$ shows a fairly close agreement with a difference of 2.9% for the real-valued normal frequency mode. Whereas in the case of non-proportional damping, the error slightly increases to 3.4% for the complex solution of the normal frequency mode. Because the eigenfrequency from the complex-valued normal mode is nominally identical to that from the real-valued normal mode, it seems reasonable to compare real-valued eigenfrequencies from the analytical and FEM model.

Table 4-1. Reception plate using partial coverage with viscoelastic material: Verification of FEM eigenfrequencies for the whole body mode through comparison with the analytical value.

Set-up	Eigenfrequency			Error	
	Analytical	FEM (real)	FEM (complex)	Analytical vs FEM (real)	Analytical vs FEM (complex)
	f_0 (Hz)	f_A (Hz)	f_A (Hz)	Δf (%)	Δf (%)
PCVM $N_v = 1264$	20.6	20.0	19.9	2.9	3.4

PCVM: Partial Coverage with Viscoelastic Material

4.4 Validation of the FEM model with experiments

This section focuses on the validation of the FEM reception plate model that incorporates the viscoelastic material. Section 4.4.1 discusses the correlation between the numerical and experimental eigenfrequencies and mode shapes, and Sections 4.4.2 and 4.4.3 address the comparison between numerical and experimental plate damping and driving-point mobility respectively.

4.4.1 Eigenfrequencies and corresponding mode shapes

The NFD (Eq. (3.9)), the mode count and the MAC (Eq. (3.10)) are used to assess the correlation between frequencies and corresponding mode shapes from FEM and EMA. Below the 31.5 Hz band, EMA and FEM results show that the first three eigenfrequencies extracted are rigid body motions which begin with one whole body mode followed by two rocking modes. The subsequent higher modes are bending modes above the 40 Hz band. Note that the eigenfrequencies and mode shapes from the FEM model of the experimental set-up of the reception plate using partial coverage with viscoelastic material were solved by real- and complex-valued eigenvalue analysis (refer back to Sections 2.3.1.1 and 2.3.2.6).

Figure 4-3 compares the eigenfrequencies of FEM from real-valued normal modes with those of EMA in a frequency range from 20 to 250 Hz, where the associated eigenfrequencies and resulting error from NFD values are listed in Table 4-2. The eigenfrequencies of complex-valued normal modes from FEM were found to be within less than 1.2% and 0.2% of the eigenfrequencies of real-valued normal modes for rigid body modes and bending modes respectively. Thus, proportional and non-proportional damping does not give exactly the same eigenfrequencies. However, the differences between the frequency pairs are typically small as noted by Ewins [125], and this occurred in these experiments too. For this reason, the eigenfrequencies from complex-valued normal modes are not considered further in this section.

For the FEM model with free boundaries, there is poor agreement with EMA for the first three eigenfrequencies, which are the whole body and rocking modes with close to zero frequency as a result of elements having zero or almost zero stiffness. In contrast, the FEM plate model using partial coverage with viscoelastic material results in a non-zero stiffness matrix. Hence, the rigid body modes are shifted to a non-zero frequency. The rigid body modes occur with one whole body mode at the plate suspension resonance and two rocking modes at the next higher frequencies. This indicates that a FEM model of a plate with free boundaries is not suitable for low frequencies to represent the modal response of the reception plate with highly damped supports around the edges. Conversely, the FEM model of the experimental set-up using partial coverage with viscoelastic material shows close agreement for the rigid body modes and bending modes that occur between 20 and 250 Hz.

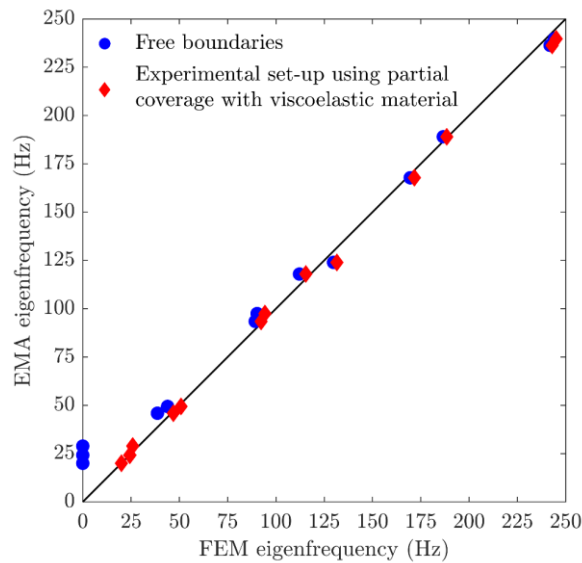


Figure 4-3. Reception plate using partial coverage with viscoelastic material: Comparison of eigenfrequencies from EMA and FEM for a reception plate with idealised free boundaries and from EMA and FEM for the reception plate of the experimental set-up using partial coverage with viscoelastic material.

Table 4-2. Reception plate using partial coverage with viscoelastic material: Eigenfrequencies from EMA and FEM for a reception plate with idealised free boundaries and from EMA and FEM for the reception plate of the experimental set-up using partial coverage with viscoelastic material.

Mode	Eigenfrequencies			Error	
	EMA: PCVM	FEM: FBC	FEM: PCVM	EMA: PCVM vs FEM: FCB	EMA: PCVM vs FEM: PCVM
	f_X (Hz)	f_A (Hz)	f_A (Hz)	NFD (%)	NFD (%)
1	20.1	3.8E-04	20.0	100	0.6
2	24.2	4.1E-04	24.3	100	0.4
3	28.9	4.5E-04	25.8	100	10.7
4	45.9	38.7	46.9	15.8	2.2
5	49.4	43.9	50.8	11.1	2.9
6	93.5	89.3	92.4	4.5	1.2
7	97.5	90.3	94.3	7.4	3.3
8	118.0	112.2	115.5	4.9	2.1
9	124.0	129.8	131.5	4.7	6.1
10	167.8	169.5	171.7	1.0	2.3
11	189.0	186.6	188.4	1.3	0.3
12	236.3	241.9	243.0	2.4	2.8
13	239.7	244.2	245.1	1.9	2.3

FBC: Free Boundary Conditions

PCVM: Partial Coverage with Viscoelastic Material

Figure 4-4 shows the mode count of the experimental set-up from FEM using partial coverage with viscoelastic material and EMA in one-third octave bands. The majority of the counted FEM modes are nearly in the same order of magnitude as the registered mode count from EMA. An exception concerns the two rocking modes that fall only into the 25 Hz band for FEM, whereas those rocking modes from EMA are found in the 25 and 31.5 Hz bands. There are no modes measured and predicted in the 40, 63 and 80 Hz bands.

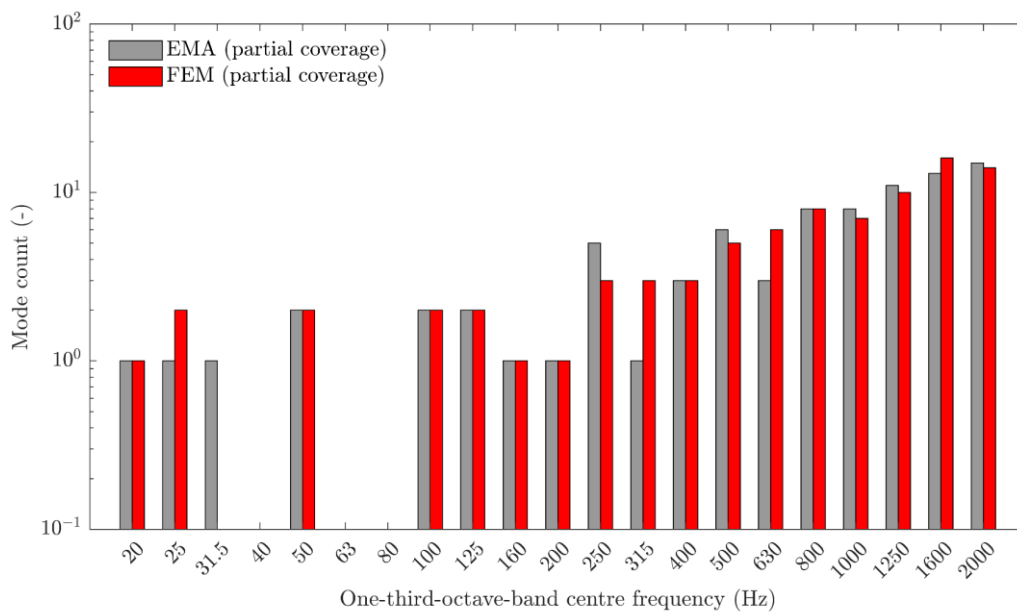
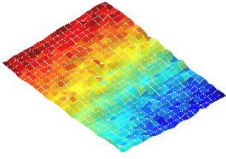
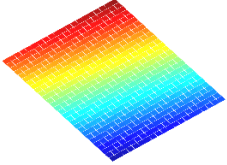
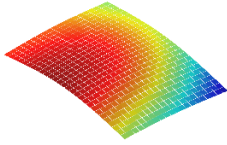
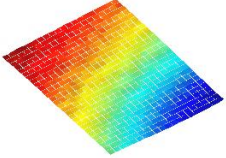
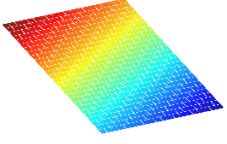
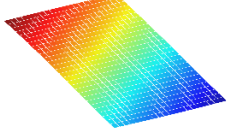
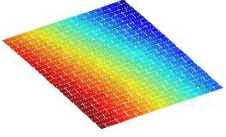
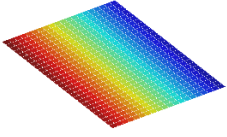
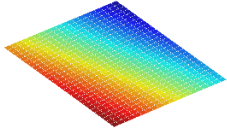
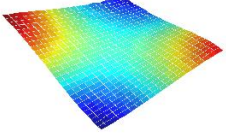
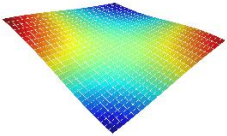
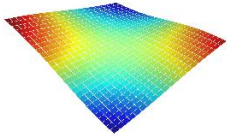
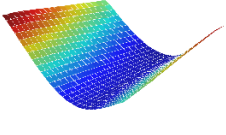
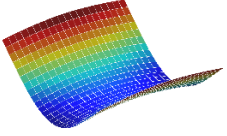
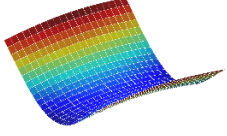
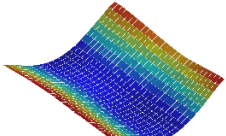
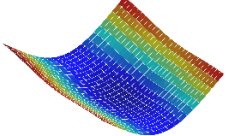
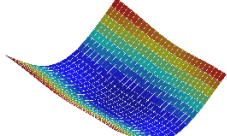


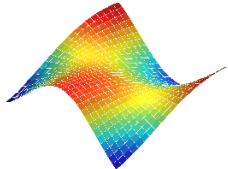
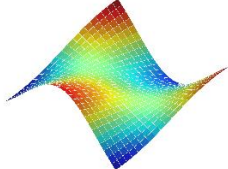
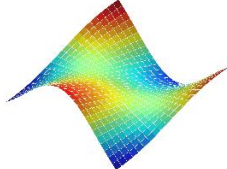
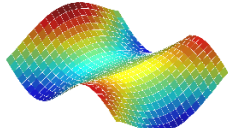
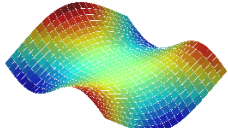
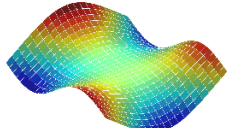
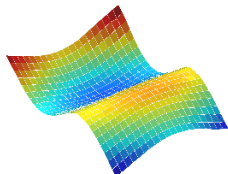
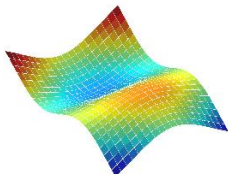
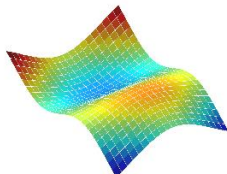
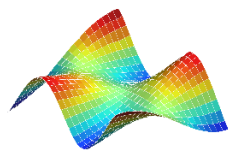
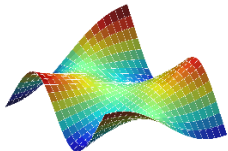
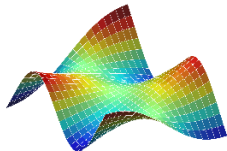
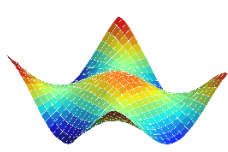
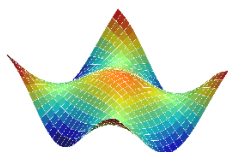
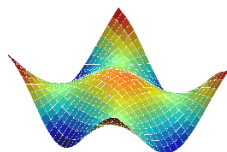
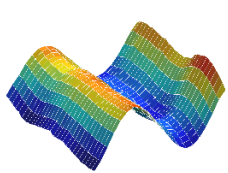
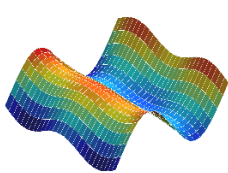
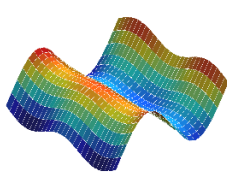
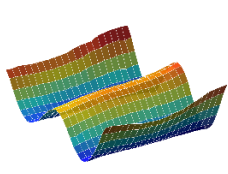
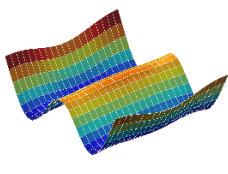
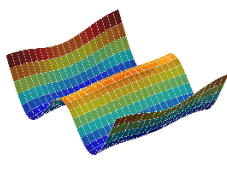
Figure 4-4. Reception plate using partial coverage with viscoelastic material: Mode count in one-third octave bands from EMA and FEM eigenfrequencies.

Table 4-3 shows the 13 mode shapes from EMA and FEM models of the reception plate with free boundaries and the experimental set-up of the reception plate using partial coverage with viscoelastic material. While complex mode shapes can be used to animate the response, the real part contains the standing wave pattern and the imaginary part represents the energy flux; hence, for a tabulated comparison, only the real-valued normal mode shapes are displayed in Table 4-3.

Table 4-3. Reception plate using partial coverage with viscoelastic material: Standing wave pattern from EMA and FEM models for a reception plate with idealised free boundaries and the reception plate of the experimental set-up using partial coverage with viscoelastic material.

Mode	Mode shapes		
	EMA: PCVM	FEM: FBC	FEM: PCVM
1			
2			
3			
4			
5			
6			

FBC: Free Boundary Conditions
PCVM: Partial Coverage with Viscoelastic Material

Mode shapes			
Mode	EMA: PCVM	FEM: FBC	FEM: PCVM
7			
8			
9			
10			
11			
12			
13			

FBC: Free Boundary Conditions
 PCVM: Partial Coverage with Viscoelastic Material

The MAC values are compared for the linear relationship between the mode shapes up to 250 Hz in order to facilitate a comparison between the two FEM models with EMA. Figure 4-5 and Table 4-4 allow the comparison of MAC for mode pairs from EMA and FEM for plate models (a) with free boundaries having extracted real-valued normal modes, (b and c) using partial coverage with viscoelastic material having extracted real- and complex-valued normal modes respectively. For FEM models that were solved to obtain real-valued normal modes, the EMA complex-valued normal modes are converted into real-valued normal modes using the simple method [125], which involves setting the phase angles to 0° or 180° (refer back to Section 3.3.3.2). While in the case that both EMA and FEM have complex-valued normal modes, the corresponding phase angle is taken into account in the MAC calculation.

For the FEM model of a plate with free boundaries using real-valued normal modes, the first three mode shapes identified as rigid body modes have a weak correlation with EMA. A high correlation is only achieved for this FEM plate model at and above the fourth mode shape where there are bending modes (see Figure 4-5a). In contrast, the linear relationship between mode shapes from EMA and FEM for the experimental set-up using partial coverage with viscoelastic material, regardless of the use of real- or complex-valued normal modes, gives strong correlation for all 13 mode shapes (see Figure 4-5b and c). Note that the differences between the MAC values from real- or complex-FEM modes are within ± 0.01 , except for the second mode (rocking mode) and the twelfth mode (bending mode), for which the differences are 0.06 and 0.05 respectively. Hence, the use of complex-to-real conversion for EMA modes and real modes of FEM is justified due to the small differences in the MAC values.

The experimental validation indicates that the FEM model of the experimental set-up of the reception plate has the viscoelastic supports correctly incorporated in the FEM model. Hence, only the FEM model using partial coverage with viscoelastic material is used for further investigations into the reception plate.

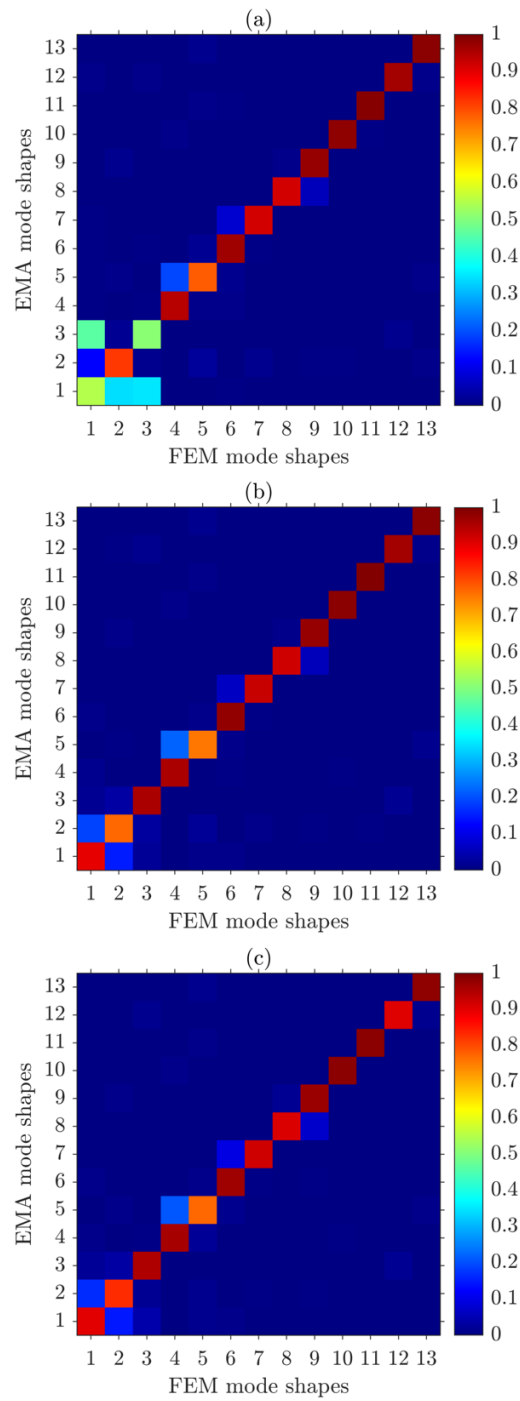


Figure 4-5. Reception plate using partial coverage with viscoelastic material: Comparison of EMA (complex-to-real or complex modes) and FEM eigenfunctions using MAC for (a) a reception plate with idealised free boundaries (real modes), (b) the reception plate of the experimental set-up using partial coverage with viscoelastic material (real modes) and (c) the reception plate of the experimental set-up using partial coverage with viscoelastic material (complex modes).

Table 4-4. Reception plate using partial coverage with viscoelastic material: Comparison of MAC values from EMA (complex-to-real or complex modes) and FEM eigenfunctions using a reception plate with idealised free boundaries (real modes) and the reception plate of the experimental set-up using partial coverage with viscoelastic material (real and complex modes).

Correlation between mode pairs			
Mode	EMA: PCVM (complex-to-real) vs FEM: FCB (real)	EMA: PCVM (complex-to-real) vs FEM: PCVM (real)	EMA: PCVM (complex) vs FEM: PCVM (complex)
	MAC	MAC	MAC
1	0.55	0.90	0.90
2	0.82	0.77	0.83
3	0.51	0.95	0.95
4	0.94	0.95	0.96
5	0.78	0.76	0.77
6	0.97	0.98	0.97
7	0.92	0.93	0.92
8	0.92	0.92	0.91
9	0.97	0.97	0.97
10	0.98	0.99	0.98
11	0.99	0.99	0.99
12	0.96	0.96	0.91
13	0.99	0.99	0.98

FCB: Free Boundary Conditions
PCVM: Partial Coverage with Viscoelastic Material

4.4.2 Damping

This section investigates the damping in three FEM models of the reception plate in Section 4.4.2.1 and the loss factors obtained from FEM and measurements in Section 4.4.2.2.

4.4.2.1 FEM model of the reception plate

Figure 4-6 shows the effect of damping on the driving-point mobility predicted using FEM models for a plate with the internal loss factor of concrete or a combination of the internal loss factor of concrete and the equivalent viscous damping using partial coverage or full coverage with viscoelastic material (refer back to Section 2.2.5). One position is chosen on the reception plate at the coordinate (1.15 m, 0.65 m), for which the driving-point mobility was determined with a frequency resolution of 1 Hz.

The results from Figure 4-6 show that the structural damping used for the internal loss factor of concrete ($\eta_{\text{int}} = 0.005$) for the reception plate with free boundaries has resonance peaks within the envelope of the upper peak limit given by Skudrzyk [164] as $\hat{Y}_{\text{dp}} = 4/(\omega\eta m)$. For this plate with free boundaries and low internal damping, it can be assumed from $\omega_{pq} = \omega_0\sqrt{1-\zeta^2}$ that the damped resonance peaks occur close to those that are undamped.

At low frequencies, a damping effect is only achieved for a plate if there is non-zero stiffness (refer back to Sections 2.3.1.1 and 4.4.1). This occurs when incorporating the highly damped viscoelastic material into the FEM model. With damping from both the internal loss factor of concrete and the damping of the viscoelastic material, the driving-point mobility is changed significantly, particularly at low frequencies. In the case that the amount of the highly damped viscoelastic material ($\eta_{\text{int}} = 0.61$) corresponds to the experimental set-up of the reception plate using partial coverage, the rigid body modes (whole body and rocking modes) are shifted from zero frequency to the resonance frequency at ≈ 20 Hz due to the viscoelastic suspension. The increase in damping by the

viscoelastic supports consequently leads to a significant decrease in the resonance peaks at low frequencies. In addition, the resonance peaks for bending modes below 100 Hz are slightly shifted in frequency; note that the first bending mode shifts to the next higher frequency band. Compared to partial coverage with viscoelastic material, full coverage significantly reduces the peak responses below 250 Hz. The frequency of the rigid body modes changes from ≈ 20 Hz for partial coverage with viscoelastic material to ≈ 54 Hz for full coverage with viscoelastic material. At these low frequencies below the fundamental bending mode, the amplitudes of the driving-point mobility tend to approach the driving-point mobility of an infinite plate.

The amount of viscoelastic material changes the rigid body mode frequencies. For partial coverage with viscoelastic material, the damping influences rigid body modes and the first bending modes by shifting the resonance frequencies, while the damping effect decreases with increasing frequency and approaches the internal damping of the concrete plate. Hence, when deciding on the type and coverage of viscoelastic material for a reception plate, it is useful to have a FEM model because the role of rigid body modes has a significant influence on the response of the plate at low frequencies.

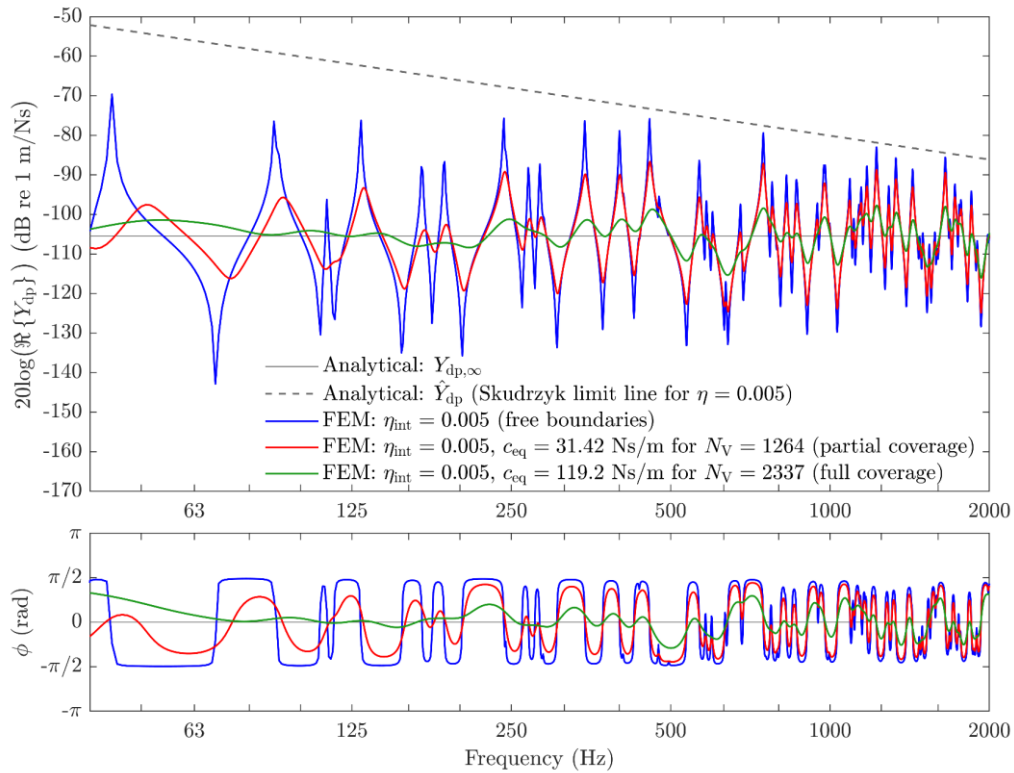


Figure 4-6. Effects of damping analysed by FEM using an isolated reception plate with structural damping and equivalent viscous damping with regard to partial and full coverage with viscoelastic material.

4.4.2.2 Loss factors from FEM and measurements

From EMA, the loss factors for the first three modes at 20.0, 24.2 and 28.9 Hz were 0.445, 0.442 and 0.632 respectively. The damping from these whole body and rocking modes were significantly higher than what is associated with bending modes when mode damping relaxes with increasing frequency to its lowest values. For bending modes at 45.9, 49.4, 93.5, 97.5, 118.0, 124.0, 167.8, 189.0 Hz, the corresponding EMA loss factors were solved with 0.242, 0.192, 0.107, 0.114, 0.074, 0.055, 0.057 and 0.051 respectively.

Figure 4-7 compares the loss factors in one-third octave bands obtained from FEM (experimental set-up with viscoelastic supports) using driving-point mobility and three different measurement methods using EMA, structural reverberation time and driving-point mobility. For EMA and driving-point

mobilities using five randomly distributed excitation positions, the individually associated loss factors from the mode frequencies are arithmetical averaged in one-third octave bands. This allows comparison with the loss factor determined from structural reverberation time measurements using one-third octave bands. The internal loss factors of concrete and viscoelastic material provide an indication of the upper and lower bounds of the overall loss factor. In the region of rigid body modes from 20 to 31.5 Hz, the loss factor is mainly determined by the high internal damping of the viscoelastic supports. However, the influence of this high damping decreases with increasing frequency, although even at the highest frequency (2 kHz), the damping is still higher than the internal loss factor of concrete (see Figure 4-6).

The measured loss factors show differences between the three different measurement methods. Below 100 Hz, where the rigid body and bending modes have well-separated resonance peaks with wide resonance skirts due to the highest damping by the viscoelastic plate supports, differences between the loss factor of up to 8 dB occur. One of the reasons for this is that in the region of whole body and rocking modes (<40 Hz), the highest loss factor that can be determined from structural reverberation time measurements is estimated to be 0.13 (≈ 111 dB) [71]. However, this upper limit depends on the filter type, and for the experimental set-up, it was possible to measure a loss factor up to ≈ 0.21 that corresponds to ≈ 113 dB. Therefore, it was necessary to use the loss factors from EMA and driving-point mobility measurements for rigid body modes below 40 Hz. For bending modes between 50 Hz and 2 kHz, the average absolute difference in the loss factor between the three measurement methods was only ≈ 1 dB, and no single method could be identified as having significantly higher accuracy.

The measured loss factor from EMA and driving point mobility is absent in the 40 Hz band. However, estimation of the reception plate power according to Eq. (2.76) requires a loss factor in each one-third octave band of interest. Therefore, a selection of loss factor values was averaged to ensure reasonable

estimates for all one-third octave bands. Linear regression was carried out after taking logarithms of frequencies and loss factors. This used loss factors from EMA and driving-point mobilities for all frequency bands from 20 Hz to 2 kHz and loss factors from the structural reverberation time are considered at and above 50 Hz. The resulting regression line is shown as a dashed curve in Figure 4-7. For FEM, interpolation was used to estimate loss factors below 100 Hz due to the lack of modal peak amplitudes in frequency bands at 25, 31.5, 40, 63 and 80 Hz. The loss factors assessed in frequency bands at 20, 50 and 100 Hz remain unchanged and were used to create a straight line between those values from 20 to 50 Hz and 50 to 100 Hz. For the well-separated rigid body modes, this is a pragmatic solution because it is unlikely that the loss factor (if it were measurable with structural reverberation times) would drop down to zero in the presence of highly damped modes in adjacent bands in the direction of the internal loss factor. The comparison of the direct injected power and the reception plate power is used to assess whether these loss factor estimates are accurate in Section 5.3.

In addition, Figure 4-7 allows a comparison of the reception plate damping from FEM and measurements when the damping was determined using the same method (frequency modes from driving-point mobility using the half-power bandwidth method). For this comparison of the damping from FEM and driving-point mobility measurements, the average absolute difference is generally in close agreement within ≈ 1 dB over the entire frequency range from 20 Hz to 2 kHz. This agreement not only provides information that the viscoelastic supports have been correctly incorporated into the FEM model but also that the assumption of the mineral wool *in vacuo* is appropriate as it has little effect on the overall damping of the reception plate. The average absolute difference of the comparison between FEM and the structural reverberation time measurement is ≈ 0.8 dB between 100 Hz and 2 kHz. For the frequency range from 500 Hz to 2 kHz, where the damping of viscoelastic material does not have a significant effect on the reception plate damping (see Figure 4-6), an absolute difference of

1.6 dB remains. It may be that the assumption of linear damping used to implement the viscoelastic material in FEM is not the appropriate choice at these high frequencies.

Overall, the good agreement between FEM and measurements allows FEM to be used in the design phase of a reception plate to predict several loss factors associated with changing the viscoelastic material type and layout. As deduced in the previous Section 4.4.1, the FEM model of the experimental set-up has no modes in the 31.5, 40, 63 and 80 Hz bands, and increasing the damping seems to be beneficial when there is a lack of modes. However, it may not be necessary to cover the entire area underneath the reception plate with viscoelastic material.

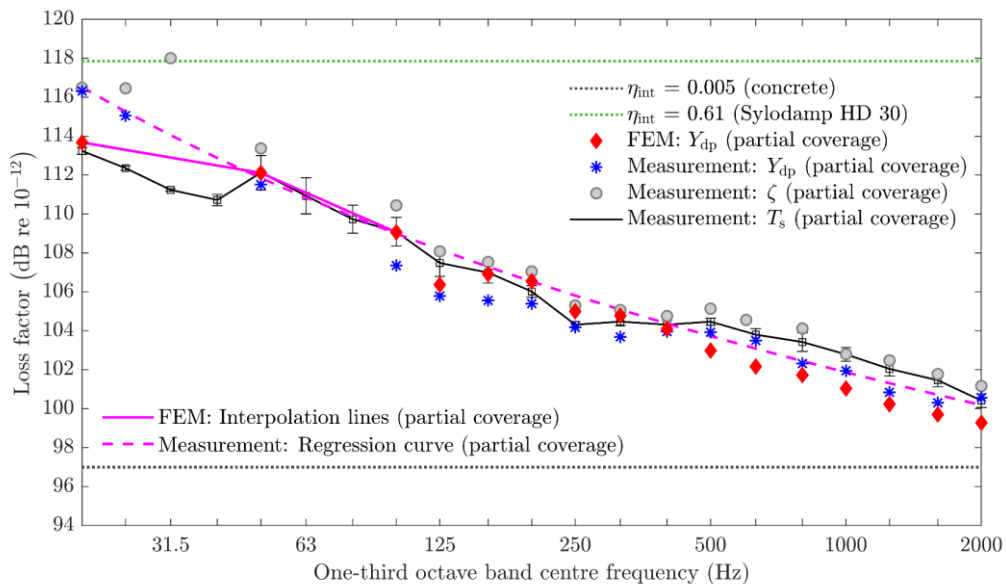


Figure 4-7. Reception plate using partial coverage with viscoelastic material: Comparison of loss factors determined from measurements using driving-point mobility (Y_{dp}), EMA (ζ) and structural reverberation time (T_s) and the FEM model using driving-point mobility (Y_{dp}).

Figure 4-8 shows the damping from the FEM models of the reception plate using partial and full coverage with viscoelastic material (see Figure 4-1b and c) when the loss factors are assessed using the driving-point mobility. For full coverage, the loss factor is (on average) 6 dB higher than for partial coverage.

As seen previously in the driving-point mobility in Figure 4-6, full coverage with viscoelastic material results in highly damped modes; hence, no loss factors below 125 Hz could be determined using the half-power bandwidth method.

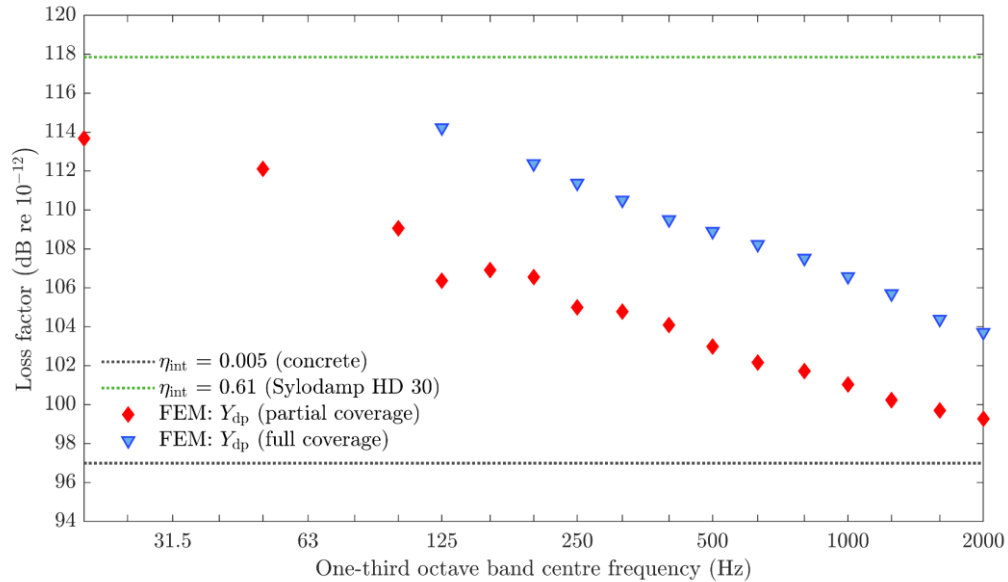


Figure 4-8. Reception plate using partial and full coverage with viscoelastic material: Comparison of loss factors determined from FEM models using driving-point mobility (Y_{dp}).

For a single isolated subsystem (i.e. the reception plate with highly damped supports) the modal overlap factor is a potentially useful descriptor as it combines the effect of damping with the frequency spacing between modes. Figure 4-9 illustrates the modal overlap factor from measurements and FEM models of a reception plate. For measurements and the FEM model of the experimental set-up using partial coverage with viscoelastic material, the results show that (a) the modal overlap factor is ≥ 1 in bands with rigid body modes and the first two bending modes between 20 and 50 Hz, (b) the modal overlap factor drops to zero in bands with no modes (40, 63 and 80 Hz for measurements and 31.5, 40, 63 and 80 Hz for FEM) and (c) the modal overlap occurs from 0.4 to 0.8 above 80 Hz with at least one bending mode in each band. The FEM model of the reception plate with free boundaries shows no modal overlap for the 20 to

31.5 Hz and 50 to 80 Hz bands due to the lack of modes. At and above 100 Hz, the modal overlap factor ranges between 0.2 and 0.3 when there is at least one mode in the bands. Only the FEM model of the reception plate using full coverage with viscoelastic material has a modal overlap factor of ≥ 1 between 125 Hz to 2 kHz. (NB Below 125 Hz, no values are plotted since no loss factors could be determined.)

The measured modal overlap factor is less than unity for the actual reception plate, which has partial coverage with regard to viscoelastic material around the plate edges. As a value of unity or greater tends to indicate a relatively uniform response, the modal overlap factor seems unlikely to be a useful descriptor for the reception plate; this is discussed further in Sections 4.6 and 5.3.2.

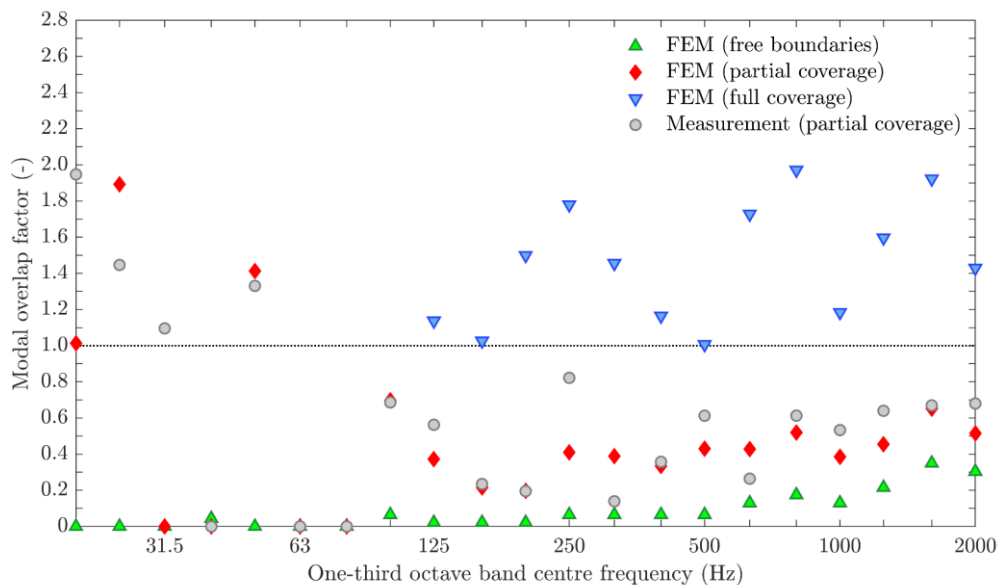


Figure 4-9. Modal overlap factor from measurements using combined driving-point mobility (Y_{dp}), EMA (ζ) and structural reverberation time (T_s) and FEM models using driving-point mobility (Y_{dp}). NB The modal overlap factor of the reception plate for the experimental set-up from measurements and FEM is assessed with the interpolation lines in the indicated frequency range from Figure 4-7.

For the calculation of the reception plate power according to EN 15657 [35], a diffuse field is required for vibration measurements. The obtained damping from FEM and measurements (see Figure 4-7) allows determining the

reverberation distance at which the direct field energy equals the diffuse field energy. Figure 4-10 shows the calculated reverberation distance, which varies with frequency since the propagation of bending waves is dispersive [71]. At and above 100 Hz, the three measurement methods and FEM have a reverberation distance of <0.1 m. Between 20 and 100 Hz, the reverberation distance has the highest values; these are 0.22 m at 20 Hz for measurements and 0.13 m at 50 Hz for FEM. These reverberation distance values can be seen as an estimate at low frequencies where only a few widely separated modes are present, and there is no approximation to a diffuse field. From these data, it is concluded that a minimum distance of 0.1 m between response positions and the source injection points is appropriate to use for determining the power injection from measurements and FEM.

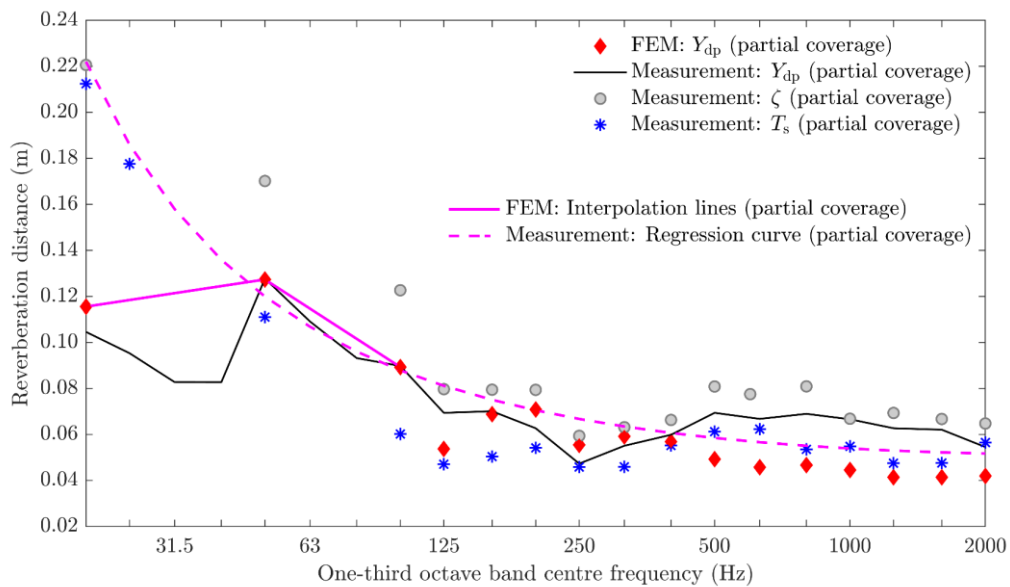


Figure 4-10. Reception plate using partial coverage with viscoelastic material: Reverberation distance determined from measurements using driving-point mobility (Y_{dp}), EMA (ζ) and structural reverberation time (T_s) and the FEM model using driving-point mobility (Y_{dp}).

4.4.3 Mobility

Figure 4-11 indicates two arbitrary positions of the driving-point mobility chosen on the reception plate. The comparison of the driving-point mobility with the real part (resistance) and phase from measurements and FEM (experimental set-up using partial coverage with viscoelastic material) for two arbitrary positions on the reception plate is shown in Figure 4-12. A reduced frequency range from 20 to 500 Hz is selected to account for the most critical frequency range where there are well-separated modes and to facilitate the comparison between measurements and FEM. Over the entire frequency range, there is close agreement between the experimental and numerical driving-point mobilities both with regard to the real part as well as phase. This indicates that the viscoelastic supports have been correctly incorporated into the FEM model and provides more evidence that the driving-point mobility has sufficient accuracy to predict damping using the half-power bandwidth method.

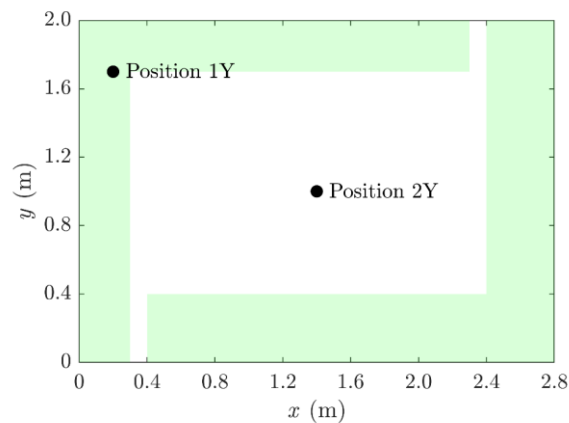


Figure 4-11. Reception plate using partial coverage with viscoelastic material: Driving-point mobility at excitation positions 1Y and 2Y. The green coloured area represents the partial coverage with viscoelastic material underneath the plate edges.

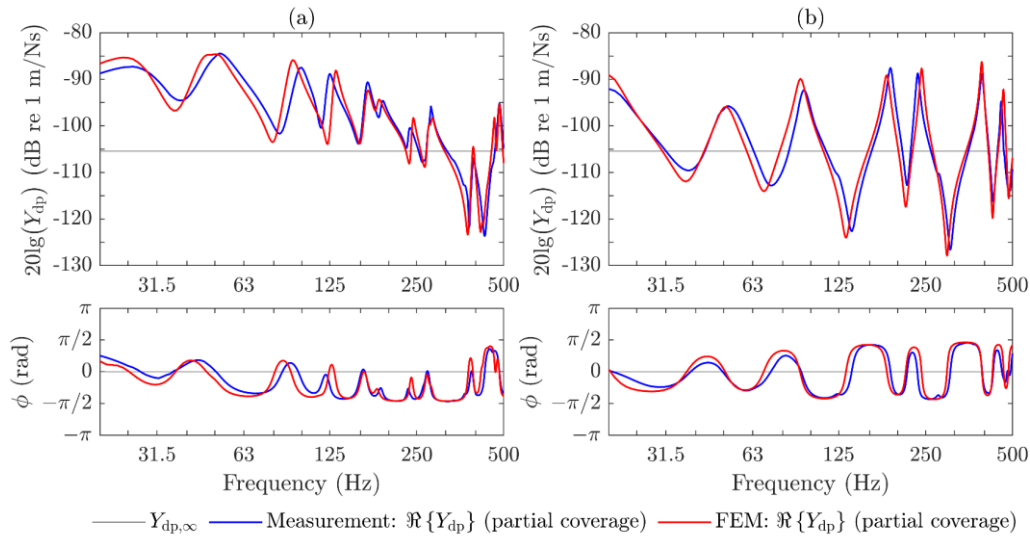


Figure 4-12. Reception plate using partial coverage with viscoelastic material: Comparison of the driving-point mobility from measurements and the FEM model at excitation positions (a) 1Y and (b) 2Y.

4.5 Spatial variations in plate velocity under harmonic forced response

A comparison of the spatial variation of plate velocity levels between measurements and FEM are now made for the experimental set-up using partial coverage with viscoelastic material. For the measurements, this was determined using a grid spaced 0.1 m apart, resulting in a total of 609 grid points which correspond to those used for EMA – see Section 3.3.3.1. The excitation was white noise for measurements (refer back to Section 3.3.6) and a uniform force using a frequency sine sweep for FEM (refer back to Section 2.3.2.4). For the FEM model, the element mesh of 0.05 m \times 0.05 m spacing was adapted to the grid spacing from EMA using velocities at nodes so that the grid corresponds to the element mesh with 0.1 m \times 0.1 m spacing.

Figure 4-14 and Figure 4-15 show the experimental and numerical contour plots using the amplitude shapes of the one-third octave band velocity levels for two single-contact source positions 1S and 5S (see Figure 4-13) from 20 Hz to 2 kHz. FEM and experimental contour plots demonstrate close agreement for the

spatial variation in velocity levels over the plate surface. Considering these results, along with the validation of the eigenfrequencies, mode shapes and damping from the previous sections, it is concluded that the FEM model can be used for numerical simulations of experiments to assess sampling strategies for single- and multiple-contact sources in Chapter 5.

In the 20 to 25 Hz bands where the rigid body modes dominate the response, the velocity levels vary by up to ≈ 14 dB across the plate for both FEM and measurements. For the experimental set-up, the rocking modes occurred in the 25 and 31.5 Hz bands, whereas the rocking modes from FEM were only in the 25 Hz band (refer back to Figure 4-4), although plotting results in one-third octave bands lead to similar vibration patterns. At and above the 40 Hz band, which is dominated by the response of the bending modes, the spatial variation of velocities increases by up to ≈ 45 dB. At and above the 50 Hz band where only bending modes occurred, it can be additionally observed that the lowest velocity levels occur in the central zone of the plate, apparently seen in the 80 Hz band of position 1S and 63 and 80 Hz bands of position 5S. At and above the 500 Hz band, the velocity levels tend to be highest in one or more corners and/or along the edges within a narrow strip width of 100 mm as has been found in previous studies (e.g. [30, 33]). Above the 630 Hz band, the vibration field has a fairly uniform variation in energy over the plate surface, which was also indicated by the standard deviation in Table 4-5. From this table, it can be seen that the standard deviation of the two single-contact source excitation positions 1S and 5S from measurements and FEM drops from 4.6 at 630 Hz to 3.3 between 800 Hz and 2 kHz (3.7 at 800 Hz, 3.5 at 1 kHz, 3.1 at 1.25 kHz, 3.0 at 1.6 kHz and 3.2 at 2 kHz).

The spatial variation in plate velocity with higher levels at edges and near corners and lower levels in the central zone gives an understanding of the vibration field on the reception plate, which can be used to assess suitable sampling strategies. Hence, the presence of higher levels near corners and edges leads to two sampling strategies in Chapter 5: (a) combining the central zone and corners using an empirical weighting as an individual approach for a particular isolated reception plate and (b) combining the central zone, corners and edge strips using an area weighting as a general approach for any isolated, rectangular reception plate.

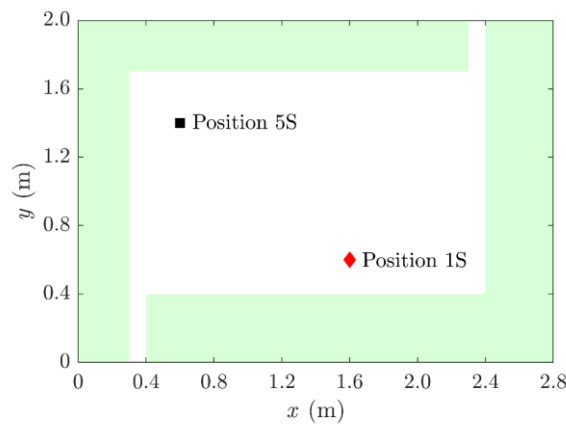


Figure 4-13. Reception plate using partial coverage with viscoelastic material: Single-contact sources at excitation positions 1S and 5S. NB The green coloured area represents the partial coverage with viscoelastic material underneath the plate edges.

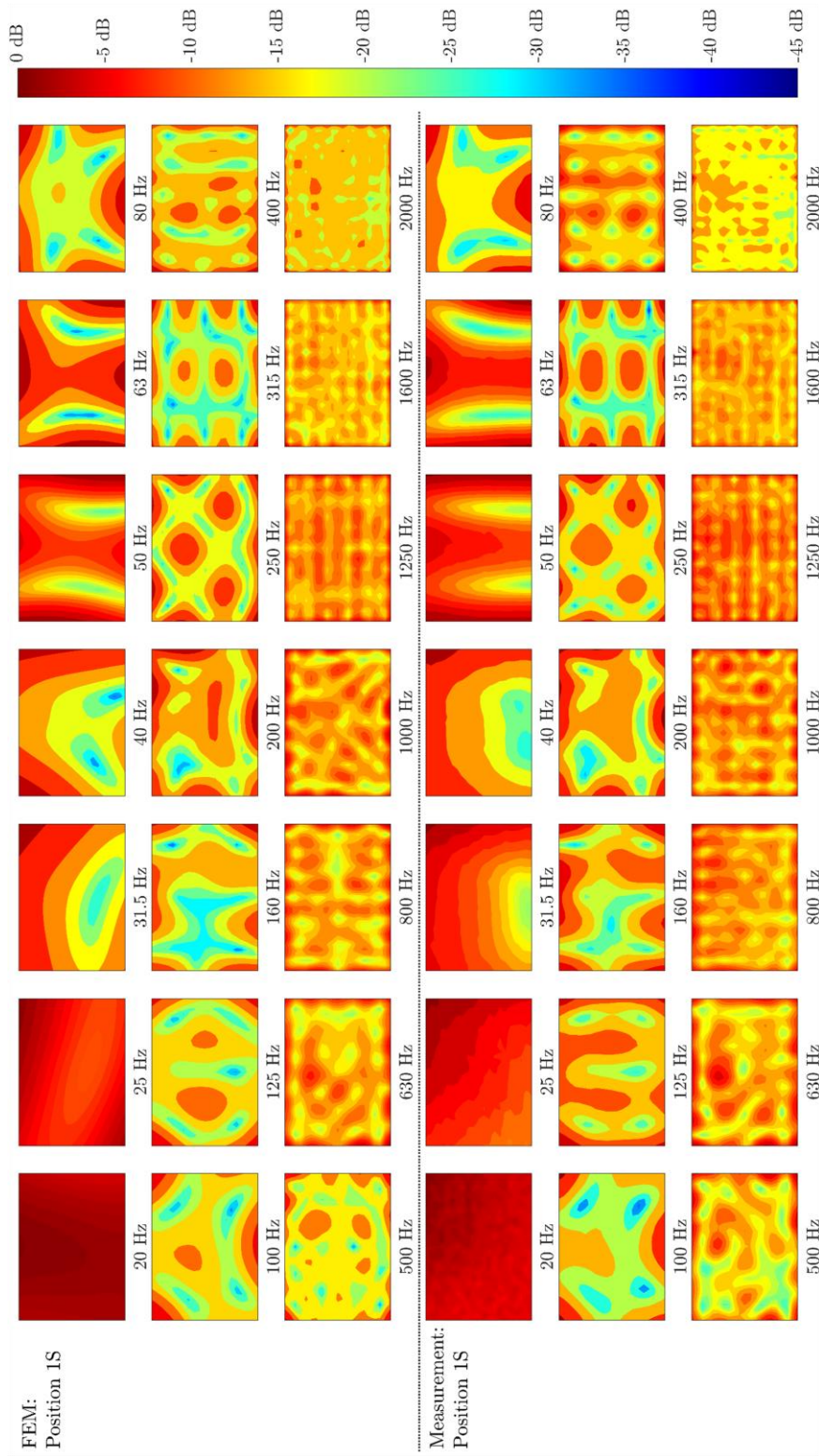


Figure 4-14. Reception plate using partial coverage with viscoelastic material: Contour plots of measured and predicted (FEM) velocity levels in one-third octave bands over the plate surface from a single-contact source at excitation position 1S. NB Velocity levels are normalised to the highest level on each individual contour plot.

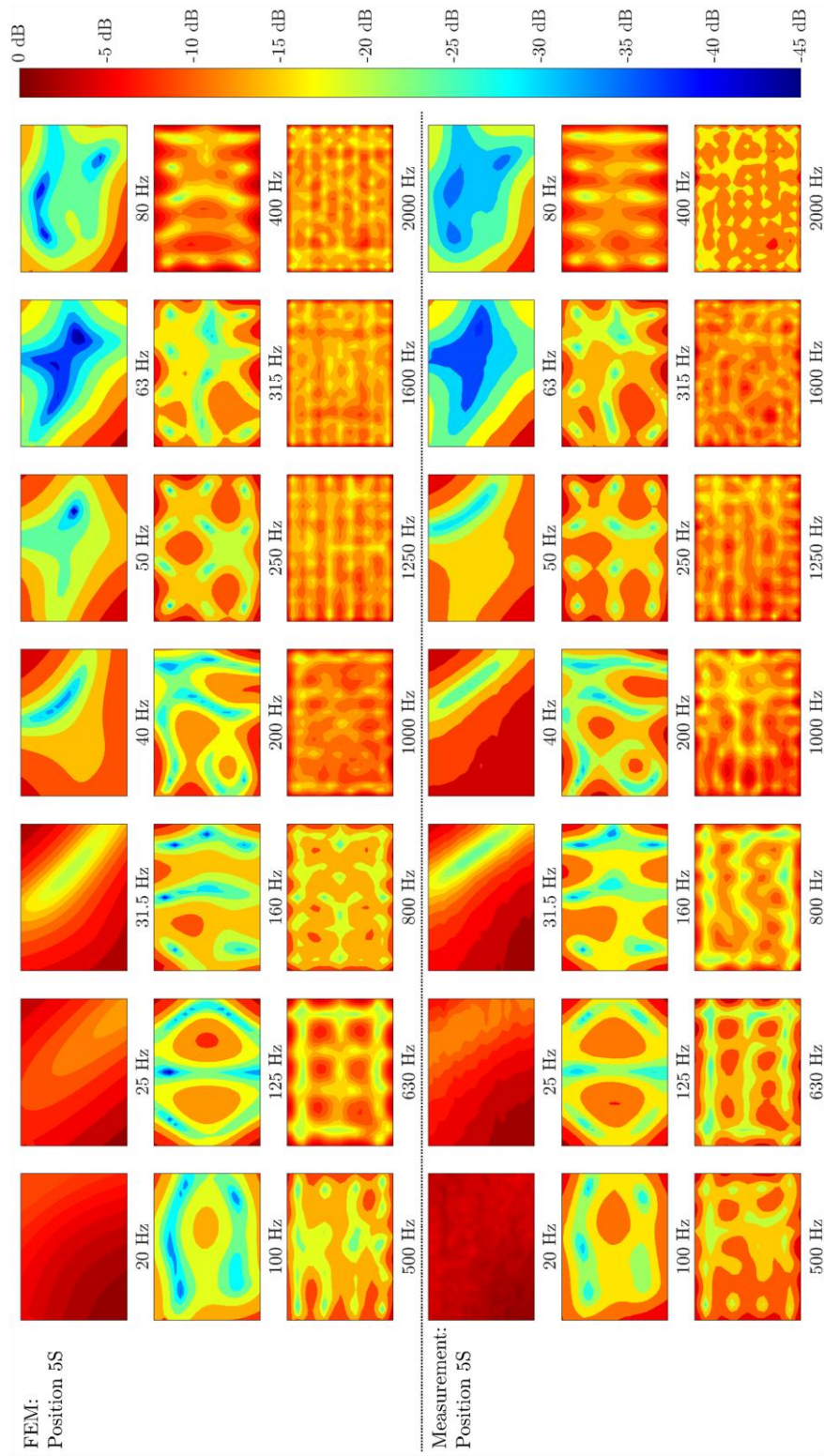


Figure 4-15. Reception plate using partial coverage with viscoelastic material: Contour plots of measured and predicted (FEM) velocity levels in one-third octave bands over the plate surface from a single-contact source at excitation position 5S. NB Velocity levels are normalised to the highest level on each individual contour plot.

Table 4-5. Reception plate using partial coverage with viscoelastic material: Standard deviation, s , determined of measured and predicted (FEM) velocity levels in one-third octave bands over the plate surface from single-contact sources at excitation positions 1S and 5S.

Frequency, f (Hz)	Standard deviation, s (dB)			
	Measurement: Position 1S	FEM: Position 1S	Measurement: Position 5S	FEM: Position 5S
20	0.9	0.8	0.9	2.4
25	3.9	2.3	3.9	2.8
31.5	5.7	5.7	5.7	5.0
40	5.5	6.1	5.5	5.7
50	5.1	5.1	5.1	5.9
63	6.5	6.2	6.5	8.8
80	6.2	5.7	6.2	6.8
100	4.7	5.0	4.7	5.4
125	5.4	4.7	5.4	6.4
160	5.2	6.1	5.2	5.4
200	5.3	5.3	5.3	6.2
250	4.3	5.3	4.3	4.8
315	4.7	5.9	4.7	4.9
400	3.7	4.2	3.7	4.2
500	3.9	4.0	3.9	4.4
630	4.9	3.8	4.9	4.6
800	3.6	3.7	3.6	3.7
1000	3.5	3.8	3.5	3.1
1250	3.1	3.1	3.1	3.1
1600	2.9	3.2	2.9	3.0
2000	3.1	3.3	3.1	3.4

4.6 Investigation into the role of rigid body modes

To gain insight into the validity of the equation for the reception plate power (Eq. (2.76)) at low-frequencies where there are widely spaced modes, it is useful to simulate the plate response. For any thin plate, the principle of superposition can be used to obtain an analytic solution for bending vibration. This can then be used to give the driving-point mobility at a position (x, y) on the plate from Eq. (2.24), which can be used to model the reception plate using FEM or EMA eigenfrequencies, eigenvectors (mode shapes) and loss factors from Section 4.4. However, the spatial variation of the vibration field over the plate complicates the assessment of the errors in the reception plate power between two well-separated modes at frequencies outside the damping-controlled region (defined by the half-power bandwidth method (Eq. (2.41))). For this reason, the approach taken here is to treat each mode as a mass-spring-dashpot system by altering the spring stiffness to give different eigenfrequencies and superposing the responses to determine the overall response. This also makes it possible to consider mass-spring-dashpot systems as representing the whole body mode, rocking modes and bending modes.

Considering Eq. (3.18) for the maximum system response at the undamped frequency to obtain the spring stiffness versus the mass and Eq. (3.19) for the damping constant that is related to the dashpot by making use of the loss factor, the driving-point mobility for a mass-spring-dashpot system can be estimated from Eq. (2.22). As a result, the power input into the system is then given by [71]

$$W_{\text{inj},n} = F_{\text{rms}}^2 \Re \{ Y_{\text{dp},n} \} = F_{\text{rms}}^2 \eta_n \omega_{0,n} m |Y_{\text{dp},n}|^2 \quad (4.3)$$

or the power input can be estimated from the system response (as with the reception plate) according to [71]

$$W_{\text{rec},n} = \omega \eta_n m v_n^2 = \omega \eta_n m F_{\text{rms}}^2 |Y_{\text{dp},n}|^2 \quad (4.4)$$

The only difference between $W_{inj,n}$ and $W_{rec,n}$ is the frequency multiplier, which is $\omega_{0,n}$ and ω respectively, and therefore the difference in the power in decibels is $10\lg(\omega_{0,n}/\omega)$, which is independent of the damping. Hence, $W_{rec,n}$ is less than $W_{inj,n}$ ($W_{rec,n} < W_{inj,n}$) in the stiffness-controlled region of the modal response (i.e. below $f_{0,n}$) and $W_{rec,n}$ is greater than $W_{inj,n}$ ($W_{rec,n} > W_{inj,n}$) in the mass-controlled region of the modal response (i.e. above $f_{0,n}$) – see also Figure 2-1.

The first step is to consider individual modes using the EMA results for eigenfrequencies and loss factors (see Section 4.4.2.2). The power input from the rigid body modes and the first three bending modes of the reception plate is shown in Figure 4-16 to illustrate the difference between $W_{inj,n}$ and $W_{rec,n}$. The frequency axis is normalised to the mode frequency in each graph. Assuming that a difference of ≈ 1 dB (in terms of magnitude) is the largest acceptable error for the comparison of both powers, this occurs at $0.79 f_{0,n}$ (towards the stiffness-controlled region) and $1.26 f_{0,n}$ (towards the mass-controlled region) for all rigid body and bending modes (see also Figure 2-1). The rigid body modes (modes 1, 2 and 3 – see Figure 4-16a, b and c) have high damping, and the difference between injected and reception plate power is approximately ± 1 dB within the damping-controlled region. The bending modes (modes 4, 5 and 6 – see Figure 4-16d, e and f) have lower damping, so the damping-controlled region appears narrower when plotted against f/f_0 . However, the difference is seen to be ± 1 dB over a wider range than the damping-controlled region. Hence, when the tolerable error is ± 1 dB, the reception plate equation is still appropriate to use just outside the damping-controlled region.

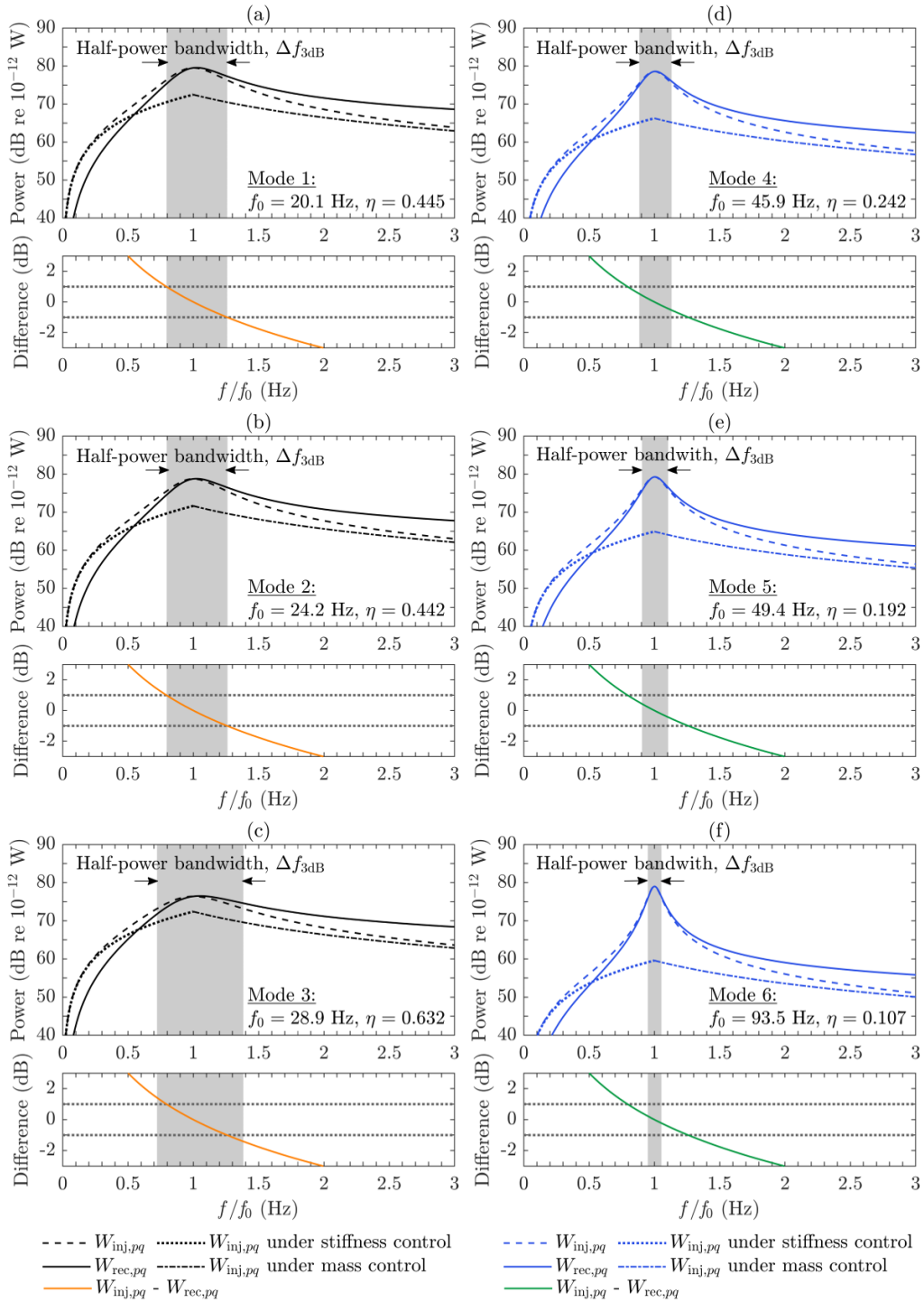


Figure 4-16. Reception plate using partial coverage with viscoelastic material: Comparison of the direct injected power and the reception plate power for (a-c) rigid body modes and (d-f) bending modes. The grey shaded area identifies the damping control region. The difference refers to the injected power minus the reception plate power with horizontal lines indicating ± 1 dB.

The next step is to assess what happens when there are adjacent modes. The corresponding Nyquist circles for driving-point mobilities of two-pole (or second-order) filters of single mass-spring-dashpot systems during force excitation in terms of amplitude and phase are determined using

$$Y_{dp,n}(\omega) = \frac{i\omega}{(k_n - \omega^2 m) + i\omega R_n} \quad (4.5)$$

Figure 4-17 shows the Nyquist plots of the three rigid body modes and the first nine bending modes using the real part versus the imaginary part of the driving-point mobility of a single mass-spring-dashpot system. Due to the roughly equal loop size, a high damped mode is represented by an open-loop, while a low damped mode has a closed-loop. In the case that the estimated start and end driving-point mobility values of a single mass-spring-dashpot system are in the vicinity of the coordinate origin, it can be assumed that the modal response is dominated by this mode. Otherwise, the modal response is influenced by adjacent modes.

As expected, the rigid body modes due to the vibration isolation by the viscoelastic supports have the highest damping, which is shown by the wide open-loop in Figure 4-17a to c. For bending modes that are widely spaced at low frequencies, higher damping is observed due to the frequency-dependent damping behaviour of the viscoelastic material. This is indicated by the open-loops in the Nyquist plots at low frequencies, especially for the first two bending modes at 50 Hz up to nearly the fourth bending mode below 100 Hz – see Figure 4-17d to g. Above 100 Hz, the damping effect decreases as the Nyquist circle approaches a closed-loop as indicated in Figure 4-17h to l.

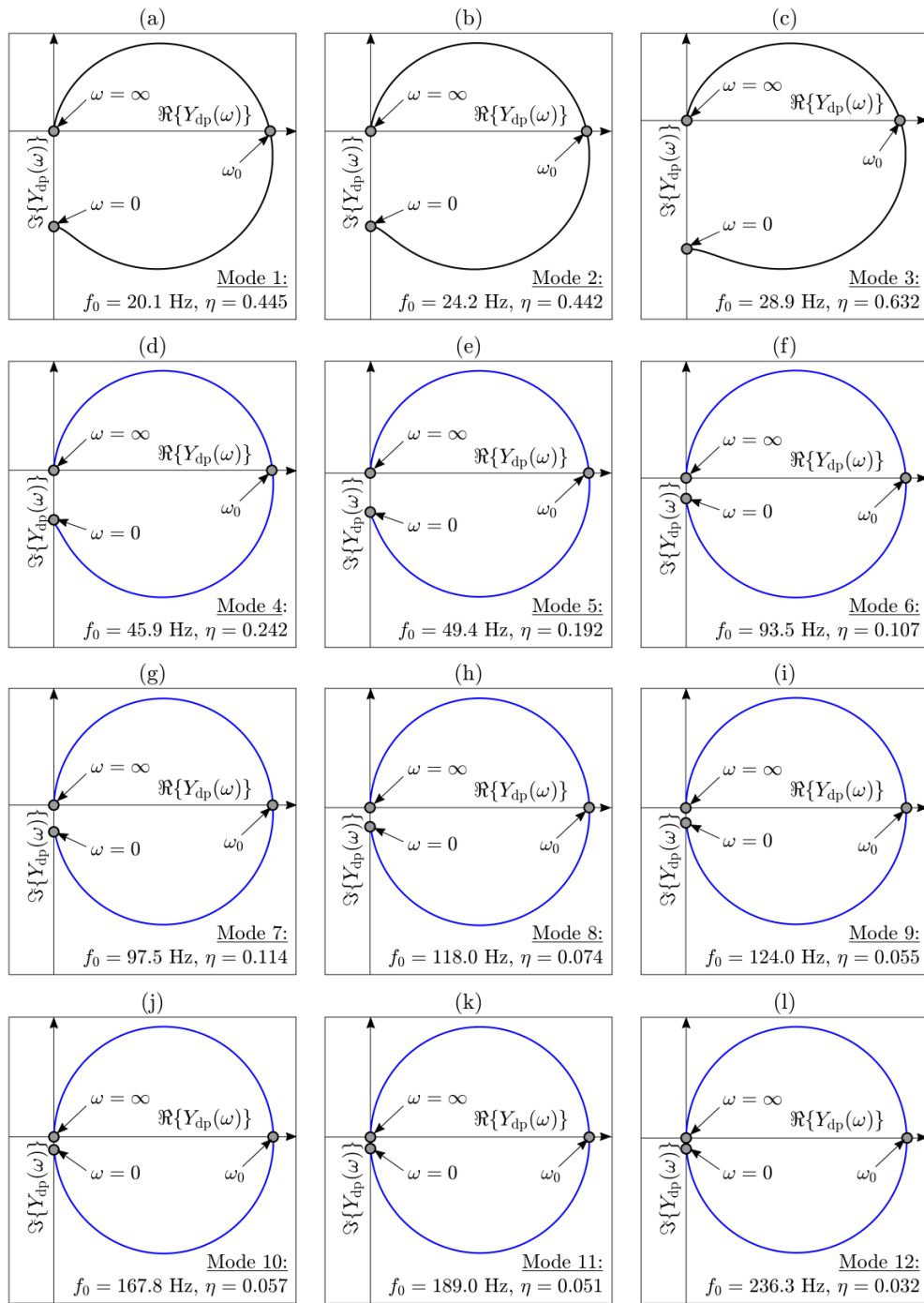


Figure 4-17. Reception plate using partial coverage with viscoelastic material: Nyquist plots from the driving-point mobility of two-pole filters using single mass-spring-dashpot systems during force excitation for (a-c) rigid body modes and (d-l) bending modes.

In the section above, only the vibration response from individual local modes was considered using mass-spring-dashpot systems. The next step is to consider a multi-modal system made up of a number of single mass-spring-dashpot systems to give the overall response up to the 630 Hz band. For a multi-modal system, the resultant powers over a wide frequency range are given by

$$W_{\text{inj}} = mF_{\text{rms}}^2 \sum_{n=1}^{\infty} \eta_n \omega_n |Y_{\text{dp},n}|^2 \quad (4.6)$$

and

$$W_{\text{rec}} = mF_{\text{rms}}^2 \sum_{n=1}^{\infty} \omega \eta_n |Y_{\text{dp},n}|^2 \quad (4.7)$$

where from the EMA results, the eigenfrequencies and loss factors from the three rigid body modes and the first 27 bending modes (see Section 4.4.2) can be used to calculate W_{inj} and W_{rec} .

Figure 4-18 shows the combined response from the first 30 modes (associated with rigid body and bending modes) in terms of the direct injected power and the reception plate power from a multi-modal system. The response is shown in terms of the single-frequency power data and one-third octave bands by summing FFT lines and using the ‘6th order Butterworth’ filter attenuation according to IEC 61260-1 [134].

The rigid body modes are below 50 Hz, but because they have high damping, they are beneficial in preventing the power from having deep troughs between mode 3 (28.9 Hz) and mode 4 (45.9 Hz) and between mode 5 (49.4 Hz) and mode 6 (93.5 Hz). This effect becomes negligible with increasing frequency as there are many more bending modes. The absolute difference between W_{inj} and W_{rec} is <1 dB for the majority of one-third octave bands from 20 to 630 Hz (except 63 and 80 Hz where it is up to 2 dB), even when there are widely spaced adjacent modes such as between bending modes 5 and 6 (49.4 to 93.5 Hz).

In practice, the direct injected power is usually carried out using narrowband FFT measurements and then combined into one-third octave bands. Therefore, as long as there are accurate estimates for the peaks and troughs with the cross-spectrum, then W_{inj} will give an accurate estimate regardless of whether there is a peak in the modal response. The reception plate power is determined with '6th order Butterworth' one-third octave band filters so that in the trough between the 49.4 Hz and 93.5 Hz modes, the filter skirts pick up some of the high response from the peaks and troughs in adjacent bands. Therefore, in addition to the beneficial damping effect from rigid body modes, the use of filters with the reception plate approach smoothes the difference between adjacent bands. Hence, where there are no modes, W_{inj} minus W_{rec} is at most -2 dB and -1.5 dB in the 63 and 80 Hz bands respectively. All other frequency bands below 630 Hz where there is at least one mode have absolute differences less than 1 dB.

This indicates that the bending mode count and the modal overlap factor are not useful to determine the validity of the reception plate method (refer back to Figure 4-4 and Figure 4-9). This assessment using mass-spring-dashpot models shows that the reception plate method may still be appropriate and give negligible errors when there are widely spaced modes at low frequencies. This will be assessed in Chapter 5 using FEM and measurements.

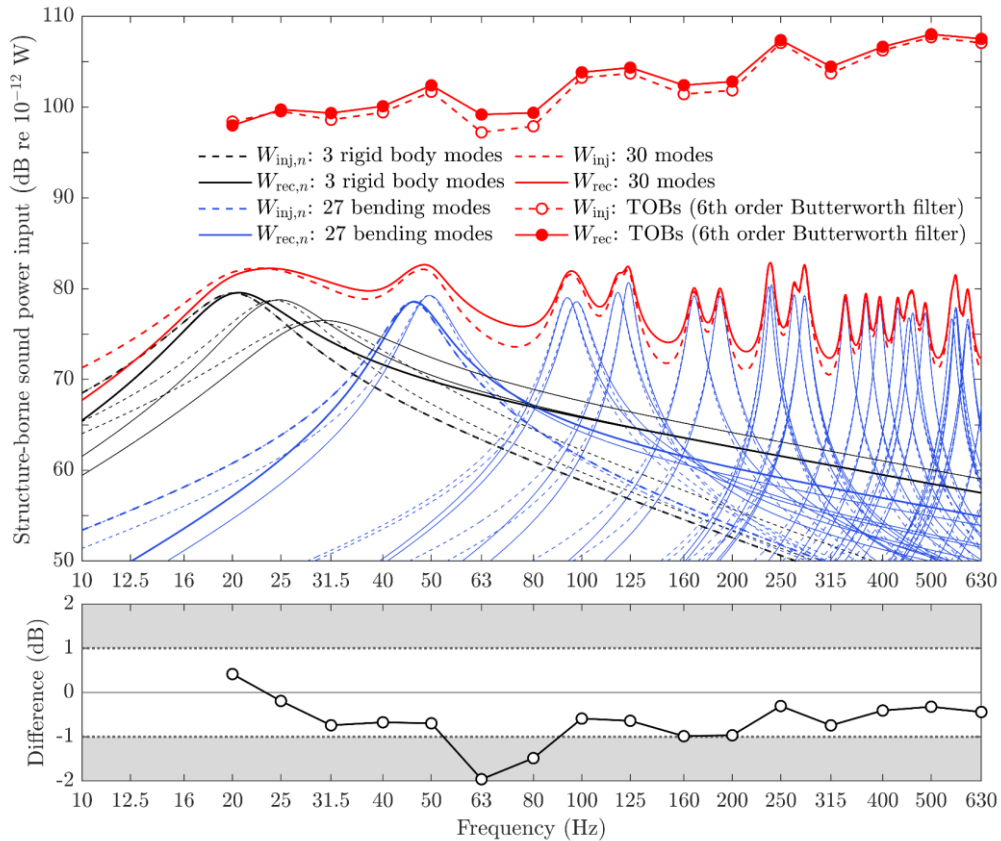


Figure 4-18. Reception plate using partial coverage with viscoelastic material: (Upper graph) Comparison of the direct injected power and the reception plate power using single mass-spring-dashpot systems of 3 rigid body modes and 27 bending modes for narrowband and TOBs. (Lower graph) Difference between direct injected power and the reception plate power in TOBs.

Figure 4-19 allows a comparison of ‘ideal’ and ‘6th order Butterworth’ one-third octave band filters for the direct injected power. These differences are negligible; hence, it is reasonable to combine narrowband FFT data into one-third octave bands by assuming that the bands are an ideal filter.

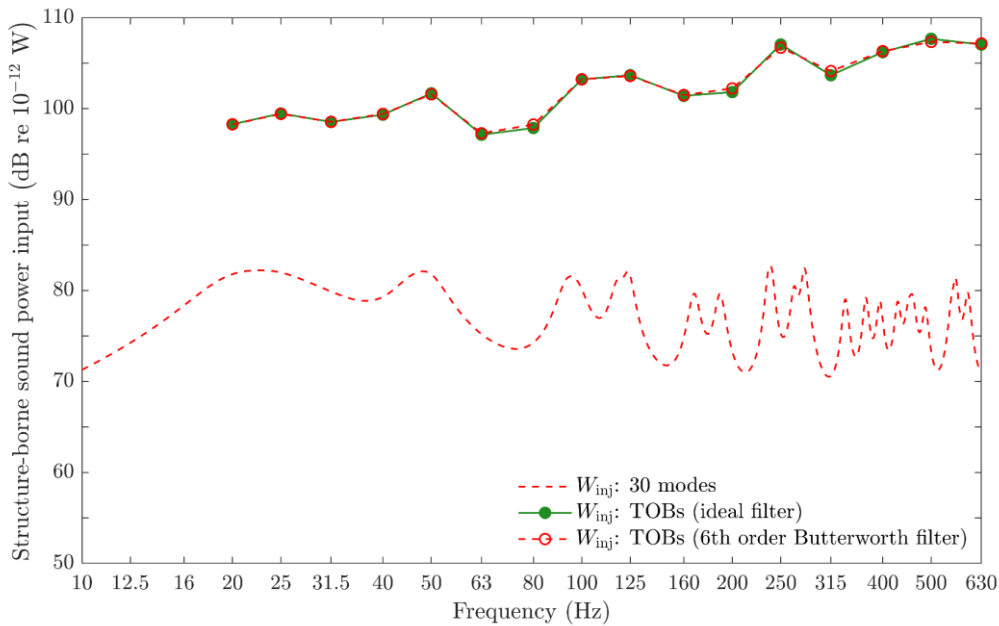


Figure 4-19. Reception plate using partial coverage with viscoelastic material: Comparison of ‘ideal’ and ‘6th order Butterworth’ filters using the direct injected power of 30 modes (3 rigid body modes and 27 bending modes from Figure 4-18).

For this particular reception plate using partial coverage with viscoelastic material, the highly damped rigid body modes help reduce the errors below 100 Hz where there are widely spaced bending modes, particularly in the 63 and 80 Hz bands where there is a lack of bending modes. These idealised models indicate that the highly damped rigid body modes help maintain the accuracy of the reception plate method at low frequencies; this is assessed further in Chapter 5.

4.7 Summary

A FEM model of a heavyweight reception plate supported by viscoelastic material has been experimentally validated with respect to eigenfrequencies (NFD), mode shapes (MAC), damping using the total loss factor of the plate and mobility. There was close agreement between FEM and measurements for both rigid body modes and bending modes. This confirms that the viscoelastic

material can be incorporated into a FEM model as independent, vertical spring-dashpot elements. The FEM model is used for numerical experiments to assess the structure-borne sound power induced by single- and multiple-contact sources in Chapter 5.

The results provide evidence that when designing a new reception plate, FEM can be used to evaluate different damping materials in terms of the stiffness and internal loss factor, layout of damping supports, plate sizes and alternative plate shapes (e.g. irregular polygon). For example, it was shown that changing the viscoelastic material from partial to full coverage would cause problems in evaluating the loss factor experimentally.

Numerical experiments with FEM using point excitation with white noise to predict the spatial variation of the velocity over the reception plate showed close agreement with measurements. This indicated that there were point-to-point variations over the plate surface of up to ≈ 20 dB in the vicinity of the rigid body modes and up to ≈ 45 dB where the response was determined by bending modes. It was also shown that higher velocity levels occur in the vicinity of corners and edge strips, while lower velocity levels occur in the central zone of the plate. These insights into the plate vibration field are used in Chapter 5 to develop sampling strategies.

The role of rigid body modes in determining the plate response was investigated using an analytical model of SDOF systems and a multi-modal system to determine the direct injected power and the reception plate power. The highly damped rigid body modes were found to be useful below 100 Hz, as they potentially extend the valid frequency range of the reception plate down to 20 Hz. This is investigated in more detail in Chapter 5.

5 Reception plate: Assessment of sampling strategies

5.1 Introduction

This chapter introduces sampling strategies related to the spatial average velocity to reliably estimate the reception plate power with a smaller number of measurement positions than with a detailed rectangular grid of positions. Based on the findings in the previous chapter that the highest velocity levels are near corners/edges and the lowest velocity levels are in the central zone of the plate, two sampling strategies, empirical and area weighting approaches, are developed and discussed in Section 5.2.

Section 5.3 compares the direct injected power and the reception plate power from single- and multiple-contact sources to assess whether both sampling strategies are valid for the determination of the reception plate power. In addition, Section 5.4 discusses the applicability of both sampling approaches with regard to the reception plate for which they are designed.

5.2 Sampling strategies to estimate the reception plate power

Whilst it is relatively quick to determine velocity levels over a fine regular grid over the entire plate surface in FEM, it is time-consuming to use a grid for commercial laboratory measurements. Therefore, a more practical procedure to measure the spatial variation in velocity over the plate surface is sought. The aim is to reduce the number of positions to a minimum whilst still giving reliable and accurate assessments of the reception plate power. This has led to the development of two sampling strategies: an empirical weighting and an area weighting. Section 5.2.1 introduces the sampling strategy using the empirical weighting as an approach that is specific to this particular reception plate, and Section 5.2.2 describes the sampling strategy using the area weighting as the general approach for any isolated, rectangular reception plate.

5.2.1 Empirical weighting as an individual approach

Testing laboratories tend to use their own design of a reception plate to fit their facility or type of machinery. Hence, it would be feasible for a laboratory to use the sampling strategy in the standard EN 15657 [35] along with an empirical weighting to improve estimates of the structure-borne sound power at low frequencies.

For the horizontal reception plate at the University of Applied Sciences Stuttgart, the results of the vibration contour plots excited by two single-contact sources show that the plate surface velocity levels tend to be larger near the corner regions than in the central region of the plate (refer back to Section 4.5). For field measurements of airborne sound insulation between rooms, similar issues have been identified for the spatial average sound pressure level in small rooms at low frequencies, and an empirical equation was developed to estimate the room average sound pressure level from corner and central zone measurements [165]. Hence, a similar approach is adopted for the reception plate

using a defined empirical weighting factor X that combines velocity level positions from each of the four corners and the central zone of the plate (see Figure 5-1). The aim is to replicate the spatial average velocity level that is determined by the full grid of measurement positions. The central zone of the plate is defined by the area that is ≥ 0.5 m away from the plate edges. This gives a combined spatial average velocity level for a suitable estimate of the empirical weighted velocity level, $L_{v,EW}$, as follows

$$L_{v,EW} = 10 \lg \left[\frac{10^{L_{v,C}/10} + X \cdot 10^{L_{v,CZ}/10}}{X + 1} \right] \quad (5.1)$$

where $L_{v,C}$ and $L_{v,CZ}$ are the plate velocity levels from the corners and the central zone of the plate respectively. The derived empirical weighting factor X is shown in Figure 5-2. $X = 1$ at frequencies up to 40 Hz, which indicates that corners and central zone are equally important. At 50 Hz, $X = 2$ and then X increases by a factor of three per doubling of the frequency band ($X = 2 + 3N_f$ where N_f indicates the number of frequencies in ascending order starting with $N_f = 1$ at 63 Hz) because the corners become less important with increasing frequency – see Figure 5-6 for central zone positions and Figure 5-7 for corner positions.

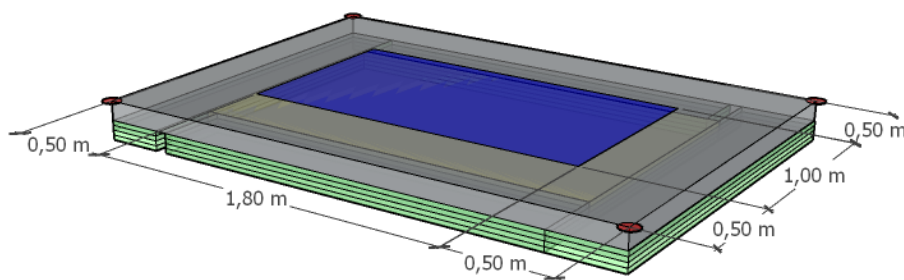


Figure 5-1. Reception plate using partial coverage with viscoelastic material (green): Schematic representation of the four corners (red) and the central zone area (blue) on the reception plate using the empirical weighting approach for velocity samples.

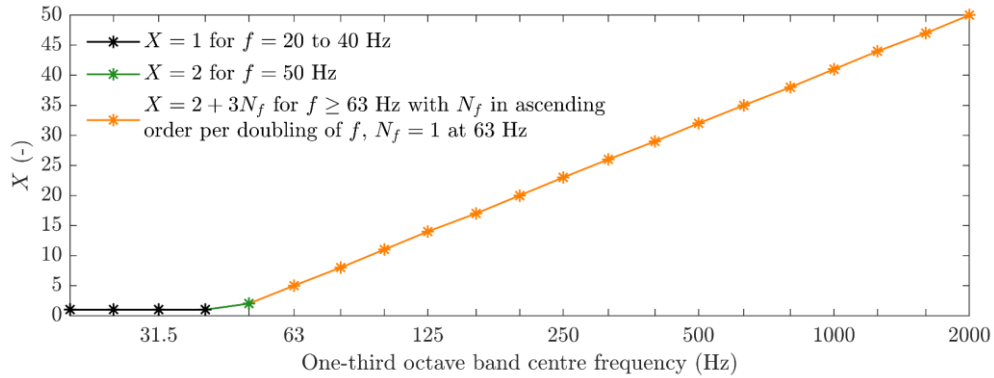


Figure 5-2. Reception plate using partial coverage with viscoelastic material: Specified weighting factor using the empirical weighting approach for velocity samples.

When using this empirical weighting approach for a reception plate with an area of 5.6 m² (refer back to Section 3.2.1) and assuming a machine covering an area of 0.36 m², measurements at four corners and five central zone positions (≥ 0.9 m apart from each other in a central zone area of 1.8 m²) could be carried out for most positions of the machine on the plate. Note that an empirical weighting is a specific approach for this particular isolated reception plate [30, 33] that satisfies the guidance in EN 15657 [35].

5.2.2 Area weighting as a general approach

In this section, a new sampling strategy is developed as a more general approach that can be used for any isolated, rectangular reception plate. The results of the contour plots derived from the two single-contact source excitation points indicates that in addition to the corners (100 mm \times 100 mm), edge strips (100 mm wide) also have high velocity levels as discussed in Section 4.5. This means that the measurement of velocity levels may not need to be limited to corner and central zone positions as used for the empirical weighting approach. This divides the plate surface into defined areas for corners, edge strips and the central zone (see Figure 5-3). Consequently, by velocity sampling over these defined areas for corners, edge strips and the central zone, an area-weighted velocity level, $L_{v,AW}$, can be calculated as follows

$$L_{v,AW} = 10 \lg \left[\frac{S_C \cdot 10^{L_{v,C}/10} + S_{ES} \cdot 10^{L_{v,ES}/10} + S_{CZ} \cdot 10^{L_{v,CZ}/10}}{S_{tot}} \right] \quad (5.2)$$

where S_C , S_{ES} and S_{CZ} are the surface areas for corners, edge strips and the central zone respectively that results in the total area of $S_{tot} = S_C + S_{ES} + S_{CZ}$ and $L_{v,C}$, $L_{v,ES}$ and $L_{v,CZ}$ are the spatial average velocity levels for corners, edge strips and the central zone respectively.

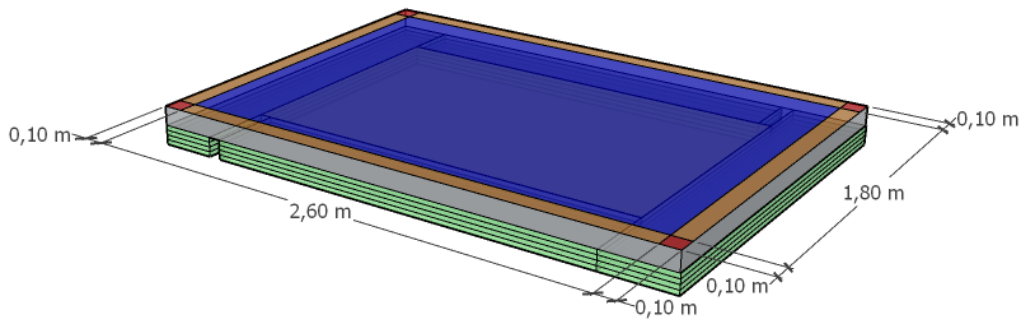


Figure 5-3. Reception plate using partial coverage with viscoelastic material (green): Schematic representation of areas for corners (red), edge strips (orange) and the central zone (blue) using the area weighting approach for velocity samples.

For the area-weighted approach to be applicable, the sample size must have sufficient points to replicate the varying velocity levels over the plate surface by areas for corners, edge strips and the central zone. Recalling that the reception plate area is 5.6 m^2 (refer back to Section 3.2.1) and a piece of building machinery often has an area less than 0.36 m^2 , it is feasible to account for measurements from four corner positions (the sampling area for each corner is defined as being within a $0.1 \text{ m} \times 0.1 \text{ m}$ square), two positions at each edge strip (the sampling area for each edge strip is defined as being between the corner squares and is 0.1 m wide with a distance of $\geq 0.8 \text{ m}$ between the positions) and eight central zone positions (the sampling area for the central zone is defined as being $\geq 0.1 \text{ m}$ apart from boundaries with a distance of $\geq 0.8 \text{ m}$ between the positions) – see Figure 5-3, where the defined areas for corners, edge strips and the central zone are 0.04 m^2 , 0.88 m^2 and 4.68 m^2 respectively.

5.3 Validation of sampling strategies

This section introduces the investigations on the power input from single- and multiple-contact sources on the reception plate. Section 5.3.1 describes the location of these source types on the reception plate, which are used for the investigation of single-contact sources in Section 5.3.2 and multiple-contact sources in Section 5.3.3.

5.3.1 Excitation positions from single- and multiple-contact sources in FEM and measurements

The characterisation of structure-borne sound sources is studied using a defined force injected at a single-contact point or at multiple-contact points perpendicular to the plate surface to determine the velocity through bending vibration. The two single-contact sources used to investigate the spatial variation in plate velocity are also used here for measurements (refer back to Figure 4-13) but with three additional positions to give a total of five as shown in Figure 5-4a. (NB It will shortly be seen that five positions are sufficient because they are similar.) In practice, domestic appliances or machines are rarely attached to the structure via a single point of contact; hence, an idealised source with multiple-contact points is assumed with four contacts arranged in a 0.6 m × 0.6 m square; this represents typical white goods. Multiple-contact sources are investigated in FEM with excitation positions that are orientated parallel or at a 45° angle to the plate edges as indicated in Figure 5-4b and Figure 5-4c. Considering that the majority of floor-standing machinery and typically all wall-mounted machinery is placed parallel to the edges of plates in buildings, this alignment type was chosen. The source alignment at an angle to the plate edges with contact points of the source close to the plate diagonal was used to assess differences in a similar way to the tapping machine being orientated at an angle to the joists on a floor. In this context, the numerical forces are applied as a purely harmonic

input of equal magnitude with zero and random phases between the contact points.

The reception plate power is determined using Eq. (2.76) for both single- and multiple-contact sources, and the direct injected power is calculated using Eq. (2.74) and Eq. (2.75) for sources with single- and multiple-contact points respectively.

Note that excitation positions on a nodal line and/or point can lead to a very low (or zero) response of the bending wavefield if no eigenfrequencies are excited, and the damping is very low. Whilst a source location on an anti-nodal line and/or point can lead to a large bending wave field response because the eigenfrequencies are excited. Where possible, an excitation position in the exact centre of the plate was avoided because some nodal lines intersect at this point. With the single- and multiple-contact sources, it was attempted to avoid positions on nodal lines for the eigenfrequencies at low frequencies (≤ 200 Hz). In practice, this might not always be possible due to multiple-contact points from machinery that have different small/large with symmetric/unsymmetric spacing that can occur as point/line/area contacts, handling of machine size/weight, etc.

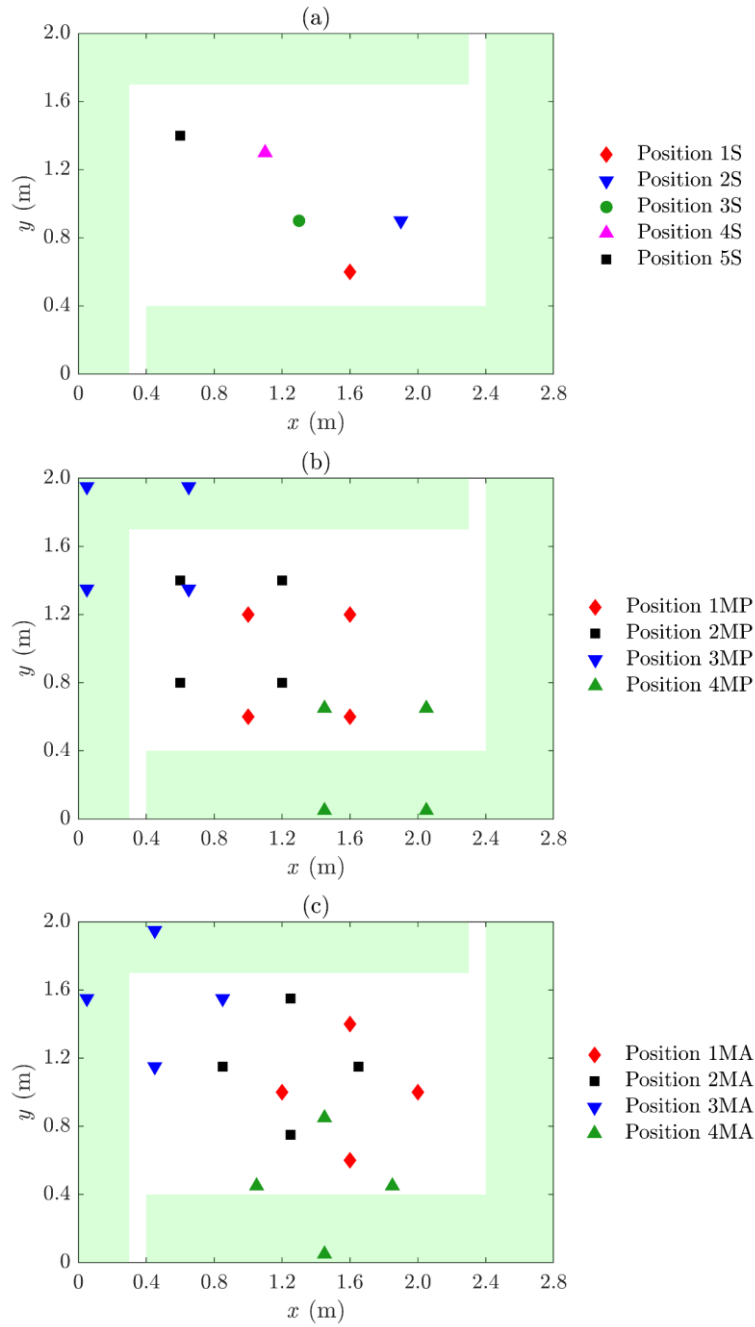


Figure 5-4. Reception plate using partial coverage with viscoelastic material excited by (a) single-contact sources at positions 1S, 2S, 3S, 4S and 5S, (b) multiple-contact sources that are aligned parallel to the plate edges at positions 1MP, 2MP, 3MP and 4MP and (c) multiple-contact sources that are aligned at an angle to the plate edges at positions 1MA, 2MA, 3MA and 4MA. NB The green coloured area represents the partial coverage with viscoelastic material underneath the plate edges.

5.3.2 Single-contact sources assessed by FEM and measurements

The first step is to get the most accurate estimate of the reception plate power using the spatial average velocity over the entire plate surface from a fine regular grid. Figure 5-5 shows the difference between the direct injected power and the reception plate power for single-contact sources using five excitation positions from S1 to S5 for FEM (see Figure 5-4) and two excitation positions S1 and S5 for measurements (see also Figure 5-4 or Figure 4-13) considering all nodes and grid points respectively. Note that for measurements, the reception plate power could not be evaluated at 20 Hz since the force signal injected by the shaker was not sufficiently strong (see Figure 3-3) to give velocity data well above the background noise (it was ≤ 6 dB).

For FEM in Figure 5-5a, it can be seen that the absolute difference between the direct injected power and the reception plate power is ≤ 1.5 dB over the entire frequency range from 20 Hz to 2 kHz. This indicates that the mesh size with element dimensions less than one-eighth of the bending wavelength (upper-frequency limit at 2 kHz) is sufficiently small, and the loss factor applied at low frequencies leads to a reasonable estimate. In addition, Figure 5-5a shows that at low frequencies where only rigid body modes occur within the 20 and 25 Hz bands, the errors are similar to higher frequencies where there are only bending modes. Similarly, the 31.5 and 40 Hz or 63 and 80 Hz bands have an absolute difference of less than 1 dB, although there are neither rigid body nor bending modes predicted in these bands.

Concerning the experimental set-up, Figure 5-5b shows the difference between the direct injected power and the reception plate power from all regular grid points for which the absolute difference occurs with 2.9 dB below 100 Hz where there are only rocking modes and the first two bending modes. This error reduces to an absolute difference of 1.3 dB between 100 Hz and 2 kHz. However, the tonal component in the input force of the shaker caused by the suspension

resonance at ≈ 34 Hz (refer back to Figure 3-3) does not lead to larger errors in the 31.5 Hz band since the underestimation is only ≈ 2 dB. This error with an underestimation of ≈ 2 dB continues in the 40 Hz band in which there is no mode to the 50 Hz band in which are located the first two bending modes at frequencies of 45.9 and 49.4 Hz. However, the error rises up to 3 dB in the 63 and 80 Hz bands where there are also no modes since the third bending mode is predicted at 93.5 Hz, which falls in the 100 Hz band. Between 100 Hz and 2 kHz, where at least one mode occurs in each band (see Figure 4-4), the absolute difference decreases to 1.3 dB.

Note that the two lowest bending modes fall in the 50 Hz band, which is usually the lowest frequency used with the reception plate approach according to EN 15657 [35]. The FEM and measurement results indicate that the highly damped whole body and rocking modes in the 20 and 25 Hz bands are useful in extending the frequency range of the reception plate to lower frequencies. In addition, the presence of the highly damped rigid body modes positively impacts the modal plate response by avoiding significant errors in the reception plate power between the whole body mode at 20.1 Hz and the first bending mode at 45.9 Hz. Hence, if the plate suspension is well-designed, rigid body modes have a beneficial effect on the accuracy of the reception plate power.

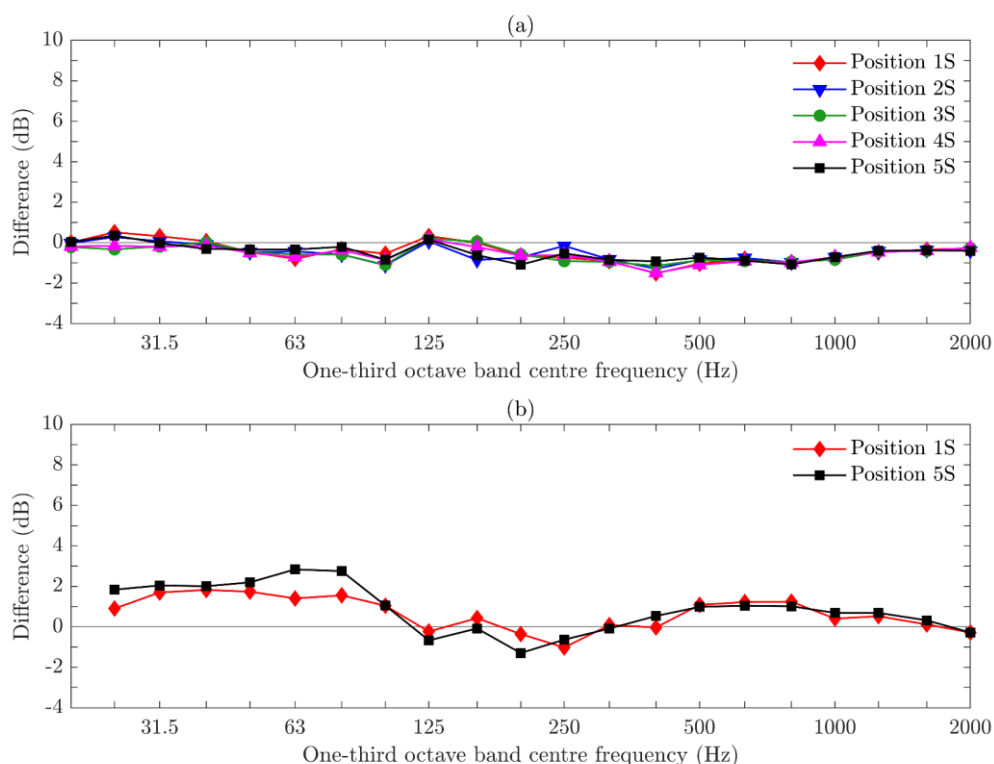


Figure 5-5. Reception plate using partial coverage with viscoelastic material: Difference between the direct injected power and the reception plate power with plate velocities using (a) average of all nodes from FEM predictions of a single-contact source for excitation positions 1S, 2S, 3S, 4S and 5S and (b) average of all grid points from measurements of a single-contact source for excitation positions 1S and 5S.

A subsequent step is to assess the degree of differences in the reception plate power that might occur when sampling only in the central zone positions (≥ 0.5 m away from boundaries). For FEM, Figure 5-6a shows that the reception plate power is underestimated in the frequency bands from 20 to 250 Hz with the largest difference of 7.8 dB in the 63 Hz band. This is significantly different to the differences of ≤ 1.3 dB when the reception plate power is determined from all nodes. The same problem occurs with measurements (see Figure 5-6b) where there are also large underestimates of the reception plate power in the same order of magnitude below 250 Hz (the largest value difference is 9.3 dB at 80 Hz) using only the central zone positions (≥ 0.5 m away from boundaries) from all grid points. It follows from this that it is not suitable to assess the reception plate

power from a sampling strategy based on the use of only central zone positions, which has already been noted in references [30, 33].

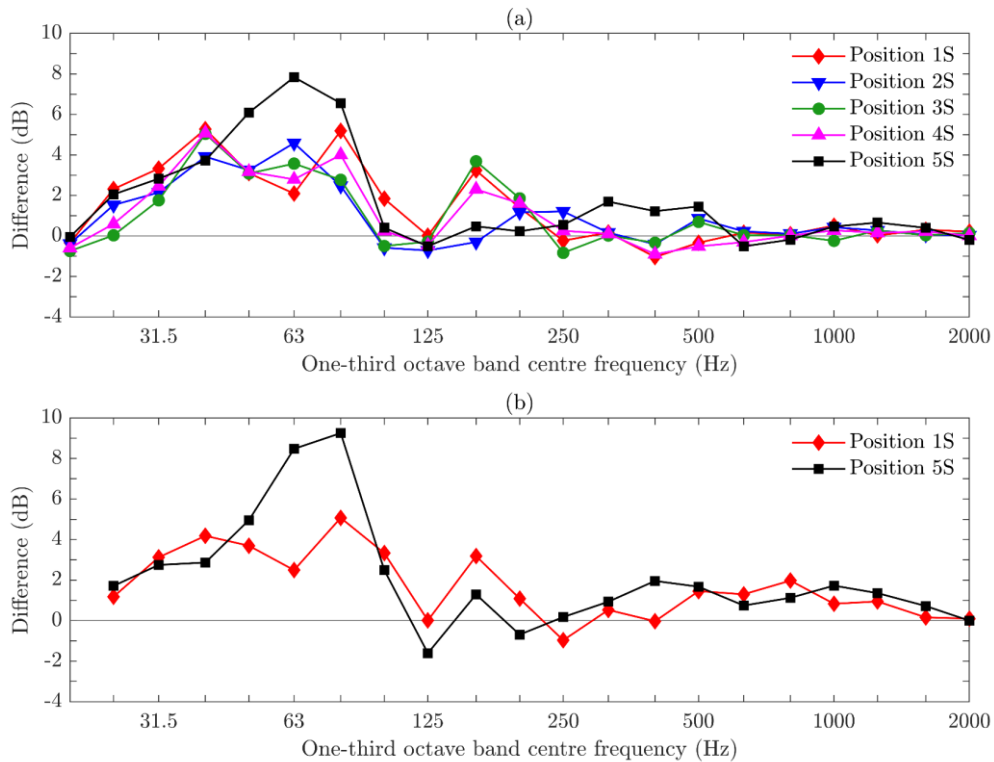


Figure 5-6. Reception plate using partial coverage with viscoelastic material: Difference between the direct injected power and the reception plate power with plate velocities using (a) average of nodes in the central zone (≥ 0.5 m away from boundaries) from FEM predictions of a single-contact source for excitation positions 1S, 2S, 3S, 4S and 5S and (b) average of grid points in the central zone (≥ 0.5 m away from boundaries) from measurements of a single-contact source for excitation positions 1S and 5S.

Using only the four corner positions, FEM data in Figure 5-7a show that the reception plate power is overestimated at and above the 25 Hz band with an average absolute difference of ≈ 9.2 dB between 100 Hz and 2 kHz (the largest absolute difference is 13.8 dB at 500 Hz). For experimental data in Figure 5-7b, very similar results are obtained with a large overestimate over the entire frequency range that reaches a plateau at 100 Hz with an absolute difference of ≈ 7.7 dB (the largest difference is 10.7 dB at 125 Hz) when only the four corner grid points are sampled. This illustrates that sampling only in the corners will

not improve low-frequency estimates. Hence, central zone and corner and/or edge positions have to be included in the sampling strategy.

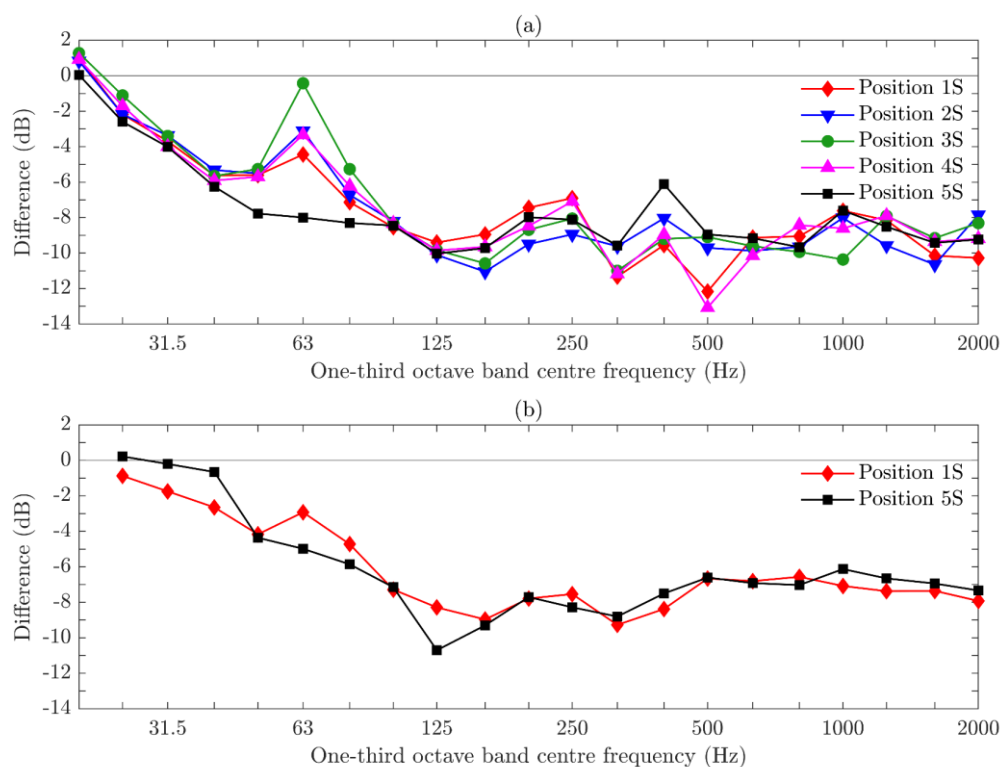


Figure 5-7. Reception plate using partial coverage with viscoelastic material: Difference between the direct injected power and the reception plate power with plate velocities using (a) average of the four corner nodes from FEM predictions of a single-contact source for excitation positions 1S, 2S, 3S, 4S and 5S and (b) average of grid points of the four corners from measurements of a single-contact source for excitation positions 1S and 5S.

From FEM investigations, it can be seen in Figure 5-8a that the empirical weighting was a reasonable approach. Note that the variation from 10 different random sets of velocity positions gives 95% confidence intervals with typical values <1 dB. This suggests that the approach is highly repeatable. However, below 100 Hz, where the mode count is low and the response of the reception plate is dominated by well-separated modes, this approach tends to have the largest absolute difference of up to 4.4 dB. At and above 100 Hz, the mode count increases to be at least one mode in each band, and the largest absolute difference improves moderately to 2.6 dB. For measurements, it can be seen in Figure 5-8b

that similar results occur with the largest absolute difference being 2.9 dB between 25 Hz and 2 kHz. The 95% confidence intervals from 10 different random sets of plate velocity positions achieve the typical <1 dB for measurements which corresponds to the 95% confidence intervals from FEM data.

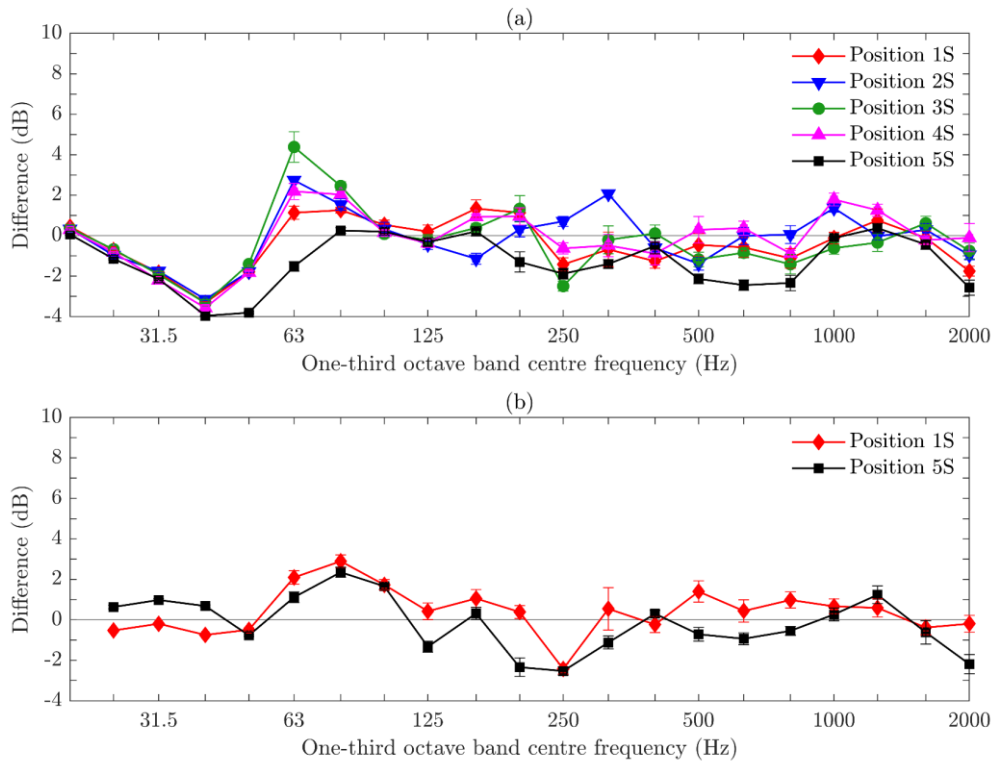


Figure 5-8. Reception plate using partial coverage with viscoelastic material: Difference between the direct injected power and the reception plate power with plate velocities calculated using empirical weighted average from (a) FEM predictions of a single-contact source for excitation positions 1S, 2S, 3S, 4S and 5S and (b) measurements of a single-contact source for excitation positions 1S and 5S. NB The 95% confidence intervals are shown from 10 different random sets of plate velocity positions that satisfy the area weighting requirements.

Using the area-weighted approach for sampling velocities, the results from FEM in Figure 5-9a show that larger differences, which occurred with the empirical weighting, can be avoided between 20 Hz and 2 kHz, which is indicated by an absolute difference of 1.2 dB. Figure 5-9b shows that this also applies to measurements using an area-weighted averaged velocity level for estimating the reception plate power, for which the largest difference is 2.0 dB between 25 Hz and 2 kHz. For FEM and measurements, the 95% confidence intervals similar to the empirical weighting are typically <1 dB for 10 different random sets of plate velocity positions.

In addition, the tonal component in the input force, which results from the shaker's suspension resonance at ≈ 34 Hz (refer back to Figure 3-3), does not produce a significantly larger error in either sampling approach compared to other bands without broadband noise below 50 Hz (shaker with a tonal component in the 31.5 Hz band). At and above 50 Hz, it was found that the error of ± 2.9 dB using the empirical weighted average velocities for the reception plate power is slightly larger (refer back to Figure 5-8b) than the error of ± 2.0 dB for the reception plate power based on area-weighted average velocities (refer back to Figure 5-9b). Hence, a good estimate of the reception plate power is not compromised by a force input from a source driven by broadband noise with a low-frequency tonal component.

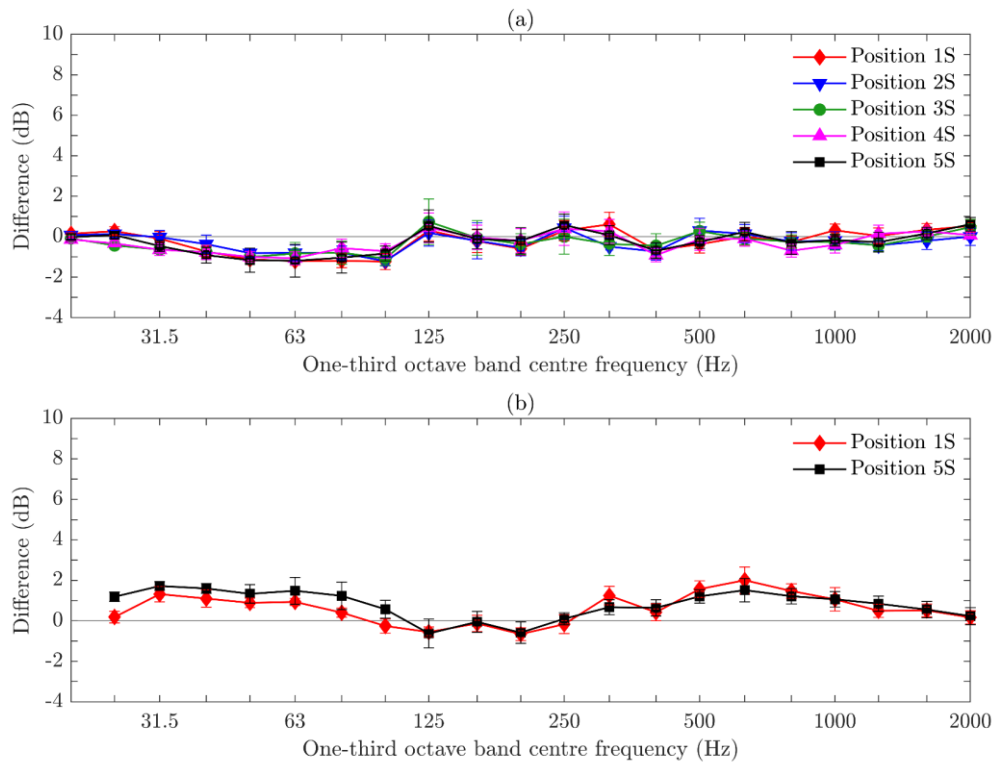


Figure 5-9. Reception plate using partial coverage with viscoelastic material: Difference between the direct injected power and the reception plate power with plate velocities calculated using area-weighted average from (a) FEM predictions of a single-contact source for excitation positions 1S, 2S, 3S, 4S and 5S and (b) measurements of a single-contact source for excitation positions 1S and 5S. NB The 95% confidence intervals are shown from 10 different random sets of plate velocity positions that satisfy the area weighting requirements.

Both numerical and experimental investigations on the reception plate power indicate that the use of the area weighting reduces the error in the reception plate power over the entire frequency range. Hence, due to its generality and accuracy, the remainder of this section focuses on the area-weighted approach for further numerical experiments of single- and multiple-contact sources.

To look at the effect of damping on rigid body modes, FEM is now used to investigate changes to the damping by ignoring the viscoelastic supports (i.e. assuming free plate boundaries) and changing the viscoelastic material from partial coverage to full coverage. For both FEM models, the comparison between

the direct injected power and the reception plate power is shown in Figure 5-10 using the area-weighting approach.

Figure 5-10a displays the comparison between both powers for the reception plate with no constraints. In Section 4.4.1, it was seen that the FEM model of a reception plate with free boundaries did not correlate with measurements in terms of eigenfrequencies and mode shapes. The lack of viscoelastic support results in rigid body modes near 0 Hz. For this type of reception plate, the largest errors occur below 80 Hz with up to ≈ 8.7 dB in the region of the rigid body modes and up to ≈ 4 dB in the region of the bending modes. This is due to the lack of heavily damped supports and therefore zero frequency and zero stiffness matrix rigid body modes. Thus, the lowest valid frequency of 20 Hz, which was found for the reception plate using partial coverage with viscoelastic material, does not hold for a reception plate with no constraints (free boundaries). However, above 80 Hz, the error reduces to an absolute difference of ≈ 1.6 dB when there is at least one mode in each one-third octave band which approaches the results of the reception plate using partial coverage with viscoelastic material.

In Section 4.4.2, it was noted that full coverage potentially introduces problems in numerically and/or experimentally determining the damping below 125 Hz. This is because the highly damped rigid body modes are moved into the 50 Hz band, which has the first two bending modes and causes a modal response that tends to approximate the mobility of an infinite plate below 125 Hz (refer back to Figure 4-6). Hence, Figure 5-10b only allows comparison between both powers between 125 Hz and 2 kHz. The error is 1.3 dB which is similar to the results for the reception plate using partial coverage with viscoelastic material.

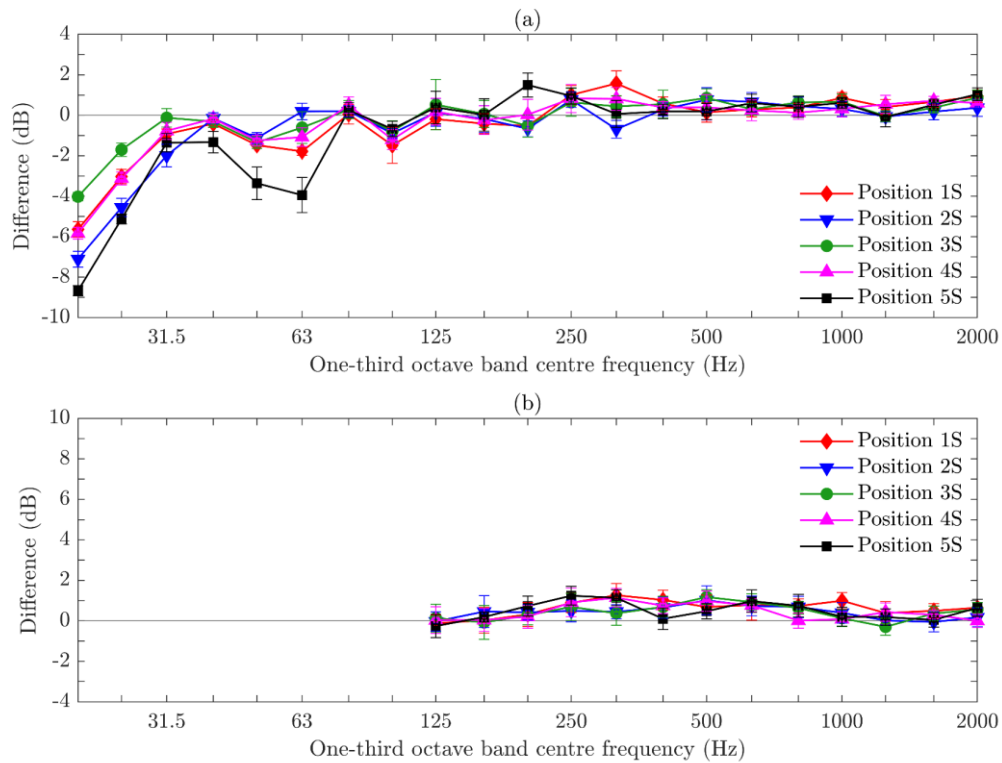


Figure 5-10. Reception plate designs that differ from the reception plate using partial coverage with viscoelastic material: FEM predictions of a single-contact source for excitation positions 1S, 2S, 3S, 4S and 5S – Difference between the direct injected power and the reception plate power using plate velocities calculated from area-weighted average in terms of (a) a reception plate with free boundaries and (b) a reception plate using full coverage with viscoelastic material. NB The 95% confidence intervals are shown from 10 different random sets of plate velocity positions that satisfy the area weighting requirements.

It can be concluded that the above-mentioned aspects of damping illustrate that the low damping for the reception plate with free boundaries leads to rigid body modes close to zero frequency due to the zero stiffness matrix. Whilst excessively high damping caused by unity viscoelastic material distribution underneath the reception plate area gives rigid body modes that are shifted into the 50 Hz band in which the first two bending modes are. For the plate with free boundaries, this results in a loss factor that equals the internal loss factor of concrete (refer back to Section 2.5.2.1), which is problematic below 80 Hz (see Figure 5-10a) when determining the reception plate power. For the reception plate using full coverage with viscoelastic material, it is problematic because the

loss factor below 125 Hz cannot be determined with FEM and/or measurements (see Figure 4-8). This is in contradiction to the requirement for loss factor data which is necessary in order to be able to estimate adequately the reception plate power. For this reason, the use of a free vibrating reception plate without considering the viscoelastic supports or a reception plate resting on a full viscoelastic layer is not appropriate at low frequencies to reliably assess a sampling strategy for spatial average velocities. Hence, the use of FEM is appropriate to set up an optimal design of a reception plate with regard to the viscoelastic damping layout and/or different plate sizes and shapes.

5.3.3 Multiple-contact sources assessed by FEM

To address the investigation of multiple-contact sources using the reception plate approach, the phases of the forces applied between the four contacts (each contact is at the corner of a $0.6\text{ m} \times 0.6\text{ m}$ square) are assumed to be zero or random. At low frequencies, it is feasible for a zero-phase difference to occur with an increasing likelihood of random-phase with increasing frequency.

For zero-phase shifts between the contact forces, Figure 5-11a shows the difference between the direct injected power and the reception plate power using all nodes for parallel-to-plate edges aligned excitation positions 1MP, 2MP, 3MP and 4MP (Figure 5-4b). For sources located in the central zone that have forces with the zero-phase difference between the contacts, the reception plate power overestimates the direct injected power by $\approx 3.3\text{ dB}$ at 500 Hz. This is because at this frequency, the contact spacing of 0.6 m along each side is nearly one-half of the bending wavelength of the plate. In the contour plots of the velocity levels from Figure 5-11b, it is apparent that the highest velocity levels occur underneath the machine for sources in the central zone of the plate. This confirms that the central zone positioned sources with a zero-phase difference impose a high response on the reception plate by forcing a half-wavelength between the contacts. This problem does not occur with sources that have at least two excitation positions near corners or edges, which is indicated by an absolute

difference of ≈ 1.3 dB. The reason for this is that sources located close to corners/edges possess sufficiently different driving-point mobility in terms of magnitude and phase at the four interface contacts, and the modal response is usually high near excited corners/edges.

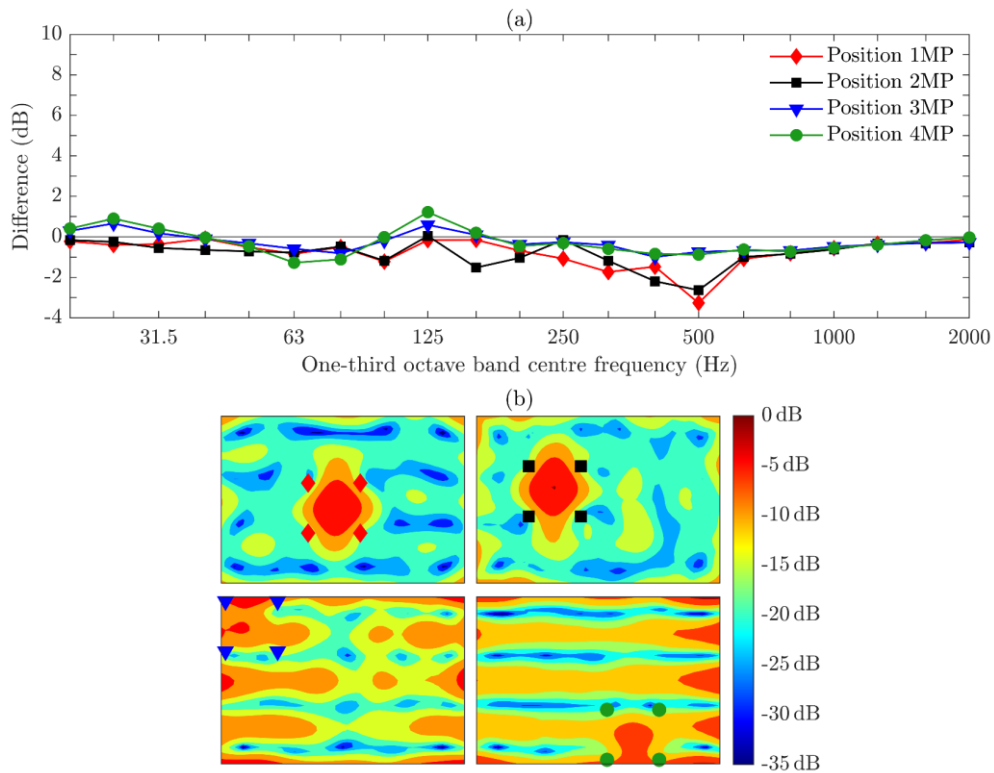


Figure 5-11. Reception plate using partial coverage with viscoelastic material: FEM predictions of a multiple-contact source having four contacts (i.e. white goods) and sides aligned parallel to the plate edges with zero-phase difference between the forces for excitation positions 1MP, 2MP, 3MP and 4MP using (a) the difference between the direct injected power and the reception plate power with averaged plate velocities from all nodes and (b) contour plots of velocity levels over the plate surface at 500 Hz with markers indicating the excitation positions.

For multiple-contact sources in the central zone, an overestimation of the reception plate power can be avoided using only velocity levels by excluding all nodes underneath the machine and up to 0.1 m away from the four contacts in $0.6 \text{ m} \times 0.6 \text{ m}$ square – see Figure 5-12a. Note that the nodes excluded with a radius of 0.1 m from each contact account for the reverberation distance (refer back to Figure 4-10). However, Figure 5-12b shows the contour plots where the

excluded nodes are indicated by a white area. At 500 Hz, the overestimation bias reduces to an absolute difference of ≈ 1.5 dB. This confirms that nodes in the area between the four contacts and up to 0.1 m away from the contacts based on the reverberation distance should be excluded. From this, it can be concluded that the reception plate power of multiple-contact sources near corners/edges with no nodes underneath the machine and up to 0.1 m away from the contacts tends to be underestimated compared to all nodes. Hence, these results demonstrate that it is beneficial to orientate multiple-contact sources, which have zero-phase contact forces and parallel alignment of their sides to the plate edges, in the central zone of the reception plate.

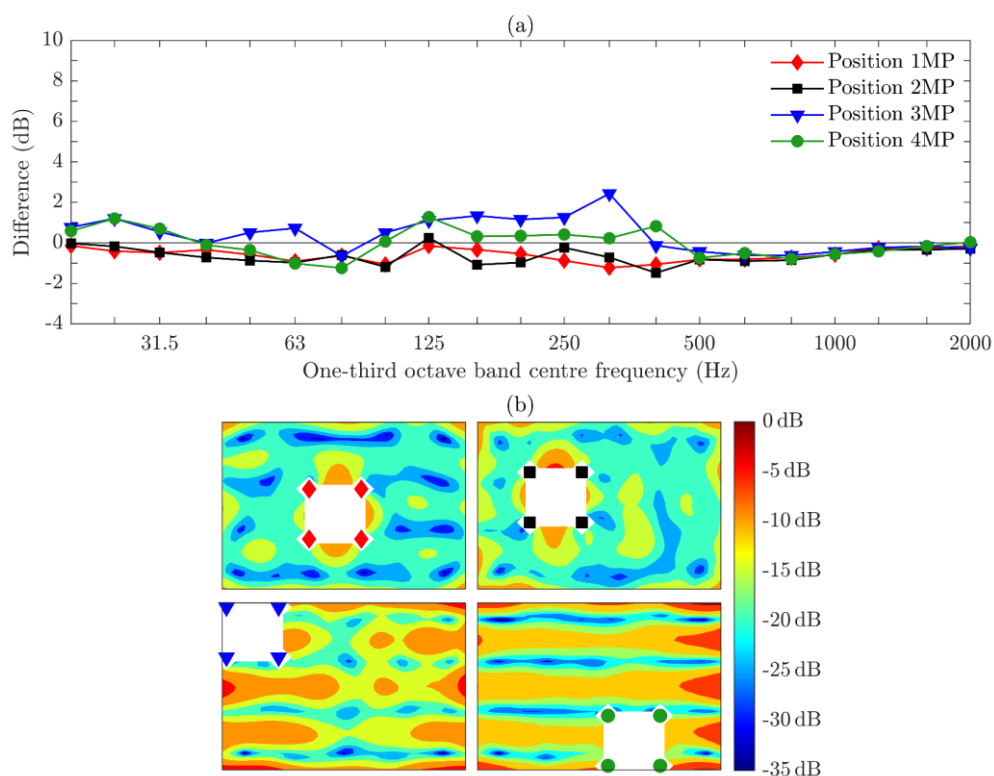


Figure 5-12. Reception plate using partial coverage with viscoelastic material: FEM predictions of a multiple-contact source having four contacts (i.e. white goods) and sides aligned parallel to the plate edges with zero-phase difference between the forces for excitation positions 1MP, 2MP, 3MP and 4MP using (a) the difference between the direct injected power and the reception plate power with averaged velocities by excluding all nodes underneath the machine and up to 0.1 m away from the four contacts (indicated by white area) and (b) contour plots of velocity levels over the plate surface at 500 Hz with markers indicating the excitation positions.

Similar results occur with the assumption of a zero-phase difference between the contact forces for multiple-contact sources aligned at an angle of 45° to the plate edges (Figure 5-4c). From Figure 5-13a, it can be seen that the absolute difference between the direct injected power and the reception plate power using all nodes has slightly improved to 2.0 dB compared to sources aligned parallel to the plate edges at 500 Hz. Considering that it is less practical to measure velocities underneath a machine and also to take into account the reverberation distance by measuring 0.1 m away from the four contacts, then the bias error from the sources in the central zone of the plate decreases to an absolute difference of ≈ 0.7 dB at 500 Hz. In contrast, sources located near corners/edges tend still to underestimate the reception plate power as shown in Figure 5-13b. These results indicate that positions near the edges and corners from multiple-contact sources under zero-phase forces at an angle to the plate edges should be avoided when excluding the nodes underneath the machine and up to 0.1 m away from the four contacts.

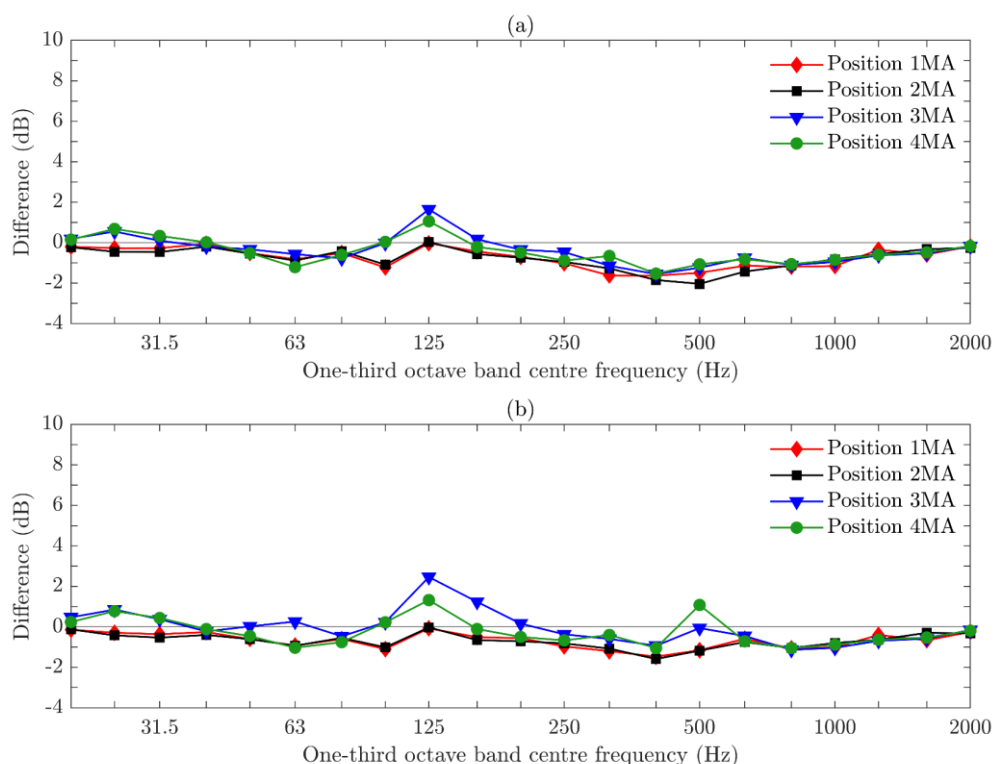


Figure 5-13. Reception plate using partial coverage with viscoelastic material: FEM predictions of a multiple-contact source having four contacts (i.e. white goods) and sides aligned at an angle to the plate edges with zero-phase difference between the forces for excitation positions 1MP, 2MP, 3MP and 4MP using the difference between the direct injected power and the reception plate power with averaged velocities (a) from all nodes and (b) by excluding all nodes underneath the machine and up to 0.1 m away from the four contacts.

Figure 5-14 shows the difference between the direct injected power and the reception plate power when the multiple-contact sources are aligned parallel to plate edges (Figure 5-4b) using the random-phase assumption for forces between the contacts. Regardless of where the sources are positioned on the reception plate, the results indicate close agreement within ± 1.5 dB when all nodes are used (see Figure 5-14a) or when all nodes underneath the machine are excluded up to 0.1 m away from the four contacts (see Figure 5-14b). By excluding nodes underneath the machine and up to 0.1 m away from the contacts, only sources located near corners/edges tend to have a slightly higher underestimation of the reception plate power up to ≈ 0.5 dB at low frequencies (particularly in the 25 Hz

band) compared to all nodes. This leads to the assumption that the variation in velocity over the plate surface caused by random-phase force excitation between the contacts is less critical for sources with sides aligned parallel to the plate edges to assess the reception plate power.

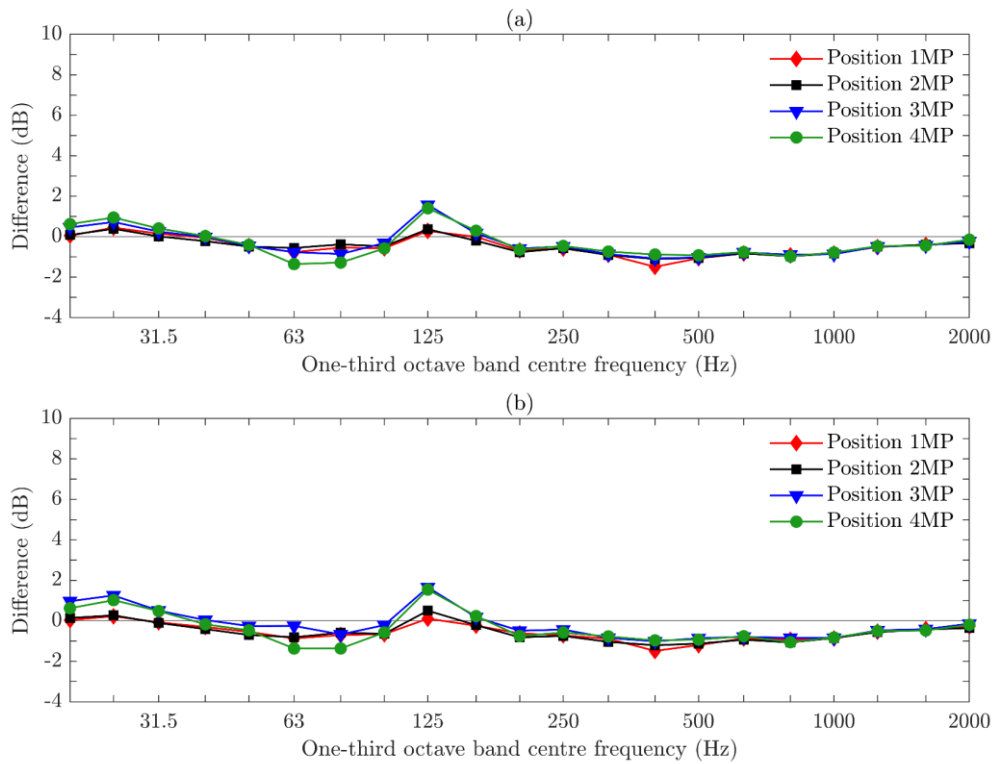


Figure 5-14. Reception plate using partial coverage with viscoelastic material: FEM predictions of a multiple-contact source having four contacts (i.e. white goods) and sides aligned parallel to the plate edges with random-phase difference between the forces for excitation positions 1MP, 2MP, 3MP and 4MP using the difference between the direct injected power and the reception plate power with averaged velocities (a) from all nodes and (b) by excluding all nodes underneath the machine and up to 0.1 m away from the four contacts.

The investigations of multiple-contact sources using zero-phase assumption show that the variation between the four contacts is larger for sources that are positioned parallel to the plate edges rather than at an angle to the plate edges. The source orientation on the reception plate with regard to the variation between the four contacts is less relevant when a random-phase difference between forces is applied. With multiple-contact sources, vibration locations may not be directly accessible in the area below the machine where potential bias for pronounced vibration levels due to zero-phase forces can occur. Therefore, positions in the area between the four contacts, typically the area directly underneath the machine for most domestic appliances (e.g. white goods or similar machines), should be excluded in order to avoid potential bias of high vibration levels. For the application of the sampling strategy, this means that the reception plate power is estimated using only, as noted, the area-weighted velocities by excluding all nodes underneath the machine and up to 0.1 m away from each contact based on the reverberation distance (refer back to Section 4.4.2).

Using the area weighting approach, Figure 5-15 shows the differences between the direct injected power and the reception plate power from all different applied phase differences between the four contacts and locations of the source on the reception plate. In the case of sources with zero-phase forces and sides that are aligned parallel to the plate edges, it can be seen that the largest absolute difference is ≈ 1.9 dB (see Figure 5-15a), which is decreased to ≈ 1.6 dB when the sources are orientated at an angle to the plate edges (see Figure 5-15b). For sources that are again aligned with sides parallel to the plate edges, but now have random-phase forces between the four contacts, the largest absolute difference is ≈ 2.2 dB (see Figure 5-15c). Hence, it can be concluded that multiple-contact sources with four contact points arranged in a square should preferably be located obliquely to the plate edges. But it is more important to average the results from several excitation positions to increase the accuracy of the reception plate method.

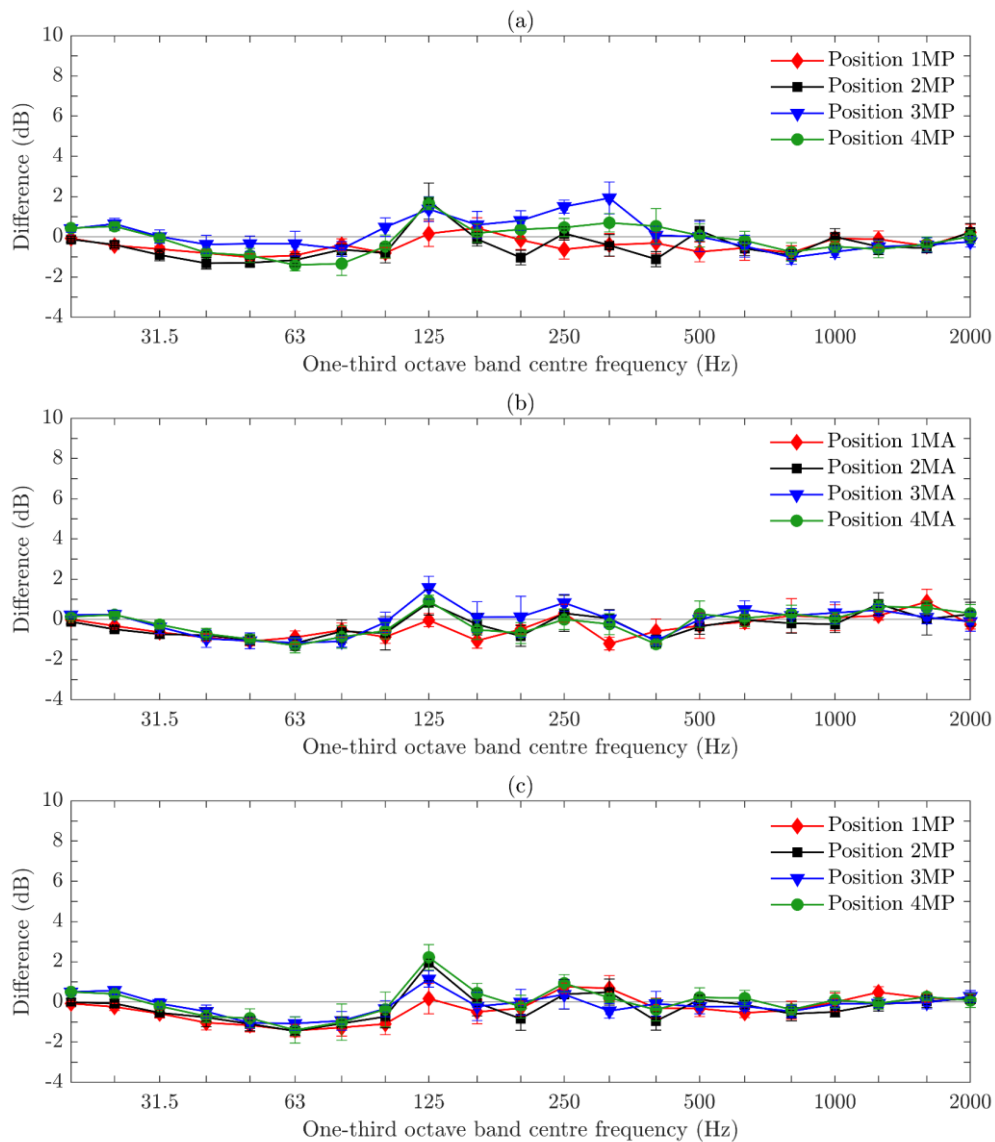


Figure 5-15. Reception plate using partial coverage with viscoelastic material: FEM predictions of a multiple-contact source having four contacts (i.e. white goods) – Difference between the direct injected power and the reception plate power calculated using the area-weighted velocity level by excluding all positions underneath the machine and up to 0.1 m away from each contact for (a) zero-phase forces with sides aligned parallel to the plate edges, (b) zero-phase forces with sides aligned to an angle to the plate edges and (c) random-phase forces with sides aligned parallel to the plate edges. NB The 95% confidence intervals are shown from 10 different random sets of plate velocity positions that satisfy the area weighting requirements.

5.4 Discussion

The empirical weighting is expected to be specific to an individual reception plate, whereas the area weighting can be treated as a more general approach. Both weighting approaches have been validated on an isolated reception plate according to EN 15657 [35], where the plate only rests on the viscoelastic supports around its edges. Note that other kinds of constraint (e.g. rigid) that deviate from the specifications in EN 15657 [35] might cause a different spatial variation in plate velocity; hence, the developed sampling strategies would need checking. This would make it necessary to investigate the spatial velocities using a fine regular grid over the plate surface with FEM or measurements. The area-weighting approach should be valid for the reception plates defined in EN 15657 [35] but for significantly larger plates (e.g. at least twice as large), it might be necessary to adjust the areas in Eq. (5.2).

For single-contact sources, the results show that the area weighting is preferable to the empirical weighting due to its generality and slightly better accuracy, particularly in the region of rigid body modes and bending modes below 100 Hz. Therefore, the area weighting approach is used to assess the empirical relationship between L_{Fmax} and short L_{eq} levels from the time-varying signals in Chapter 6, which is needed to predict L_{Fmax} levels in heavyweight buildings in Chapter 7. In Chapter 8, the empirical weighting approach is used for the case study of a toilet flush since the measurement data was not available to use the area-weighted approach.

5.5 Summary

This chapter investigated improvements to vibration sampling for the reception plate to reduce the uncertainty in the determination of the structure borne-sound power injected by single- and multiple-contact broadband sources. For single-contact sources, the comparison between the direct injected power

and the reception plate power from FEM and measurements indicated that only sampling velocity from positions in the central zone of the plate leads to underestimates of the reception plate power by up to ≈ 9 dB below 100 Hz. This results from the exclusion of velocity levels near corners and/or edges of the plate that are higher than those in the central zone.

Two sampling strategies were developed that combined measured velocities at corners and/or edges with the central zone. The first sampling strategy focused on an empirical weighting of velocities that would be specific to a particular reception plate. This approach combined sampling velocities in the four corners and the central zone using an empirical weighting factor that reduced the influence of the higher velocities of the corners with increasing frequency. The second strategy was a more general approach that used an area weighting based on sampling velocities in the corners, on the strips at the edges and in the central zone of the plate.

Measurements from single-contact sources were used to validate the two numerical devised sampling approaches. For single-contact sources, the reception plate power for the empirical weighting approach led to errors of up to ≈ 4.4 dB, while the area weighting approach gave errors up to 2 dB. Hence, the area weighting approach gives lower errors than previously established by Späh and Gibbs [33] below 100 Hz. To investigate a more realistic simulation of a machine with multiple contacts, the area-weighted approach was used with a four-contact simulated source. As with a single-contact source, this also resulted in errors up to 2 dB. The investigations showed that the area between the contacts (typically the area underneath the machine) and within the reverberation distance (≥ 0.1 m) should be excluded when the phase between the forces at the contacts are not known (which is a common situation). It was also found that multiple-contact sources with a rectangular arrangement between the contacts should preferably be aligned at an oblique angle to the plate edges.

Using a frequency sweep from 1 Hz to 2.5 kHz, the FEM model of the experimental set-up using partial coverage with viscoelastic material indicated

that the reception plate power is estimated with sufficient accuracy regardless of whether the vibrational response is determined in the region of the whole body, rocking or bending modes. In addition, the experimental work showed that a single-contact source excited by white noise with a low-frequency tonal component is valid to predict the injected structure-borne sound power even when the tonal component is in the frequency range (≈ 34 Hz) of the predominant rigid body modes. Hence, it could be shown that the lower frequency limit of 50 Hz can be extended down to 20 Hz (i.e. above the whole body mode caused by bouncing resonance due to viscoelastic supported plate with free edges). This reduction in the uncertainty at low frequencies by using these sampling strategies is beneficial because machinery often injects high levels of structure-borne sound power below 100 Hz.

6 Empirical relationships between L_{Fmax} and short L_{eq} for time-varying signals

6.1 Introduction

The characterisation of structure-borne sound sources is currently defined in EN 15657 [35] for steady-state operating conditions to provide input data for the prediction of sound levels according to EN 12354-5 [11] in adjacent rooms. However, there are many types of building machinery that operate under time-varying conditions for which many European countries require L_{Fmax} for the sound pressure level in adjacent rooms.

This chapter investigates whether the reception plate can be used to determine short (125 ms) L_{eq} vibration measurements in one-third octave bands from which L_{Fmax} as a room sound pressure level in the field situation can be estimated using an empirical correction. The aim is to determine an empirical correction for sound and vibration that could be used to estimate L_{Fmax} from short (125 ms) L_{eq} data using ramped noise signals. An assessment of the signal-processing carried out for these time-varying signals with PULSE to estimate $\max\{L_{eq,125ms}\}$ from L_{Fmax} , $L_{F,125ms}$ and $L_{eq,125ms}$ was given in Section 3.3.7.2, and the diffuse field assumptions are presented in Section 6.2 based on the definitions in Section 2.4.2. This approach is now applied to estimate an

empirical correction from $\max\{L_{\text{eq},125\text{ms}}\}$ to L_{Fmax} in Section 6.3, for which the time-varying signals are played directly into the measurement system and shaker on the reception plate and also the separating floor in the building-like situation. The empirical correction is the difference $L_{\text{Fmax}} - \max\{L_{\text{eq},125\text{ms}}\}$. In addition, this section also discusses the empirical correction obtained from the sound pressure level caused by the shaker injecting the time-varying structure-borne sound power into the floor, which is radiated as airborne sound into the receiving room in the building-like situation.

6.2 Diffuse field assumption for test constructions

To describe the 2D and 3D reverberant fields for the test constructions, it is necessary to determine the mean free path and the corresponding average time it takes for the wave energy to travel the mean free path (refer back to Section 2.4.2). This means that the test constructions should have a shorter time for waves to travel the mean free path than the 125 ms averaging time, so there is sufficient time to develop a reverberant field in order to be able to predict L_{Fmax} from $\max\{L_{\text{eq},125\text{ms}}\}$ measurements.

The mean free path is 1.83 m for the reception plate, 3.46 m for the concrete floor and 2.43 m for the receiving room in the building-like situation. Converting this distance into the time-to-mean free path gives a range from 5 ms at 50 Hz to 1 ms at 3.15 kHz for the reception plate and 8 ms at 50 Hz to 1 ms at 3.15 kHz for the separating floor in the building-like situation due to dispersive bending waves [71] and 7 ms over the entire frequency range for the room in the building-like situation due to constant sound waves (refer back to orientate on Figure 2-7). These times that correspond to the mean free paths are less than 1/16 of the 125 ms averaging time; hence, it is reasonable to consider the reception plate, floor and room in the building-like situation to assess the empirical correction.

6.3 Empirical correction from short L_{eq} to L_{Fmax}

This section addresses the relationship between short L_{eq} and L_{Fmax} using ramped noise signals to assess an empirical correction based on velocity and sound pressure levels in terms of $\max\{L_{\text{eq},125\text{ms}}\}$ and L_{Fmax} as has been described in Section 3.3.7. Experiments are used to approach an empirical correction from signals that are played directly into the measurement system and subsequently from the experimental work on the reception plate as well as on the concrete floor and in the receiving room in the building-like situation. These measurement data are used to estimate a specific empirical correction based on all the different ramped noise signals (Section 6.3.1) and an empirical correction with a single number from the results of the specific empirical correction of all ramp signals for white noise (Section 6.3.2).

6.3.1 Specific empirical correction for known time-varying signals

The time-varying signals are created using ramped white noise (refer back to Section 3.3.7.1). Therefore, white noise is considered as a steady-state signal and is usually measured using L_{eq} , but the random fluctuations mean that when considering $\max\{L_{\text{eq},125\text{ms}}\}$, it is feasible that there would be an empirical correction if L_{Fmax} was measured.

Hence, the first step is to use white noise without any ramp as a benchmark to assess whether it might be reasonable to use an empirical correction with the time-varying signals of ramped white noise. Figure 6-1 shows $L_{\text{Fmax}} - \max\{L_{\text{eq},125\text{ms}}\}$ in one-third octave bands for steady-state white noise played directly into the measurement system. The correction tends towards 0 dB with increasing frequency. The minimum, maximum and frequency average values are 0.5, 3.0 and 1.5 dB respectively.

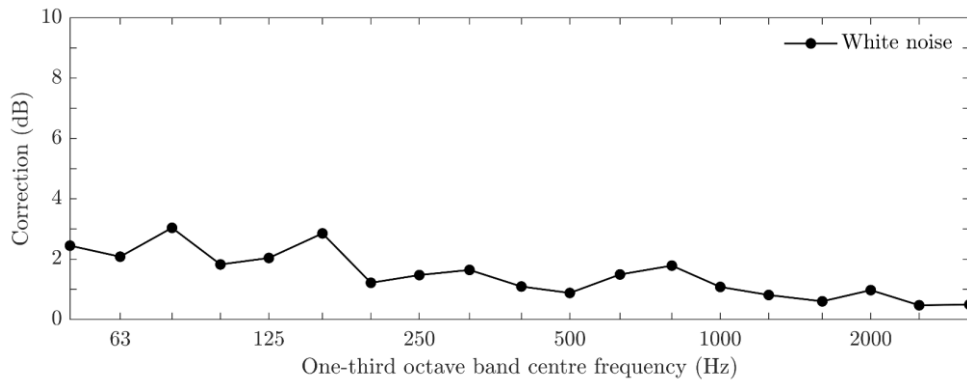


Figure 6-1. Wav file of 20 s white noise: $L_{F_{\max}} - \max\{L_{\text{eq},125\text{ms}}\}$ using the signal played directly into the measurement system.

For ramped noise signals, the frequency-dependent correction in one-third octave bands (referred to as the specific empirical correction) is shown in Figure 6-2 to Figure 6-6, for which the minimum, maximum and frequency average values are given in Table 6-1 to Table 6-5. All these results differ significantly from the benchmark value of 1.5 dB for white noise, and therefore it is reasonable to use a correction term for all these types of ramped white noise.

For ramp durations ≥ 500 ms, the average correction values are similar to within ≈ 1.1 dB. In general, the 10 dB ramp level gave empirical corrections that were slightly lower than for the 20/30/40 dB ramp levels. This was most evident with the 125 ms ramp duration where the 10 dB ramp level resulted in a correction that was ≈ 2.6 dB below that for the 20/30/40 dB ramp levels – see Figure 6-2. However, the difference between the average correction for the 10 dB ramp level and 20/30/40 dB ramp levels reduces to ≈ 1.2 dB for ramp durations of ≥ 500 ms – see Figure 6-3 to Figure 6-6. Hence, the correction for the 10 dB ramp level is smaller than with the 20/30/40 dB ramp levels, where the latter are similar to each other. This feature occurs when the signal is directly played into the measurement system, into the shaker on the reception plate and the concrete floor in the building-like situation where the radiated power in the receiving room adopts a very similar level course. Below 125 Hz, the 10 dB ramp level with increasing ramp duration approaches the 20/30/40 dB ramp

levels, particularly for ramp durations from 500 ms to 5 s, but still differs above 125 Hz.

The shortest ramp duration of 125 ms was the same length as the exponential averaging time for $L_{F_{\max}}$ and the linear averaging time of $\max\{L_{\text{eq},125\text{ms}}\}$. For this reason, the empirical correction might have been expected to vary significantly between the direct signal, the reception plate, the floor and the room; however, the average corrections were similar and within ≈ 1.1 dB.

Regardless of whether the signals are obtained from the signal directly played into the measurement system, velocity levels in terms of the signal played into a shaker on the reception plate and the concrete floor in the building-like situation or sound pressure levels (radiated from the floor due to shaker vibration) in the field situation, the curves for the empirical correction show no strong variation at and above 125 Hz. This makes it possible to list the minimum, maximum and frequency average values from the curves of various ramp durations with the several ramp levels in Table 6-1 to Table 6-5.

These results show that the signal that is directly played into the measurement system has an average correction of ≈ 4.8 dB for the 10 dB ramp levels for all ramp durations. The average corrections of 20/30/40 dB ramp levels are ≈ 7.6 dB, ≈ 6.0 dB, ≈ 6.1 dB, ≈ 5.9 dB and ≈ 6.0 dB for the 125 ms, 500 ms, 1 s, 2 s and 5 s ramp durations respectively.

The corrections determined on the reception plate are similar to those when the signal is played directly into the measurement system. For all ramp durations with 10 dB ramp levels, there is an average correction of ≈ 5.1 dB, which differs by 0.3 dB from the signal when it is directly played into the measurement system. The 20/30/40 dB ramp levels have average corrections of ≈ 7.4 dB, ≈ 6.5 dB, ≈ 6.2 dB, ≈ 6.2 dB and ≈ 6.4 dB for the 125 ms, 500 ms, 1 s, 2 s and 5 s ramp durations respectively. These results differ from the signal that is directly played into the measurement system only by ≈ 0.5 dB.

Similar results occur for measurements on the concrete floor in the building-like situation in which the average correction is ≈ 4.9 dB for 10 dB ramp levels of all ramp durations, and the average corrections with the 20/30/40 dB ramp levels are ≈ 7.1 dB, ≈ 6.4 dB, ≈ 6.1 dB, ≈ 6.0 dB and ≈ 6.2 dB according to 125 ms, 500 ms, 1 s, 2 s and 5 s ramp durations respectively. Once again, the results are within ≈ 0.5 dB when compared to the signal that is played directly into the measurement system.

The same pattern is also seen for measurements in the receiving room in the building-like situation. For the 10 dB ramp level, there is an average correction of ≈ 5.0 dB when all ramp durations are considered. With ramp levels of 20/30/40 dB, these give average corrections of ≈ 6.9 dB, ≈ 6.6 dB, ≈ 6.3 dB, ≈ 6.2 dB and ≈ 6.4 dB corresponding to ramp durations with 125 ms, 500 ms, 1 s, 2 s and 5 s respectively. These values are within ≈ 1 dB of the correction when the signal is directly played into the measurement system.

In summary, for the specific empirical correction can be stated that for ramp levels of (a) 10 dB for all ramp durations it is reasonable to assume that $L_{Fmax} - \max\{L_{eq,125ms}\} \approx 5$ dB, (b) 20, 30 and 40 dB for a ramp duration of 125 ms it is reasonable to assume that $L_{Fmax} - \max\{L_{eq,125ms}\} \approx 7.5$ dB and (c) 20, 30 and 40 dB with ramp durations ≥ 500 ms it is reasonable to assume that $L_{Fmax} - \max\{L_{eq,125ms}\} \approx 6$ dB.

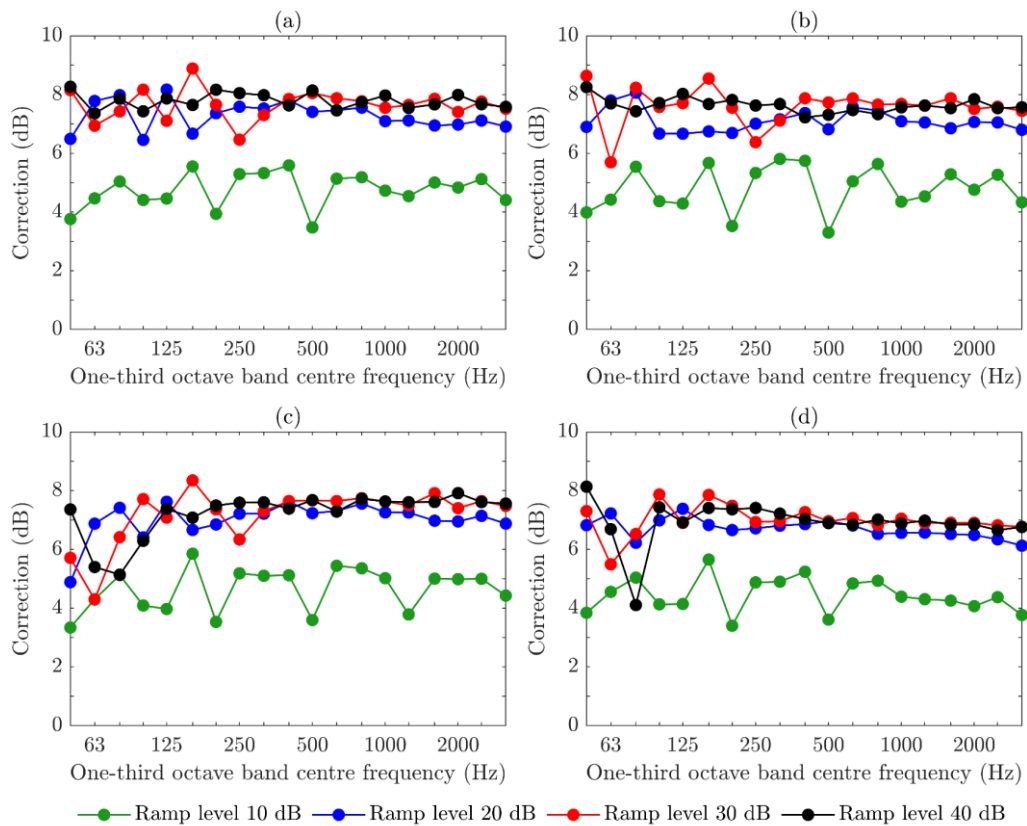


Figure 6-2. Wav files of 125 ms ramp duration with ramp levels of 10/20/30/40 dB: The specific empirical correction, $L_{F_{\max}} - \max\{L_{\text{eq},125\text{ms}}\}$, is shown for (a) the signal directly played into the measurement system, (b) the vibration field of the signal played into the shaker on the reception plate, (c) the vibration field of the signal played into the shaker on the concrete floor in the building-like situation and (d) the sound field in the receiving room from the signal played into the shaker on the concrete floor in the building-like situation.

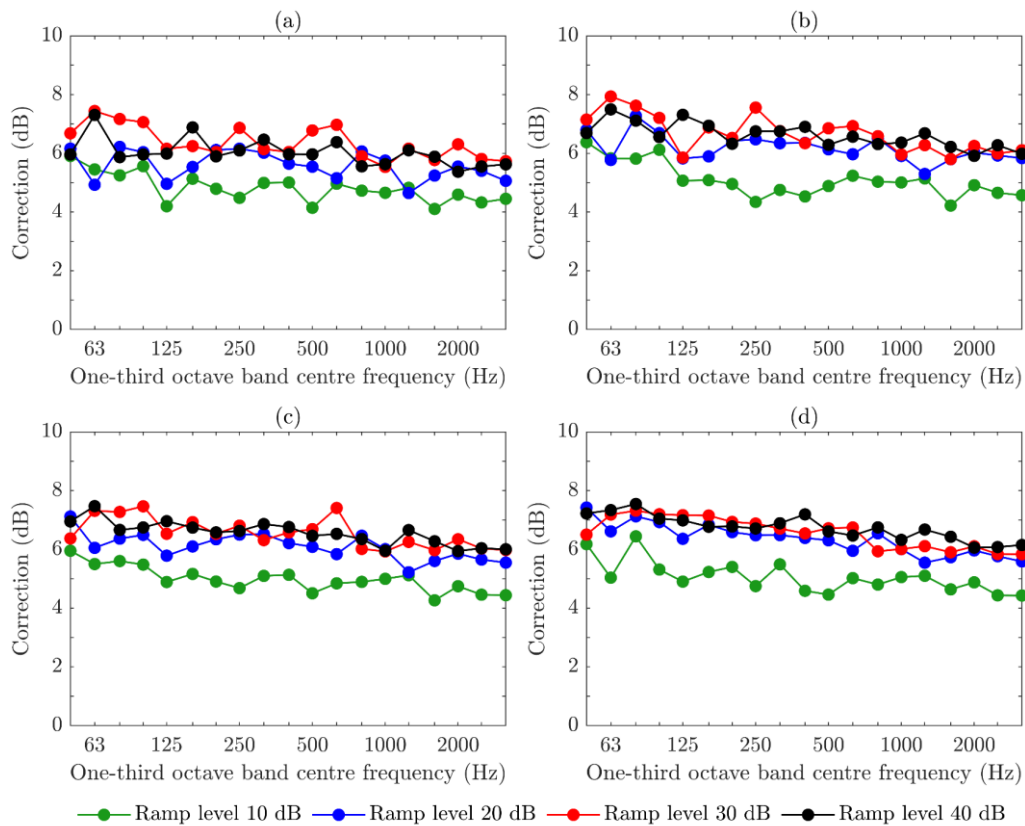


Figure 6-3. Wav files of 500 ms ramp duration with ramp levels of 10/20/30/40 dB: The specific empirical correction, $L_{F_{\max}} - \max\{L_{eq,125ms}\}$, is shown for (a) the signal directly played into the measurement system, (b) the vibration field of the signal played into the shaker on the reception plate, (c) the vibration field of the signal played into the shaker on the concrete floor in the building-like situation and (d) the sound field in the receiving room from the signal played into the shaker on the concrete floor in the building-like situation.

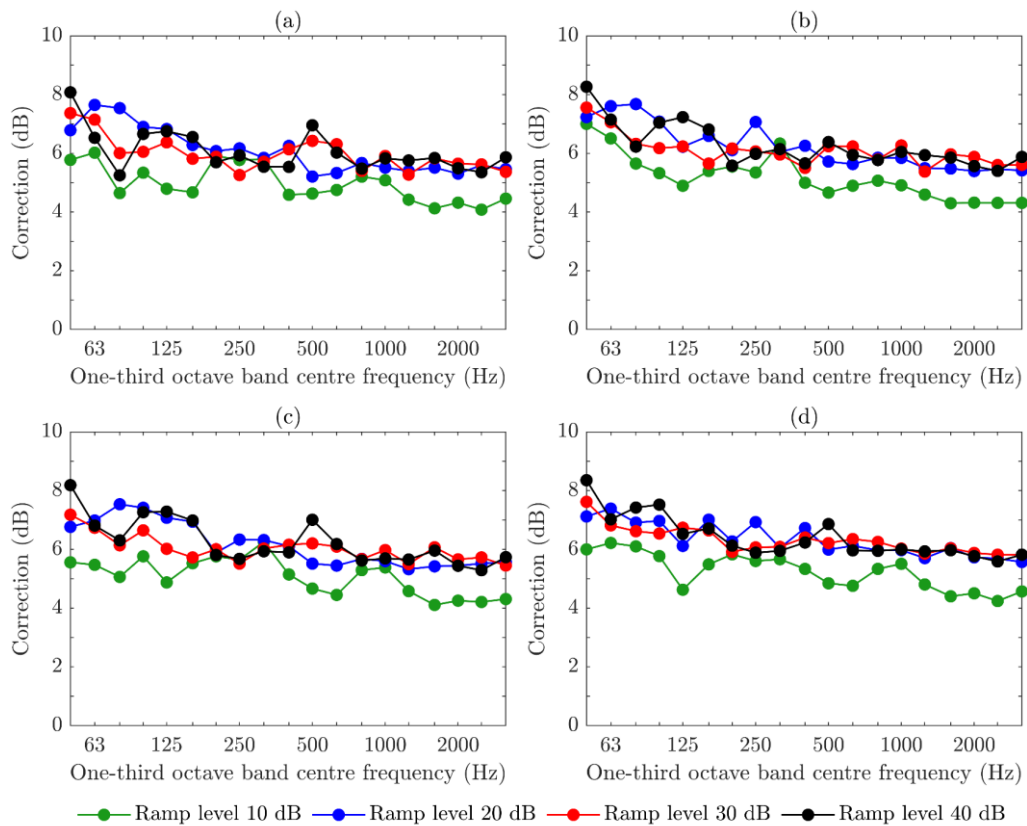


Figure 6-4. Wav files of 1 s ramp duration with ramp levels of 10/20/30/40 dB: The specific empirical correction, $L_{F_{\max}} - \max\{L_{eq,125ms}\}$, is shown for (a) the signal directly played into the measurement system, (b) the vibration field of the signal played into the shaker on the reception plate, (c) the vibration field of the signal played into the shaker on the concrete floor in the building-like situation and (d) the sound field in the receiving room from the signal played into the shaker on the concrete floor in the building-like situation.

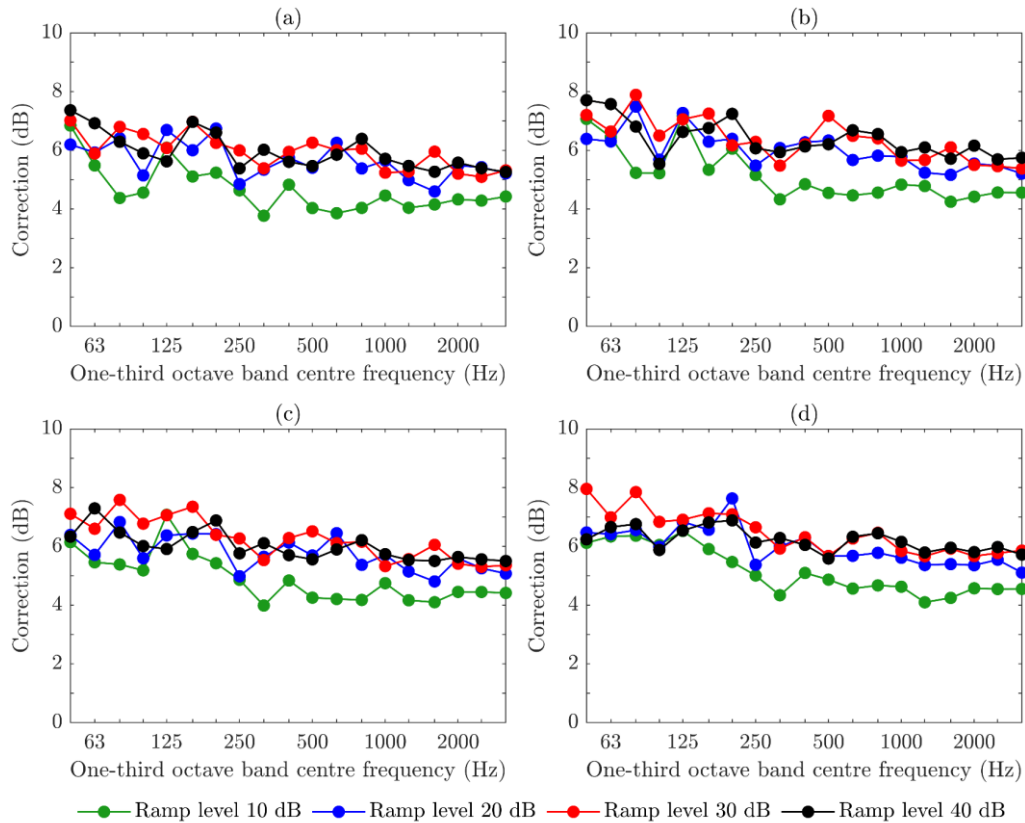


Figure 6-5. Wav files of 2 s ramp duration with ramp levels of 10/20/30/40 dB: The specific empirical correction, $L_{Fmax} - \max\{L_{eq,125ms}\}$, is shown for (a) the signal directly played into the measurement system, (b) the vibration field of the signal played into the shaker on the reception plate, (c) the vibration field of the signal played into the shaker on the concrete floor in the building-like situation and (d) the sound field in the receiving room from the signal played into the shaker on the concrete floor in the building-like situation.

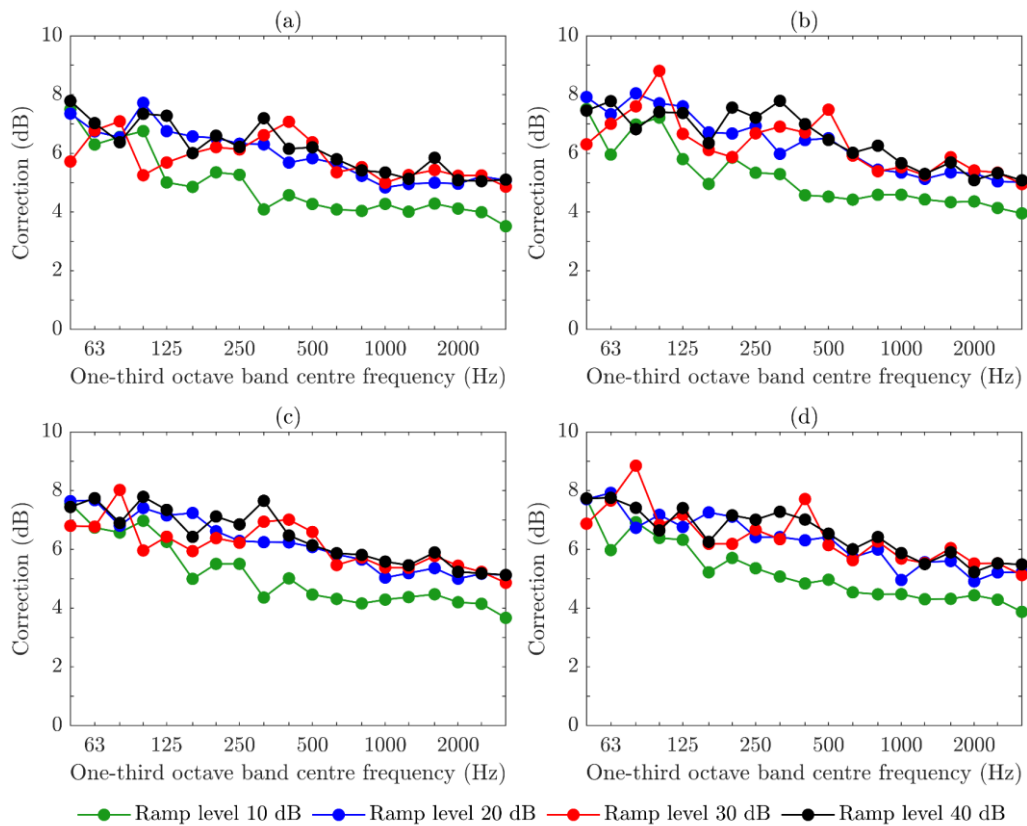


Figure 6-6. Wav files of 5 s ramp duration with ramp levels of 10/20/30/40 dB: The specific empirical correction, $L_{F_{\max}} - \max\{L_{eq,125ms}\}$, is shown for (a) the signal directly played into the measurement system, (b) the vibration field of the signal played into the shaker on the reception plate, (c) the vibration field of the signal played into the shaker on the concrete floor in the building-like situation and (d) the sound field in the receiving room from the signal played into the shaker on the concrete floor in the building-like situation.

Table 6-1. Wav files of 125 ms ramp duration with ramp levels of 10/20/30/40 dB: The specific empirical correction, $L_{Fmax} - \max\{L_{eq,125ms}\}$, with regard to minimum (MIN), maximum (MAX) and average (AVG) levels.

Ramp level	Wav files directly played into the measurement system to determine signal levels (estimated)			Wav files played into the shaker on the reception plate to determine plate velocity levels (estimated)		
	MIN (dB)	MAX (dB)	AVG (dB)	MIN (dB)	MAX (dB)	AVG (dB)
10 dB	3.5	5.6	4.7	3.3	5.8	4.8
20 dB	6.5	8.2	7.3	6.7	8.1	7.1
30 dB	6.5	8.9	7.7	5.7	8.6	7.6
40 dB	7.4	8.3	7.8	7.2	8.3	7.6
Ramp level	Wav files played into the shaker on the concrete floor in the building-like situation to determine plate velocity levels (estimated)			Wav files played into the shaker on the concrete floor in the building-like situation to determine room sound pressure levels (estimated)		
	MIN (dB)	MAX (dB)	AVG (dB)	MIN (dB)	MAX (dB)	AVG (dB)
10 dB	3.3	5.9	4.6	3.4	5.7	4.4
20 dB	4.9	7.6	7.0	6.1	7.4	6.7
30 dB	4.3	8.3	7.2	5.5	7.9	7.0
40 dB	5.1	7.9	7.2	4.1	8.1	6.9

Table 6-2. Wav files of 500 ms ramp duration with ramp levels of 10/20/30/40 dB: The specific empirical correction, $L_{Fmax} - \max\{L_{eq,125ms}\}$, with regard to minimum (MIN), maximum (MAX) and average (AVG) levels.

Ramp level	Wav files directly played into the measurement system to determine signal levels (estimated)			Wav files played into the shaker on the reception plate to determine plate velocity levels (estimated)		
	MIN (dB)	MAX (dB)	AVG (dB)	MIN (dB)	MAX (dB)	AVG (dB)
10 dB	4.1	5.9	4.8	4.2	6.4	5.1
20 dB	4.6	6.2	5.6	5.3	7.3	6.2
30 dB	5.5	7.4	6.4	5.8	7.9	6.7
40 dB	5.4	7.3	6.0	5.9	7.5	6.6

Ramp level	Wav files played into the shaker on the concrete floor in the building-like situation to determine plate velocity levels (estimated)			Wav files played into the shaker on the concrete floor in the building-like situation to determine room sound pressure levels (estimated)		
	MIN (dB)	MAX (dB)	AVG (dB)	MIN (dB)	MAX (dB)	AVG (dB)
10 dB	4.3	6.0	5.0	4.4	6.4	5.1
20 dB	5.2	7.1	6.1	5.5	7.4	6.4
30 dB	5.9	7.5	6.6	5.8	7.3	6.6
40 dB	5.9	7.5	6.6	6.1	7.5	6.7

Table 6-3. Wav files of 1 s ramp duration with ramp levels of 10/20/30/40 dB: The specific empirical correction, $L_{Fmax} - \max\{L_{eq,125ms}\}$, with regard to minimum (MIN), maximum (MAX) and average (AVG) levels.

Ramp level	Wav files directly played into the measurement system to determine signal levels (estimated)			Wav files played into the shaker on the reception plate to determine plate velocity levels (estimated)		
	MIN (dB)	MAX (dB)	AVG (dB)	MIN (dB)	MAX (dB)	AVG (dB)
10 dB	4.1	6.0	5.0	4.3	7.0	5.2
20 dB	5.2	7.6	6.1	5.4	7.7	6.2
30 dB	5.3	7.4	6.0	5.4	7.6	6.1
40 dB	5.3	8.1	6.1	5.4	8.3	6.3
Ramp level	Wav files played into the shaker on the concrete floor in the building-like situation to determine plate velocity levels (estimated)			Wav files played into the shaker on the concrete floor in the building-like situation to determine room sound pressure levels (estimated)		
	MIN (dB)	MAX (dB)	AVG (dB)	MIN (dB)	MAX (dB)	AVG (dB)
10 dB	4.1	6.3	5.1	4.2	6.2	5.2
20 dB	5.3	7.5	6.2	5.6	7.4	6.3
30 dB	5.5	7.2	6.0	5.8	7.6	6.3
40 dB	5.3	8.2	6.2	5.6	8.4	6.4

Table 6-4. Wav file of 2 s ramp duration with ramp levels of 10/20/30/40 dB: The specific empirical correction, $L_{F_{\max}} - \max\{L_{\text{eq},125\text{ms}}\}$, with regard to minimum (MIN), maximum (MAX) and average (AVG) levels.

Ramp level	Wav files directly played into the measurement system to determine signal levels (estimated)			Wav files played into the shaker on the reception plate to determine plate velocity levels (estimated)		
	MIN (dB)	MAX (dB)	AVG (dB)	MIN (dB)	MAX (dB)	AVG (dB)
10 dB	3.8	6.8	4.7	4.2	7.2	5.1
20 dB	4.6	6.7	5.7	5.2	7.5	6.0
30 dB	5.1	7.0	6.0	5.4	7.9	6.3
40 dB	5.3	7.4	6.0	5.5	7.7	6.4
Ramp level	Wav files played into the shaker on the concrete floor in the building-like situation to determine plate velocity levels (estimated)			Wav files played into the shaker on the concrete floor in the building-like situation to determine room sound pressure levels (estimated)		
	MIN (dB)	MAX (dB)	AVG (dB)	MIN (dB)	MAX (dB)	AVG (dB)
10 dB	4.0	7.1	4.9	4.1	6.5	5.2
20 dB	4.8	6.8	5.8	5.1	7.6	6.0
30 dB	5.3	7.6	6.3	5.7	8.0	6.5
40 dB	5.5	7.3	6.0	5.6	6.9	6.2

Table 6-5. Wav files of 5 s ramp duration with ramp levels of 10/20/30/40 dB: The specific empirical correction, $L_{Fmax} - \max\{L_{eq,125ms}\}$, with regard to minimum (MIN), maximum (MAX) and average (AVG) levels.

Ramp level	Wav files directly played into the measurement system to determine signal levels (estimated)			Wav files played into the shaker on the reception plate to determine plate velocity levels (estimated)		
	MIN (dB)	MAX (dB)	AVG (dB)	MIN (dB)	MAX (dB)	AVG (dB)
10 dB	3.5	7.5	4.9	4.0	7.5	5.2
20 dB	4.8	7.7	6.0	5.0	8.0	6.3
30 dB	4.9	7.1	5.8	5.0	8.8	6.3
40 dB	5.1	7.8	6.2	5.1	7.8	6.5
Ramp level	Wav files played into the shaker on the concrete floor in the building-like situation to determine plate velocity levels (estimated)			Wav files played into the shaker on the concrete floor in the building-like situation to determine room sound pressure levels (estimated)		
	MIN (dB)	MAX (dB)	AVG (dB)	MIN (dB)	MAX (dB)	AVG (dB)
10 dB	3.7	7.6	5.1	3.9	7.7	5.2
20 dB	5.0	7.7	6.2	4.9	7.9	6.3
30 dB	4.9	8.0	6.1	5.1	8.8	6.4
40 dB	5.1	7.8	6.4	5.2	7.8	6.5

6.3.2 Single-number empirical correction

Specific empirical corrections have been determined for a range of ramp durations and ramp levels that are expected to occur with building machinery. In practice, (a) the ramp durations and ramp levels for individual pieces of building equipment tested are not known and would be time-consuming to determine, (b) the final application is to determine $L_{p,Fmax}$ in the field situation and (c) a prediction of $L_{p,Fmax}$ in building acoustics that is within ± 3 dB is likely to be sufficient. Therefore, it would be beneficial and reasonable to have a single value for the empirical correction. The lack of information regarding ramp durations and ramp levels of the building equipment makes it convenient to adopt a single-number empirical correction for use in simplified SEA models such as EN 12354-5 [11]. The SEA prediction of $L_{p,Fmax}$ levels from converted short $L_{p,eq}$ levels due to the use of the empirical corrections are discussed in Chapter 7.

Using the data in Table 6-1 to Table 6-5, six average corrections for each measurement situation are calculated for a 10 dB ramp level with all ramp durations and 20/30/40 dB ramp levels for each ramp duration (125 ms, 500 ms, 1 s, 2 s and 5 s). These average corrections range from 4.8 to 7.6 dB (these are similar to the specific empirical corrections, which were in a range from 5 to 7.5 dB). A single average correction equal to the average of these six values for each measurement situation gives (a) ≈ 6.1 dB for the signal directly played into the measurement system, (b) ≈ 6.3 dB for measurements on the reception plate, (c) ≈ 6.1 dB for measurements on the separating floor in the building-like situation and (d) ≈ 6.2 dB for measurements in the receiving room in the building-like situation.

Hence, for the prediction of L_{Fmax} (or $L_{p,Fmax}$) in the field situation, it would be reasonable to consider the integer value of 6 dB as a single-number empirical correction. The implications of choosing this value are that 10 dB ramp levels for all ramp durations and 20/30/40 dB ramp levels with a ramp duration of

125 ms overestimate or underestimate L_{Fmax} by ≈ 1 dB, but it provides closer estimates for 20/30/40 dB ramp levels with ramp durations ≥ 500 ms.

6.4 Summary

This chapter considered the empirical correction in terms of the difference between L_{Fmax} and $\max\{L_{eq,125ms}\}$ in one-third octave bands that were investigated for time-varying signals (a) sent directly into the measurement system, sent to a shaker into (b) the concrete reception plate and (c) the concrete floor in the building-like situation as well as (d) the sound radiation into the room for the latter signal situation in the building-like situation. The time-varying signal comprised different increasing/decreasing ramp durations of 125 ms to 5 s with increasing/decreasing ramp levels from 10 to 40 dB.

Two empirical corrections were developed: a specific empirical correction to take into account the ramp- and level-dependent corrections and a single-number empirical correction to simplify the approach. The results of the specific empirical correction indicate that for ramp levels of (a) 10 dB for all ramp durations has $L_{Fmax} - \max\{L_{eq,125ms}\} \approx 5$ dB, (b) 20, 30 and 40 dB with a ramp duration of 125 ms has $L_{Fmax} - \max\{L_{eq,125ms}\} \approx 7.5$ dB and (c) 20, 30 and 40 dB with ramp durations ≥ 500 ms has $L_{Fmax} - \max\{L_{eq,125ms}\} \approx 6$ dB. A value of 6 dB was proposed as a single-number empirical correction which was assessed from all ramp- and level-dependent average differences from the 20 time-varying signals from experiments. Since this approach is based on time-varying signals as a function of ramped white noise, the empirical correction is replicated in Chapter 8 using a real structure-borne sound source in the form of a toilet flush on the reception plate test rig.

For structure-borne sound sources with time-varying components, this empirical correction method provides the potential to use simplified SEA models

such as EN 12354-5 [11] to determine L_{Fmax} rather than requiring more complex models such as TSEA. In the next chapter, these empirical corrections are used to predict L_{Fmax} from $\max\{L_{eq,125ms}\}$ levels using ramped noise signals.

7 Prediction of L_{Fmax} from time-varying structure-borne sound sources in heavyweight buildings

7.1 Introduction

Using TSEA, it is possible to predict sound levels from heavy transient impact sources in terms of L_{Fmax} (e.g. footsteps, rubber ball or bang machine with a very short impact time of less than 20 ms) [17, 18]. For SEA or simplified SEA models according to EN 12354-5 [11], no approach is currently available that can be used to predict L_{Fmax} sound levels from the time-varying ramp excitations that occur from building machinery (or heavy impacts) in heavyweight buildings. Many types of building equipment such as washing machines, pumps and boilers have different operating cycles, which are approximately broadband signals that ramp up and down in terms of their structure-borne sound power input. Therefore, this chapter investigates the same time-varying signals based on white noise from Section 3.3.7.1 but injecting these signals into the reception plate to determine $\max\{L_{eq,125ms}\}$. This can then be used as input data for SEA predictions by making use of the empirical corrections to convert the estimated velocity and sound pressure levels from $\max\{L_{eq,125ms}\}$ to L_{Fmax} . To determine the reception plate power, the sampling approach used is the area-weighted

approach from Section 5.2.2. For experiments either on the reception plate or building-like situation, the signal processing of time-varying signals followed the approach given in Section 3.3.7.2.

Section 7.2 builds on the work in Chapter 6 using the reception plate excited by a shaker from time-varying ramp signals to determine $\max\{L_{\text{eq},125\text{ms}}\}$ and predict L_{Fmax} using the empirical corrections for the plate velocity and cavity sound pressure levels in one-third octave bands using SEA. These predicted L_{Fmax} levels in one-third octave bands are compared with measurements. In the field situation, the assessment of noise from building equipment or machines often requires L_{AFmax} ; therefore, Section 7.3 investigates whether L_{AFmax} levels can be estimated from frequency-dependent L_{Fmax} levels.

7.2 Experimental validation of L_{Fmax} prediction using empirical corrections

This section discusses how an SEA model can be used to estimate L_{Fmax} from reception plate measurements of $\max\{L_{\text{eq},125\text{ms}}\}$ using the specific or single-number empirical correction from Section 6.3. In Section 7.2.1, the specific empirical correction is initially applied to validate the predicted L_{Fmax} levels against measured L_{Fmax} levels from the vibration field on the concrete floor and the sound field in the receiving room in the building-like situation. In Section 7.3.2, the focus is on the prediction of L_{Fmax} using the single-number empirical correction as the final application relates to the L_{Fmax} prediction in the sound field of the receiving room.

7.2.1 Specific empirical correction

A two-subsystem SEA model of a coupled room-plate system is used to simulate direct sound transmission (refer back to Section 2.4.1) with structure-borne sound power input into the plate for which the results are compared with measurements in the building-like situation.

Experiments were carried out to obtain the SEA input data of the coupled room-plate system in terms of the vibrational power of the shaker induced by ramped noise signals, the radiation efficiency, the loss factors of the plate and the receiving room as well as from the calculated coupling loss factors of the plate to the room (and vice versa) – see Figure 7-1.

Figure 7-1a shows the installed structure-borne sound powers in terms of $\max\{L_{\text{eq},125\text{ms}}\}$ levels for the building-like situation that are quantified from reception plate powers with the mobility technique using the time-varying signals played directly into a shaker on the reception plate. These installed powers are required as input data for SEA predictions (refer back to Section 2.5.2.2). In addition, the radiation efficiency is used with experimental data (see Figure 7-1b) because (a) the floor and room have low mode counts at low frequencies for which there is a trough at 63 Hz in the measured radiation efficiency and (b) the measured radiation efficiency is specific to the mechanical source and source position and is therefore expected to give lowest errors. Note that the radiation efficiency approach from Leppington [137, 138, 139] using Eq. (2.64) to Eq. (2.66) (refer back to Section 2.4.1.3) is intended for airborne excitation and is not specific to a mechanical source and source position.

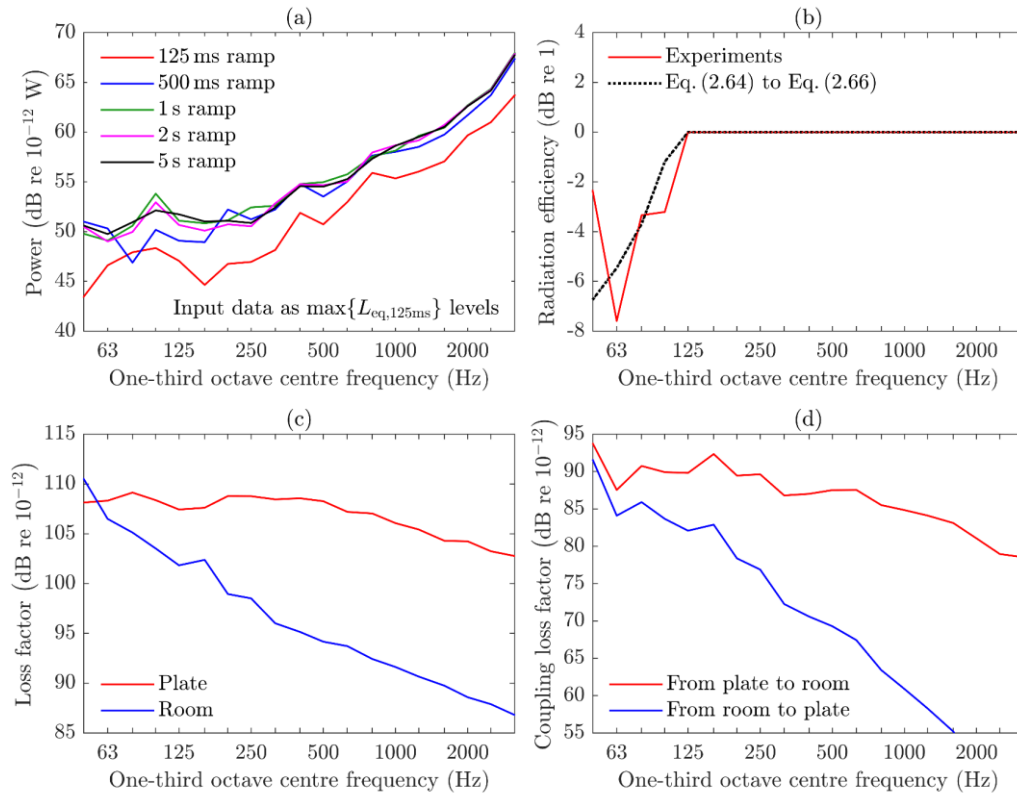


Figure 7-1. Experiments to determine the input data for the two-subsystem SEA model of a coupled room-plate system for (a) the installed vibrational input power of the ramped noise signals injected by a shaker for examples of 125 ms, 500 ms, 1 s, 2 s and 5 s ramps with a ramp level of 20 dB, (b) the radiation efficiency, (c) the loss factors of the plate and the room and (d) the coupling loss factors from the plate to the room (and vice versa).

It is necessary to define an acceptable difference between the SEA predictions from a two-subsystem model and measurements; hence, an acceptable error can be reasonably assumed to be ± 5 dB in the low-frequency range up to 200 Hz where a low mode count occurs and ± 3 dB in the mid- and high-frequency range from 250 Hz to 3.15 kHz where a significantly higher mode count occurs. The acceptable error is larger at low frequencies because there are larger uncertainties in measurements of the reverberation time and the spatial variation of the plate velocity and the sound pressure in the room due to well-separated modes. These acceptable error limits are used for all results from the comparison between SEA predictions and measurements. Note that the differences between predicted and

measured $L_{F_{\max}}$ are calculated using the predicted $L_{F_{\max}}$ minus the measured $L_{F_{\max}}$.

Using SEA, the $L_{F_{\max}}$ velocity levels of the plate subsystem and the $L_{F_{\max}}$ sound pressure levels of the cavity subsystem resulting from the predicted $\max\{L_{\text{eq},125\text{ms}}\}$ levels combined with the specific empirical correction are discussed in Sections 7.2.1.1 and 7.2.1.2 respectively.

7.2.1.1 Prediction of $L_{v,F_{\max}}$ on the separating floor

Figure 7-2 shows the difference between the predicted and measured spatial average velocity in terms of $L_{v,F_{\max}}$ on the concrete floor in the building-like situation. The results indicate that SEA is suitable to predict the vibration of the concrete floor within the acceptable error limits for all ramp durations and ramp levels. The largest absolute difference of ≈ 4.7 dB occurs at 100 Hz for the 125 ms ramp. It is also noted that the specific empirical correction tends to drop to lower values at high frequencies compared to the average difference found for this correction in Section 6.3.1.

In general, it can be observed that there is no significant offset in the prediction of the vibration response on the concrete floor in the building-like situation. Thus, the prediction appears to slightly overestimate the plate vibration levels for the 125 ms ramp between 50 and 100 Hz. In addition, the prediction also tends to slightly overestimate the plate vibration levels for all ramps between 630 Hz and 3.15 kHz. However, all predicted vibration levels are still within the specified acceptable error limits in all one-third octave frequency bands from 50 Hz to 3.15 kHz, which gives evidence that the specific empirical correction is suitable to use.

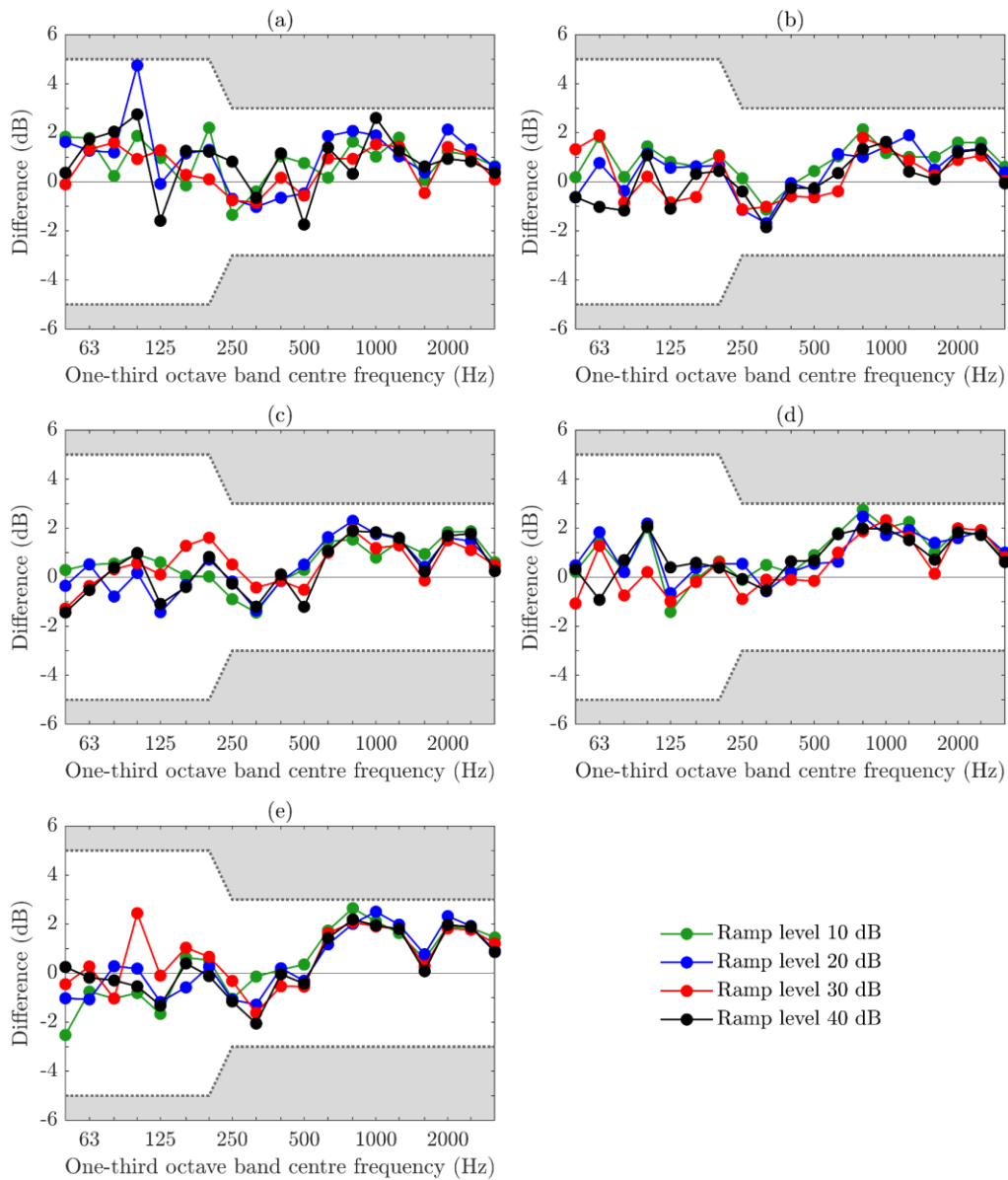


Figure 7-2. Wav files of 125 ms, 500 ms, 1 s, 2 s and 5 s ramp durations with ramp levels of 10/20/30/40 dB: The specific empirical correction of velocity levels in terms of predicted $L_{v,Fmax}$ minus measured $L_{v,Fmax}$ for (a) 125 ms ramp, (b) 500 ms ramp, (c) 1 s ramp, (d) 2 s ramp and (e) 5 s ramp.

7.2.1.2 Prediction of $L_{p,Fmax}$ in the receiving room

The differences between the predicted and measured sound pressure levels in terms of $L_{p,Fmax}$ in the receiving room in the building-like situation are shown in Figure 7-3. The $L_{p,Fmax}$ predicted by SEA using the specific empirical correction follows a similar pattern to that observed for plate velocity levels in Section 7.2.1.1. However, there is an exception where the sound level is slightly higher than the acceptable error limits; this occurs for the 125 ms ramp where the prediction appears to slightly overestimate the sound field in the receiving room over nearly the entire frequency range but is largely within the acceptable error limits. Only at 2.5 kHz, the acceptable error limits are exceeded by up to 0.7 dB. In contrast, ramp durations ≥ 500 ms are within the acceptable error limits, and there is an offset at which the prediction slightly overestimates the measurement.

In general, $L_{p,Fmax}$ levels tend to be overestimated with the 125 ms ramp duration, which is the same time used for the short L_{eq} level. For ramp durations ≥ 500 ms, the difference is within the acceptable error limits with SEA tending to overestimate $L_{p,Fmax}$. However, such differences are similar to SEA predictions of airborne or impact sound insulation from steady-state sources with only direct sound transmission.

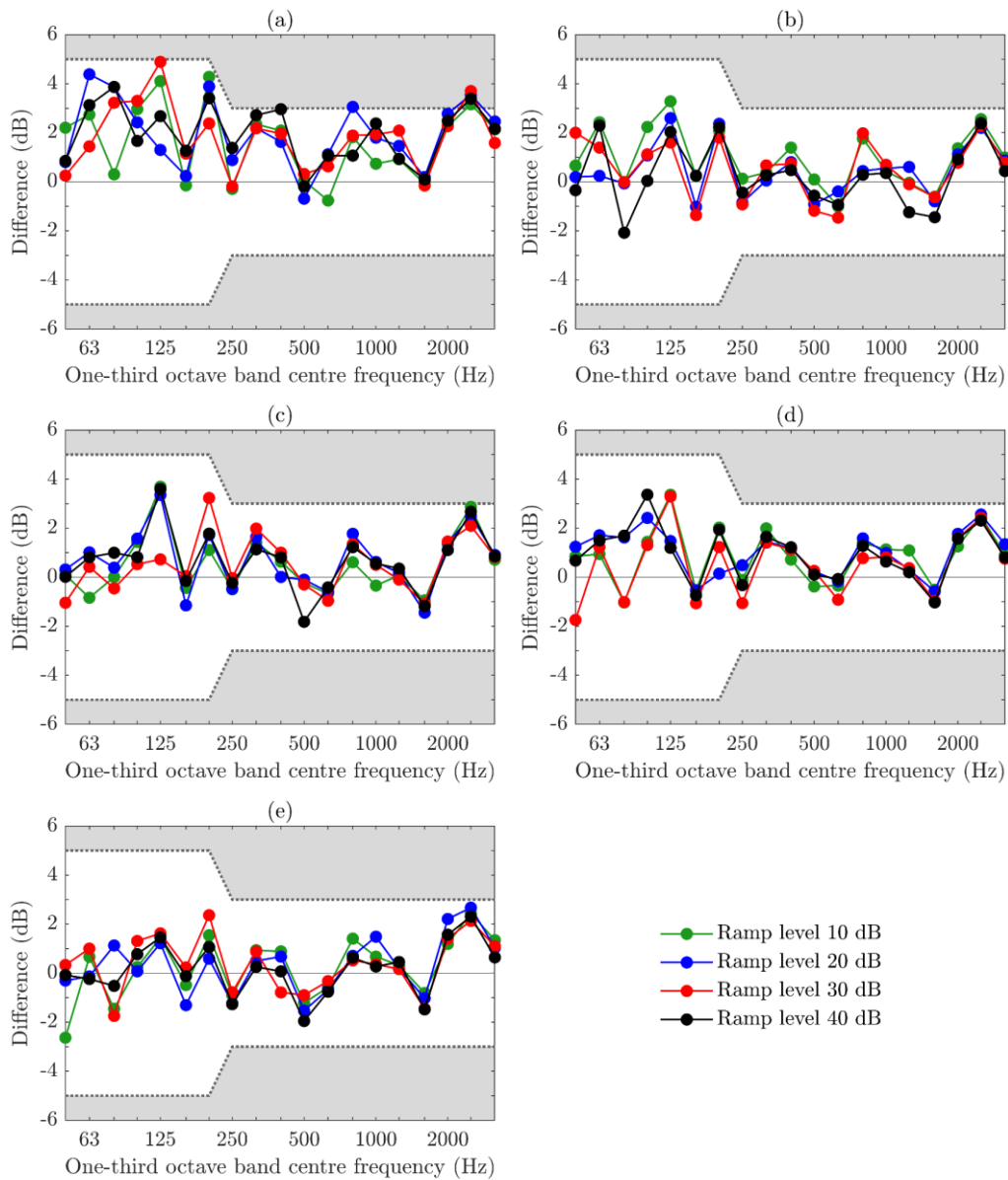


Figure 7-3. Wav files of 125 ms, 500 ms, 1 s, 2 s and 5 s ramp durations with ramp levels of 10/20/30/40 dB: The specific empirical correction of sound pressure levels in terms of predicted $L_{p,Fmax}$ minus measured $L_{p,Fmax}$ for (a) 125 ms ramp, (b) 500 ms ramp, (c) 1 s ramp, (d) 2 s ramp and (e) 5 s ramp.

7.2.2 Single-number empirical correction

The results from Section 7.2.1 give evidence that the specific empirical correction is appropriate to predict direct sound transmission from time-varying signals in terms of $L_{p,Fmax}$ within ± 5 dB below 250 Hz and ± 3 dB between 250 Hz and 3.15 kHz according to the acceptable error limits from the introduction section of this chapter. Therefore, the introduced single-number empirical correction could be feasible and useful for the sake of simplicity when $L_{p,Fmax}$ is predicted in the sound field of nearby rooms in heavyweight buildings using simplified SEA approaches such as EN 12354-5 [11].

In general, Figure 7-4 indicates that for all ramp durations with ramp levels of 20/30/40 dB, the error is within the acceptable error limits. With a ramp level of 10 dB for all ramp durations, the prediction is occasionally overestimated beyond the acceptable error. In the sound field nominally, a few overestimations are observed outside the acceptable error limits where the largest error of 1.2 dB occurs at 2.5 kHz, and all other errors at 125, 200, 315 and 400 Hz and 2 and 3.15 kHz are less than 0.5 dB. These results indicate that the use of this simplification using just a single-number empirical correction is sufficient for an SEA-based approach like EN 12354-5 [11], where other errors will tend to be larger. Hence, a single number for an empirical correction is reasonable to assume when estimating the sound pressure level from $\max\{L_{eq,125ms}\}$ to L_{Fmax} for time-varying cycles from building machinery in adjacent rooms in heavyweight buildings.

Note that only the direct structure-borne sound transmission to a nearby room is considered in which the flanking transmission is suppressed due to the independent wall linings (refer back to the description of the flanking laboratory from Section 3.2.2). In practice, the structure-borne sound transmission will involve diagonal, vertical and horizontal flanking transmission by any other structural paths into adjacent rooms in heavyweight buildings than only this

nominally separating floor used in this study. In these situations, however, the propagation times for bending waves across heavyweight components such as walls and floors are sufficiently short (refer back to Figure 2-7) that the use of $\max\{L_{\text{eq},125\text{ms}}\}$ can be considered appropriate to predict L_{Fmax} . In addition, previous work with TSEA on the prediction of sound pressure levels in relation to L_{Fmax} [17, 18] has shown that the prediction should also work in heavyweight buildings when there is flanking transmission.

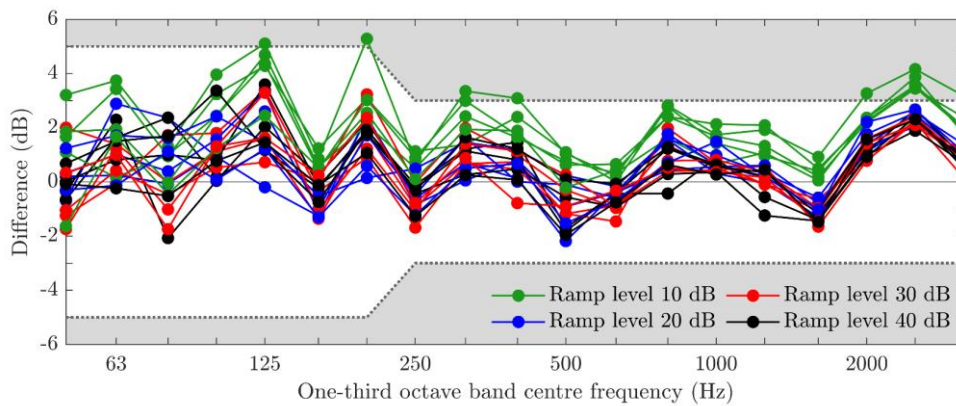


Figure 7-4. Wav files of 125 ms, 500 ms, 1 s, 2 s and 5 s ramp durations with ramp levels of 10/20/30/40 dB: The single-number empirical correction of predicted and measured sound pressure levels in terms of predicted $L_{\text{p,Fmax}}$ minus measured $L_{\text{p,Fmax}}$.

7.3 Consideration of L_{AFmax} from frequency-dependent L_{Fmax} in the field situation

Considering that L_{AFmax} is often required for building equipment or machinery operating in a nearby room (e.g. ÖNORM B 8115-2 [12], SIA 181 [13] and VDI 4100 [14]), it is necessary to know whether it is feasible to determine L_{AFmax} from L_{Fmax} in one-third octave or octave bands by subtracting the A-weighting and energetically summing them. Recalling that the L_{AFmax} measurements were performed using a high-pass filter above 20 Hz and a low-pass filter below 6.4 kHz (see Section 3.3.7.2). Therefore, for the prediction of L_{AFmax} , A-weighting was applied to L_{Fmax} values from 20 Hz to 5 kHz.

Using the approach given in Section 3.3.7.2, the measured $\max\{L_{AF,125ms}\}$ using $L_{AF,125ms}$ levels as well as A-weighted and energetic summed $L_{F,125ms}$ levels for ramp durations from 125 ms to 5 s and ramp levels from 10 to 40 dB are assessed and compared with measured L_{AFmax} levels, which is shown in Figure 7-5 in order to check the appropriateness for the comparison between measured L_{AFmax} and predicted L_{AFmax} from L_{Fmax} . The results indicate that the estimation of $\max\{L_{AF,125ms}\}$ from $\max\{L_{F,125ms}\}$ only slightly overestimates L_{AFmax} with an error ranging from ≈ 0.1 to ≈ 0.3 dB.

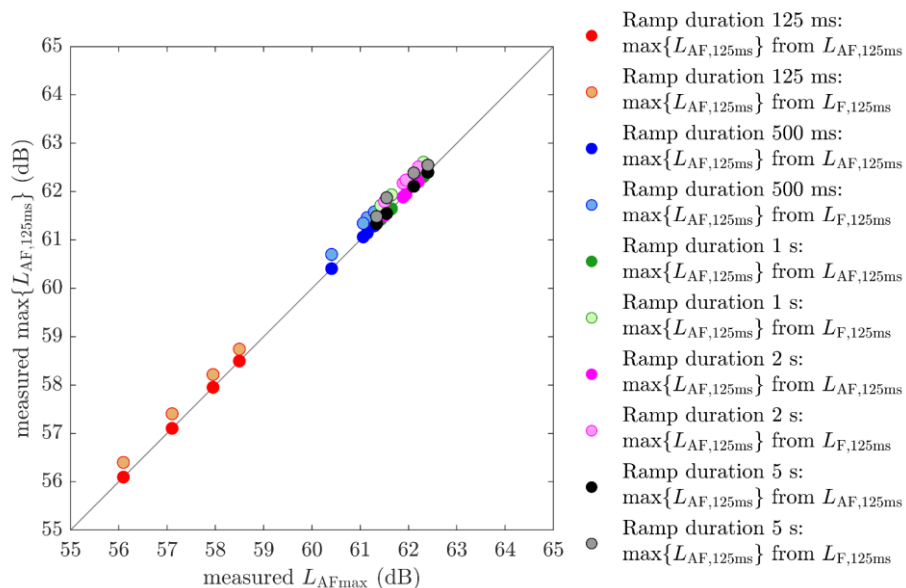


Figure 7-5. Wav files of 125 ms, 500 ms, 1 s, 2 s and 5 s ramp durations with ramp levels of 10/20/30/40 dB: Comparison of L_{AFmax} and $\max\{L_{AF,125ms}\}$ levels in terms of measured $L_{AF,125ms}$ and $L_{F,125ms}$.

The results from Figure 7-5 confirm that the prediction of L_{AFmax} from L_{Fmax} is suitable, and the frequency-dependent L_{AFmax} thus obtained can be converted into a single value using an energy summation. A discussion on the results of L_{AFmax} obtained from $\max\{L_{eq,125ms}\}$ to L_{Fmax} using the specific empirical correction and the single-number empirical correction is given in Section 7.3.1 and Section 7.3.2 respectively.

7.3.1 Specific empirical correction

Figure 7-6 allows the comparison of predicted and measured L_{AFmax} when energetically summed L_{Fmax} levels with subtracted A-weighting are used from $\max\{L_{eq,125ms}\}$ in conjunction with the specific empirical correction for which in Table 7-1 the corresponding level differences, ΔL_{AFmax} , in terms of predicted minus measured L_{AFmax} levels are given. Using the specific empirical correction to finally assess L_{AFmax} , the largest differences occur for the 125 ms ramp with all ramp levels from 10 to 40 dB. (NB In Figure 7-3a, there was already a tendency that the prediction tended to overestimate the measurements from the 125 ms ramp using the specific empirical correction.) For ramp durations ≥ 500 ms, the majority of the differences are within ± 0.5 dB, while for the 125 ms ramp, the prediction appears to overestimate the measurements by ≤ 2.0 dB. However, this would be suitable for most applications in building acoustics.

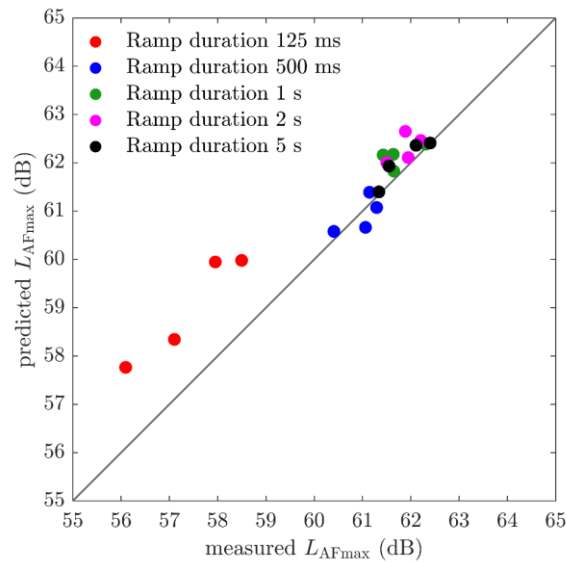


Figure 7-6. Wav files of 125 ms, 500 ms, 1 s, 2 s and 5 s ramp durations with ramp levels of 10/20/30/40 dB: Comparison of the specific empirical correction using predicted and measured A-weighted sound pressure levels, L_{AFmax} .

Table 7-1. Wav files of 125 ms, 500 ms, 1 s, 2 s and 5 s ramp durations with ramp levels of 10/20/30/40 dB: Difference between the predicted and measured A-weighted sound pressure levels, L_{AFmax} , when using the specific empirical correction.

	Ramp levels	10 dB	20 dB	30 dB	40 dB
ΔL_{AFmax} (dB)	125 ms ramp	1.5	2.0	1.2	1.7
	500 ms ramp	0.2	0.2	-0.2	-0.4
	1 s ramp	0.5	0.7	0.1	0.2
	2 s ramp	0.8	0.5	0.3	0.2
	5 s ramp	0.0	0.4	0.3	0.1

7.3.2 Single-number empirical correction

Figure 7-7 and Table 7-2 illustrate the results of the differences for the predicted and measured L_{AFmax} from L_{Fmax} when the single-number empirical correction is applied. Using the single-number empirical correction to predict L_{AFmax} from L_{Fmax} , the largest differences between the predicted L_{AFmax} and

measured L_{AFmax} are found for the 125 ms, 500 ms, 1 s, 2 s and 5 s ramp durations with a ramp level of 10 dB as indicated in Figure 7-4 when using the single-number empirical correction for the prediction of L_{Fmax} from $\max\{L_{eq,125ms}\}$. In this situation, the largest difference in the single-number empirical correction is from 1 to 2.5 dB. Whereas, for 125 ms, 500 ms, 1 s, 2 s and 5 s ramp durations and ramp levels of 20, 30 and 40 dB, most of the differences are within ± 0.4 dB. However, the level differences, ΔL_{AFmax} , in Table 7-2 are mainly in a similar range as the ΔL_{AFmax} levels in Table 7-1. The prediction also tends to overestimate the measurements by ≤ 2.5 dB; here, this differs only in that instead of the 125 ms ramp of all ramp levels, the focus changes to all ramp durations with a ramp level of 10 dB. Overall, it can be concluded that the error is acceptable for most building acoustic applications.

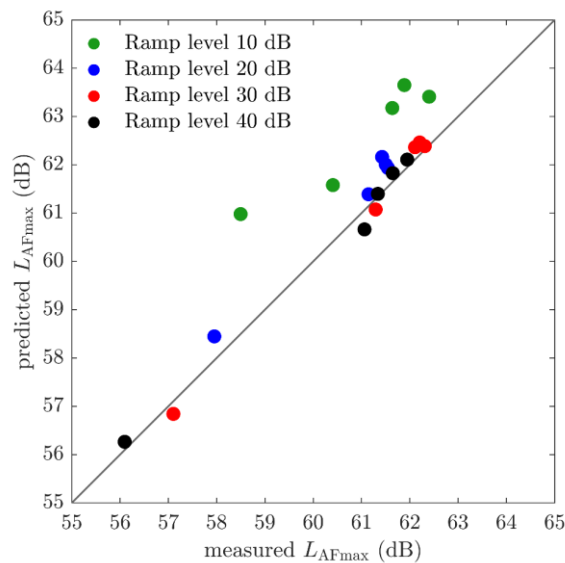


Figure 7-7. Wav files of 125 ms, 500 ms, 1 s, 2 s and 5 s ramp durations with ramp levels of 10/20/30/40 dB: Comparison of the single-number empirical correction using predicted and measured A-weighted sound pressure levels, L_{AFmax} .

Table 7-2. Wav files of 125 ms, 500 ms, 1 s, 2 s and 5 s ramp durations with ramp levels of 10/20/30/40 dB: Difference between the predicted and measured A-weighted sound pressure levels, L_{AFmax} , when using the single-number empirical correction.

	Ramp levels	10 dB	20 dB	30 dB	40 dB
ΔL_{AFmax} (dB)	125 ms ramp	2.5	0.5	-0.3	0.2
	500 ms ramp	1.2	0.2	-0.2	-0.4
	1 s ramp	1.5	0.7	0.1	0.2
	2 s ramp	1.8	0.5	0.3	0.2
	5 s ramp	1.0	0.4	0.3	0.1

7.4 Summary

This chapter assessed the feasibility of predicting L_{Fmax} from reception plate measurements of $\max\{L_{eq,125ms}\}$ using a specific and single-number empirical correction derived from ramped noise signals representing building equipment for ramp durations from 125 ms to 5 s with increasing/decreasing levels of 10, 20, 30 and 40 dB. The comparison between SEA predicted and measured L_{Fmax} values in one-third octave bands typically show that the agreement was within ± 3 dB for direct sound transmission in a heavyweight building. Previous work from TSEA-based models [17, 18] provides evidence that this should also be applicable when flanking transmission is used in heavyweight buildings to predict the sound pressure levels in terms of L_{Fmax} .

For convenience, a single-number empirical correction is appropriate rather than a ramp- and level-dependent correction as used for the specific empirical correction. This could be used for simplified SEA-based models such as EN 12354-5 [11]. The largest error was up to 0.7 dB (specific empirical correction) and 1.1 dB (single-number empirical correction) at 2.5 kHz beyond the acceptable error limits defined with ± 5 dB up to 200 Hz and ± 3 dB between 250 Hz and 3.15 kHz. These errors only occurred for the 10dB ramp level. Such

resulting errors are still justifiable for an SEA-based approach where other errors (e.g. reverberation time measurements, spatial variation of the cavity sound pressure and plate velocity) will tend to be larger. Hence, the investigations indicated that a single-number empirical correction is reasonable to estimate $L_{F_{\max}}$ (or $L_{p,F_{\max}}$) in the receiving room. In addition, investigations have been shown that it is feasible to estimate $L_{AF_{\max}}$ from predicted one-third octave band $L_{F_{\max}}$ values with close agreement.

In conclusion, the empirical correction approach has the potential to be incorporated into EN 15657 [35] and EN 12354-5 [11] so that the estimation of $L_{F_{\max}}$ levels can be carried out at the design stage before machinery with time-varying structure-borne sound power is installed in a heavyweight building.

8 Case study: Toilet flush

8.1 Introduction

Noise emitted by sanitary equipment can be complex because it often leads to more than one transient event, and the power is injected into more than one plate (e.g. a wall and a floor). However, it is a broadband signal, which makes it a reasonable comparison with the ramped noise signals in Chapter 6. In addition, the time-varying flush cycle of the toilet is complex because structure-borne sound excitation is simultaneously transmitted to the wall and floor. Therefore, in this chapter, a toilet flush is assessed as part of a modern installation system that is designed to go in front of the heavyweight wall. Thus, this case study provides a challenging validation of the empirical correction from Chapter 6 on the reception plate.

Section 8.2 explains the sanitary installation system. Section 8.3 describes the experiments carried out on the reception plate test rig using the time-varying toilet flush cycle to assess the empirical correction from the relationship between L_{Fmax} and $\max\{L_{eq,125ms}\}$ in order to verify whether this can also be estimated from a real time-varying structure-borne sound source. A discussion of the problems that can occur when measuring time-varying sources with multiple ramps in their operation cycles is given in Section 8.4.

8.2 Source description

This section describes the sanitary installation system built upon the reception plate test rig for investigations in Section 8.2.1 and the toilet flush in its operation mode as a structure-borne sound source with transient excitation in Section 8.2.2. The reception plate test rig consists of three reception plates as indicated in Section 3.2.1, and the system injects power into two of these plates (one horizontal and one vertical plate).

8.2.1 Sanitary installation system

Modern sanitary installation systems (e.g. Geberit GIS) link the installation of sanitary equipment such as bathtub, washbasin, toilet, fresh- and wastewater pipes using a load-bearing frame on the bathroom wall. Figure 8-1a shows the measurement set-up of the pre-wall installation system with the sanitary equipment installed having point and line contacts to the horizontal and vertical reception plates of the test rig but without the typical installation shaft for fresh- and wastewater pipes. The load-bearing steel frame system is connected by screwed steel mounting brackets which are decoupled by natural soundproofing cork material (point contacts) using five brackets on the horizontal reception plate and four on the vertical reception plate (see Figure 8-1d). The load-bearing frame system (see Figure 8-1c) supports the fresh- and wastewater pipes and the cistern (Geberit UPpowerflush) and is covered with plasterboard panels that are decoupled from the reception plates by elastic self-adhesive Cross-linked Polyethylene (PE-X) insulation strips (resilient line contacts).

The sanitary equipment consists of the bathtub, washbasin and toilet. The bathtub is supported by four feet on the horizontal reception plate (point contacts), the bathtub rim is decoupled by PE-X insulation strips (resilient line contacts) from the reception plate and the pre-wall installation system. The bathtub cladding is made of rigid foam panels sealed with acrylic to the reception plates and pre-wall installation system (line contacts). The washbasin and the

toilet are attached to the pre-wall installation system using a soundproofing set made of Polyethylene (PE) foam between the installation components. Figure 8-1b shows the toilet mounted on the pre-wall installation system. There is no direct contact with the horizontal and vertical reception plates. The time-varying operating cycle of a toilet flush is described in the next section.



Figure 8-1. Case study of a toilet flush: (a) measurement set-up for the pre-wall installation system (Geberit GIS) with sanitary equipment, (b) the toilet, (c) the load-bearing frame including the installations of the cistern and the fresh- and wastewater pipes and (d) cork layered brackets which fix the frame to the reception plate test rig [37]. This sanitary installation system is installed without the installation shaft for the fresh- and wastewater supply.

Although this is a highly engineered installation with control of the water pressure, there are still small variations in the structure-borne sound power between flushes. For this reason, detailed measurements were taken from two flushes for discussion in this chapter.

8.2.2 Operating mode of a time-varying toilet flush cycle

Figure 8-1a shows the pre-wall installation system on the reception plate test rig. Only the transient excitation from the toilet flush of the available sanitary equipment (see Figure 8-1b) is used for measurements. The structure-borne sound transmission into the horizontal and vertical reception plates is initiated when the toilet button is pushed to start the flushing process. This pulls up a chain or tripping device through a plastic rod connected to the flush valve, therefore releasing the cistern water into the bowl. The water flows around the side of the bowl and is siphoned to the drainpipe to remove the waste. For this experimental work, there is no waste, only flushing water. The water runs out of the cistern in less than 10 s, so the float ball drops to the bottom of the cistern. This starts the refilling process (≈ 45 s) by turning on the inlet valve to bring water from the water supply into the cistern. Simultaneously, once the cistern is empty, the flush valve is sealed, which remains closed due to the new water stored in the cistern. However, during the refilling process, the water flows from the base of the fill valve from the supply pipe through the refill tube to the over float tube. As the water rises in the cistern, the float fill eventually rises to a certain height of water at which the inlet valve is closed to stop the further filling of the cistern.

Figure 8-2 shows an example of time-varying velocity levels of a toilet flush for an operating cycle measured on the horizontal and vertical reception plates. Accelerometer positions were chosen as described in Section 5.2.1. The structure-borne sound from the source under operation is injected via point and line contacts of the pre-wall installation system into two reception plates. The measurer started the analyser then gently stepped on the reception plate to press

the button (toilet flush), after which the measurer stepped off the plate. Hence, the measurer was only on the plate for the first ≈ 3.5 s, and there was no evidence of a significant increase in the background vibration level during this time. Figure 8-2a indicates the two regions of the flushing and refilling process from a toilet flush cycle, for which the velocity-time-amplitude spectra are shown in Figure 8-2b and c for the horizontal and vertical reception plate respectively. Note that Figure 8-2a shows the energy summation of $L_{F,125ms}$ in the free run from the horizontal and vertical reception plates.

For this time-varying source, there are complex mechanical mechanisms due to a large number of components that are involved (described above), and it is difficult to clearly identify which mechanical device causes the various velocity peaks. The highest peak level and the highest ramp level occur with ramp A (see Figure 8-2a, b and c); this is likely to be caused by the flushing process started by the pressing of the button and/or the opening of the flush valve by the lifting mechanism. The peak that occurs in the final ramp (ramp D) at the end of the refilling process is likely to be generated by the closing inlet valve of the water supply.

The flush cycle is defined by a flushing and refilling process in which four ramps A, B, C and D in the time-varying velocity level on the reception plate can be clearly identified in Figure 8-2. A more detailed graph of the flushing process is shown in Figure 8-3a in terms of the summed velocity levels. This shows that the peaks in ramps A, B and C occur at 2.875, 4.25 and 6.125 s respectively. However, the peaks in the one-third octave band levels do not necessarily occur at these times. Figure 8-3b, c, d, e, f and g show the individual increasing/decreasing ramp levels in the frequency band at which the highest ramp duration occurs in ramps A, B and C.

Since the peak in ramp A has the highest summed velocity level during the toilet flush cycle, this ramp is used to quantify L_{Fmax} and $\max\{L_{eq,125ms}\}$ on the horizontal and vertical reception plates. This allows the source to be used to

assess the empirical correction that was obtained from ramped noise signals in Section 6.3.

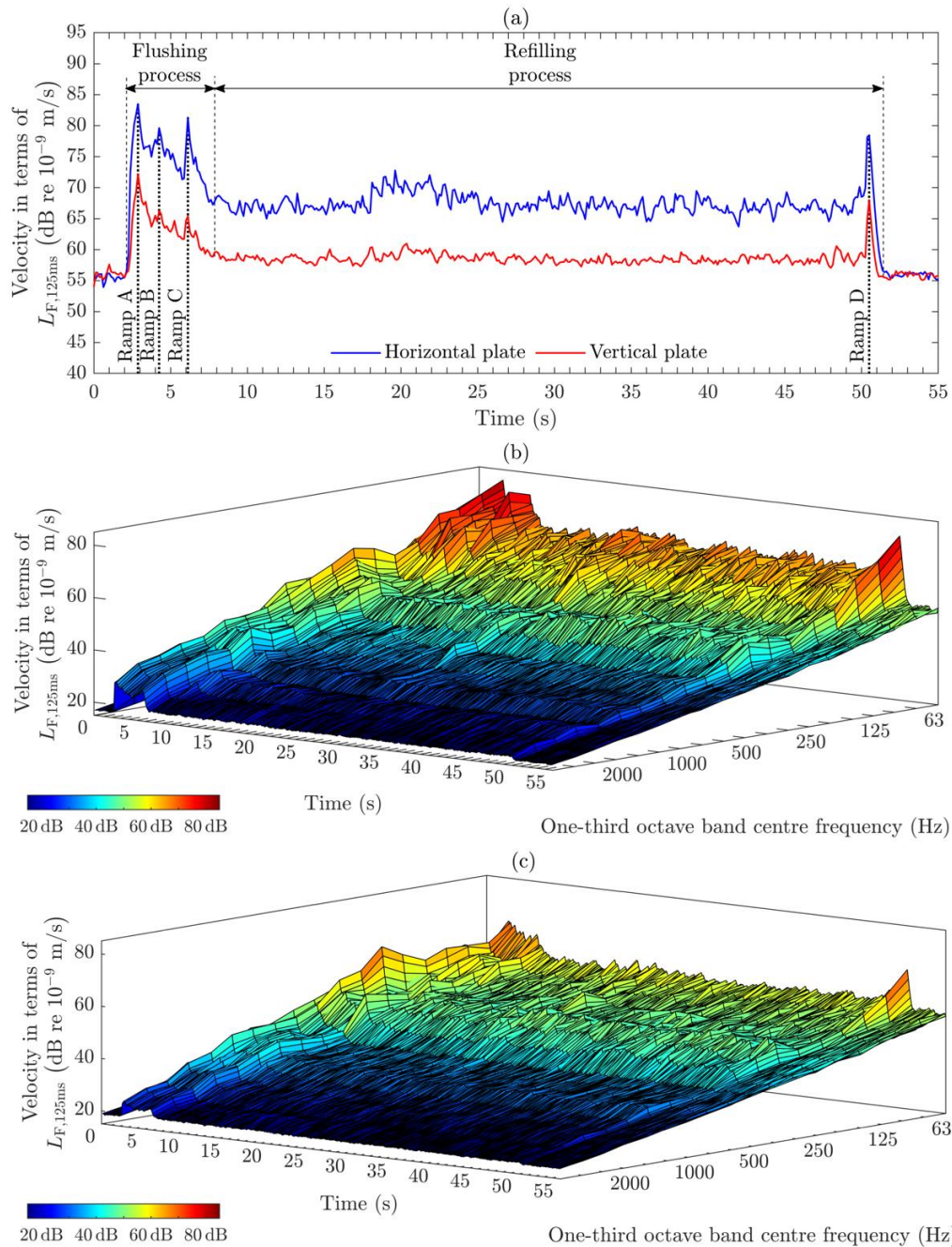


Figure 8-2. Case study of a toilet flush. Time-varying velocity levels in terms of $L_{F,125ms}$ in the free run during a flush cycle: (a) the summed velocity levels in one-third octave bands over time are shown from multi-buffer measurements on (b) the horizontal reception plate and (c) the vertical reception plate.

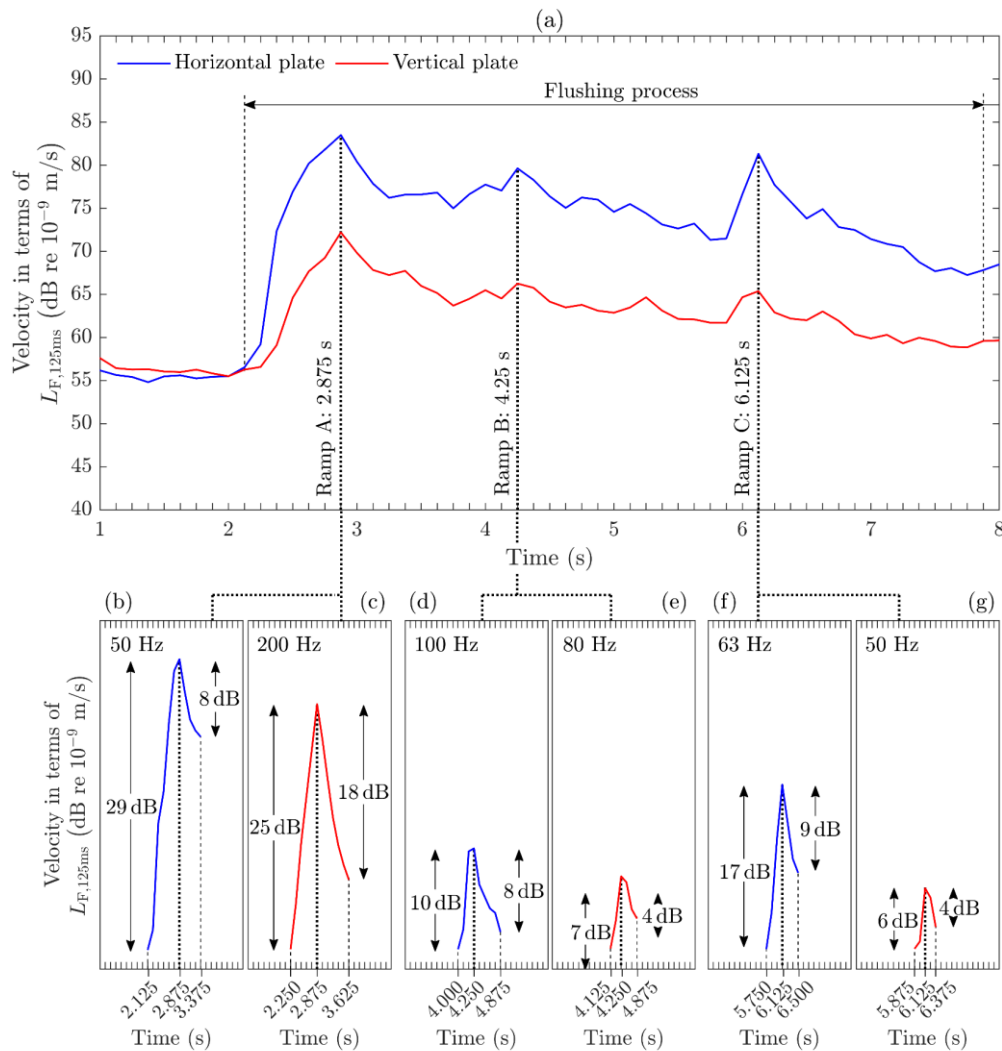


Figure 8-3. Case study of a toilet flush: Definition of ramps A, B and C from the flushing process for (a) the summed velocity levels from all the filters over time and multi-buffer measurements from (b) to (g) in order to obtain their ramp levels over time using the single frequency band at which the highest ramp durations occur.

8.3 Experiments on the reception plate test rig

This section describes the simultaneous measurement of vibration levels from the time-varying toilet flush on the horizontal and vertical reception plates during an operating cycle. Section 8.3.1 concerns the processing of L_{Fmax} , $\max\{L_{F,125ms}\}$ and $\max\{L_{eq,125ms}\}$ according to the approach introduced in

Section 3.3.7.2. For the relationship between L_{Fmax} and $\max\{L_{eq,125ms}\}$ from a toilet flush cycle, the specific empirical correction is discussed in Section 8.3.2 based on the approach in Section 6.3.1. Section 8.3.3 compares the results of the specific empirical correction from the toilet flush with that from ramped noise signals. In addition, the single-number empirical correction from Section 6.3.2 is considered by subtracting it from the specific empirical correction from the toilet flush cycle, and this is compared with the results of the ramped noise signals.

As mentioned in Chapter 5, the toilet flush vibration response is based on the empirical weighting approach to determine the spatial average velocity levels on the reception plate (Section 5.2.1). This is because the measurements were carried out at an earlier stage in the research before the area-weighting approach had been developed as a more general approach for any isolated, rectangular reception plate. The empirical weighting approach was individual to the horizontal reception plate but is a reasonable estimate for the vertical plate due to its similarity.

8.3.1 Processing of short L_{eq} and L_{Fmax}

The time period of a toilet flush for one operating cycle was ≈ 50 s when measured on the horizontal and vertical reception plates (see Figure 8-2a). Note that the toilet flush button was initiated ≈ 2 s after the start of the measurement period so that only background noise existed at the beginning of the measurement. The following data were recorded: (a) L_{Fmax} , (b) maximum hold values for $L_{F,125ms}$, (c) free run values for $L_{F,125ms}$ and (d) maximum hold values for $L_{eq,125ms}$. The reason that data was collected in a free run as well as with maximum hold was because of the complexity of the time-varying signal; hence, it was necessary to check whether L_{Fmax} equals $\max\{L_{F,125ms}\}$ for the peak in the ramp of interest. For (a), the analyser had a gate-off trigger that

stopped recording data after 4.5 s, whereas (b), (c) and (d) were determined from the entire measurement period. The time period of 4.5 s included ramp A and B but avoided recording peak levels from ramp C, which had higher peak levels than ramp A in some one-third octave bands. It was not considered appropriate to use a shorter time period to try and only include ramp A because the time taken by the measurer to step on and off the plate and press the toilet flush button varied slightly each time. An assessment is made as to whether this affected the data. This was also a good test for the second lower peak that occurred with ramp B to see whether that ramp had a negative effect on the accuracy of the peak levels from the first peak in ramp A.

In Figure 8-2 and Figure 8-3a, it can be seen that there are well-separated, pronounced and distinguishable peak shapes in the plate velocity of a flush cycle. Since the unfiltered time signal was not measured, the first step was to use the filtered signal in the form of the time-varying summed velocity level to estimate the time at which the highest level occurs (see Figure 8-2a and Figure 8-3a). The peak with the highest summed velocity level for both reception plates occurred for ramp A. In the second step, this information was reconciled with the multi-buffer measurements (velocity-time-amplitude spectra) in terms of $L_{F,125ms}$ from the free run to determine the ramp durations and ramp levels on both reception plates (see Figure 8-2b and c that is shown in detail on Figure 8-3b and c).

For the two toilet flush cycles, the ramp durations and the ramp levels for ramp A are given in Table 8-1. These depend on whether the ramp is increasing or decreasing; hence, two values are given. The results indicate that the ramp durations and ramp levels slightly vary between operating cycles due to the complexity of the mechanical toilet flush process. In the frequency domain, Figure 8-4 shows the L_{Fmax} levels in one-third octave bands from six toilet flush cycles (this includes the two toilet flush cycles indicated as 1 and 2 that are used in this chapter) on the horizontal and vertical reception plate. Hence, although the ramp time and durations vary slightly, this only results in variations of up to

6.3 dB in one-third octave bands. This indicates reasonable repeatability for such a complex source.

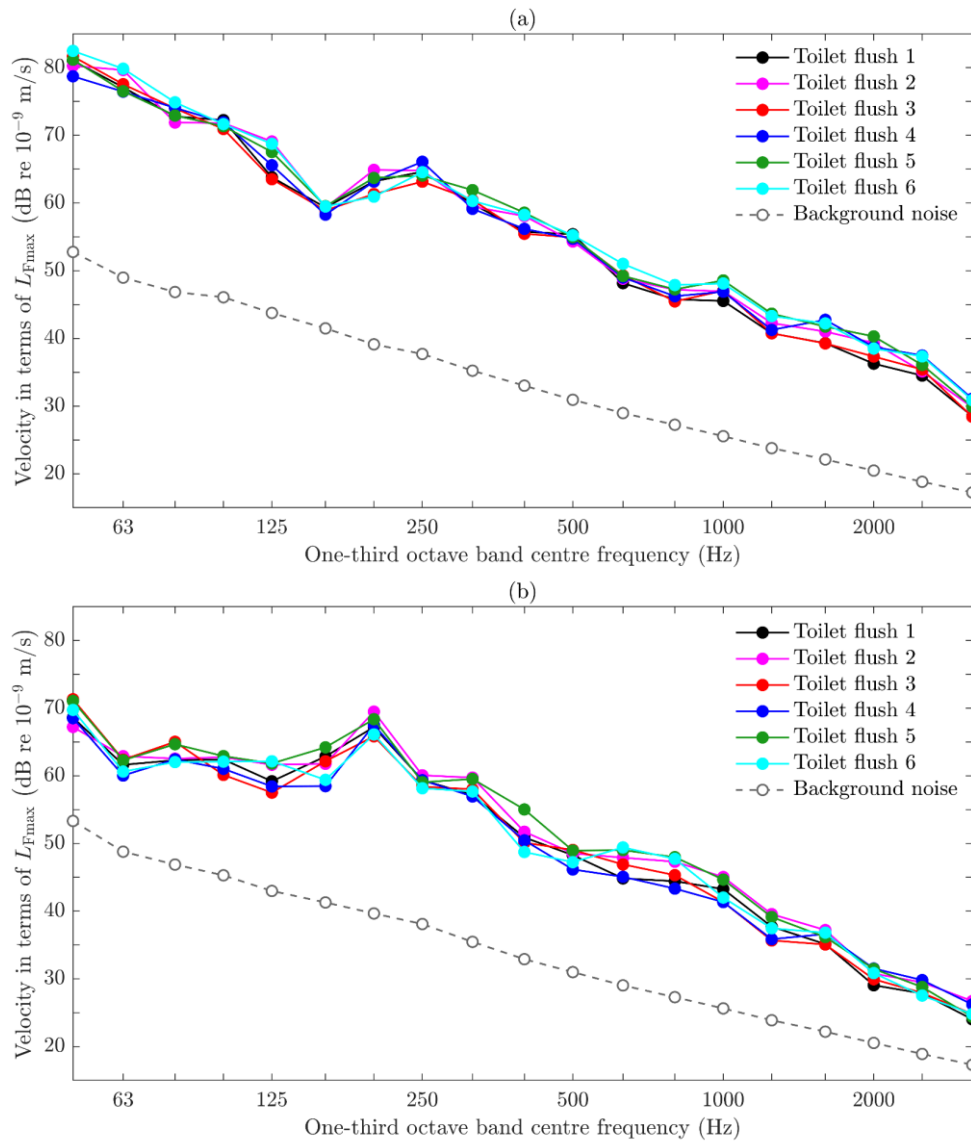


Figure 8-4. Case study of a toilet flush: Repeatability using L_{Fmax} of ramp A determined from six toilet flush cycles on (a) the horizontal reception plate and (b) the vertical reception plate.

Overall, it can be seen from Table 8-1 that the increasing/decreasing ramp durations are within a range from 500 ms to 1 s, while the increasing/decreasing ramp levels differ from each other; being in a range between 20 and 30 dB for

increasing ramp levels and 10 and 20 dB for decreasing ramp levels. The ramped noise signals had equal increasing and decreasing ramp durations but the toilet flush cycles (refer back to Section 3.3.7.1) have different increasing and decreasing ramp durations.

Table 8-1. Case study of a toilet flush: Information on the peak of ramp A with regard to ramp durations and ramp levels for two toilet flush cycles.

Reception plate	Toilet flush 1		Toilet flush 2	
	Horizontal	Vertical	Horizontal	Vertical
Frequency at which highest ramp duration occurs (Hz)	50	200	50	200
Time at which peak in the first ramp occurs (s)	2.875	2.875	2.750	2.750
Increasing ramp duration (ms)	750	625	750	625
Decreasing ramp duration (ms)	500	750	500	750
Increasing ramp level (dB)	29	25	29	27
Decreasing ramp level (dB)	8	18	8	19

Using this information about the ramp durations and ramp levels for both toilet flushes in Table 8-1, the processing of L_{Fmax} and maximum hold values for $L_{F,125ms}$ and $L_{eq,125ms}$ was performed as described in Section 3.3.7.2 without taking into account the additional three 125 ms time slices after the peak of the unfiltered signal since the ramp information yielded from the filtered signal and not from the unfiltered signal in the framework of this case study. In addition, measurements of $L_{F,125ms}$ in the free run were used to ensure the accuracy of the gate-off trigger settings for stopping L_{Fmax} measurements.

For the example of ‘toilet flush 1’, Figure 8-5, Figure 8-6 and Figure 8-7 show the simultaneously measured time-varying velocity levels in terms of the maximum hold values for $L_{F,125ms}$, the free-run values for $L_{F,125ms}$ and the maximum hold values for $L_{eq,125ms}$ respectively on the horizontal and vertical reception plates.

There are several ramps in the operating cycle (see Figure 8-2a or Figure 8-3a); hence, a check is made on whether L_{Fmax} equals $\max\{L_{F,125ms}\}$ for the peak in one of these ramps, ramp A (2.875 s). Since the L_{Fmax} measurements were stopped by a gate-off trigger at 4.5 s and a subsequent ramp, ramp B (4.25 s), occurred between ramp A and the recorded L_{Fmax} data up to the specified gate-off trigger. (NB Ramp C (6.125 s) and ramp D (50,5 s) do not affect the L_{Fmax} data record and therefore are not taken into account for analysis.) To make this information more accessible, Figure 8-5 and Figure 8-6 are used to visualise the times of the ramps A and B as well as the gate-off trigger for L_{Fmax} with multi-buffer measurements in terms of maximum hold and free run values for $L_{F,125ms}$ from ‘toilet flush 1’ on the horizontal and vertical reception plate. The dark blue line and the red line indicate the time at which $\max\{L_{F,125ms}\}$ occurs for ramp A and ramp B respectively. The light blue line indicates the time at which the gate-off trigger for L_{Fmax} stops. However, from Figure 8-8, it is seen that the comparison of the difference between maximum hold values for $L_{F,125ms}$ at 2.875 s (represented by the dark blue line) and L_{Fmax} at 4.5 s (represented by the light blue line) leads to L_{Fmax} levels that correspond to $\max\{L_{F,125ms}\}$ peak values in ramp A. In addition, all differences between free run values for $L_{F,125ms}$ from 0 to 2.75 s and 3 to 4.375 s (time period during which ramp B by 4.25 s occurs – represented by the red line) and L_{Fmax} at 4.5 s are less than $\max\{L_{F,125ms}\}$ for ramp A. Therefore, these results from Figure 8-8 confirm that

the gate-off trigger of 4.5 s was adequately specified for the time period used to relate L_{Fmax} to $\max\{L_{eq,125ms}\}$ for the peak in ramp A.

As described in Section 3.3.7.2, the determination of the actual $\max\{L_{eq,125ms}\}$ requires careful attention because it has been found that $\max\{L_{eq,125ms}\}$ is related to L_{Fmax} at the time at which $L_{Fmax} = \max\{L_{F,125ms}\}$ for the peak in the ramp occurs in all frequency bands. Therefore, identifying the actual $\max\{L_{eq,125ms}\}$ becomes increasingly important with complex sources such as a toilet flush that have several ramps in an operating cycle. Hence, only the dark blue line is taken over into Figure 8-7, which represents the maximum hold values for $L_{eq,125ms}$ from 'toilet flush 1' on both the horizontal and vertical plate since this line indicates the time for $\max\{L_{eq,125ms}\}$ that corresponds to the time at which L_{Fmax} equals $\max\{L_{F,125ms}\}$ for the peak in ramp A in all frequency bands.

The two peak values for L_{Fmax} and $\max\{L_{eq,125ms}\}$ in ramp A (represented by the dark blue line) are used in the following sections to investigate whether the empirical correction of $L_{Fmax} - \max\{L_{eq,125ms}\}$ from ramped noise signals can be replicated with a real source such as the complex toilet flush cycle used in this case study.

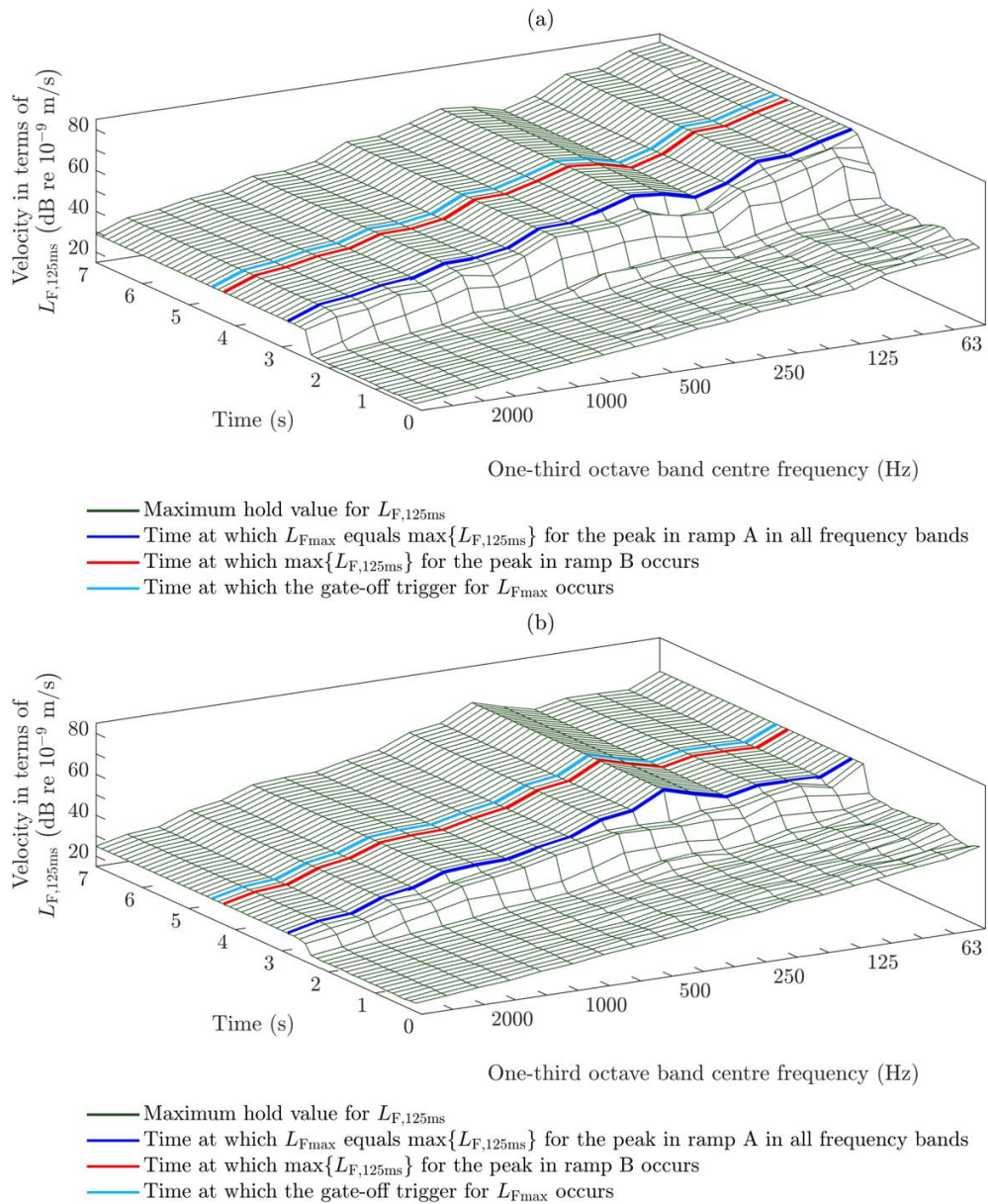


Figure 8-5. Case study of a toilet flush: Multi-buffer measurements for velocity levels in terms of $L_{F,125ms}$ starting from a time of 0 s up to 7 s with maximum hold measured on (a) the horizontal reception plate and (b) the vertical reception plate. The time-varying operating cycle is based on the example ‘toilet flush 1’ in Table 8-1.

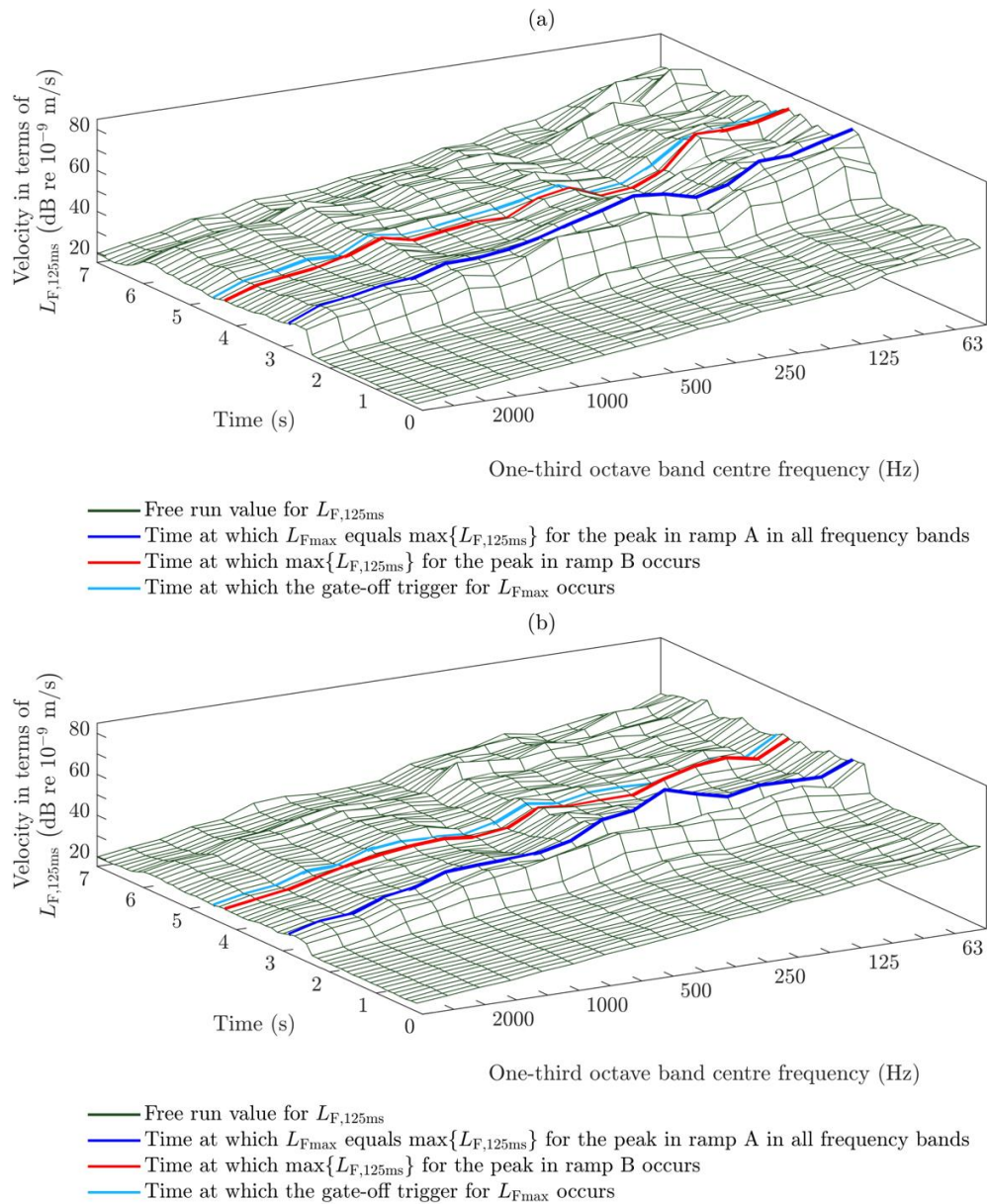


Figure 8-6. Case study of a toilet flush: Multi-buffer measurements for velocity levels in terms of $L_{F,125ms}$ starting from a time of 0 s up to 7 s with a free run measured on (a) the horizontal reception plate and (b) the vertical reception plate. The time-varying operating cycle is based on the example ‘toilet flush 1’ in Table 8-1.

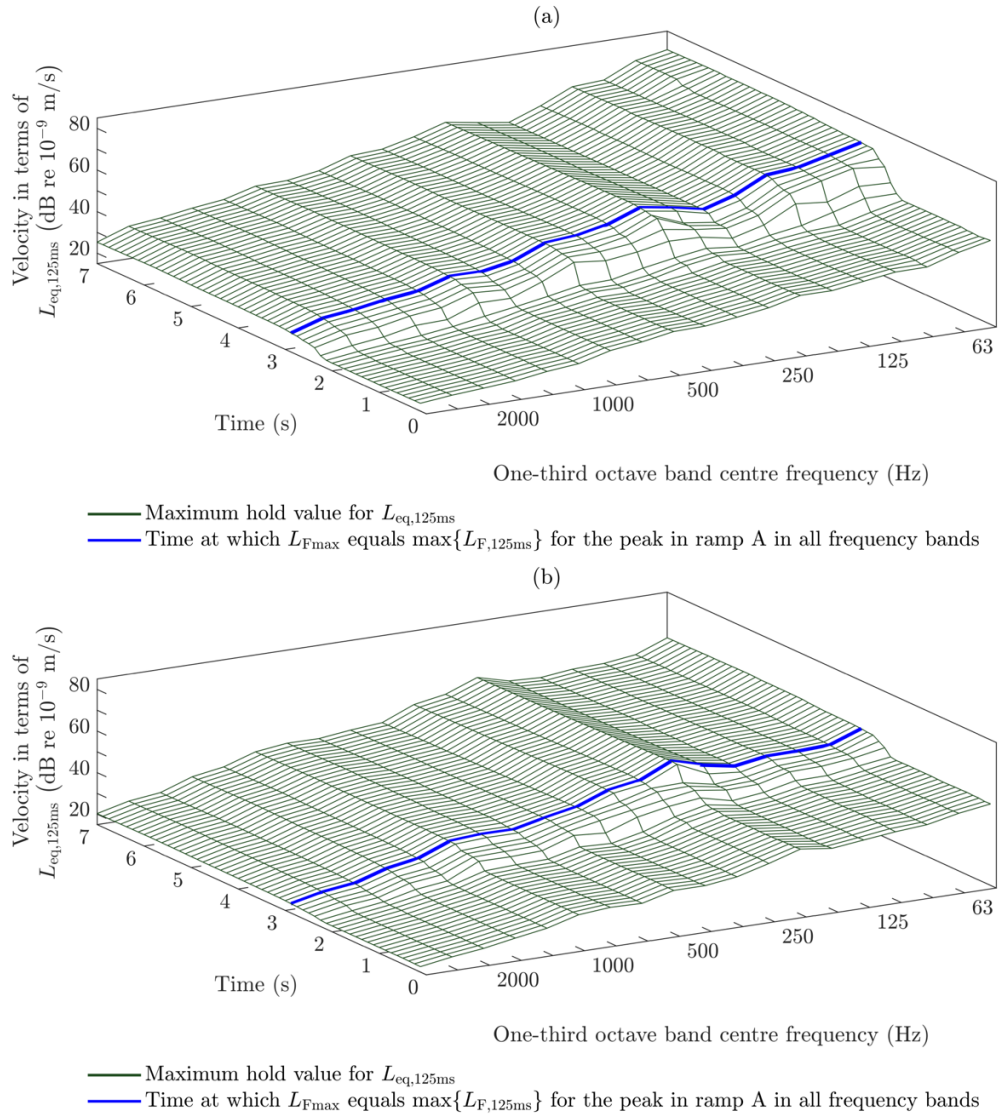


Figure 8-7. Case study of a toilet flush: Multi-buffer measurements for velocity levels in terms of $L_{eq,125ms}$ starting from a time of 0 s up to 7 s with maximum hold measured on (a) the horizontal reception plate and (b) the vertical reception plate. The time-varying operating cycle is based on the example ‘toilet flush 1’ in Table 8-1.

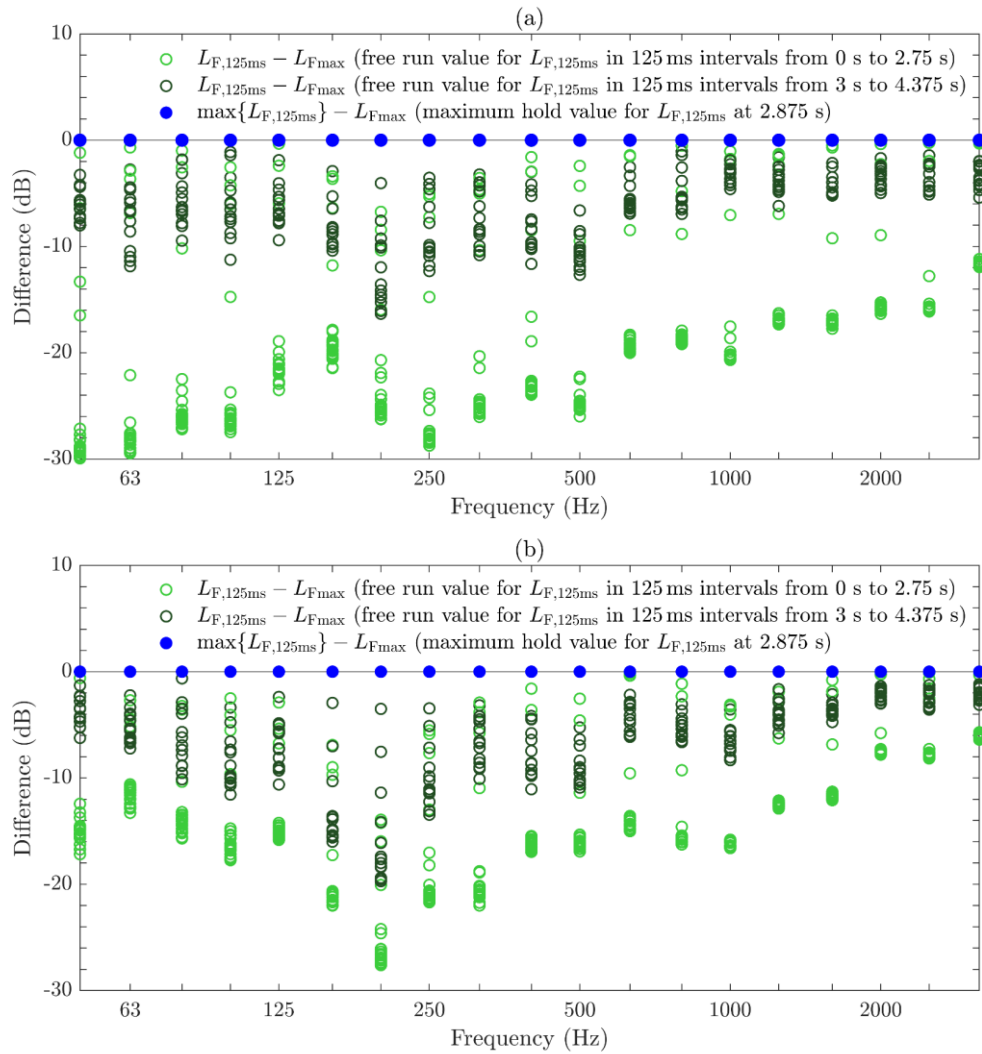


Figure 8-8. Case study of a toilet flush: Difference between $L_{F,125ms}$ in the free run and L_{Fmax} and difference between $\max\{L_{F,125ms}\}$ and L_{Fmax} when measured on (a) the horizontal reception plate and (b) the vertical reception plate. The time-varying operating cycle is based on the example ‘toilet flush 1’ in Table 8-1.

8.3.2 Empirical correction from short L_{eq} to L_{Fmax}

For the two examples of the toilet flush for the peak in ramp A, the specific empirical correction, $L_{Fmax} - \max\{L_{eq,125ms}\}$, is assessed according to Section 6.3.1 with L_{Fmax} and $\max\{L_{eq,125ms}\}$ determined using the processing procedure described in Section 8.3.1. Figure 8-9 shows the comparison of the specific empirical correction from ‘toilet flush 1’ and ‘toilet flush 2’ (for details see Table 8-1) measured on the horizontal and vertical reception plate for which the associated minimum, maximum and frequency average values are listed in Table 8-2.

For each reception plate, the two toilet flushes result in average corrections that only differ by up to ≈ 0.2 dB; hence, it is reasonable to use an average correction. By averaging the results from ‘toilet flush 1’ and ‘toilet flush 2’ with increasing/decreasing ramp durations ranging from 500 to 750 ms and ramp levels ranging from ≈ 10 to ≈ 30 dB for ramp A gives an average correction of ≈ 6.3 and ≈ 6.4 dB for the horizontal and vertical plate respectively. Hence, for a toilet flush, it is reasonable to use the empirical correction established in Section 6.3.1; this was $L_{Fmax} - \max\{L_{eq,125ms}\} \approx 6$ dB. In addition, the results show that it is reasonable to assume that if the decreasing ramp has a steeper gradient than the increasing ramp, only the increasing ramp is likely to affect L_{Fmax} and $\max\{L_{eq,125ms}\}$.

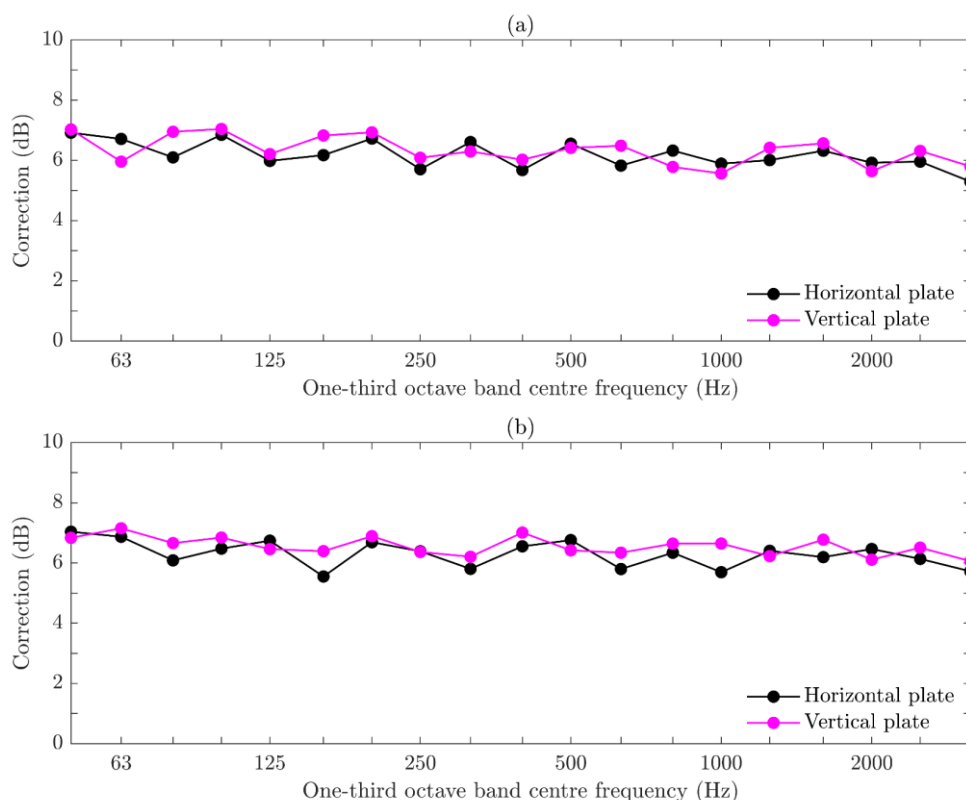


Figure 8-9. Case study of a toilet flush: The specific empirical correction, $L_{Fmax} - \max\{L_{eq,125ms}\}$, using the peak in ramp A of the filtered toilet flush signal for (a) 'toilet flush 1' and (b) 'toilet flush 2' from Table 8-1 measured on the horizontal and vertical reception plate.

Table 8-2. Case study of a toilet flush: The specific empirical correction, $L_{Fmax} - \max\{L_{eq,125ms}\}$, with regard to minimum (MIN), maximum (MAX) and average (AVG) levels using the peak in ramp A of the filtered toilet flush signal for 'toilet flush 1' and 'toilet flush 2' from Table 8-1 measured on the horizontal and vertical reception plate.

Reception plate	Toilet flush	Increasing ramp duration (ms)	Increasing ramp level (dB)	MIN (dB)	MAX (dB)	AVG (dB)
Horizontal	1	750	29	5.3	6.9	6.2
	2			5.6	7.0	6.3
Vertical	1	625	25	5.6	7.0	6.3
	2			5.8	7.2	6.6

8.3.3 Comparison with time-varying signals of ramped noise

Section 8.3.3.1 compares the specific empirical correction ($L_{F_{\max}} - \max \{L_{\text{eq},125\text{ms}}\}$) from the toilet flushes with those from the ramped noise signals. Section 8.3.3.2 highlights the comparison between the toilet flushes and ramped noise signals using the single-number empirical correction that is subtracted from the specific empirical correction. Recalling from Table 8-1 that ramp A of the two toilet flush cycles consists of increasing/decreasing ramp durations from 500 to 750 ms, which increase with a ramp level from ≈ 20 to ≈ 30 dB but decrease with a ramp level of ≈ 10 or ≈ 20 dB; hence, this comparison is performed with ramp durations of 500 ms and 1 s and ramp levels of 10, 20 and 30 dB for the ramped noise signals.

8.3.3.1 Specific empirical correction

The specific empirical correction of $L_{F_{\max}} - \max \{L_{\text{eq},125\text{ms}}\}$ from ‘toilet flush 1’ and ‘toilet flush 2’ was obtained from the empirical weighting for the vibration sampling specific designed for a particular isolated reception plate. Figure 8-10 and Figure 8-11 allow comparison of the average correction for ramped noise signals using ramp levels of 10, 20 and 30 dB for (a) 500 ms and (b) 1 s. For this comparison, the specific empirical correction of time-varying signals was also determined by the empirical weighting of sampled velocity levels for an individual reception plate since these values differ by only 0.1 dB from the area weighting of sampled velocity levels designed for any isolated, rectangular reception plate. Therefore, for the obtained specific empirical corrections from empirical weighted velocity levels, which related to an individual reception plate, for both the toilet flushes and ramped noise signals, the associated frequency-average values are listed in Table 8-3. Although the decreasing ramp is noted in the table, it is not expected that the decreasing ramp level and decreasing ramp duration would have a significant effect on $L_{F_{\max}}$. The average correction from two toilet flushes with ramp durations (increasing) from 625 to 750 ms and ramp

levels (increasing) between ≈ 20 and ≈ 30 dB was similar to the ramped noise signals for the 500 ms and 1 s ramp and ramp levels of 20 and 30 dB over the entire frequency range from 50 Hz to 3.15 kHz that only differ by 0.1 dB. The agreement between the specific empirical correction of the two toilet flushes with the correction from the ramped noise signals indicates an offset of up to ≈ 1.2 dB; thus, it is reasonable to assume that the decreasing ramp duration and decreasing ramp level do not have a significant effect on $L_{F_{\max}}$ and $\max\{L_{\text{eq},125\text{ms}}\}$.

The specific empirical correction of ≈ 6 dB from the toilet flushes (peak in ramp A) has been assessed with increasing ramp durations ≥ 500 ms and increasing ramp levels ≥ 20 dB. This corresponds to the specific empirical correction of ≈ 6 dB that was identified with ramped noise signals with ramp durations ≥ 500 ms and ramp levels of 20, 30 and 40 dB. Thus, the results from toilet flushes and ramped noise signals confirm that the specific empirical correction is appropriate for real sources with the reception plate.

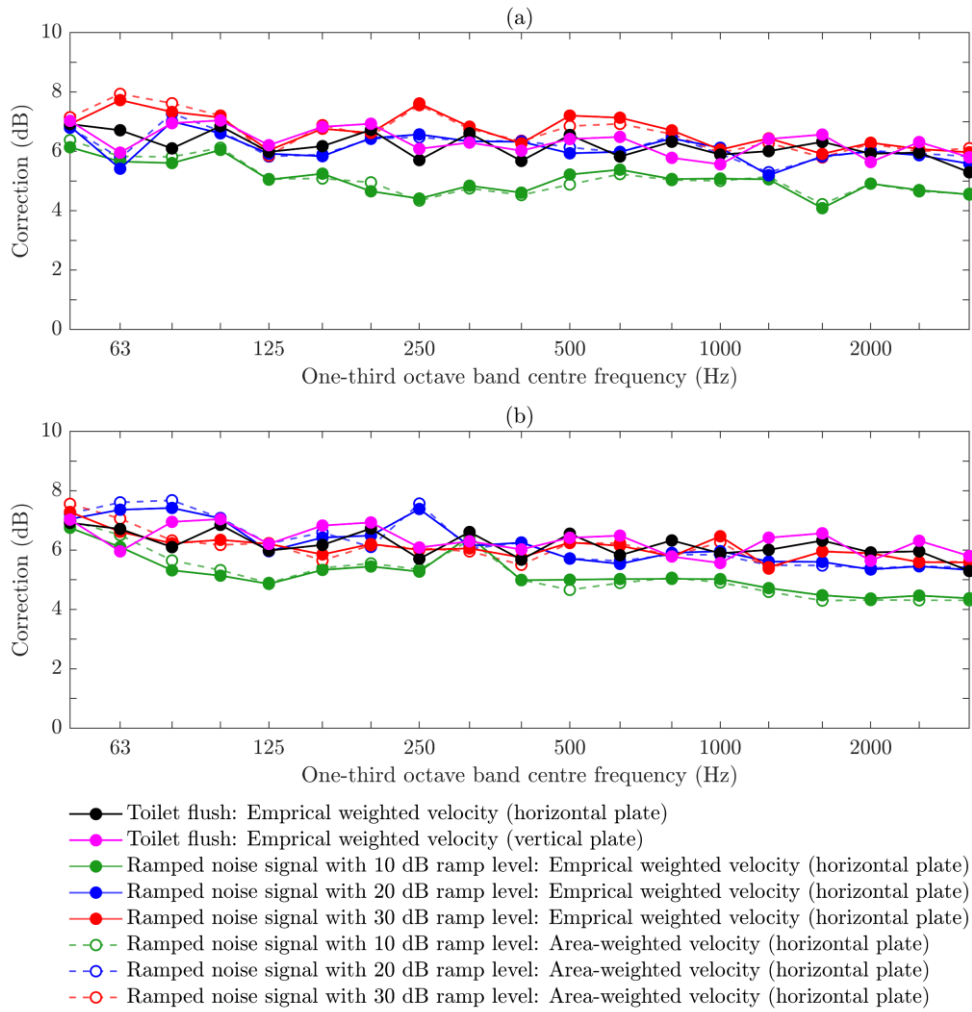


Figure 8-10. Case study of a toilet flush: Comparison of the specific empirical correction, $L_{Fmax} - \max\{L_{eq,125ms}\}$, using the empirical weighted velocity levels for ‘toilet flush 1’ from Table 8-1 measured on the horizontal and vertical reception plate as well as the empirical weighted and area-weighted velocity levels for ramped noise signals measured on the horizontal reception plate from (a) the 500 ms ramp with ramp levels of 10/20/30 dB and (b) the 1 s ramp with ramp levels of 10/20/30 dB.

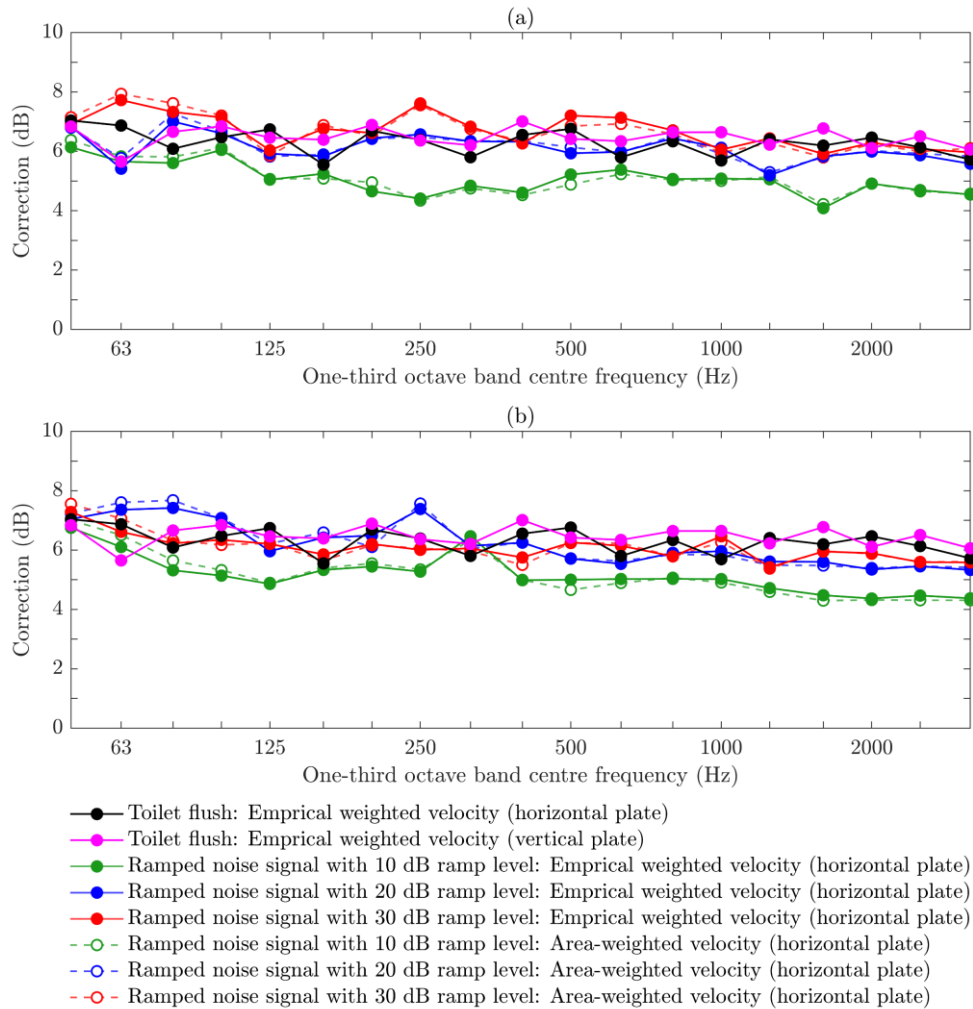


Figure 8-11. Case study of a toilet flush: Comparison of the specific empirical correction, $L_{Fmax} - \max\{L_{eq,125ms}\}$, using the empirical weighted velocity levels for ‘toilet flush 2’ from Table 8-1 measured on the horizontal and vertical reception plate as well as the empirical weighted and area-weighted velocity levels for ramped noise signals measured on the horizontal reception plate from (a) the 500 ms ramp with ramp levels of 10/20/30 dB and (b) the 1 s ramp with ramp levels of 10/20/30 dB.

Table 8-3. Case study of a toilet flush: Comparison of the specific empirical correction, $L_{Fmax} - \max\{L_{eq,125ms}\}$, using the empirical weighted velocity levels for ‘toilet flush 1’ and ‘toilet flush 2’ from Table 8-1 measured on the horizontal and vertical reception plate as well as empirical weighted velocity levels for ramped noise signals measured on the horizontal reception plate from (a) the 500 ms ramp with ramp levels of 10/20/30 dB and (b) the 1 s ramp with ramp levels of 10/20/30 dB.

Reception plate	Sampling strategy	Source	Increasing ramp duration	Increasing ramp level	AVG (dB)
Horizontal	Empirical weighting	Toilet flush 1	750 ms	29 dB	6.2
		Toilet flush 2	750 ms	29 dB	6.5
Vertical	Empirical weighting	Toilet flush 1	625 ms	25 dB	6.3
		Toilet flush 2	625 ms	27 dB	6.6
Horizontal	Empirical weighting*	Ramped noise signals	500 ms	10 dB	5.1
				20 dB	6.1
				30 dB	6.7
			1 s	10 dB	5.2
				20 dB	6.2
				30 dB	6.1

* Note that the specific empirical correction values obtained from the empirical weighted sampling of velocity levels for an individual isolated reception plate differ by 0.1 dB from the specific empirical correction determined from the area-weighted sampling of velocity levels for any isolated, rectangular reception plate.

8.3.3.2 Single-number empirical correction

To make a practical, efficient laboratory reception plate procedure, it should not be necessary to perform time-consuming, complex measurements to establish the time-varying output of building machinery. A single-number empirical correction of 6 dB has been derived from the specific empirical correction of known ramped noise signals (see Section 6.3.2) that should provide a more general approach for simplified SEA-based prediction models such as EN 12354-5 [11]. However, this single-number empirical correction is used in combination with the specific empirical correction from Section 8.3.3.1 in the

form of $L_{Fmax} - \max\{L_{eq,125ms}\} - 6$ dB for the two toilet flushes and ramped noise signals.

Figure 8-12 and Figure 8-13 show, as expected, the same pattern as that for the specific empirical correction from the previous Section 8.3.3.1 since only a single value of 6 dB is subtracted. Hence, the comparison below is only discussed for the increasing ramps as it is not suggested that decreasing ramps have a significant effect on the average correction (refer back to Table 8-2). Note that the difference between specific and single-number empirical correction should ideally approach 0 dB when both corrections are considered with 6 dB.

When comparing ramped noise signals using ramp durations of 500 Hz and 1 s with ramp levels of 20 and 30 dB, the results obtained on the horizontal plate for ‘toilet flush 1’ and ‘toilet flush 2’ both have an increasing ramp duration of 750 s with an increasing ramp level of 29 dB that leads to an average difference of ≈ 0.2 dB. From ‘toilet flush 1’ and ‘toilet flush 2’, which have ramp durations of 625 ms and ramp levels of 25 and 27 dB assessed on the vertical reception plate, the comparison with ramped noise signals differs by ≈ 0.5 dB on average.

Regardless of the horizontal and vertical reception plate, the comparison of both toilet flushes for increasing ramp durations of 625 and 750 ms with increasing ramp levels of 25 and 29 dB gives the largest average difference of up to ≈ 0.3 dB. This is identical to the results of ramped noise signals with ramp levels of 20 and 30 dB for ramp durations from 500 ms to 1 s (the largest difference is also up to ≈ 0.3 dB) for the horizontal plate (see Figure 8-12 and Figure 8-13).

A single value of 6 dB is specified for an empirical correction from ramped noise signals (Section 7.2.2) as a reasonably robust single-number empirical correction for the prediction of L_{Fmax} from $\max\{L_{eq,125ms}\}$ for real sources with a time-varying operating cycle such as a toilet flush. This demonstrates that the single-number empirical correction has the potential to be adopted in simplified SEA-based prediction models such as EN 12354-5 [11].

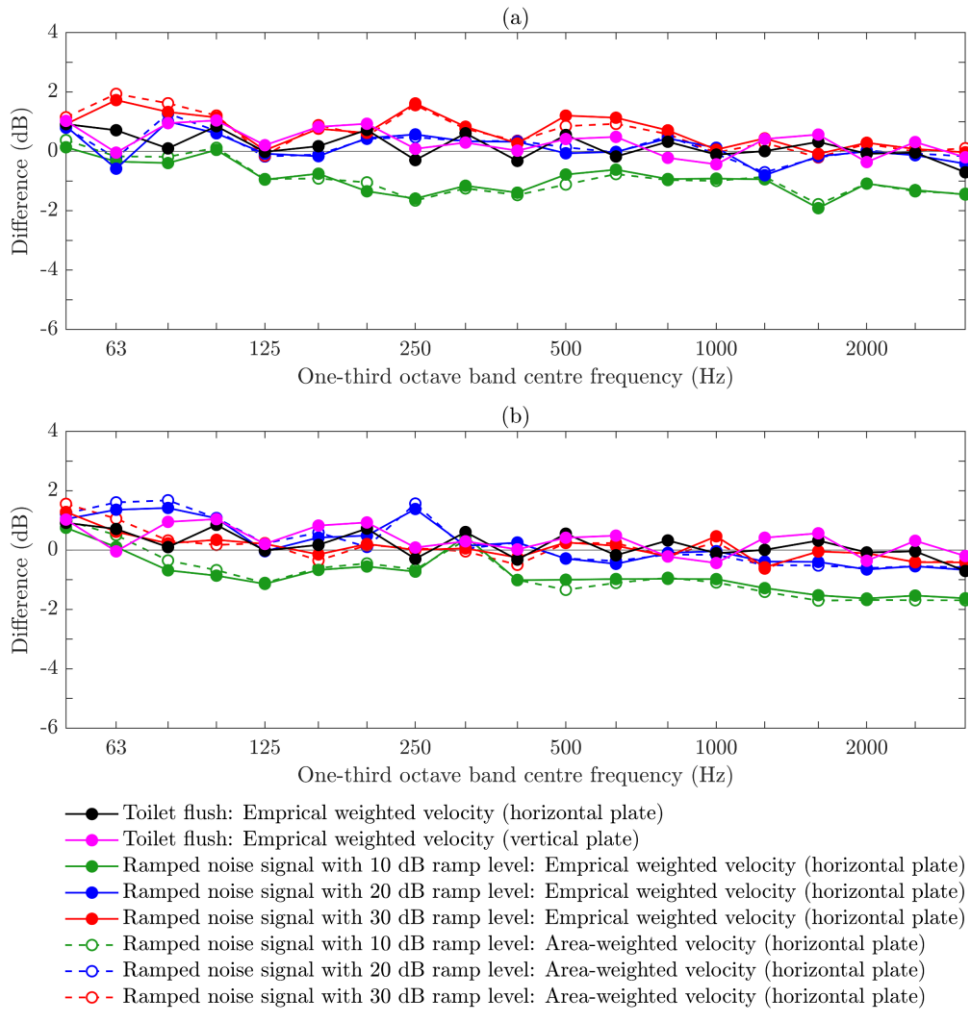


Figure 8-12. Case study of a toilet flush: $L_{Fmax} - \max\{L_{eq,125ms}\} - 6$ dB using the empirical weighted velocity levels for ‘toilet flush 1’ from Table 8-1 measured on the horizontal and vertical reception plate as well as the empirical weighted and area-weighted velocity levels for ramped noise signals measured on the horizontal reception plate from (a) the 500 ms ramp with ramp levels of 10/20/30 dB and (b) the 1 s ramp with ramp levels of 10/20/30 dB.

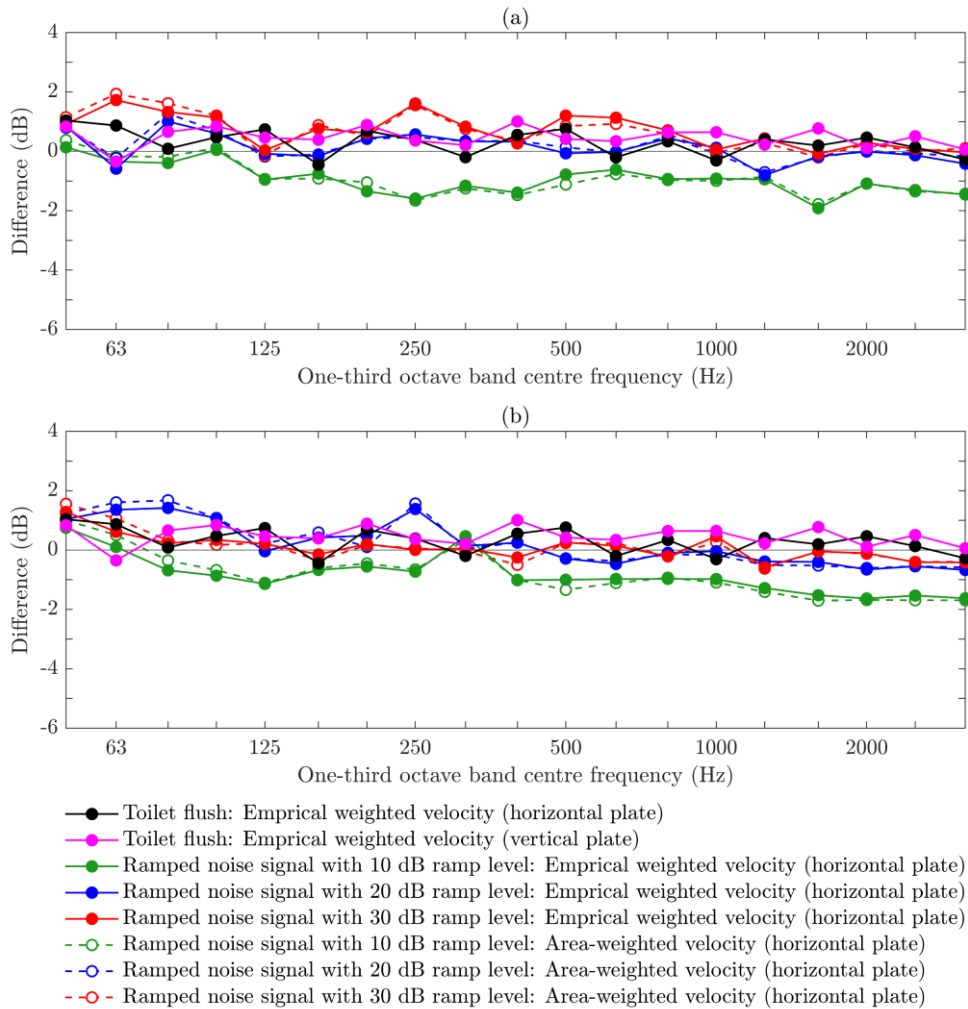


Figure 8-13. Case study of a toilet flush: $L_{F_{\max}} - \max\{L_{eq,125ms}\} - 6$ dB using the empirical weighted velocity levels for ‘toilet flush 2’ from Table 8-1 measured on the horizontal and vertical reception plate as well as the empirical weighted and area-weighted velocity levels for ramped noise signals measured on the horizontal reception plate from (a) the 500 ms ramp with ramp levels of 10/20/30 dB and (b) the 1 s ramp with ramp levels of 10/20/30 dB.

8.4 Discussion

The comparison between the two toilet flushes and ramped noise signals shows that the specific and single-number empirical corrections are valid for this real building equipment source as well as a simplified source. This real source had complex time-varying operating cycles. To investigate time-varying signals from real sources that have multiple ramps where the ramp of interest does not appear first, it is advisable to use gate-on and/or gate-off triggers. These trigger types make it possible to start the measurement at a specific time with a gate-on trigger event that continues until a gate-off trigger event occurs to stop the measurement. Hence, adjusting only the ramp of interest with gate-on/off triggers avoids L_{Fmax} being affected by other ramps. However, this assumes that the time-varying operating cycle of a source is known, which would otherwise require $L_{F,125ms}$ from a free run of an entire operating cycle of a time-varying source to be measured to identify the ramps. This would allow gate-on and/or gate-off triggers to be set correctly to obtain suitable data in terms of simultaneously measured L_{Fmax} , $L_{F,125ms}$ and $L_{eq,125ms}$ for the ramp of interest. Hence, knowledge of the time-varying signal is necessary when determining L_{Fmax} , $\max\{L_{F,125ms}\}$ and $\max\{L_{eq,125ms}\}$ levels for time-varying signals with multiple ramps.

8.5 Summary

This chapter investigated the relationship between L_{Fmax} and short L_{eq} using a toilet flush as a case study with a time-varying operating cycle to assess whether a real source can replicate the empirical correction from ramped noise signals based on the investigations in Chapter 6.

The time-varying flush cycle generated several distinct peaks in the velocity on the reception plates so that the worst-case situation identified with the peak

in the first ramp (from signal processing based on the discussion in Chapter 3 and this chapter, referred to as ramp A) was used to determine the empirical correction. The ramp A from two examples of the toilet flush had increasing/decreasing ramp durations from 500 to 750 ms with increasing ramp levels >20 dB and decreasing ramp levels of <20 dB. From peak levels obtained for ramp A, the specific empirical correction was estimated to be $L_{Fmax} - \max\{L_{eq,125ms}\} \approx 6$ dB. The results indicated that it is reasonable to assume that the steeper gradient of the increasing ramp affected L_{Fmax} and $\max\{L_{eq,125ms}\}$ levels. Hence, it is reasonable to propose that a single-number empirical correction of 6 dB could be adopted in SEA or simplified SEA-based prediction models such as EN 12354-5 [11]. The derived specific and single-number empirical corrections from two toilet flushes were compared with those from ramped noise signals for which the results were in the same order of magnitude.

In practice, time-varying operating cycles of real sources often consist of several pronounced ramps as demonstrated by the time-varying flush cycle in this chapter. From time-varying sources that inject such a characteristic vibration into the structure, measurements can be controlled using gate-on and/or gate-off triggers. Therefore, gate-on and gate-off triggers could be beneficial to be able to measure only the peak of the ramp of interest from a cyclic structure-borne sound source.

9 Conclusions

9.1 Introduction

In this chapter, the main findings of this thesis are summarised along with suggestions for potential future work.

The objectives of this thesis were to assess the accuracy of the reception plate method, to characterise the power injection from structure-borne sound sources and to investigate an empirical correction based on the relationship between L_{Fmax} and short (125 ms) L_{eq} for the SEA predictions of L_{Fmax} from time-varying structure-borne sound sources in heavyweight buildings. The conclusions from these two aspects are discussed in Section 9.2 and 9.3. Finally, recommendations for future work are given in Section 9.4 that build on the developments relating to the experimental and numerical structure-borne sound characterisation using a reception plate and the prediction of L_{Fmax} and L_{AFmax} from $\max\{L_{eq,125ms}\}$ in conjunction with the proposed empirical correction in buildings.

9.2 Structure-borne sound power characterisation using a reception plate

A FEM model has been validated for a reception plate that incorporated viscoelastic supports around the plate edges according to the experimental set-up to consider the increased damping effect on the vibration response of the dynamic system, particularly evident at low frequencies. The experimental validation of the FEM model was carried out using eigenfrequencies, mode shapes, loss factors, mobilities and spatial variation in plate vibration response with considerations on the dynamic properties of rigid body and bending modes. The validated FEM model for the reception plate in Chapter 4 provide evidence that when designing a new reception plate set-up for a laboratory, FEM modelling can be used to assess different damping materials for layouts and types as well as different plate sizes and shapes (e.g. irregular, rectangular, etc.).

For single-contact sources, the most accurate reception plate power was determined using velocity samples on a fine regular grid over the entire plate surface; this gave an error of ± 1.3 dB. This facilitated an assessment of potential errors that occur when the reception plate power is determined from fewer velocity samples since distinct local variations in the plate vibration response were expected due to the low modal density at low frequencies. For FEM and measurements, the use of velocity responses based on a fine regular grid in the central zone of the plate (≥ 500 mm away from edges) resulted in an underestimation in the reception plate power of up to ≈ 9 dB below 100 Hz. This led to a sampling approach of velocity levels that combined the four corner positions and central zone positions of the plate with an empirical weighting factor for an individual design of a reception plate. Since the spatial variation in plate velocity from measurements and FEM indicated high velocity levels in the vicinity of the plate edges in addition to the higher velocity levels at the four plate corners; a second sampling approach for velocity levels based on an area weighting for any isolated, rectangular reception plate was specified to consider

higher levels at corners/edge strips as well as the central zone. The empirical weighting and area weighting approaches give the possibility to avoid time-consuming measurements with a fine regular grid of positions over the entire plate surface. Using FEM and measurements, both approaches were validated with single-contact sources to analyse the accuracy of the reception plate method according to EN 15657 [35].

The results of the reception plate power indicated that the empirical weighting led to an error of up to 4.5 dB below 80 Hz, which decreased to less than 3 dB at and above 80 Hz, while the area weighting gave an error of less than 2 dB over the entire frequency range from 20 Hz to 2 kHz. Therefore, the area weighting has advantages in accuracy compared to the empirical weighting. Below 100 Hz, the area weighting led to errors in the reception plate power that are smaller than that in the sampling approach of Späh and Gibbs [33].

Subsequently, FEM was used with the area weighting approach to investigate multiple-contact sources with either zero- and random-phase forces between the four contact points in a square of 0.6 m × 0.6 m (representing white goods) and different source orientations on the reception plate. Numerical experiments for this type of source showed that in absence of detailed knowledge of the force phase difference between the contacts, all positions within the surface projected area of the sources between the contacts (typically the area underneath the machine) and the reverberation distance from the contacts should be avoided. Without any information on phase differences between the forces at the contacts, it was shown that these sources should be rather arranged at an oblique angle to the plate edges when determining the reception plate power. Using the area weighting approach to sampling the spatial average velocity led to errors in the reception plate power for the multiple-contact sources that were similar to those for single-contact sources.

The validated FEM model of the laboratory reception plate showed that the reception plate approach is valid for single- and multiple-contact sources regardless of whether the modal response is determined by rigid body modes or

bending modes. Based on FEM and analytical models (mass-spring-dashpot system and multi-modal system), highly damped rigid body modes were found to be beneficial in allowing estimates of the structure-borne sound power where the first few bending modes were relatively widely spaced (below 100 Hz). For a 100 mm concrete reception plate with dimensions 2.0 m \times 2.8 m, it is therefore appropriate to consider the lowest valid frequency as 20 Hz rather than an arbitrary lower frequency used in building acoustics such as 50 Hz. This lower frequency limit is important because measurements reported in this thesis for building machinery show that it often injects considerable structure-borne sound power down to 20 Hz. At these low frequencies, the vibrational power of building machinery is not always broadband but often has low-frequency tonal components. A broadband single-contact source with a tonal component in the frequency region of rigid body modes was used for measurements. For the determination of the reception plate power, this led to an error of 3 dB for the empirical weighting, which reduced to 2 dB for the area weighting. Hence, a lower frequency limit of 20 Hz is possible for this specific reception plate.

9.3 Prediction of L_{Fmax} from time-varying signals using SEA

The results in this thesis show that it is feasible to predict the Fast time-weighted maximum sound pressure level, L_{Fmax} , from maximum short (125 ms) equivalent continuous levels, $\max\{L_{eq,125ms}\}$, in an adjacent room in a heavyweight building using SEA.

The aim was to identify $\max\{L_{eq,125ms}\}$ at the time when L_{Fmax} equals $\max\{L_{F,125ms}\}$ for the relevant peak in a transient event in each frequency band. To identify the relationship between L_{Fmax} and $\max\{L_{eq,125ms}\}$, a specific empirical correction was determined from time-varying signals with increasing/decreasing ramp durations from 125 ms to 5 s and increasing/decreasing ramp

levels of 10, 20, 30 and 40 dB. Estimates of the specific empirical correction used measurements of (a) the signal sent directly into the measurement system, (b) the vibration field of the signals sent directly into a shaker on the heavyweight reception plate and (c) the vibration field of the signals sent directly into a shaker on the heavyweight floor in the building-like situation as well as (d) in the sound field of the receiving room from the radiation of the injected vibration by the shaker into the floor in the building-like situation. The measurement processing of L_{Fmax} , $L_{F,125ms}$ and $L_{eq,125ms}$ was validated using a MATLAB SLM. The results showed that the specific empirical correction had some dependency on the ramp duration and ramp level so that the specific empirical correction (a) for a ramp level of 10 dB and all ramp durations was 5 dB, (b) for ramp levels of 20, 30 and 40 dB with a ramp duration of 125 ms was 7 dB and (c) for ramp levels of 20, 30 and 40 dB with ramp durations ≥ 500 ms was 6 dB. However, this variation was considered to be sufficiently small that an average correction could be used for SEA modelling. Measured and SEA predicted L_{Fmax} levels from time-varying signals for all ramp durations and levels were typically within ± 3 dB for direct sound transmission in the frequency range from 50 Hz to 3.15 kHz.

For practical reasons, the ramp- and level-dependent specific empirical corrections have been simplified to a single-number empirical correction of 6 dB for inclusion in simplified SEA-based models such as EN 12354-5 [11]. Time-varying signals for all ramp durations and ramp levels of 20, 30 and 40 dB led to a similar agreement in the single-number empirical correction as the specific empirical correction between L_{Fmax} from SEA predictions and measurements. It was only for time-varying signals with ramp levels of 10 dB that the predicted L_{Fmax} levels tended to slightly overestimate the measured L_{Fmax} levels by < 4 dB in several frequency bands.

An assessment was made of the calculation of L_{AFmax} from L_{Fmax} in one-third octave bands. This is needed to assess the requirements based on L_{AFmax} for

installation noise in some European countries (e.g. ÖNORM B 8115-2 [12] in Austria, SIA 181 [13] in Switzerland and VDI 4100 [14] in Germany). For this purpose, the frequency-dependent L_{Fmax} levels that were obtained using both the specific and single-number empirical correction were modified with the A-weighting values and energetically summed. When measured and predicted L_{AFmax} levels were compared, these led to good agreement from -0.4 to 2.0 dB in terms of the specific empirical correction and -0.4 to 2.5 dB in terms of the single-number empirical correction.

An experimental case study was carried out using a toilet flush that simultaneously injected structure-borne sound power via point and line contacts into two reception plates. Analysis of L_{Fmax} and $\max\{L_{eq,125ms}\}$ showed that empirical corrections can be determined from the time-varying signals. The results of two toilet flushes gave evidence that the relationship between L_{Fmax} and $\max\{L_{eq,125ms}\}$ was 6 dB for both the specific and single-number empirical correction. In addition, it was shown that even the frequency-dependent toilet flush data had a similar order of magnitude to that of the ramped noise signals. These results confirmed that the specific and single-number empirical correction obtained from ramped noise signals can be replicated using a real source with a cyclic time-varying operation on the reception plate.

9.4 Suggestions for future work

Based on the summary above, future work is divided into two main parts relating to (a) structure-borne sound characterisation with the reception plate approach (Section 9.4.1) and (b) prediction of L_{Fmax} from time-varying structure-borne sound sources in heavyweight buildings (Section 9.4.2).

9.4.1 Structure-borne sound power characterisation using a reception plate

FEM modelling was used for a horizontal reception plate resting on viscoelastic supports with high internal damping according to EN 15657 [35]. The consideration of the viscoelastic material is important for the adequate application of the reception plate method to set the rigid body mode at the suspension resonance to lower or higher frequencies depending on the reception plate layout. This is because the reception plate power is dominated by a modal vibration response through well-separated bending modes at low frequencies causing uncertainties in the prediction of the structure-borne sound power from sources when an optimal design for rigid body modes is absent. Further research could therefore focus on the FEM modelling of different reception plate layouts in terms of the size and shape as well as viscoelastic material arrangements in terms of the damping amount and the associated frequency tolerance of the suspension resonance.

FEM modelling of the viscoelastic supports was incorporated using linear damping, which resulted in good agreement with regard to the estimation of the loss factor and the comparison between the direct injected power and the reception plate power. However, at high frequencies, the linear modelled loss factors from FEM differed slightly from the measured loss factors. Hence, future work could implement the viscoelastic material in FEM using non-linear damping to assess whether the prediction of the loss factor is more accurate.

In this thesis, a uniform force with a frequency sweep was used to determine the direct injected power and the reception plate power. However, FEM allows the assessment of the random vibration response of steady-state excitations such as from a single-contact shaker or multiple-contact machinery if the PSD data of these sources are available. This could be investigated in future work with time-varying excitations to simulate real sources.

To determine the reception plate power from FEM and measurements, the area-weighted velocity level approach was shown to be valid at frequencies in the region of whole body, rocking and bending modes. Also, the area weighting approach had smaller errors than achieved in previous experimental studies (e.g. [33, 42]) involving more than one laboratory. Hence, future work could assess the area-weighting approach in a round-robin test. In addition, since the area weighting approach is designed only for isolated reception plates based on requirements specified in EN 15657 [35], it could be investigated in further work whether this sampling strategy for velocity samples is suitable when a reception plate is (partially) constrained along one/two edges (e.g. viscoelastic material or structural components). Future work could also focus on converting the area weighting approach for isolated reception plates to coupled reception plates having simply-supported or clamped boundaries (e.g. walls and floors).

9.4.2 Prediction of L_{Fmax} from time-varying signals using SEA

A time-varying flush cycle has been assessed as a real source to assess the relationship between L_{Fmax} and $\max\{L_{eq,125ms}\}$ using the reception plate test rig (EN 15657 [35]). The results yield an empirical correction that gave close agreement with the empirical corrections obtained from time-varying signals using a shaker with ramped broadband noise on the reception plate. To encourage industry/manufacturers to use the empirical correction in simplified SEA-based prediction models (e.g. EN 12354-5 [11]), it would be useful to have more examples of different types of machinery with time-varying operating cycles to engage industry with the approach developed in this thesis.

The validity of the empirical corrections has been validated for heavyweight buildings. For lightweight buildings and hybrid buildings (combination of lightweight and heavyweight constructions) such as modular fabricated homes, the short L_{eq} approach could be assessed with two stage reception plate method (EN 15657 [35]).

References

- [1] D. A. Sarigiannis (2013), Combined or multiple exposure to health stressors in indoor built environments, World Health Organization (WHO), Regional Office for Europe, An evidence-based review prepared for the WHO training workshop "Multiple environmental exposures and risks", Copenhagen, pp. 1-82.
- [2] S. Kunkel, E. Kontonasiou, A. Arcipowska, F. Mariottini and B. Atanasiu (2015), Indoor air quality, thermal comfort and daylight: Analysis of residential building regulations in eight EU member states, Building Performance Institute Europe, ISBN: 978-9-4911-4310-6.
- [3] D. Mumovic, J. Palmer, M. Davies, M. Orme, I. Ridley, T. Oreszczyn, C. Judd, R. Critchlow, H. A. Medina, G. Pilmoor, C. Pearson and P. Way (2009), Winter indoor air quality, thermal comfort and acoustic performance of newly built secondary schools in England, *Building and Environment*, 44(7), pp. 1466-1477.
- [4] Y. Al horr, M. Arif, M. Katafygiotou, A. Mazroei, A. Kaushik and E. Elsarrag (2016), Impact of indoor environmental quality on occupant well-being and comfort: A review of the literature, *International Journal of Sustainable Built Environment*, 5(1), pp. 1-11.
- [5] C. Grimwood (1997), Complaints about poor sound insulation between dwellings in England and Wales, *Applied Acoustics*, 52(3/4), pp. 211-223.
- [6] F. Ljunggren, C. Simmons and K. Hagberg (2014), Correlation between sound insulation and occupants' perception – Proposal of alternative single number rating of impact sound, *Applied Acoustics*, 85, pp. 57-68.
- [7] F. Ljunggren, C. Simmons and R. Öqvist (2017), Correlation between sound insulation and occupants' perception – Proposal of alternative single number rating of impact sound, part II, *Applied Acoustics*, 123, pp. 143-151.

References

- [8] ISO/TS 19488:2021, Acoustics – Acoustic classification of dwellings, International Committee for Standardization approved by Technical Committee for Electrotechnical Standardization.
- [9] EN ISO 12354-1:2017, Building acoustics – Estimation of acoustic performance of buildings from the performance of elements – Part 1: Airborne sound insulation between rooms, International Committee for Standardization approved by European Committee for Standardization.
- [10] EN ISO 12354-2:2017, Building acoustics – Estimation of acoustic performance of buildings from the performance of elements – Part 2: Impact sound insulation between rooms, International Committee for Standardization approved by European Committee for Standardization.
- [11] EN 12354-5:2009, Building acoustics – Estimation of acoustic performance of building from the performance of elements – Part 5: Sound levels due to the service equipment, European Committee for Standardization.
- [12] ÖNORM B 8115-2:2021, Schallschutz und Raumakustik im Hochbau – Teil 2: Methodik zur Ermittlung von Schallschutzniveaus (Sound insulation and room acoustics in building construction – Part 2: Methodology for the determination of sound insulation levels), Austrian Standards International.
- [13] SIA 181:2020, Schallschutz im Hochbau (Sound insulation in buildings), Swiss Society of Engineers and Architects.
- [14] VDI 4100:2012, Schallschutz im Hochbau – Wohnungen – Beurteilung und Vorschläge für erhöhten Schallschutz (Sound insulation between rooms in buildings – Dwellings – Assessment and proposals for enhanced sound insulation between rooms), Association of German Engineers.
- [15] M. Robinson and C. Hopkins (2014), Prediction of maximum time-weighted sound and vibration levels using transient statistical energy analysis – Part 1: Theory and numerical implementation, *Acta Acustica united with Acustica*, 100(1), pp. 46-56.
- [16] M. Robinson and C. Hopkins (2014), Prediction of maximum time-weighted sound and vibration levels using transient statistical energy analysis – Part 2: Experimental validation, *Acta Acustica united with Acustica*, 100(1), pp. 57-66.
- [17] M. Robinson and C. Hopkins (2015), Prediction of maximum fast time-weighted sound pressure levels due to transient excitation from the rubber ball and human footsteps, *Building and Environment*, 94(2), pp. 810-820.
- [18] S. Hirakawa and C. Hopkins (2018), Experimental determination of transient structure-borne sound power from heavy impact sources on heavyweight floors with floating floors using an inverse form of transient statistical energy analysis, *Applied Acoustics*, 140, pp. 74-82.
- [19] B. M. Gibbs (2013), Uncertainties in predicting structure-borne sound power input into buildings, *The Journal of the Acoustical Society of America*, 133(5), pp. 2678-2689.

- [20] EN ISO 3741:2010, Acoustics – Determination of sound power levels and sound energy levels of noise sources using sound pressure – Precision methods for reverberation test rooms, International Committee for Standardization approved by European Committee for Standardization.
- [21] EN ISO 3745:2012+A1:2017, Acoustics – Determination of sound power levels and sound energy levels of noise sources using sound pressure – Precision methods for anechoic rooms and hemi-anechoic rooms, International Committee for Standardization approved by European Committee for Standardization.
- [22] B. M. Gibbs (1994), Structure-borne sound sources in buildings, *Building Acoustics*, 1(4), pp. 313-329.
- [23] B. A. T. Petersson and B. M. Gibbs (2000), Towards a structure-borne sound source characterization, *Applied Acoustics*, 61(3), pp. 325-343.
- [24] T. ten Wolde and G. R. Gedefelt (1987), Development of standard measurement methods for structureborne sound emission, *Noise Control Engineering Journal*, 28(1), 5-14.
- [25] B. M. Gibbs (1999), Sources of structure-borne sound in buildings, *Proceedings of the Institute of Acoustics*, 21(3), 1-8.
- [26] J. Su and C. M. Mak (2002), Direct measurement of moment mobility and a moment excitation system, *Applied Acoustics*, 63(2), pp. 139-151.
- [27] C. Höller (2013), Indirect methods of obtaining activity and mobility of structure-borne sound sources, PhD Thesis, University of Liverpool.
- [28] S. H. Yap and B. M. Gibbs (1999), Structure-borne sound transmission from machines in buildings, Part 1: Indirect measurement of force at the machine-receiver interface of a single and multi-point connected system by a reciprocal method, *Journal of Sound and Vibration*, 222(1) pp. 85-98.
- [29] S. H. Yap and B. M. Gibbs (1999), Structure-borne sound transmission from machines in buildings, Part 2: Indirect measurement of force and moment at the machine-receiver interface of a single point connected system by a reciprocal method, *Journal of Sound and Vibration*, 222(1), pp. 99-113.
- [30] M. M. Späh (2006), Characterisation of structure-borne sound sources in buildings, PhD Thesis, University of Liverpool.
- [31] J. Scheck (2011), Characterisation of lightweight stairs as structure-borne sound sources, PhD Thesis, University of Liverpool.
- [32] N. Qi and B. M. Gibbs (2005), Structure-borne power from machines in buildings: Prediction of installed power from laboratory measurements, *Proceedings of the 4th European Congress on Acoustics, Budapest*, pp. 1901-1905.

References

- [33] M. M. Späh and B. M. Gibbs (2009), Reception plate method for characterisation of structure-borne sound sources in buildings: Assumptions and application, *Applied Acoustics*, 70(2), pp. 361-368.
- [34] M. M. Späh and B. M. Gibbs (2009), Reception plate method for characterisation of structure-borne sound sources in buildings: Installed power and sound pressure from laboratory data, *Applied Acoustics*, 70(11-12), pp. 1431-1439.
- [35] EN 15657:2017, Acoustic properties of building elements and of buildings – Laboratory measurement of structure-borne sound from building service equipment for all installation conditions, European Committee for Standardization.
- [36] EN 15657-1:2009, Acoustic properties of building elements and of buildings – Laboratory measurement of airborne and structure-borne sound from building equipment – Part 1: Simplified cases where the equipment mobilities are much higher than the receiver mobilities, taking whirlpool baths as an example, European Committee for Standardization.
- [37] S. Reinhold, J. Scheck, M. Schneider, A. Ruff, H.-M. Fischer and B. Zeitler (2013 to 2016), Nachhaltiger Schallschutz gebäudetechnischer Anlagen in energetisch optimierten Gebäuden – Teilprojekt 1, Stuttgart, German Federal Ministry of Education and Research in the program FHprofUnt, Grant Reference: 03FH089PB2, Grant Dates: 01.03.2013 to 31.10.2016.
- [38] B. M. Gibbs (2009), Granularity in structure-borne sound source characterisation, *Proceedings of the 3rd Congress on Noise and Vibration Emerging Methods*, Oxford, pp. 1-11.
- [39] K. H. Lai, A. T. Moorhouse and B. M. Gibbs (2015), Experimental round-robin evaluation on structure-borne sound source force-power test methods, *Proceedings of the 44th International Congress and Exposition on Noise Control Engineering*, San Francisco, pp. 170-180.
- [40] K. H. Lai, A. T. Moorhouse and B. M. Gibbs (2016), Experimental round-robin evaluation of structure-borne sound source force-power test methods, *Noise Control Engineering Journal*, 64(2), pp. 170-180.
- [41] B. M. Gibbs, G. Seiffert and K. H. Lai (2016), Uncertainties in the two-stage reception plate method for source characterisation and prediction of structure-borne sound power, *Acta Acustica united with Acustica*, 102(3), pp. 441-451.
- [42] C. Höller and B. M. Gibbs (2018), Source substitution method for obtaining the power transmission from vibrating sources in buildings, *Applied Acoustics*, 141, pp. 240-249.
- [43] B. C. Bloss and M. D. Rao (2005), Estimation of frequency-averaged loss factors by the power injection and the impulse response decay methods, *The Journal of the Acoustical Society of America*, 117(1), pp. 240-249.

- [44] C. Hopkins and M. Robinson (2013), On the evaluation of decay curves to determine structural reverberation times for building elements, *Acta Acustica united with Acustica*, 99(2), pp. 226-244.
- [45] C. Hopkins and M. Robinson (2014), Using transient and steady-state SEA to assess potential errors in the measurement of structure-borne sound power input from machinery on coupled reception plates, *Applied Acoustics*, 79, pp. 35-41.
- [46] T. Padois, S. Prenant, V. Rolland, R. Chérif, O. Robin, N. Atalla, M. Etchessahar, R. Klop, S. L. Chapleau, T. Dupont and O. Doutres (2019), Comparison of the reception plate method and the inverse force method for assessing the power of a dummy vibratory source, *Proceedings of the 26th International Congress on Sound and Vibration*, Montreal, pp. 1-8.
- [47] V. Wittstock, M. Villot and J. Scheck (2011), Results of a round robin on structure-borne sound power, *Proceedings of the 6th European Congress on Acoustics*, Aalborg, pp. 2327-2332.
- [48] L. Cremer and M. Heckl (1967), *Körperschall: Physikalische Grundlagen und Technische Anwendungen*, Springer, ISBN: 978-3-642-49629-5.
- [49] L. Cremer, M. Heckl and E. E. Ungar (1973), *Structure-borne sound: Structural vibrations and sound radiation at audio frequencies*, Springer, ISBN: 978-3-662-10120-9.
- [50] E. E. Ungar (1980), *Structureborne sound in buildings: Needed practical research in light of the current state of the art*, National Technical Information Service, United States Department of Commerce, Technical Report: NBS-GCR 80-248, Technical Report No. 4309, Washington, pp. 1-50.
- [51] T. Kihlman (1978), Urgent need for structure-borne sound source data, *Proceedings of the 7th International Conference and Exposition on Noise Control Engineering*, San Francisco, pp. 343-348.
- [52] B. A. T. Petersson and J. Plunt (1982), On effective mobilities in the prediction of structure-borne sound transmission between a source structure and a receiving structure, Part I: Theoretical background and basic experimental studies, *Journal of Sound and Vibration*, 82(4), pp. 517-529.
- [53] B. A. T. Petersson (1999), An experimental technique for dynamic characteristics at large structural interfaces, *Proceedings of the 6th International Congress of Sound and Vibration*, Copenhagen, pp. 2175-2182.
- [54] J. Su, A. T. Moorhouse and B. M. Gibbs (1995), Towards a practical characterization for structure-borne sound sources based on mobility techniques, *Journal of Sound and Vibration*, 185(4), pp. 737-741.
- [55] L. Ji, B. R. Mace and R. J. Pinnington (2003), A power mode approach to estimating vibrational power transmitted by multiple sources, *Journal of Sound and Vibration*, 265(2), pp. 387-399.

References

- [56] R. J. Pinnington and D. C. R. Pearce (1990), Multipole expansion of the vibration transmission between a source and a receiver, *Journal of Sound and Vibration*, 142(3), pp. 461-479.
- [57] B. A. T. Petersson and B. M. Gibbs (1993), Use of the source descriptor concept in studies of multi-point and multi-directional vibrational sources, *Journal of Sound and Vibration*, 168(1), pp. 157-176.
- [58] J. M. Mondot and B. A. T. Petersson (1987), Characterization of structure-borne sound sources: The source descriptor and the coupling function, *Journal of Sound and Vibration*, 114(3), pp. 507-518.
- [59] B. M. Gibbs, B. A. T. Petersson and S. Qiu (1991), The characterization of structure-borne emission of building services machinery using the source descriptor concept, *Noise Control Engineering Journal*, 37(2), pp. 53-61.
- [60] M. H. A. Janssens and J. W. Verheij (2000), A pseudo-forces methodology to be used in characterization of structure-borne sound sources, *Applied Acoustics*, 61(3), pp. 285-308.
- [61] M. Ohlrich (1998), A simple structural power method for determining the vibratory strength of machinery sources, *Proceedings of the 3rd European Conference and Exposition on Noise Control Engineering*, Munich, pp. 383-288.
- [62] M. Heckl (1988), Excitation of sound in structures, *Proceedings of the 17th International Conference and Exposition on Noise Control Engineering*, Avignon, pp. 497-502.
- [63] T. Hiramatsu, H. Ohkawa, M. Koyasu and K. Ishii (1988), Studies on the reference vibration source to be used for the determination of vibromotive force of machinery by the reception plate method, *Proceedings of the 17th International Conference and Exposition on Noise Control Engineering*, Avignon, pp. 461-466.
- [64] H. A. Bonhoff and B. A. T. Petersson (2010), Towards a structure-borne sound source characterization for design and optimization, *Proceedings of the 10th International Congress on Recent Advances in Structural Dynamics*, Southampton, pp. 1-12.
- [65] H. A. Bonhoff and B. A. T. Petersson (2010), Towards a structure-borne sound source characterization for low-noise design, *Technische Universität Berlin, Institute of Fluid Mechanics and Engineering Acoustics*, Preprint submitted to *Applied Acoustics*, pp. 1-35.
- [66] B. M. Gibbs, N. Qi and A. T. Moorhouse (2007), A practical characterisation for vibro-acoustic sources in buildings, *Acta Acustica united with Acustica*, 93(1), pp. 84-93.
- [67] B. M. Gibbs and B. A. T. Petersson (1995), Rating of machines as structure-borne sound sources, *Proceedings of the Institute of Acoustics*, 17(4), pp. 139-146.

- [68] B. M. Gibbs (2007), Machines as sources of structure-borne sound: Can source power be measured, can installed power be predicted?, *Proceedings of the Institute of Acoustics*, 29(5), pp. 1-18.
- [69] B. M. Gibbs, R. Cookson and N. Qi (2008), Vibration activity and mobility of structure-borne sound sources by a reception plate method, *The Journal of the Acoustical Society of America*, 123(6), pp. 4199-4209.
- [70] M. Schröder (1954), Die statistischen Parameter der Frequenzkurven von großen Räumen, *Acta Acustica united with Acustica*, 4(2), pp. 594-600.
- [71] C. Hopkins (2007), *Sound insulation*, Butterworth-Heinemann, ISBN: 978-0-7506-6526-1.
- [72] E. B. Davis (2006), Characterization of structure-borne noise sources using a reverberant or anechoic plate, *Proceedings of the 35th International Conference and Exposition on Noise Control Engineering*, Honolulu, pp. 848-855.
- [73] P. Schevenels (2011), Investigation of the source-structure-sound interaction in the framework of the source characterisation and sound radiation of vibrating sources in buildings, PhD Thesis, Katholieke University Leuven.
- [74] L. De Geetere, B. Ingelaere and P. Schevenels (2008), Uncertainties and repeatability of the reception plate method, *Proceedings of the 2nd Joint Conference of the Acoustical Society of America and European Acoustics Association*, Paris, pp. 2677-2682.
- [75] S. Reinhold, C. Hopkins and B. Zeitler (2017), Low-frequency structure-borne sound power measurements using heavyweight reception plates, *Proceedings of the 24th International Congress on Sound and Vibration*, London, pp. 1-8.
- [76] S. Reinhold, C. Hopkins and B. Zeitler (2018), Structure-borne sound power characterisation from single and multiple contact sources at low frequencies using heavyweight reception plates, *Proceedings of the 44th Annual Conference on Acoustics*, Munich, pp. 1468-1471.
- [77] F. Jacobsen and J. H. Rindel (1987), Time reversed decay measurements, *Journal of Sound and Vibration*, 117(1), pp. 187-190.
- [78] EN ISO 10848-1:2017, *Acoustics – Laboratory and field measurement of flanking transmission for airborne, impact and building service equipment sound between adjoining rooms – Part 1: Frame document*, International Committee for Standardization approved by European Committee for Standardization.
- [79] P. Gardonio and M. J. Brennan (2002), On the origins and development of mobility and impedance methods in structural dynamics, *Journal of Sound and Vibration*, 249(3), pp. 557-573.
- [80] P. Gardonio and M. J. Brennan (2005), Chapter 9: Mobility and impedance methods in structural dynamics, In F. Fahy and J. Walker, *Advanced applications in acoustics, noise and vibration*, Taylor & Francis, ISBN: 0-415-23729-7.

References

- [81] J. Tourret and L. Gavric (1994), Numerical study of the reverberant reception plate method for structureborne noise characterization of small compact machines, Proceedings of the 23th International Conference and Exposition on Noise Control Engineering, Senlis, pp. 215-220.
- [82] A. W. Leissa (1969), Vibration of plates, Scientific and Technical Information Division, National Aeronautics and Space Administration, Technical Report No. NASA SP-160, Washington, pp. 1-353.
- [83] O. C. Zienkiewicz, R. L. Taylor and J. Z. Zhu (2005), The finite element method: Its basis and fundamentals, Butterworth-Heinemann, ISBN: 978-0-7506-6431-8.
- [84] K.-J. Bathe (2014), Finite element procedures, K.-J. Bathe, ISBN: 978-0-9790-0495-7.
- [85] A. Hrennikoff (1941), Solution of problems in elasticity by the framework method, Journal of Applied Mechanics, 8(4), pp. A169-A175.
- [86] R. Courant (1943), Variational methods for the solution of problems of equilibrium and vibrations, Bulletin of the American Mathematical Society, 49(1), pp. 2165-2187.
- [87] W. Prager and J. L. Synge (1947), Approximations in elasticity based on the concept of function space, Quarterly of Applied Mathematics, 5(3), pp. 241-269.
- [88] R. W. Clough (2004), Early history of the finite element method from the view point of a pioneer, International Journal for Numerical Methods in Engineering, 60(1), pp. 283-287.
- [89] O. C. Zienkiewicz (1977), The finite element method, McGraw-Hill, ISBN: 978-0-0708-4072-0.
- [90] J.-L. Batoz, K.-J. Bathe and L.-W. Ho (1980), A study of three-node triangular plate bending elements, International Journal for Numerical Methods in Engineering, 15(12), pp. 1771-1812.
- [91] M.-K. Song, I.-S. Han and S.-H. Kim (2004), Adaptive finite element buckling analysis of folded plate structures using variable-node flat shell elements, KSCE Journal of Civil Engineering, 8(6), 635-641.
- [92] M. M. Hrabok and T. M. Hrudey (1984), A review and catalogue of plate bending finite elements, Computer & Structures, 19(3), pp.479-495.
- [93] F. Ihlenburg (1998), Finite element analysis of acoustic scattering, Springer, ISBN: 978-0-387-98319-8.
- [94] L. L. Thompson and P. M. Pinsky (1996), A space-time finite element method for structural acoustics in infinite domains – Part 1: Formulation, stability and convergence, Computer Methods in Applied Mechanics and Engineering, 132(3-4), pp. 195-227.

- [95] S. Marburg (2002), Six boundary elements per wavelength: Is that enough?, *Journal of Computational Acoustics*, 10(1), pp. 25-51.
- [96] B. J. Lazan (1968), *Damping of materials and members in structural mechanics*, Pergamon Press, ISBN: 978-0-0800-2934-4.
- [97] V. Wittstock and H. Bietz (2009), Characterising sources of structure-borne sound by the two plate method, *Proceeding of the 3rd Conference on Noise and Vibration Emerging Methods*, Oxford, pp. 1-12.
- [98] R. H. Lyon (1970), What good is statistical energy analysis anyway?, *Shock and Vibration Digest*, 2(6), pp. 1-9.
- [99] R. H. Lyon (1975), *Statistical energy analysis of dynamical systems: Theory and applications*, MIT Press, ISBN: 978-0-2626-2175-5.
- [100] R. H. Lyon and G. Maidanik (1962), Power flow between linearly coupled oscillators, *The Journal of the Acoustical Society of America*, 34(5), pp. 623-639.
- [101] R. H. Lyon and R. G. DeJong (1995), *Theory and application of statistical energy analysis*, Butterworth-Heinemann, ISBN: 978-0-7506-9111-6.
- [102] R. J. M. Craik (1996), *Sound transmission through buildings using statistical energy analysis*, Gower, ISBN: 978-0-5660-7572-8.
- [103] C. H. Hodges and J. Woodhouse (1986), Theories of noise and vibration transmission in complex structures, *Reports on Progress in Physics*, 49(2), pp. 107-170.
- [104] M. J. Crocker and A. J. Price (1969), Sound transmission using statistical energy analysis, *Journal of Sound and Vibration*, 9(3), pp. 469-486.
- [105] B. M. Gibbs (1974), *The direct and indirect transmission of vibrational energy in building structures*, PhD Thesis, Aston University.
- [106] B. M. Gibbs and C. L. S. Gilford (1976), The use of power flow methods for the assessment of sound transmission in building structures, *Journal of Sound and Vibration*, 49(2), pp. 267-286.
- [107] R. J. M. Craik (1982), The prediction of sound transmission through buildings using statistical energy analysis, *Journal of Sound and Vibration*, 82(4), pp. 505-516.
- [108] R. J. M. Craik, J. A. Steel and D. I. Evans (1991), Statistical energy analysis of structure-borne sound transmission at low frequencies, *Journal of Sound and Vibration*, 144(1), pp. 95-107.
- [109] C. Hopkins (2000), *Structure-borne sound transmission between coupled plates*, PhD Thesis, Heriot-Watt University.
- [110] C. Hopkins (2002), Statistical energy analysis of coupled plate systems with low modal density and low modal overlap, *Journal of Sound and Vibration*, 251(2), pp. 193-214.

References

- [111] E. Gerretsen (1979), Calculation of the sound transmission between dwellings by partitions and flanking structures, *Applied Acoustics*, 12(6), pp. 413-433.
- [112] E. Gerretsen (1986), Calculation of airborne and impact sound insulation between dwellings, *Applied Acoustics*, 19(4), pp. 245-264.
- [113] E. Gerretsen (1993), Estimation of air-borne and structure-borne sound transmission from machinery in buildings, *Applied Acoustics*, 40(3), pp. 255-265.
- [114] prEN 12354-5:2004, Building acoustics – Estimation of acoustic performance of buildings from the performance of elements – Part 5: Sound levels due to the service equipment, European Committee for Standardization.
- [115] S. Kimura and K. Inoue (1989), Practical calculation of floor impact sound by impedance method, *Applied Acoustics*, 26(4), pp. 263-292.
- [116] S. Schönwald, B. Zeitler and T. R. T. Nightingale (2010), Influence of receive room properties on impact sound pressure level measured with heavy impact sources, *Proceedings of the 1st European Congress on Sound and Vibration*, Ljubljana, pp. 1-8.
- [117] S. Schönwald, B. Zeitler and T. R. T. Nightingale (2010), Influence of receive room properties on impact sound pressure level measured with heavy impact sources, National Research Council Canada, Technical Report: RR-303, Ottawa, pp. 1-25.
- [118] JIS A 1418-2:2019, Acoustics – Measurement of floor impact sound insulation of buildings – Part 2: Method using standard heavy impact sources, Japanese Standard Association.
- [119] G. Kirchhoff (1876), *Vorlesung über mathematische Physik – Mechanik*, Teubner, Collection: European Libraries, Open Library Edition: OL6927036M, URL: archive.org/details/vorlesungenberm02kircoog (Accessed 28/05/2019).
- [120] A. E. H. Love (1892), *A treatise on the mathematical theory of elasticity*, Cambridge University Press, HAL Open Access Archive: hal-01307751, URL: hal.archives-ouvertes.fr/hal-01307751/document (Accessed 28/05/2019).
- [121] E. Ventsel and T. Krauthammer (2001), *Thin plates and shells: Theory, analysis, and applications*, Taylor & Francis, ISBN: 978-0-8247-0575-6.
- [122] S. Timoshenko and S. Woinowsky-Krieger (1959), *Theory of plates and shells*, McGraw-Hill, ISBN: 978-0-0706-4779-4.
- [123] R. S. Langley (1994), Elastic wave transmission coefficients and coupling loss factors for structural junctions between curved panels, *Journal of Sound and Vibration*, 169(3), pp. 297-317.
- [124] C. W. de Silva (2005), *Vibration and shock handbook*, Taylor & Francis, ISBN: 978-0-8493-1580-0.
- [125] D. J. Ewins (2000), *Modal testing: Theory, practice and application*, Research Studies Press, ISBN: 978-0-8638-0218-8.

- [126] Simulia (2014), Abaqus/CAE 6.14: Online documentation, Dassault Systèmes, Build ID: 2014_04_18-11.27.55 44621.
- [127] E. Oñate (2009), Structural analysis with the finite element method: Linear statics – Volume 1: Basis and solids, Springer, ISBN: 978-1-4020-8733-2.
- [128] C. H. Gür and J. Pan (2009), Handbook of thermal process modeling of steels, Taylor & Francis, ISBN: 978-0-8493-5019-1.
- [129] C. Beisbart and N. J. Saam (2019), Computer simulation validation: Fundamental concepts, methodological frameworks, and philosophical perspectives, Springer, ISBN: 978-3-319-70766-2.
- [130] E. Reisner (1945), The effect of transverse shear deformation on the bending of elastic plates, *Journal of Applied Mechanics*, 12(2), pp. A69-A77.
- [131] R. D. Mindlin (1951), Influence of rotatory inertia and shear on flexural motions of isotropic, elastic plates, *Journal of Applied Mechanics*, 18(1), pp. 31-38.
- [132] L. Gaul, S. Bohlen and S. Kempfle (1985), Transient and forced oscillations of systems with constant hysteretic damping, *Mechanics Research Communications*, 12(4), pp. 187-201.
- [133] K. Eriksson, D. Estep, P. Hansbo and C. Johnson (1996), Computational differential equations, Cambridge University Press, ISBN: 978-0-521-56738-1.
- [134] EN 61260-1:2014, Electroacoustics – Octave-band and fractional-octave-band filters – Part 1: Specifications (IEC 61260-1:2014), European Committee for Standardization.
- [135] H. Kuttruff (2009), Room acoustics, Taylor & Francis, ISBN: 978-0-203-87637-4.
- [136] R. J. M. Craik (1981), Damping of building structures, *Applied Acoustics*, 14(5), pp. 347-359.
- [137] F. G. Leppington, E. G. Broadbent and K. H. Heron (1982), The acoustic radiation efficiency of rectangular panels, *Proceedings of the Royal Society of London, A* 382, pp. 245-271.
- [138] F. G. Leppington, E. G. Broadbent and K. H. Heron (1984), Acoustic radiation from rectangular panels with constrained edges, *Proceedings of the Royal Society of London, A* 393, pp. 67-84.
- [139] F. G. Leppington (1996), Acoustic radiation from plates into a wedge-shaped fluid region: Application to the free plate problem, *Proceedings of the Royal Society of London, A* 452, pp. 1745-1764.
- [140] EN 61672-1:2013, Electroacoustics – Sound level meters – Part 1: Specifications (IEC 61672-1:2013), European Committee for Standardization.
- [141] M. Robinson (2012), Prediction of sound and vibration response using transient statistical energy analysis, PhD Thesis, University of Liverpool.

References

- [142] C. W. Kosten (1960), The mean free path in room acoustics, *Acta Acustica united with Acustica*, 10(4), pp. 245-250.
- [143] Getzner Werkstoffe GmbH, Material data sheet for Sylodamp HD 30, Product Identifier Number: DB-HD-30-E-V05.
- [144] EN ISO 10140-5:2021, Acoustics – Laboratory measurement of sound insulation of building elements – Part 5: Requirements for test facilities and equipment, International Committee for Standardization approved by European Committee for Standardization.
- [145] J. T. Broch (1984), Mechanical vibration and shock measurements, Brüel & Kjær, ISBN: 87-87355-34-5.
- [146] G. F. Lang and D. Snyder (2001), Understanding the physics of electrodynamic shaker performance, *Sound and Vibration*, 35(10), pp. 24-33.
- [147] M. Serridge and T. R. Licht (1987), Piezoelectric accelerometer and vibration preamplifiers: Theory and application handbook, Brüel & Kjær, Booklet: DK BB 0694-12.
- [148] MEScope Application Note 15, Multi-reference curve fitting to find closely-coupled modes, Vibrant Technology, URL: appnotes.vibetech.com/AppNote15.pdf (Accessed 19/10/2020).
- [149] R. J. Allemang and D. L. Brown (2006), A complete review of the complex mode indicator function (CMIF) with applications, Proceedings of ISMA2006: International Conference on Noise and Vibration Engineering, Heverlee, pp. 3209-3246.
- [150] MEScope Application Note 13, Introduction to modal curve fitting, Vibrant Technology, URL: appnotes.vibetech.com/AppNote13.pdf (Accessed 19/10/2020).
- [151] C. Y. Shih, Y. G. Tsuei, R. J. Allemang and D. L. Brown (1988), Complex mode indication function and its applications to spatial domain parameter estimation, Proceeding of the 7th International Modal Analysis Conference, Las Vegas, pp. 1-8.
- [152] O. Døssing (1988), Structural testing – Part 1: Mechanical mobility measurements, Brüel & Kjær, Booklet: DK BR 0458-12.
- [153] EN ISO 3382-1:2009, Acoustics – Measurement of room acoustic parameters – Part 1: Performance spaces, International Committee for Standardization approved by European Committee for Standardization.
- [154] EN ISO 3382-2:2008, Acoustics – Measurement of room acoustic parameters – Part 2: Reverberation time in ordinary rooms, International Committee for Standardization approved by European Committee for Standardization.
- [155] R. B. Randall (1987), Frequency analysis, Brüel & Kjær, ISBN: 87-87355-07-8.

- [156] S. Gade and H. Herlufsen (1987), Windows to FFT analysis (Part1), Brüel & Kjær, Technical Review Number: 3, ISSN: 007-2621, BV 0031-11.
- [157] M. Robinson and C. Hopkins (2014), Effects of signal processing on the measurement of maximum sound pressure levels, *Applied Acoustics*, 77, pp. 11-19.
- [158] ANSI S1.11:2004, Specification for octave-band and fractional-octave-band analog and digital filters, American National Standards Institute.
- [159] MATLAB R2021a (2021), fdesign.octave: Octave filter specification, MathWorks, URL: de.mathworks.com/help/dsp/ref/fdesign.octave.html (Accessed 27/03/2021).
- [160] A. Brandt (2011), Noise and vibration analysis: Signal analysis and experimental procedures, John Wiley & Sons, ISBN: 978-0-470-97817-7.
- [161] R. J. M. Craik (1982), The measurement of the material properties of building structures, *Applied Acoustics*, 15(4), pp. 275-282.
- [162] M. R. Schroeder (1965), New method for measuring reverberation time, *Journal of the Acoustical Society of America*, 37, pp. 409-412.
- [163] EN 29052-1:1992, Acoustics – Method for the determination of dynamic stiffness – Part 1: Materials used under floating floors in dwellings, European Committee for Standardization.
- [164] E. Skudrzyk (1980), The mean-value method of predicting the dynamic response of complex vibrators, *The Journal of the Acoustical Society of America*, 67(4), pp. 1105-1135.
- [165] C. Hopkins and P. Turner (2005), Field measurement of airborne sound insulation between rooms with non-diffuse sound fields at low frequencies, *Applied Acoustics*, 66(12), pp. 1339-1382.

Appendices

- Appendix A FEM modelling procedure using correction factor for a different modification of spring-dashpot elements (Chapter 4)
- Appendix B Published papers in peer-reviewed journals and conference proceedings

Appendix A. FEM modelling procedure using correction factor for a different modification of spring-dashpot elements (Chapter 4)

In FEM, the experimental set-up of the reception plate using partial coverage with viscoelastic material is modelled considering a spring-dashpot element distribution of $N_v = 360$, which are arranged around the plate edges at the corner nodes of two STRI3 elements (corresponding to a square of 100 mm \times 100 mm) – Figure A-1. When Eq. (4.1) is used, the spring stiffness and the damping constant is then calculated with $k = 71813$ N/m and $R = 131.8$ Ns/m respectively. Using this new spring-dashpot element distribution to incorporate the viscoelastic material into the FEM model, the results are compared with the FEM model using $N_v = 1264$ for the partial coverage with viscoelastic material and are validated with measurements as described in Section 4.4. Since it was found that for a highly damped reception plate, the complex frequency extraction in FEM is not significantly different to the results from eigenvalue extraction analysis, only the latter is used to obtain the real-valued normal modes. The validation procedure is introduced using from measurements and FEM (a) the eigenfrequencies, mode count and mode shapes (refer back to Section 4.4.1), (b) damping (refer back to Section 4.4.2) and (c) the driving-point mobility (refer back to Section 4.4.3).

Figure A-2 compares the eigenfrequencies with corresponding values in Table A-1, Figure A-3 illustrates the mode count, Figure A-4 shows the MAC of correlated mode shapes with corresponding values in Table A-2, Figure A-5 and Figure A-6 display the damping and driving-point mobility respectively.

Close agreement between measured and predicted eigenfrequencies, mode counts, MAC from correlated mode pairs, damping and driving-point mobility indicate that the results from the partial spring-dashpot modelling with $N_v = 360$ is nearly identical to the results from the partial spring-dashpot modelling with $N_v = 1264$. Note that one of the rocking modes is shifted from the 25 Hz band for the FEM model using $N_v = 1264$ to the 31.5 Hz band for the

FEM model using $N_v = 360$, which corresponds to the EMA results. However, these results give evidence that Eq. (4.1) from Section 4.2 is valid as a good modification descriptor of spring-dashpot systems to incorporate the viscoelastic supports of the reception plate with sufficient accuracy in FEM.

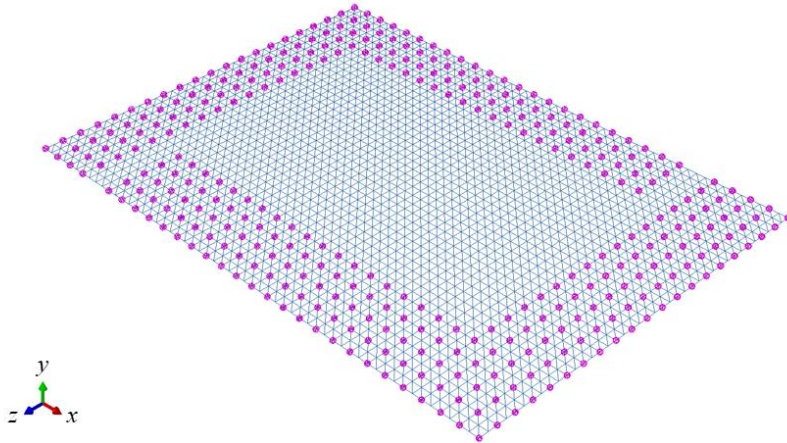


Figure A-1. FEM model of a reception plate using partial coverage with a viscoelastic material distribution of $N_v = 360$, which corresponds to the coverage of viscoelastic material distribution of $N_v = 1264$ in Figure 4-1b.

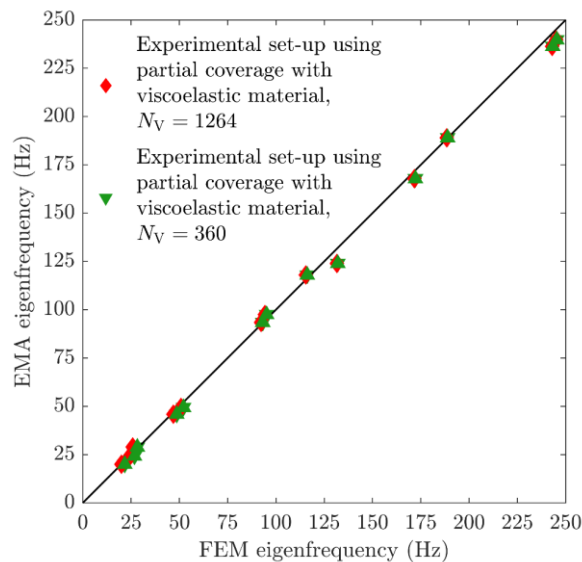


Figure A-2. Reception plate using partial coverage with viscoelastic material: Comparison of eigenfrequencies from EMA and FEM for the reception plate of the experimental set-up using partial coverage with viscoelastic material distributions of $N_v = 1264$ and $N_v = 360$.

Table A-1. Reception plate using partial coverage with viscoelastic material: Eigenfrequencies from EMA and FEM for the reception plate of the experimental set-up using partial coverage with viscoelastic material distributions of $N_V = 1264$ and $N_V = 360$.

Mode	Eigenfrequencies			Error	
	EMA: PSVM	FEM: PCVM $N_V = 1264$	FEM: PCVM $N_V = 360$	EMA: PSVM vs FEM: PCVM $N_V = 1264$	EMA: PSVM vs FEM: PCVM $N_V = 360$
	f_x (Hz)	f_A (Hz)	f_A (Hz)	NFD (%)	NFD (%)
1	20.1	20.0	21.6	0.6	7.6
2	24.2	24.3	26.5	0.4	9.6
3	28.9	25.8	28.2	10.7	2.3
4	45.9	46.9	48.7	2.2	5.7
5	49.4	50.8	52.2	2.9	5.3
6	93.5	92.4	93.2	1.2	0.4
7	97.5	94.3	95.2	3.3	2.4
8	118.0	115.5	116.2	2.1	1.5
9	124.0	131.5	132.0	6.1	6.1
10	167.8	171.7	172.2	2.3	2.6
11	189.0	188.4	188.9	0.3	0.1
12	236.3	243.0	243.3	2.8	2.9
13	239.7	245.1	245.4	2.3	2.3

PCVM: Partial Coverage with Viscoelastic Material

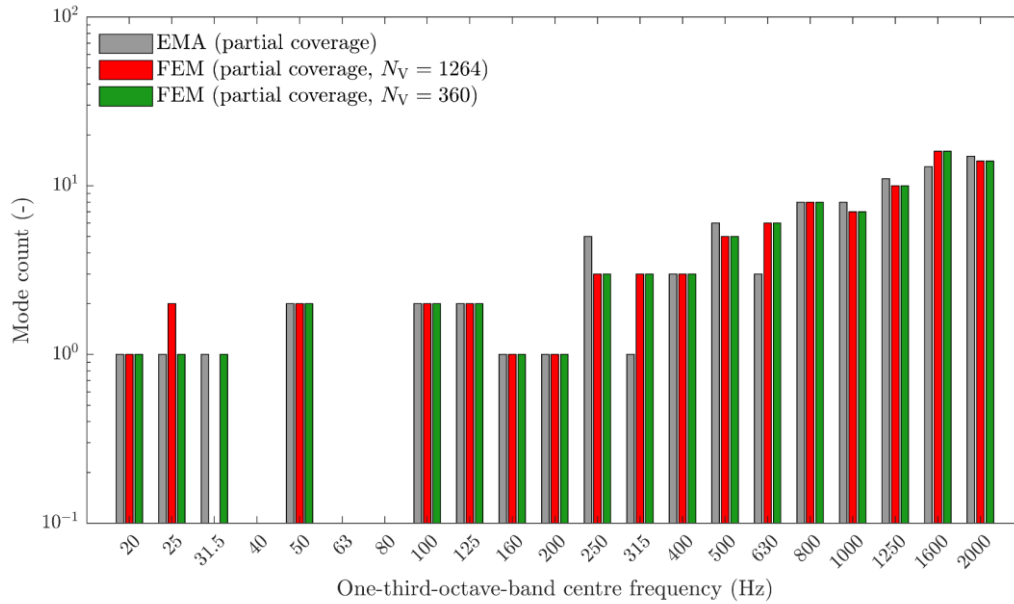


Figure A-3. Reception plate using partial coverage with viscoelastic material: Mode count in one-third octave bands from EMA and FEM eigenfrequencies for the reception plate of the experimental set-up using partial coverage with viscoelastic material distributions of $N_V = 1264$ and $N_V = 360$.

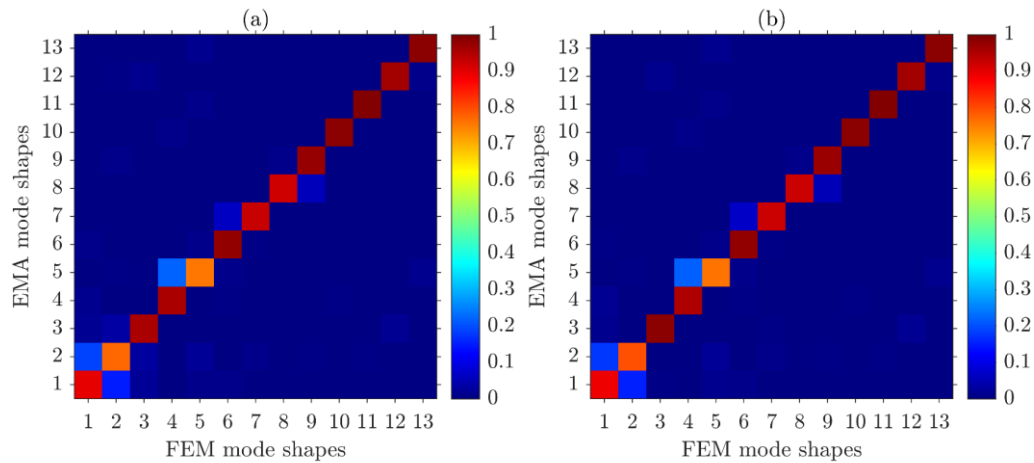


Figure A-4. Reception plate using partial coverage with viscoelastic material: Comparison of EMA (complex-to-real) and FEM (real) eigenfunctions using MAC for the reception plate of the experimental set-up using partial coverage with viscoelastic material distributions of (a) $N_V = 1264$ and (b) $N_V = 360$.

Table A-2 Reception plate using partial coverage with viscoelastic material: Comparison of MAC values from EMA (complex-to-real) and FEM (real) eigenfunctions for the reception plate of the experimental set-up using partial coverage with viscoelastic material distributions of $N_v = 1264$ and $N_v = 360$.

Mode	Correlation between mode pairs	
	EMA: PCVM vs FEM: PCVM $N_v = 1264$	EMA: PCVM vs FEM: PCVM $N_v = 360$
	MAC	MAC
1	0.90	0.89
2	0.77	0.80
3	0.95	0.99
4	0.95	0.95
5	0.76	0.76
6	0.98	0.98
7	0.93	0.92
8	0.92	0.92
9	0.97	0.97
10	0.99	0.99
11	0.99	0.99
12	0.96	0.96
13	0.99	0.99

PCVM: Partial Coverage with Viscoelastic Material

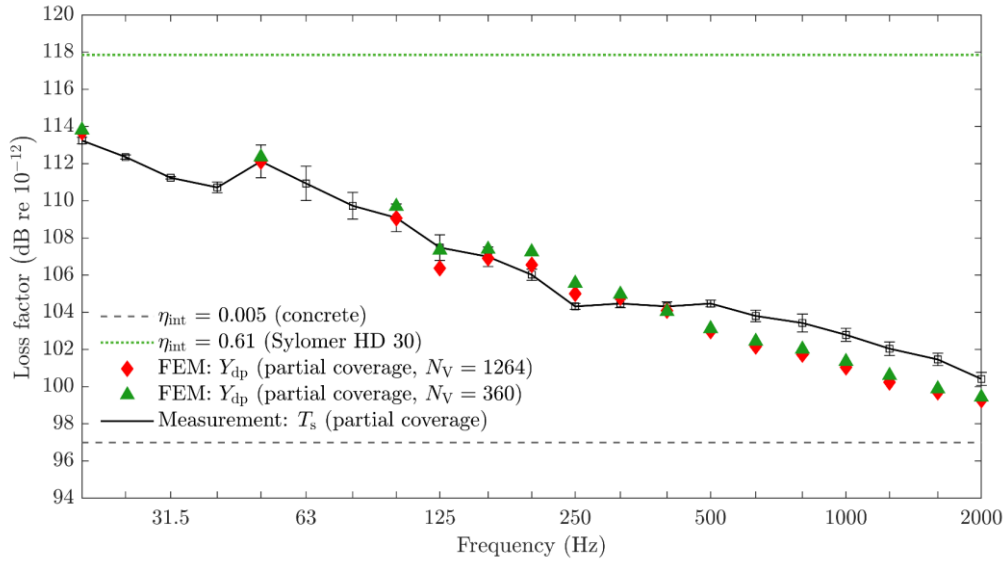


Figure A-5. Reception plate using partial coverage with viscoelastic material: Comparison of loss factors determined from measurements using structural reverberation time (T_s) and the FEM model using driving-point mobility (Y_{dp}).

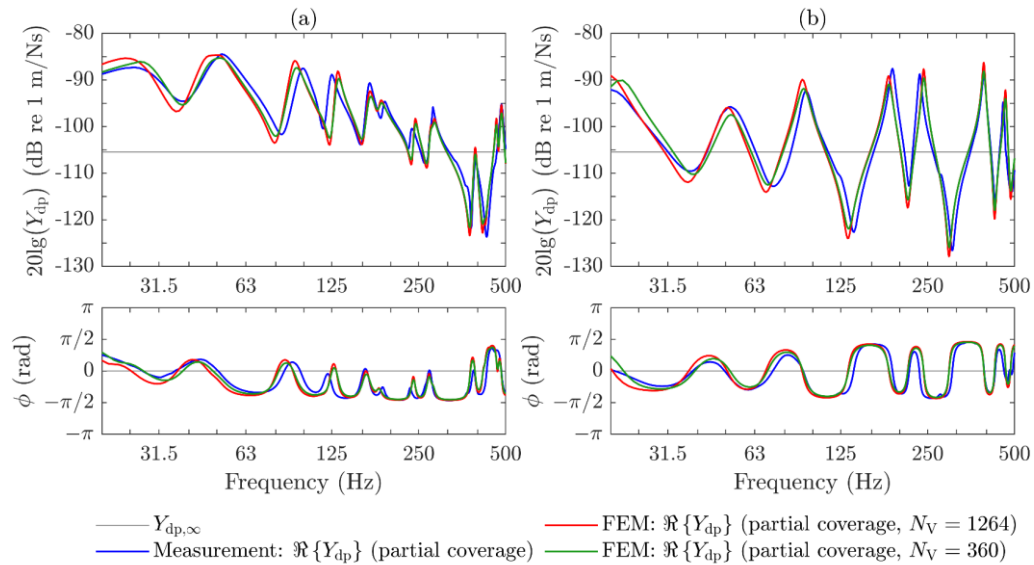


Figure A-6. Reception plate using partial coverage with viscoelastic material: Comparison of the driving-point mobility from measurements and the FEM model at excitation positions (a) 1Y and (b) 2Y as defined in Figure 4-11.

Appendix B. Published papers in peer-reviewed journals and conference proceedings

Journal articles

- **S. Reinhold**, C. Hopkins (2021), Sampling procedures on reception plates to quantify structure-borne sound power from machinery, *Applied Acoustics*, 172, pp. 1-11.

Conference papers

- **S. Reinhold**, C. Hopkins and G. Seiffert (2019), Prediction of maximum Fast time-weighted sound pressure levels from time-varying structure-borne sound sources in heavyweight buildings, *Proceedings of 23rd International Congress on Acoustics, Aachen*, pp. 1248-1254.
- **S. Reinhold**, C. Hopkins and G. Seiffert (2018), Estimating maximum Fast time-weighted vibration levels from short equivalent continuous vibration level measurements of structure-borne sound sources on heavyweight plates, *Proceedings of the 11th European Congress and Exposition on Noise Control Engineering, Heraklion*, pp. 1609-1616.
- **S. Reinhold**, C. Hopkins and B. Zeitler (2018), Structure-borne sound power characterisation from single and multiple contact sources at low frequencies using heavyweight reception plates, *Proceedings of the 44th Annual Conference on Acoustics, Munich*, pp. 1468-1471.
- **S. Reinhold**, C. Hopkins and B. Zeitler (2017), Low-frequency structure-borne sound power measurements using heavyweight reception plates, *Proceedings of the 24th International Congress on Sound and Vibration, London*, pp. 1-8.
- **S. Reinhold**, C. Hopkins and B. Zeitler (2017), Numerical simulation of a laboratory reception plate using finite elements, *Proceedings of the 43rd Annual Conference on Acoustics, Kiel*, pp. 525-528.
- **S. Reinhold**, C. Hopkins and B. Zeitler (2016), Finite element simulation of a laboratory reception plate for structure-borne sound power measurements, *Proceedings of the 45th International Congress and Exposition on Noise Control Engineering, Hamburg*, pp. 3734-3742.